N° d'ordre : 2867

Université Bordeaux I – Institut Européen de Chimie et Biologie

THESE

presentée par

RALF P. RICHTER

pour obtenir le grade de

DOCTEUR

Formation de Membranes Lipidiques sur Support Solide et Assemblage Bidimensionnel de Protéines.

Une Etude par Microscopie à Force Atomique et Microbalance à Cristal de Quartz avec Mesure de Dissipation.

The Formation of Solid-Supported Lipid Membranes and Two-Dimensional Assembly of Proteins.

A Study Combining Atomic Force Microscopy and Quartz Crystal Microbalance with Dissipation Monitoring.

Soutenue le 26 Octobre 2004

Après avis de :

Mme.	P. BASSEREAU, Directeur de Recherches CNRS, Institut Curie	Rapporteur
M.	B. KASEMO, Professeur, Université de Göteborg, CHALMERS, Suède	Rapporteur

Jury :

M.	B. DESBAT, Directeur de Recherches CNRS, Université Bordeaux I	Président
Mme.	P. BASSEREAU, Directeur de Recherches CNRS, Institut Curie	Rapporteur
M.	B. KASEMO, Professeur, Université de Göteborg, CHALMERS, Suède	Rapporteur
M.	J.-P. AIME, Directeur de Recherches CNRS, Université Bordeaux I	Rapporteur
Mme.	R. ODA, Chargée de Recherches CNRS, IECB, Université Bordeaux I	Examinateur
M.	A. BRISSON, Professeur des Universités, IECB, Université Bordeaux I	Directeur de thèse

Le doute est un état mental désagréable,
mais la certitude est ridicule.

Doubt is not a pleasant condition,
but certainty is an absurd one.

Voltaire, *Lettre à Fréderic le Grand*, 1767

Für meine Eltern,
pentru Cristina

Acknowledgements

I would like to express my sincere and full gratitude to Alain Brisson. You were a serious supervisor and team-builder that provided the environment, guidance and interest that I needed and desired. I am grateful that you have accepted and supported my commitment aside the PhD. Your sincere criticism, respect and clarity will be a benchmark for my future work.

It has been truly rewarding to have Bengt Kasemo in the jury. Without his advice, inside and outside science, during the last seven years, I would likely not stand where I am today. Thank you for having taken your time and effort to act as opponent!

Un grand merci à Patricia Bassereau qui a accepté d'être rapporteur et a pris le temps de lire et de commenter ce manuscrit.

J'exprime ma gratitude à Bernard Desbat, Reiko Oda et Jean-Pierre Aimé pour m'avoir fait l'honneur de présider et de participer à mon jury de thèse.

Mes profonds remerciements vont à l'équipe Brisson à Bordeaux pour son travail très efficace et son atmosphère fort stimulante aux interfaces scientifiques et « socioculturelles ». My thanks go also to the former team in Groningen.

My gratitude goes to Ilya Reviakine for having me introduced to the world of AFM and for many illuminating discussions around aspects of the work presented here. I sincerely acknowledge the discussions with Fredrik Höök throughout the years about issues related to the world of QCM-D. I am greatly indebted to Wim Hermens for sharing his experience in ellipsometry and adsorption kinetics upon his extended visit in Bordeaux and for allowing me to spend a short but very intense time in his lab in Maastricht. Thanks also to Aleš Benda and Martin Beneš for illuminating discussions around ellipsometry.

It is hard to pin down the effect of a few years in Sweden and at Q-Sense in a few words. Two years of pre-PhD experience in a company helped shaping the way I could approach my research project and allowed having a fresh vision on academic life. My sincere gratitude goes to all the people at Q-Sense for accepting my priorities and for providing full support during the PhD-time. I wish that this example encourages similar agreements between industry, academia and future PhD students. Tack ska ni ha!

Merci, tack, mulțumesc, bedankt, danke, hvala, ačiū, дякую, xiè xiè, ευχαριστώ, dziękuję… My thanks go to my friends, wherever they reside for the moment. The activities and insights outside my scientific world that you help create provide balance and stimulation.

Cele mai sincere multumiri Cristinei : pentru dragoste, incurajari, rabdare... Cu siguranta, nu am fost intotdeauna usor de suportat, cu precadere inaintea definitivarii tezei. Mi-as dori mult sa ne vedeti construindu-ne viitorul impreuna.

Meine tiefster und aufrichtiger Dank geht an meine Eltern. Die Fundamente für diese und kommende Arbeiten wurden durch Euch und Eure Erziehung gelegt. Die Erfahrung lehrt, wie wenig von dem, was man in jungen Jahren als selbstverständlich ansieht, es auch wirklich ist.

Table of Contents

I. Introduction

I.1. Objectives and Outline

A major aim in this work was to characterize, in detail, two self-organization processes of both fundamental scientific and biotechnological interest: the formation of solid-supported lipid bilayers (SLBs) and the ordering in two dimensions of proteins bound to SLBs. A second objective was to demonstrate the value of combining advanced surface-sensitive characterization techniques, in particular atomic force microscopy (AFM) and quartz crystal microbalance with dissipation monitoring (QCM-D) (and to some extent ellipsometry), in order to obtain a detailed description of self-assembly processes confined to two dimensions.

Chapter I will give a brief overview of the biomolecules involved in this study, the employed characterization techniques and the solid supports used. The approach taken to combine AFM and QCM-D on identical supports is presented in Chapter II. Two technical bottle-necks, the deposition of mica on QCM-D crystals and the control of the interaction between the AFM-tip and solid-supported lipid assemblies, had to be solved in order to take advantage of the complementarities of these techniques and are described. Chapter III covers the characterization of the formation of SLBs by the technique of vesicle spreading and addresses the question of how lipids are distributed between the SLB-leaflets. Chapter IV is dedicated to the adsorption and two-dimensional (2D) self-assembly of the protein annexin A5 on SLBs.

This work has given rise to several articles, published in or submitted to peer-reviewed journals. They constitute the scientific backbone of this thesis and are implemented in their original style. In order to put the work presented in these publications into a broader perspective and to shine light on relevant issues that are not explicitly covered by the articles, these are preceded by brief introductions.

Uniting physically advanced characterization techniques, biological specimens as well as material science behind solid surfaces, this thesis is part of a truly interdisciplinary enterprise. The scope of this work prohibits covering all aspects in detail and I ask for forgiveness (and feedback), in case specialists in each of the fields may discover some shortcomings in the presentation.

I.2.

Supported Lipid Bilayers

I.2.1. Lipids and their self-organization

Much of the fascinating properties of lipids result from the molecules' ambivalent attitude towards water. Lipid molecules typically consist of a hydrophilic head group and one or several hydrophobic tails, the combination of which determines their properties, including the self-assembly behavior.

I.2.1.1. The molecular properties of lipids

The most common lipids in biological membranes are phospholipids, their name stemming from the phosphate[i] found in their headgroups. The phospholipids' polar (and thus hydrophilic) headgroups can be distinguished by their size and charge (Figure I.1).

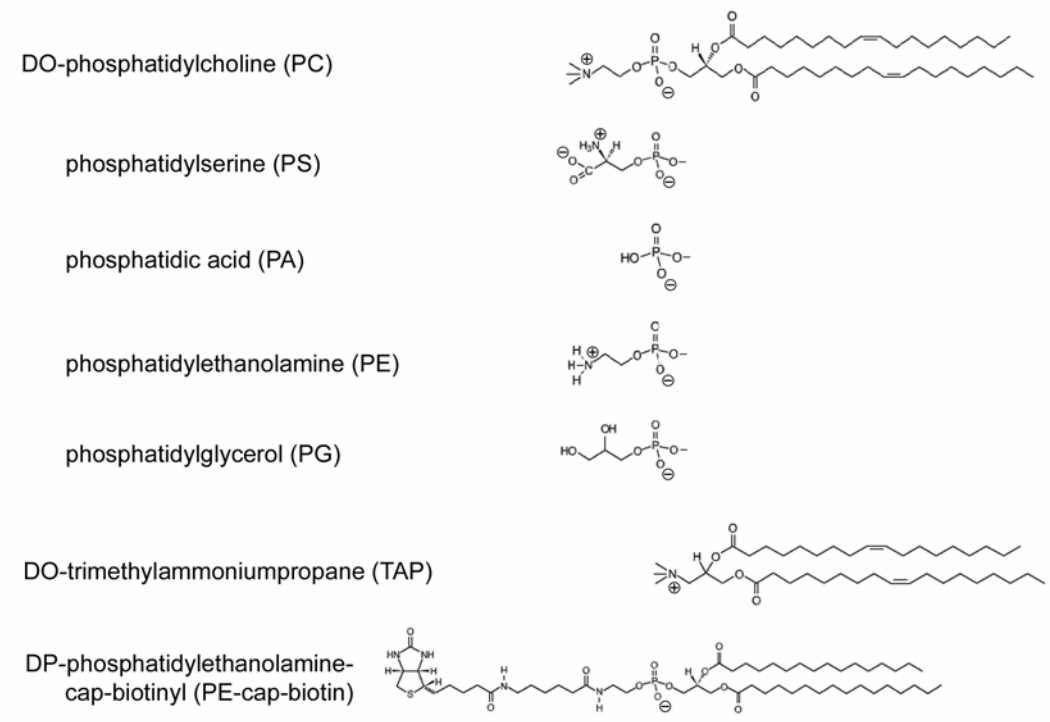

FIGURE I.1 Structure and nomenclature of some common lipid headgroups. Charges at around physiological pH are indicated. The amino group in PE and PS can be deprotonated at higher pH, while the carboxyl group in PS can be protonated at lower pH. The chemical link including the tails is added for DOPC, DOTAP and DPPE-lc-biotin. Counter ions were omitted for reasons of clarity.

In the frame of our study we used phosphatidylcholine (PC), essentially for the zwitterionic property of this naturally most abundant headgroup, and phosphatidylserine (PS), as it carries an overall negative charge at neutral pH. The list of headgroups relevant for our study is complemented by

[i] The presence of phosphorus provides a rather convenient way to quantify the overall phospholipid concentration in a given solution[1].

trimethylammonium-propane (TAP), an artificial, cationic group, earlier used to study the (electrostatic) interaction with nucleic acids[2,3], and biotinoyl-aminohexanoyl-phosphatidylethanolamine (PE-lc-biotin), designed for specific binding of streptavidin (Figure I.1).

The tails are non-polar (and thus hydrophobic) acyl chains. The length of the chains and the number of double bonds can vary substantially. Most common acyl chains have a length between 14 and 20 carbons and none or one double bond inducing a kink in the otherwise straight chain. Table I.1 summarizes the properties of some common tails and their nomenclature. Tail combinations used in our study were mostly di-oleoyl (DO), to form DOPC, DOPS and DOTAP, though di-palmitoyl (DP) was used for the biotin-tagged lipid (DPPE-lc-biotin).

TABLE I.1 Nomenclature and structure of some common lipid tails.

Name	Structure	Number of carbon atoms	Number of double bonds
Myristoyl (M)	$CH_3(CH_2)_{12}COO$-	14	0
Palmitoyl (P)	$CH_3(CH_2)_{14}COO$-	16	0
Stearoyl (S)	$CH_3(CH_2)_{16}COO$-	18	0
Oleoyl (O)	$CH_3(CH_2)_7CH{=}CH(CH_2)_7COO$-	18	1
Linoleoyl (L)	$CH_3(CH_2)_4CH{=}CHCH_2CH{=}CH(CH_2)_7COO$-	18	2

I.2.1.2. Self-assembly

The amphiphilic nature of the lipid molecules is at the origin of their tendency to self-assemble in aqueous solution. As the ordering of water in the environment of the hydrophobic tails is associated with entropic costs (the hydrophobic effect[ii]), the lipids self-assemble and form a shield of headgroups that hides the tails from the surrounding water[6,7].

The shape of the assembly depends on the molecular structure of its constituents and in a simple approximation, it can be determined by the shape factor[7] (Figure I.2, see figure legend for details). Lipids have been observed to assemble into a multitude of shapes, among them planar bilayers, micelles, hexagonal or inverted hexagonal phases and tubes (Figure I.2). However, the naturally most abundant self-assembly structure are bilayers. In this structure, two lipid monolayers are apposed such that the tails are sandwiched between two sheets of headgroups (Figure I.2).

[ii] Note that the fundamental concept of ordering of water is reassessed today as newly developing techniques allow probing the molecular structure of water at interfaces[4,5].

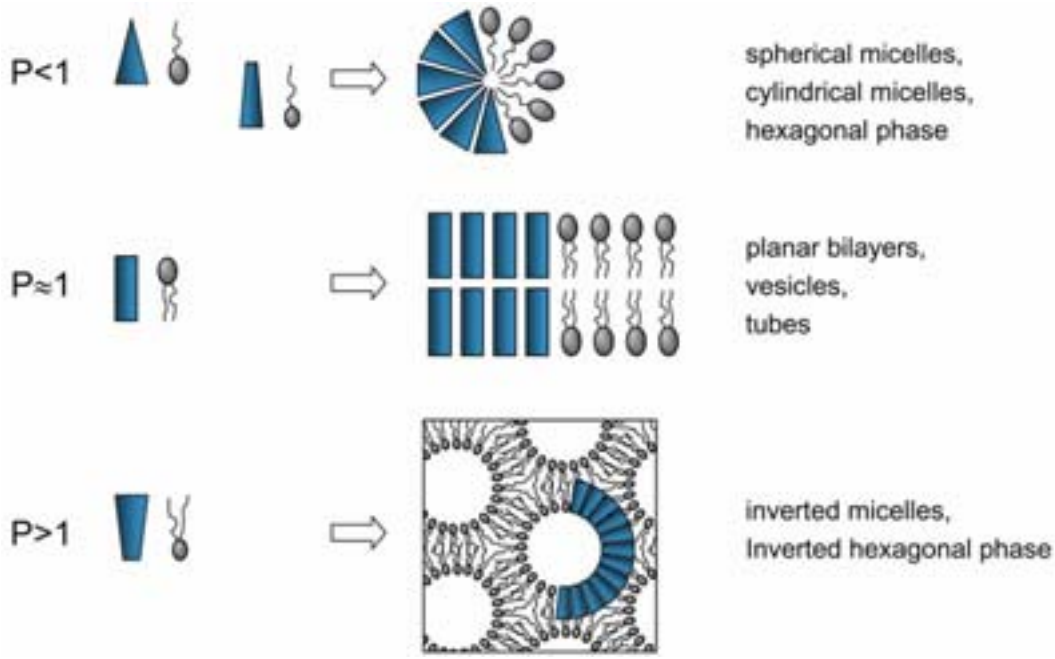

FIGURE I.2 Schematic presentation of various shapes of lipid assemblies. In a simple approximation[7], the shape of the assembly is determined by the shape factor, $P = \frac{\nu}{l_c}\frac{1}{a_0}$, with ν, a_0 and l_c being the volume occupied by the hydrocarbon chain(s), the optimal headgroup area and the critical chain length, respectively. P = 1 corresponds to an apparent cylindrical shape of the lipid molecules, leading to bilayer-like aggregates.

In the following, the influence of the headgroup and the tails on some essential properties of lipid bilayers is briefly summarized:

- Lipid bilayers exist in different thermodynamic phases, in particular the gel phase, L_β, and the liquid crystalline phase (henceforth called fluid phase), L_α. The phase transition temperature, T_m, increases with tail length and strongly decreases with the number of double bonds (Table I.2). Also, the nature of the headgroup and the presence of (divalent) ions can influence T_m. The coefficient of lateral diffusion is generally around a few $\mu m^2/s$ in the fluid phase[6] and decreases by at least two orders of magnitude in the gel phase. In mixtures of different lipids, separation between two thermodynamic phases can occur.
- The charge of the lipid bilayers is essentially determined by the charge of the constituting headgroups. Note that all (phospho)lipids are either charged or zwitterionic at neutral pH. The charges and/or the polarity of the headgroups can have various consequences on the interaction of the headgroups with its environment, i.e., surrounding lipids, ions or water.
- The surface area occupied per lipid molecule can vary considerably (Table I.2), depending on temperature, ionic strength, headgroup and tail. Double bonds in the tails tend to increase the surface area.
- Bilayers are highly selective in their permeability. While water can be shuttled rather fast (30-40 μm/s)[8] through fluid membranes, the membrane is highly impermeable to common ions, such as Na^+ (10^{-10}μm/s)[9] and Cl^- (10^{-7}μm/s)[9].

H^+ and OH^- are in the intermediate range ($1..10^{-4}$μm/s)[10]. Permeability is affected by the charge and the size of the molecules and by the composition of the membrane, in particular its cholesterol content.

- The solubility of lipid monomers in aqueous solution is in general very low (~10^{-10} M)[10] and decreases with the tail length. For comparison, the total lipid concentrations usually employed in our studies were in the range of 10^{-4} M. The residence time of lipids in the bilayer is typically in the range of hours[7,11].
- Due to the energy barrier associated to moving a polar headgroup through the hydrophobic interior of the membrane, the exchange of lipids between the two leaflets of a bilayer (flip-flop) is considered difficult. Flip-flop rates observed experimentally on non-stressed fluid bilayers are typically in the range of hours to days[11-13]. Flip-flop rates depend strongly on the headgroup composition and temperature and increase slightly with tail length[11,14].

TABLE I.2 Some basic properties of common lipids.

Lipid	T_m (°C)	Surface area per lipid [a), e)] (Å^2)	Molecular weight [f)] (g/mol)
DOPC	-22[e)]	72	786.15
DPPC	41.3[e)]	44.5	734.05
egg PC [b)]	-15[e)]	62	760.09 [h)]
DPPE	63[e)]		691.97
egg PE [b)]		42	744.05 [h)]
DOPS	-11[f)]	67[g)]	810.04
PS [d)]		50-100[c)]	
DOTAP	~0[f)]		698.55
DPPE-CAP-biotin			1053.40

[a)] at room temperature; [b)] from egg-yolk; [c)] surface area depends on pH and presence of multivalent ions; [d)] from beef brain; [e)] from ref. [6]; [f)] from ref. [15]; [g)] in 100 mM LiCl, pH 7.4, from ref. [16]; [h)] average molecular weight

Lipid bilayers constitute the two-dimensional continuum into (and onto) which proteins are embedded (and attached), forming highly complex and dynamic assemblies: biological membranes.

I.2.2. Biological membranes and their models

Biological membranes play key roles in cell life, acting as transporters, barriers or communicators between the inside and outside cellular worlds and participating in various intra- and extracellular processes.

The history of unraveling the nature of biological membranes[6,17] is an excellent example for truly interdisciplinary work, inspired by biology, chemistry and physics over the 20th century. Using the film balance, developed by Langmuir[18] shortly before, Gorter and Grendl[19] determined that the surface area covered by a monolayer of lipids extracted from red blood cells corresponded to about two times the outer surface of red blood cells. Although their calculation contained

some errors, they concluded correctly that the cells are covered by a bilayer. Robertson, confirming this observation by electron microscopy, proposed the bilayer structure to be universal for all cells and organelles[20]. Later, differential scanning calorimetry, X-ray diffraction, magnetic resonance methods and fluorescence[21] provided evidence for phase transitions in membranes, the structure and flexibility of the bilayer and the mobility, in two dimensions, of the incorporated lipids[22]. These ingredients, together with the notion of peripheral and integral membrane proteins, formed the building stones for the fluid mosaic model by Singer and Nicolson[23] (Figure I.3).

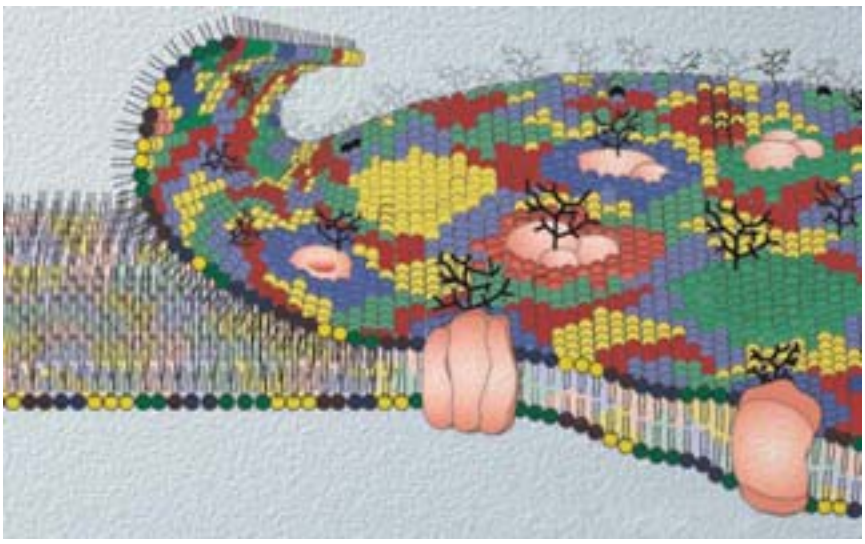

FIGURE I.3 The fluid mosaic model for biological membranes as initially proposed by Singer and Nicolson[23]. Adapted from ref. [17].

Since the end of the 80's, it has been increasingly recognized that lipids and membrane proteins can segregate into nm- to μm-sized dynamic domains that fulfill distinct biological functions, such as sorting, trafficking and signaling[24-28]. Also the dynamic aspects of the asymmetry of lipid distribution between the leaflets of an SLB have been recognized[29,30]. It should be born in mind that the plasma membrane for some cells is renewed within about one hour[31], reflecting that not only the membrane itself but also its interaction with the environment is highly dynamic. These investigations have been made possible by advances in techniques with high spatial or temporal resolution such as atomic force microscopy, nuclear magnetic resonance (NMR) or various fluorescence techniques.

Solving the enigmas of membrane structure and function has always required the interplay between investigations of whole cells and of simplified models of biological membranes. Some of them are liposomes and giant vesicles in solution, lipid monolayers at the air-water interface, black lipid films, membrane patches at pipettes and solid-supported membranes (Figure I.4). The model systems that are used in this study, unilamellar vesicles and supported lipid bilayers, will be described in more detail.

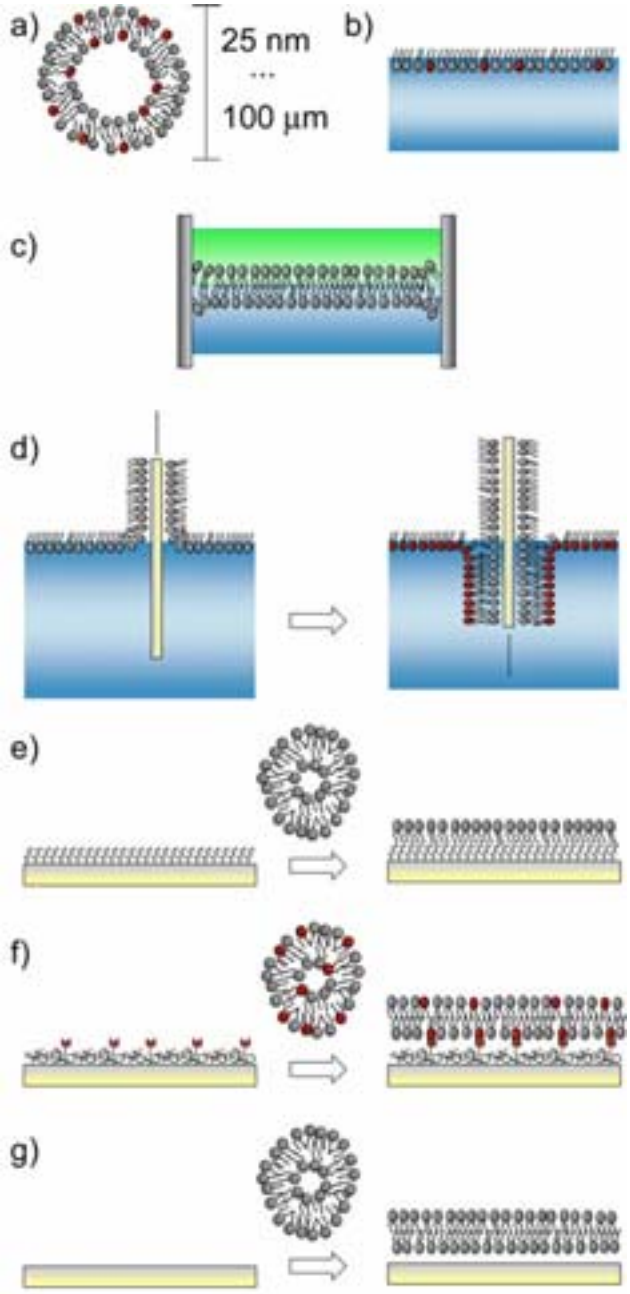

FIGURE I.4 Models of biological membranes: (a) liposomes: hollow spheres (25 nm to 100 µm in diameter) enveloped by a bilayer of lipid molecules; (b) lipid monolayers at the air-water interface; (c) black lipid membranes suspended over an aperture between two aqueous phases; (d) Langmuir-Blodgett method, which allows the transfer of lipid mono- and multi-layers from the air-water interface to a solid support; (e) self-assembled monolayers (SAMs, e.g., thiols on Au or silanes on glass or silica), a second lipid layer can be deposited by spontaneous disruption of liposomes; (f) deposition of a polymer coating with tethers followed by the spontaneous spreading of liposomes, so that the polymer creates a cushion between support and bilayer; (g) spontaneous spreading of liposomes or membranes on mica, glass, and silica.

I.2.2.1. Unilamellar vesicles

Since the establishment of vesicles (or liposomes) as model systems in the 60's a multitude of preparation techniques[32-34] has emerged to create unilamellar vesicles, among them sonication, extrusion[35], detergent dialysis, reverse phase

evaporation[36], solvent injection[37,38], or electroformation[39]. With this battery of methods unilamellar vesicles with a mean radius ranging from ~10 nm (by sonication) up to ~50 µm (by electroformation) and a more or less narrow size distribution[iii] can be prepared.

Consisting, in their most simple form, of a closed bilayer that separates an inner compartment from the outside, these systems allowed, in conjunction with theory, to study a multitude of principle features of lipid bilayers, such as their mechanical properties[42-46], membrane adhesion and fusion[43,47], membrane permeability[48] or lipid diffusion in membranes.

In our studies, sonicated unilamellar vesicles (SUVs) where employed (for a preparation procedure see ref. [49]). Each of these small vesicles with a mean diameter between 20 and 30 nm accommodates around 3000 lipid molecules. The SUVs' high curvature induces constraints on the packing of lipids that can lead to an asymmetrical distribution between the inner and the outer leaflet both in number (60-75% of the total lipid content reside in the outer leaflet[6,34]) and in species[34,50]. Also, the amount of confined water is rather small, making up less than 30% of the total vesicle volume. Even though SUVs are likely not thermodynamically stable, the barrier for spontaneous fusion into larger vesicles is so high, that they can remain trapped in their metastable phase for weeks or months under appropriate storing conditions.

I.2.2.2. Supported lipid bilayers

Following the pioneering work by McConnell and collaborators[51], (models of) biological membranes deposited on solid supports have become very popular[52,53], both for studying basic membrane processes and for possible biotechnological applications[54-56]. The growing interest in confining (model) membranes on surfaces has been nourished by the emergence of a multitude of surface-sensitive characterization methods (see below), advanced surface patterning methods[55,57-60] and liquid handling systems (microfluidics)[61].

A multitude of methods has been proposed to create supported lipid bilayers (SLBs) and related hybrid forms, the most common being Langmuir-type approaches (Langmuir-Blodgett or Langmuir-Schäfer deposition)[62-65], micelle dilution[66,67] and, in particular, the spreading of vesicles on various preconditioned supports (Figure I.4)[57,64,68-72]. Each method provides model membranes with particular characteristics in their capacity to mimic certain parameters of a biological membrane, their quality and their stability and, consequently, may find use in different applications.

Different characterization techniques have traditionally been used to investigate the physico-chemical and structural properties of respective surface-confined lipid structures. The physical parameters measured by different techniques are often not straightforwardly comparable (see also below). As an example, single residual

[iii] It is often neglected, though, that the size distribution of vesicles can be rather large and that its determination is not a trivial task[40,41].

vesicles are immediately apparent by atomic force microscopy (AFM) (under proper imaging conditions, see also Chapter II), while the persistence of such small defects would hardly be detected by optical methods such as fluorescence recovery after photobleaching (FRAP). Comparative approaches to characterize the bilayer quality with a multitude of techniques or to characterize different approaches of bilayer preparation with the same technique[64,68] are yet rare, which makes it difficult to compare the quality of supported lipid membranes formed by different methods.

The formation of SLBs by spontaneous deposition of vesicles on hydrophilic solid supports is attractive by its simplicity. It has been demonstrated that SLBs with very few defects can be formed with this one-step procedure (see Chapter III). The fact that SLBs form a fluid two-dimensional space allowing free diffusion in translation and rotation of lipid molecules and lipid-associated proteins makes them well suited to analyze lipid domain formation[73-81], intermembrane interactions[82,83] or membrane processes such as protein adsorption[84,85], protein self-assembly[74,77,86], protein localization at lipid phase boundaries[87], and protein function[63].

However, a comprehensive physical understanding of the driving forces and structural intermediates in the SLB-formation process started to emerge only recently. Both theoretical and experimental work during the last decade has considerably improved the understanding of the mechanisms underlying the formation of SLBs. Interestingly, the choice of the solid support appears critical for the formation of an SLB. While SLBs form on silica, glass, or mica, they do not form on gold or (in some cases) TiO_2 in otherwise identical conditions. A better understanding of the mechanisms of SLB formation – with extensive interaction between theory and experiments – will improve the preparation of SLBs and other surface-confined lipid structures, such as tethered[88,89], polymer-cushioned[64,72,90] or pore-spanning[91,92] lipid membranes. Elucidating the formation of SLBs is one focus of the work presented in this thesis. The results, together with a brief overview of the mechanisms involved in and the parameters influencing SLB-formation are presented in Chapter III.

I.3. Annexin A5

I.3.1. Fundamentals and biological function

The protein annexin A5 constitutes a member of the annexin superfamily (reviewed in refs. [93,94]). These proteins share the property to interact with negatively charged lipids in a calcium dependent manner. While the C-terminal is highly conserved among the annexins and comprises the (primary) sites for membrane binding, their individuality is determined by the variable N-terminal. For annexin A5, the N-terminal is short, which makes it the prototype of the annexins.

While the function of annexin A5 (as that of most other annexins) is presently not well understood, it has been proposed to be involved in membrane-related processes, such as the inhibition of blood coagulation[95,96], acting as protective shields against thrombosis[97,98].

Besides functional aspects, annexin A5 is particularly interesting for biotechnological applications as it combines (at least) three attractive properties: (i) reversible adsorption to membranes that can be tuned by the Ca^{2+}-content in solution and by the DOPS-content in the membrane, (ii) the ability of the membrane-bound protein to form extended two-dimensional (2D) assemblies of controlled structure and (iii) very good long-term stability.

I.3.2. Structure and membrane binding properties of Annexin A5

The monomer of annexin A5 (Figure I.5a) consists of four domains, each of them being around 70 amino acids long and consisting of five alpha helices, making up a total mass of 35 kDa. In side-view, annexin A5 presents an overall flat, slightly curved shape (Figure I.5b). X-ray crystallographic data has revealed a (varying) number of bound calcium ions, all of them being located in peripheral loops at the convex side of the molecule[93,99,100]. Annexin A5 binds with its convex side to the membrane, and the Ca^{2+}-binding sites have been implicated in the membrane interaction[93]. Little is, however, known about their exact role and stoichiometry. The overall structure of annexin A5 appears to change little upon binding to the membrane[101] (see also below) and the geometry of membrane and annexin A5 suggests a close proximity between a large part of the convex periphery of annexin A5 and the lipid headgroups[102]. Fluorescence measurements, though, indicate a conformational change in a loop in domain III that contains the molecule's only tryptophan at position 187 (Trp-187)[103,104]. In accordance, two different 3D structures have been found. While otherwise being identical, the loop was buried in the interior of the domain (and no Ca^{2+} binding was present there) in one structure[100,105], whereas the loop stuck out and bound Ca^{2+} in the other structure[106,107]. More recently, it has been confirmed that the protein can also bind to pure DOPC and to pure cholesterol monolayers at high Ca^{2+} concentrations[108].

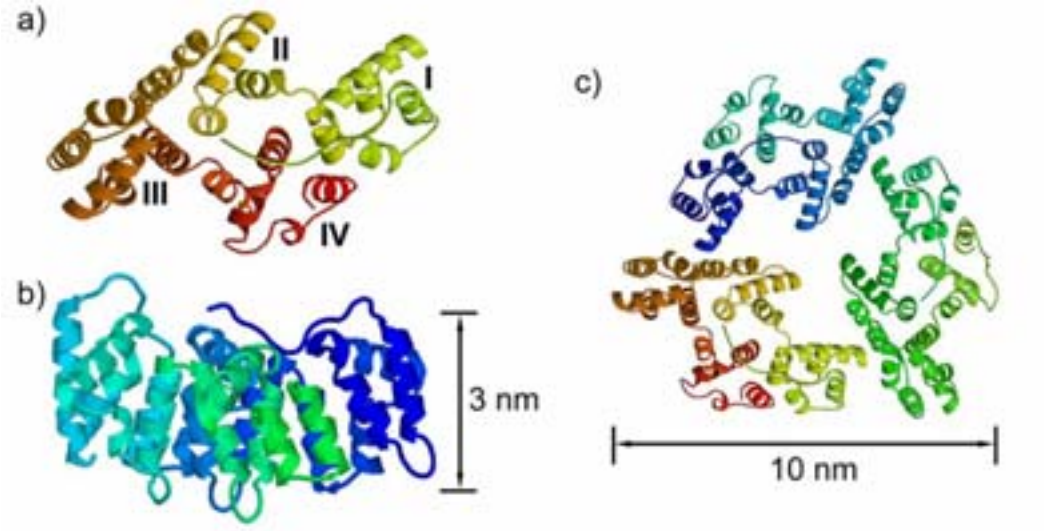

FIGURE I.5 Atomic model of annexin A5. (a) Top view of a monomer of annexin A5 with annotated domains[100]. (b) Side view of a monomer. The lower (convex) side binds to the membrane. (c) The crystallographic trimer[106] viewed along the three-fold axis (top-view). Adapted from ref. [101].

I.3.3. Self-assembly of Annexin A5

When confined in two dimensions, as by the adsorption to lipid bilayers (mica-SLBs[109]) or to monolayers (at the air-water interface[110]), annexin A5 is commonly observed to undergo supramolecular self-assembly[111]. The self-assembly steps involved are schematically shown in Figure I.6.

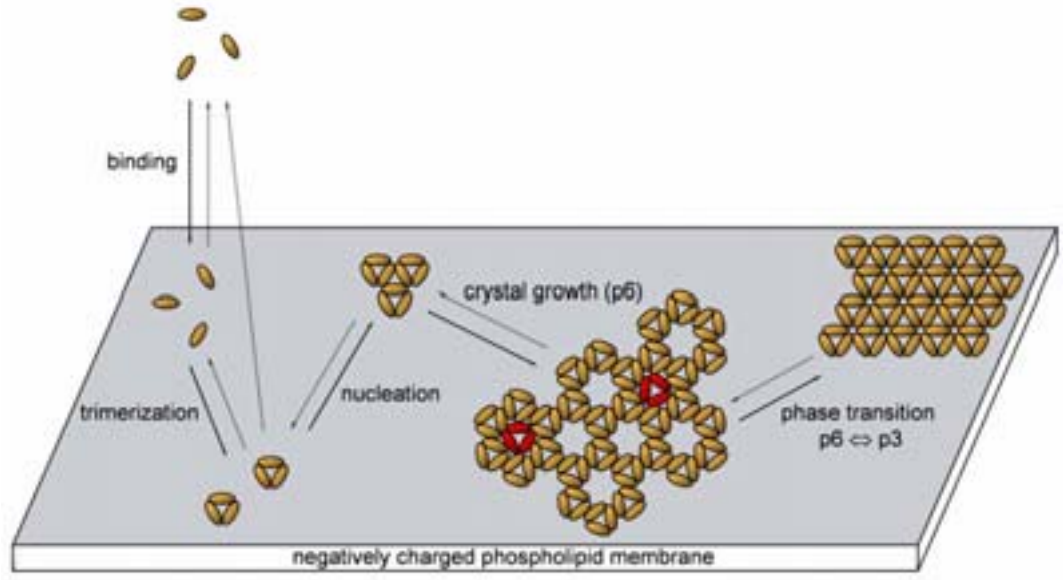

FIGURE I.6 Scheme of the 2D self-assembly of annexin A5 on a negatively charged phospholipid membrane[108,112]. Monomeric annexin A5 binds to the membrane in a calcium-dependent manner where it forms trimers. The trimers crystallize in two dimensions. The holes in the honey-comb-like p6-lattice can be filled by additional non-crystalline trimers (marked in red), also called "central trimers". At high protein coverage, a transition into a more densely packed crystal form (p3) can occur.

Annexin A5's most common 2D crystalline assemblies exhibit p3 or p6 symmetry, though other forms have also been observed[113]. Reviakine et al. have demonstrated that the transition between the low density p6-crystal and the high density p3-crystal is reversible on mica-SLBs containing DOPS, concluding that this solid-solid phase transition is of first order[112]. Importantly, a trimer of annexin A5 (Figure I.5c) was identified as the building block not only in all two-dimensional crystals of membrane bound annexin A5[113] but also in all reported three-dimensional crystals of the soluble protein[99].

Isolated membrane-bound trimers have frequently been observed in non-crystalline form underlining the stability of this oligomer confined in two dimensions. In strong contrast, trimers could not be observed in solution under physiological conditions[108]. As the structural differences between surface-bound and soluble annexin A5 are rather small it may be tempting to attribute the protein's propensity for trimerization and crystallization to short-ranged and orientation-dependent attractive interactions that can act in a significant manner only when the protein is suitably pre-oriented, such as by the binding to the membrane. Indeed, a rather simple model based on localized short-range interactions with strong orientation-dependence was able to reproduce the main features of the phase transition between the crystalline states of annexin A5[114].

While the structural intermediates and the final states in the process of adsorption and self-assembly of annexin A5 have been investigated extensively[108], comparably little is known about the kinetics of this process. The kinetics is expected to be of relevance both for the biological function of annexin A5 and for its biotechnological applications. The characterization of the kinetics of adsorption and self-assembly, presented in Chapter IV, constitutes a second focus in this work. Our investigations also revealed some surprises about the self-assembly of annexin A5 on SLBs formed on other surfaces than mica. Notably, we find that the 2D-crystallization is strongly constraint on SLBs formed on silica or glass.

I.4. Characterization techniques

The emergence of research fields coined by terms such as "nanotechnology" and "biotechnology" would not have been possible without the development of advanced characterization techniques that link the nanoscopic, microscopic and macroscopic levels. The ideal of an analytical tool that can see and measure everything from the size of an atom to the size of a cell, however, is likely to remain a distant goal for some time ahead. Each technique presents advantages and limitations in terms of the parameters characterized, the required environment, the invasiveness, the resolution in time and space. Consequently, a multitude of methods is necessary to give a comprehensive picture of relevant parameters and to allow for the identification of artifacts. Complementary aspects and *in situ* combination on the same specimen promise results that are more than just the sum of the results of the constituent techniques.

Interfaces, in particular solid-liquid interfaces, constitute by their nature a playground for many particular physical effects. Utilizing these effects, a multitude of surface-sensitive techniques has emerged over the last century. Some methods exploit the interface for the generation of a measurable signal (such as surface plasmon resonance (SPR)[115], ellipsometry[116], sum-frequency generation (SFG)[117], fluorescence interference contrast microscopy (FLIC)[118,119], reflection interference contrast microscopy (RICM)[120] or the surface force apparatus (SFA)[7]), its confinement (total internal reflection fluorescence microscopy (TIRFM)[121], total internal reflection microscopy (TIRM)[122], surface-plasmon fluorescence spectroscopy (SPFS)[123]) or its enhancement (surface-enhanced Raman scattering (SERS)). Other techniques simply utilize the interface in order to immobilize the sample and/or to confine it into two dimensions (atomic force microscopy (AFM), quartz crystal microbalance with dissipation monitoring (QCM-D))[iv].

For the studies presented here, we have made extensive use of several surface-sensitive methods. Whereas AFM, QCM-D and the combination of both techniques (see Chapter II) constitute the main focus, results were further complemented by ellipsometry. A common denominator of these techniques is their applicability in aqueous environment, close to physiological conditions. However, the measurement principles and thus the extracted parameters differ substantially. In the following a brief overview of the techniques is given and some complementarities are outlined.

I.4.1. Atomic Force Microscopy (AFM)

Since the invention of the scanning tunneling microscope[124] a vast range of scanning probe techniques has seen the day. The working principle is the same for all of them: a tiny probe moves over a sample with (sub-) nanometer precision in

[iv] The list of enumerated techniques, all of which are applicable in liquid environment, is supplemented by a large range of surface characterization techniques that operate in air or in vacuum, such as scanning tunneling microscopy (STM), scanning electron microscopy (SEM) or X-ray photoelectron spectroscopy (XPS).

order to detect local physical or chemical (or biological) properties. Probably the most prominent member of these techniques today is the AFM[125,126], which allows to take a direct look and touch on objects in the nanometer scale in virtually any environment. In the following, I will focus on the application of AFM in liquid.

I.4.1.1. The working principle

In the AFM a microscopic probe (the tip) is mounted on a soft cantilever, the deflection of which can be monitored with high precision by an optical detection system (Figure I.7). The sample is moved with respect to the tip by means of piezoelectric elements (the scanner) and the interactions between the apex of the tip and the sample are controlled by a feedback loop. Consequently, information about the surface topography of the sample, but also about the interaction forces between tip and sample (both normal forces and friction) can be obtained.

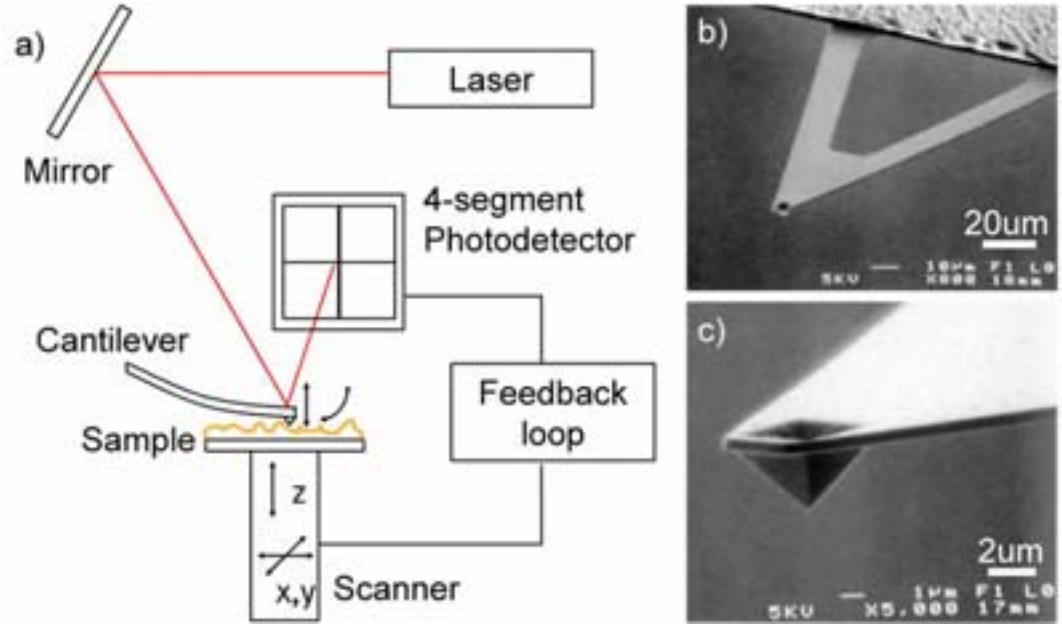

FIGURE I.7 (a) Schematic presentation of the AFM-setup. (b) Scanning electron micrograph of a cantilever commonly used for measurements in fluid. The AFM-tip is situated at the end of the cantilever (c).

In order to illustrate the sensitivity and geometry of the AFM-setup we may substitute a molecule as small as a protein by a medium-sized strawberry. This would imply that we were to use a tip the size and the shape of the pyramid in front of the Louvre in Paris to scan the contours of the fruit. Moreover, with today's resolution it would (almost) be possible to detect the seeds on the surface of the strawberry![v] With a cantilever spring constant, k, of a few 10 mN/m and a sensitivity in the measurement of the deflection, x, of better than 1 Å, forces $F = k \cdot x$ in the order of pN can in principle be detected.

[v] In order to be consistent with the pressure exerted between tip and sample, however, the strawberry should stand the pressure of a heavy motorbike parked on it.

In the traditional and most straightforward mode of operation, the tip is maintained in permanent contact with the sample while scanning over it (*contact mode*) (Figure I.8a). Normal forces can be kept at a low level (50-100 pN) by adjusting the cantilever deflection with the feedback loop. Lateral forces, however, may reach considerably higher values[127], in particular upon approach of specimens with high aspect ratio, and can significantly perturb soft samples. This limitation was overcome by promoting the oscillation of the cantilever and measuring the modulation in amplitude induced by the vicinity of the sample as a signal instead of the static deflection of the cantilever (*tapping mode*) (Figure I.8b). Tapping mode is better adapted for imaging molecules with high aspect ratio, such as isolated proteins, fibres or nucleic acid strands (DNA). The intrinsic resolution of tapping mode is though somewhat lower[128] and, consequently, contact mode remains a valuable alternative for high-resolution imaging of samples with small surface corrugations, such as protein two-dimensional crystals[109,129-131].

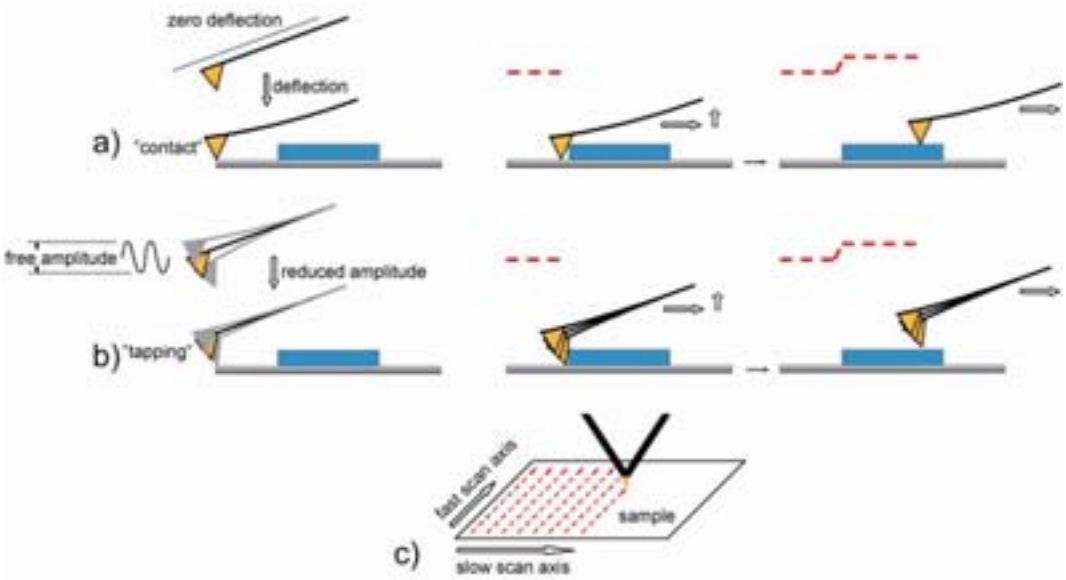

FIGURE I.8 Schematic presentation of the two most common AFM-imaging modes. (a) Contact mode: the tip is approached towards the sample until a predefined cantilever deflection is reached. Upon scanning, the deflection (force) is maintained constant by adjusting the distance between tip and sample. The normal movement of the tip with respect to the sample gives the topographic information (height image, *red dotted line*). (b) Tapping mode: The amplitude of the vibrating cantilever is reduced upon approach. During scanning the amplitude is maintained constant. The normal movement of the tip with respect to the sample gives the topographic information (height image, *red dotted line*). (c) The sample is scanned line by line (*red dotted arrows*). The direction in which the scan line (the line pattern) is traced defines the fast (slow) scan axis.

I.4.1.2. Biological AFM

The potential of AFM in aqueous environment became apparent soon after the introduction of the AFM, when biological specimens could be characterized with molecular resolution[132,133]. By now a great variety of biomolecules - proteins, lipids, nucleic acids - and their assemblies, up to the level of cells[134] and organelles[135], has been taken “under the tip” in order to be imaged, pulled or moved.

Due to their biological relevance and potential biotechnological applications, lipid assemblies have been attractive objects for AFM-investigations. The possibility of forming supported lipid membranes flat on the nanometer scale, made of various lipid compositions, has allowed for detailed studies of phase transitions[127,136-138], domain formation[74,75,77-80,139-141] and the interaction of proteins[73,87,142,143] or peptides with membranes[77,144]. Numerous studies have reported on the physical properties of SLBs and SLB-patches[75,145-148] or immobilized vesicles[137,149-151]. Until recently, however, surprisingly few studies were dedicated to the kinetic aspects of SLB-formation[152-154]. The experimental difficulties associated with imaging different lipid structures (see Chapters II and III) may provide an explanation.

2D crystalline assemblies of membrane (bound) proteins have early been identified as promising objects to obtain sub-nanometer lateral resolution[127,133,155]. In conjunction with other structural methods (X-ray crystallography and transmission electron microscopy), structural questions could be settled, such as subunit stoichiometry[156], handedness[157] and tilt[158]. Thanks to its application *in-situ*, dynamic aspects of molecular structure and function could be mapped[159,160]. A milestone, in particular with respect to the studies presented in Chapter IV, is the monitoring of the self-assembly of annexin A5 into 2D crystals by Reviakine and coworkers[112,142].

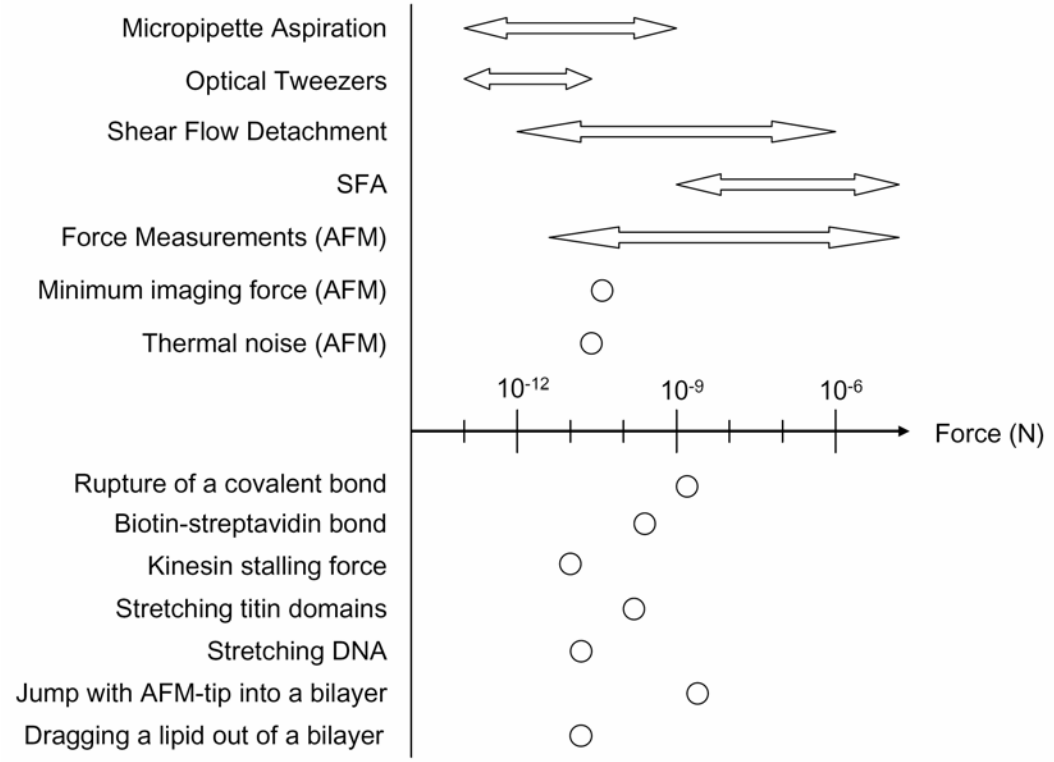

FIGRUE I.9 Forces commonly observed for the interaction of biomolecules and their assemblies (lower panel). The upper panel shows the force range accessible by AFM and other techniques.

In comparison to 2D crystals, high-resolution imaging of less ordered assemblies has proven more difficult, though some successes have recently been reported[161-163]. With the recognition of the role that fibrous structures play in many diseases

(Alzheimer's disease, prion-mediated diseases, late-onset diabetes), AFM has become attractive to study the structure and formation of amyloid fibrils[164,165]. On the level of single molecules, structural aspects of DNA have been mapped[2,166] and changes in coiling and polymerase activity could be followed in real time[167-169]. Despite some remarkable exceptions[73], the imaging of single proteins has proven difficult[127,170].

Apart from imaging, important contributions in the characterization of biomolecules came from force measurements[171]. By pulling on single molecules, the AFM allowed exploring mechanical and thermodynamic properties such as the resistance to external force[172,173], the unfolding of proteins[174] or DNA[175] and the unzipping of proteins from membranes[176]. Figure I.9 may give an impression of the force range covered by biomolecular interactions and the force range accessible by AFM and other techniques.

I.4.1.3. The intricate interaction between tip and sample

Literature is rich in examples on the multitude of effects that can come into play when an AFM-tip, mediated by the aqueous environment, gets in touch with a (soft) specimen. Illustrative examples are the delicate role of solution ions in the immobilization and high-resolution imaging of DNA[166,168,177] and proteins[178-181], the notorious overestimation of the width of DNA[127], the relative ease with which many protein 2D-crystals can be imaged as compared to non-ordered protein assemblies or isolated proteins[170], the effect of electrostatic interactions on the apparent height of lipid bilayers[180] or proteins[182], tip-induced lipid ordering[183] or the "water-ski" effect[145] and contrast inversion[75,146] that occur on lipid bilayers upon modulation of scanning speed or force.

From the understanding of such phenomena unique approaches to characterize specimens at the nanometer scale have emerged. Some of them are the mapping of surface charges[184-186] down to submolecular level[187], the monitoring of tip-induced conformational changes in proteins[129] and lipid assemblies[148,188] or the development of functionalized AFM-tips or supports[189].

While these developments broaden the range of applications for the AFM they also clearly demonstrate the intricacy of AFM-imaging[127]. Many things need to come together to allow for the proper imaging of biological specimens, importantly, (i) the proper immobilization of the sample, (ii) a well defined and appropriate tip-shape and (iii) a well controlled interaction between tip and sample. Despite tremendous advances and a longstanding recognition of these aspects, imposed constraints remain substantial and generic approaches to tackle these limitations are scarce. Therefore, the AFM investigation of biological specimens remains a task that requires advanced experimental skills, patience, and a profound understanding of what is happening when the AFM-tip touches the sample (for illustration see also Chapters II and III).

Thanks to its application *in-situ*, the AFM features the unique potential to follow, with a spatial resolution in the (sub-)nanometer range, the kinetics of processes in real time. However, a limiting factor to date is the time of image acquisition being in the range of minutes for commercially available AFMs. With the advent of

short cantilevers[190], modified experimental design[191,192] and controllers[193] an image acquisition rate of one second has become reality[191], joined with an enhanced force sensitivity[190]. While these advances are very promising, it remains to be demonstrated that they can be combined with high lateral resolution.

I.4.2. Quartz Crystal Microbalance with Dissipation Monitoring (QCM-D)

The QCM-D technique, based on the traditional quartz crystal microbalance (QCM), was developed in the 90's by Rodahl and coworkers[194]. Enabling the quantification of deposited masses and the characterization of the viscoelastic properties of thin layers, the technique has by now become an established tool in research relating surfaces and soft matter.

While the adsorption of proteins to solid supports[195-198] was one of the first applications, various biologically relevant questions have since been investigated by QCM(-D), such as the action of enzymes[199], the hybridization of nucleotide strands[200,201]; functional aspects of supported lipid membranes (SLBs)[202-206], DNA-drug interactions[207], protein cross-linking[208,209], the adhesion and spreading of cells[210,211].

Thanks to monitoring the dissipation (D), the QCM-D is more than a mass sensor, providing additional information about the structural state of the adsorbed film. This renders the technique particularly promising as a characterization technique for the development and validation of bio-functionalized surfaces[59,212,213] for biomedical, sensing[214] or bio-chip applications. Some examples, besides supported lipid bilayers[49,69,206,215-220], are polyelectrolyte multilayers[221-224], thin polymer coatings[225] or anti-coagulant coatings[226-228].

I.4.2.1. The working principle

The QCM-D technique is based on measuring the resonance behavior of a quartz crystal oscillator operating in shear mode. Due to its piezoelectric properties, the mechanical oscillation of the quartz can be excited by applying an oscillating electric field across the crystal. Once excited, the free mechanical oscillation can be monitored by measuring the decaying electric field. From the decay curve the resonance frequency, f, and the dissipation, D, are deduced (Figure I.10, see the figure legend for details). Tracking the changes, Δf and ΔD, of the two parameters, induced by the deposited material, allows characterizing adsorption processes and structural changes of the surface adlayer in real time. The time resolution of the QCM-D technique is in principle limited by the decay time of the oscillation (range of milliseconds). Today's instruments commonly operate at a resolution slightly better than one second, an important difference to the time resolution of the AFM (see Chapter II).

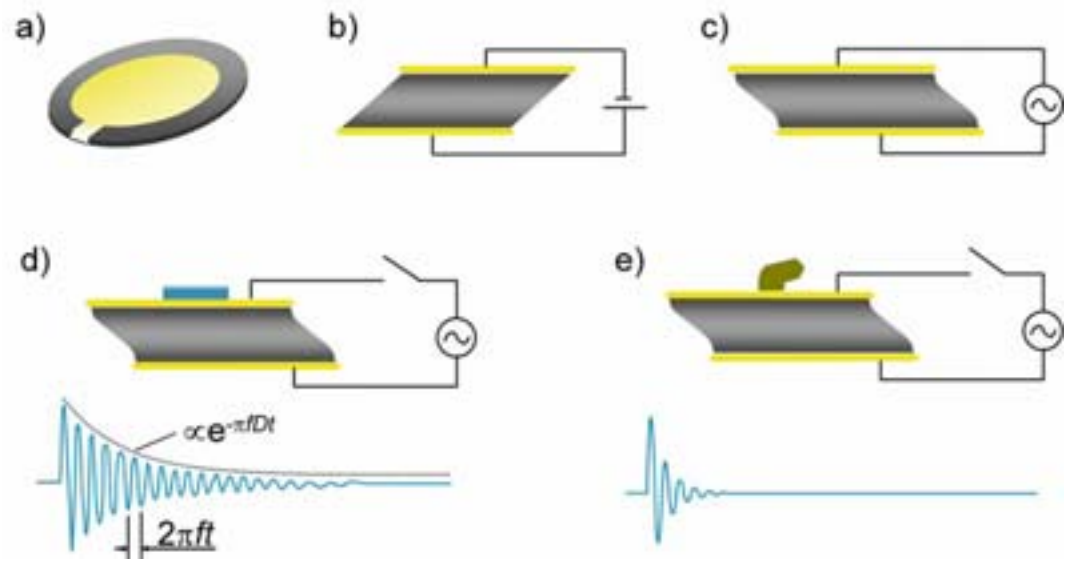

FIGURE I.10 Schematic presentation of the QCM-D working principle. The piezoelectric quartz crystal is sandwiched between two gold electrodes (a). The application of an electric field across the crystal results in shear motion of the crystal (b). Resonance in the shear motion can be excited with an oscillating field of appropriate frequency (c). After cutting the driving circuit, the freely decaying oscillation of the crystal is monitored (d, e). The temporal change in the crystal's movement, $A(t)$, can be fitted by $A(t) = A_0 \exp(-\pi f D t)\sin(2\pi f t + \phi)$ in order to extract the resonance frequency, f, and the dissipation, D (D is the reverse of the well known Q-factor). Attachment of a rigid mass (d) to the crystal's surface will only lead to a decreases in f, while a soft (viscoelastic) mass (e) will also affect D. Monitoring changes in f and D allows thus to follow interfacial processes in real time.

I.4.2.2. Determining adsorbed masses

Already in the 50's Sauerbrey[229] derived a simple relationship between the adsorbed mass, Δm, and the change in frequency, Δf:

$$\Delta m = -\frac{\nu_q \rho_q}{2 f_0^2}\frac{\Delta f_n}{n} = -C\frac{\Delta f_n}{n}, \qquad (1)$$

which laid the fundamentals for the conventional use of the QCM as a mass sensor. The speed of sound, $\nu_q = 3340\ \mathrm{m\cdot s^{-1}}$, and the density, $\rho_q = 2.65\ \mathrm{g\cdot cm^{-3}}$ are properties intrinsic to the quartz, while the fundamental frequency, f_0, is determined by the thickness, t_q, of the quartz plate (to a first approximation, $f_0 = \upsilon_q / 2t_q$) which can be reproduced with an accuracy of far better than 1%. The mass sensitivity constant, C, is thus independent from the adsorbate and determined without any further need for calibration. For commonly used sensors ($f_0 = 5$ MHz), $C = 17.7\ \mathrm{ng\cdot cm^{-2}\cdot Hz^{-1}}$. The resolution in frequency is currently in the range of 0.2 Hz (in liquid), corresponding to a mass resolution of a few $\mathrm{ng\cdot cm^{-2}}$. Apart from the oscillation at the fundamental mode ($n = 1$), higher harmonics can also be excited ($f_n \approx nf_0$ with the overtone number, $n = 3, 5, 7$).

While thin film monitors based on the Sauerbrey equation do an excellent job in many applications in air and in vacuum, it is important to note that the equation is vstrictly valid only for adsorbed masses that are (i) small (compared to the mass

of the crystal), (ii) evenly distributed, (iii) rigid and (iv) coupled with no slip. Out of the enumerated limitations, the constraint on rigidity is particularly severe for biological applications. As both the bulk liquid and most biomaterials are soft matter, equation (1) becomes an approximation of *per se* uncertain accuracy.

I.4.2.3. The dissipation

In contrast to rigid films, the viscoelastic properties of soft matter give rise to energy dissipation ($\Delta D > 0$). Consequently, monitoring of the dissipation has resulted in a couple of substantial improvements in the characterization of soft matter, both on the qualitative and on the quantitative level.

Qualitatively, the dissipation allows to trace phase transitions, i.e. to distinguish between different "adsorption states" of the surface-bound material. This is particularly illustrated by its capacity to distinguish between intact adsorbed vesicles and supported lipid bilayers (SLBs). This distinction, first reported by Keller and Kasemo[69] has pioneered significant advances in the understanding of the process of SLB-formation[49,215,218]. Other examples are the stiffening of a protein film upon crosslinking[208] or the hybridization of immobilized nucleotide strands[200]. Minor differences in the adsorption behavior and in particular its coverage dependence are best visualized in the ΔD-Δf-plot, and can serve as a marker for anomalous adsorption (for an example see figure 2 in Paper V).

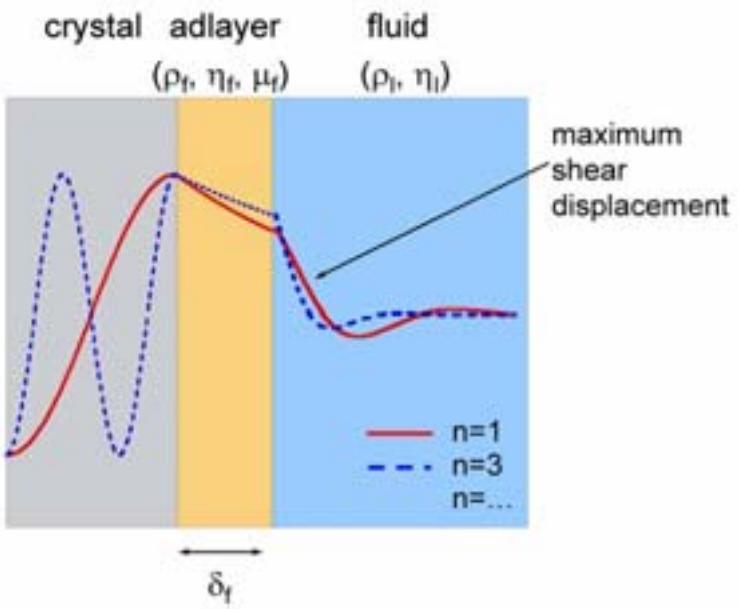

FIGURE I.11 The viscoelastic model according to Voinova et al.[230]. The shear wave excited by the quartz crystal propagates and is dissipated in the adsorbed media. The model describes the relationship between the viscoelastic properties (viscosity, η_f , and shear modulus, μ_f) of a film of homogeneous thickness, δ_f, and density, ρ_f, immersed in a Newtonian bulk liquid (with density, ρ_l, and viscosity, η_l) and the corresponding changes in frequency, Δf_n, and dissipation, ΔD_n, for multiple overtones (n = 1, 3, 5, 7). A fitting routine, implemented in the software QTools (Q-Sense, Sweden), enables to deduce the properties of the adsorbed film from the QCM-D response[212].

The door to quantitative approaches has been opened by the development of advanced models that account for the viscoelastic properties of the bulk fluid

and/or the adsorbed film[230-233]. In particular, the model by Voinova et al.[230] established a relationship between the properties of an adsorbed layer (i.e., its thickness, density, viscosity and shear modulus) immersed in bulk liquid on the one hand and the shifts in frequency and dissipation (at several overtones) on the other hand (Figure I.11, see the figure legend for details).

At first hand, the model offered a possibility to evaluate the accuracy of the Sauerbrey approximation[212]. As a rule of thumb, equation (1) is not valid for thin films (immersed in aqueous environment) that exhibit $\Delta D/\Delta f < 0.2 \cdot 10^{-6} \mathrm{Hz}^{-1}$. In order to determine the correct adsorbed mass for such highly dissipative films and/or to deduce the viscoelastic properties together with the film thickness, the full model has been applied successfully to various adsorbed layers[212,234], including protein films[208,209,212], layers of vesicles[216] and aqueous films of immobilized DNA[201]. It should, however, be kept in mind that the model may still be an oversimplified representation of reality. In particular, the assumption of film homogeneity and the description of the viscoelastic properties by a simple Voigt-Kelvin (or Maxwell) model may not hold for some applications.

I.4.2.4. The role of water

The QCM-D senses all material that is mechanically excited. Measured masses therefore include water that is coupled to the adsorbed film. This is an important difference compared to optical mass-sensitive techniques (such as SPR, ellipsometry, reflectometry or optical waveguide lightmode spectroscopy (OWLS)). Being sensitive to changes in the optical density between adsorbate and bulk water they essentially sense the dry adsorbate mass. This renders optical techniques and QCM-D highly complementary as their combination allows determining the hydration state of soft layers[198,209,219,235]. In some cases, such as immobilized polymers in brush-conformation or immobilized nucleotide strands, water can contribute more than 90% of the mass, thus significantly increasing the sensitivity of the QCM-D[201]. Furthermore, the amount of water that is sensed per unit of dry mass may vary as a function of coverage and can thus have some influence on the apparent kinetics of adsorption and desorption processes[236].

It should be noted that the role taken up by water in the dissipative processes is currently not entirely understood. Depending on the environment, water may exhibit different apparent properties, ranging from a rigid body (when being confined in holes of a rigid film)[237,238], over a highly viscoelastic material (in conjunction with a viscoelastic matrix)[201] to bulk water (when being unconfined)[232,238].

I.4.2.5. The influence of the oscillations on the solid-liquid interface

Given that the solid-liquid interface is mechanically excited, one may be concerned, whether the oscillation can influence interfacial process or even lead to slip[239]. Under common operating conditions, the amplitude of oscillation does not

exceed 1 nm in aqueous media[vi]. Even though the oscillation with high amplitudes (10 nm and more) has been shown to appreciably influence interfacial processes such as adsorption, desorption or local mixing[241-243], no or minor effects have yet been observed for low oscillation amplitudes[243] on hydrophilic surfaces. Consequently, the above-mentioned non-slip condition seems to hold for the QCM-D in liquid and the technique is thus essentially non-invasive.

I.4.2.6. Support materials

In contrast to most optical techniques that rely strongly on the optical properties of the interface, the sensing capabilities of the QCM-D rely on the quartz crystal itself. Hence, the crystal can be covered with a multitude of supports without perturbing the QCM-D signal. Common examples are thin films of metals (Au), oxides (SiO_2, TiO_2) or polymers that can be applied by evaporation, sputtering or spin-coating, respectively. The limiting factor is the thickness of the applied film. Rigid films can be applied in thicknesses that exceed 10 μm without disturbing the signal appreciably, as demonstrated for glued metal foils[244] or mica[219] (see also Chapter II).

I.4.2.7. Modes of operation

In the framework of the present studies the QCM-D has been operated in two principally different modes of operation, exchange mode and flow mode (Figure I.12). Whereas the exchange mode constitutes the simplest and most robust mode of operation, the flow mode is superior at relatively small sample concentrations (less than 5 μg/mL) as the flow limits depletion (enrichment) of the bulk upon adsorption (desorption) of sample to (from) the sensor surface or the chamber walls.

[vi] Borovsky et al.[240] report an empirical formula of $A = 1.4\ Q\ V$ for the maximum amplitude, A (in pm), with Q ($= D^{-1}$) and V being the quality factor and the drive voltage (in Volt), respectively. For common experimental values of $V = 0.14$ mV (corresponding to a driving voltage of 1 in QSoft (Q-Sense, Sweden)) and $D = 350 \cdot 10^{-6}$ in water ($20 \cdot 10^{-6}$ in air) this gives an amplitude of $A = 0.6$ nm (10 nm).

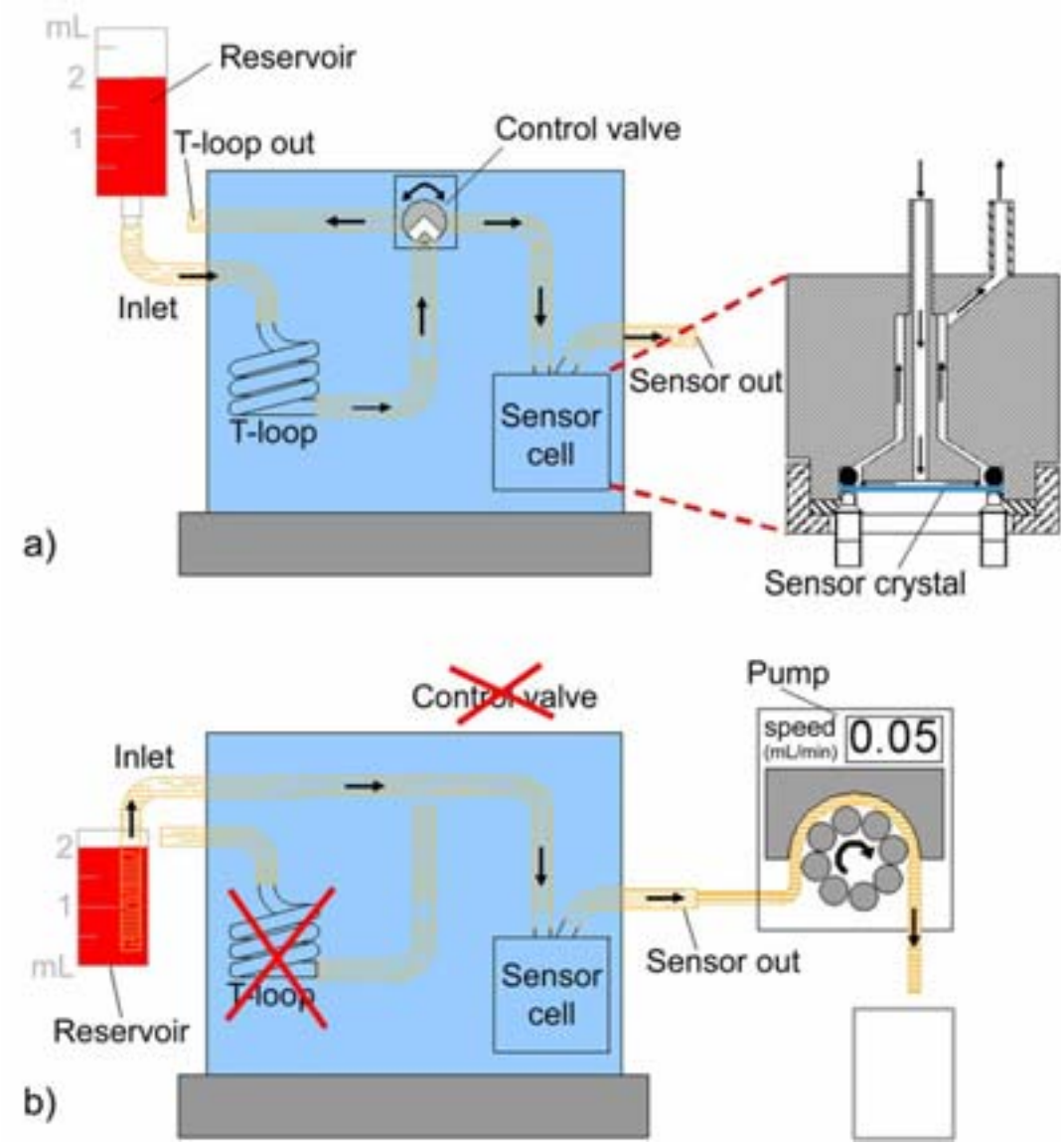

FIGURE I.12 Schematic description of the liquid-handling system for QCM-D measurements. The liquid path is indicated with arrows. (a) The exchange mode allows for rapid exchange of different solutions. The control valve is closed by default and only opened for rapid liquid transfer. The solution is (i) transferred from the reservoir to the T-loop and (ii) remains there during a given time (2 min in our experiments) for temperature stabilization prior to (iii) delivery to the sensor cell. Steps (i) to (iii) are repeated for subsequent samples or rinsing steps. The cross-section of the sensor cell (right) reveals the axial symmetric flow geometry. The liquid is injected over the center of the crystal (impinging jet) and leaves at its periphery. The liquid volume in the sensor cell is ~50 µL. 1.5 mL and 0.5 mL of liquid are required for complete exchange in the T-loop and in the sensor cell, respectively. Each exchange step takes a few seconds. (b) Flow mode: The liquid flows continuously through the chamber, driven by a peristaltic pump. Usual flow rates are in the range of 1 µL/s. T-loop and valve are bypassed.

I.4.3. Ellipsometry

The principle of ellipsometry has already been elucidated more than a century ago[245-247]. The technique is based on the measurement of the changes in the polarization of elliptically polarized light upon reflection at an interface. The ellipsometric angles are sensitive to thin films of organic material deposited on the

reflecting surface, down to masses in the range of a few ng·cm^{-2}. The instrument comes in different setups, of which the null-ellipsometer is likely the most robust.

I.4.3.1. The null-ellipsometer

In the null-ellipsometer setup, the polarizing angles of two prisms, the polarizer, *P*, and the analyzer, *A*, are adjusted by stepping motors such as to minimize the intensity of the outcoming light[vii] (figure I.13a-b, see legend for details). The time resolution is in the range of several seconds and limited by the stepping motors. The ellipsometric angles, Δ and ψ, can be directly determined from *P* and *A*, respectively, with some simple selection rules[247]. The (complex) reflection coefficients for the light polarized parallel, r_p, and perpendicular, r_s, to the plane of incidence, are related to the ellipsometric angles by

$$\frac{r_p}{r_s} = \tan\Psi \exp(i\Delta). \qquad (2)$$

The relationship between the film properties and the ellipsometric angles is in general not linear. Using an established model, however, both the thickness, *d*, and the refractive index, *n*, of a surface-bound film can, in principle, be determined[247,248]. Assuming the Lorentz-Lorenz relation for the solution-containing film to be correct, the adsorbed (dry) mass, *m*, can then be derived as[248]

$$m = 3\left(\frac{A_p}{M_p}\left(n_b^2+2\right) - V_p\left(n_b^2-1\right)\right)^{-1} \frac{n+n_b}{n^2+2} d\left(n-n_b\right), \qquad (3)$$

with A_p, M_p, V_p and n_b the molar refractivity per unit volume, the molecular weight and the partial specific volume of the probe and the refractive index of the buffer, respectively. In practice, the errors associated with *d* and n-n_b can be rather high, in particular for nanometer-thin films. The errors are, though, covariant, i.e., the product $d(n-n_b)$ and thus the adsorbed mass can be determined with much better accuracy.

It should be noted that the relationship between the film properties and the ellipsometric angles, in addition to being non-linear, depends strongly on the angle of incidence and the employed support. The scenario is further complicated for applications in liquid, as the light path usually crosses additional interfaces and bulk matter, such as the walls of the cuvette or the aqueous solution. This may rationalize the importance of well-controlled surfaces, a well-designed liquid cell and good calibration in order to correctly determine *m* (or even *d* and *n*) by ellipsometry. In case a good calibration is not available or only relative changes are of interest, changes in Δ (or ψ) are often directly employed as a measure for the adsorbed mass, e.g., for kinetic analysis[249]. This approach should though be

[vii] Ideally, the outcoming intensity should be zero, in german ”null”, hence the name of this setup.

employed with care, as the assumed linearity between *m* and Δ cannot be taken for granted.

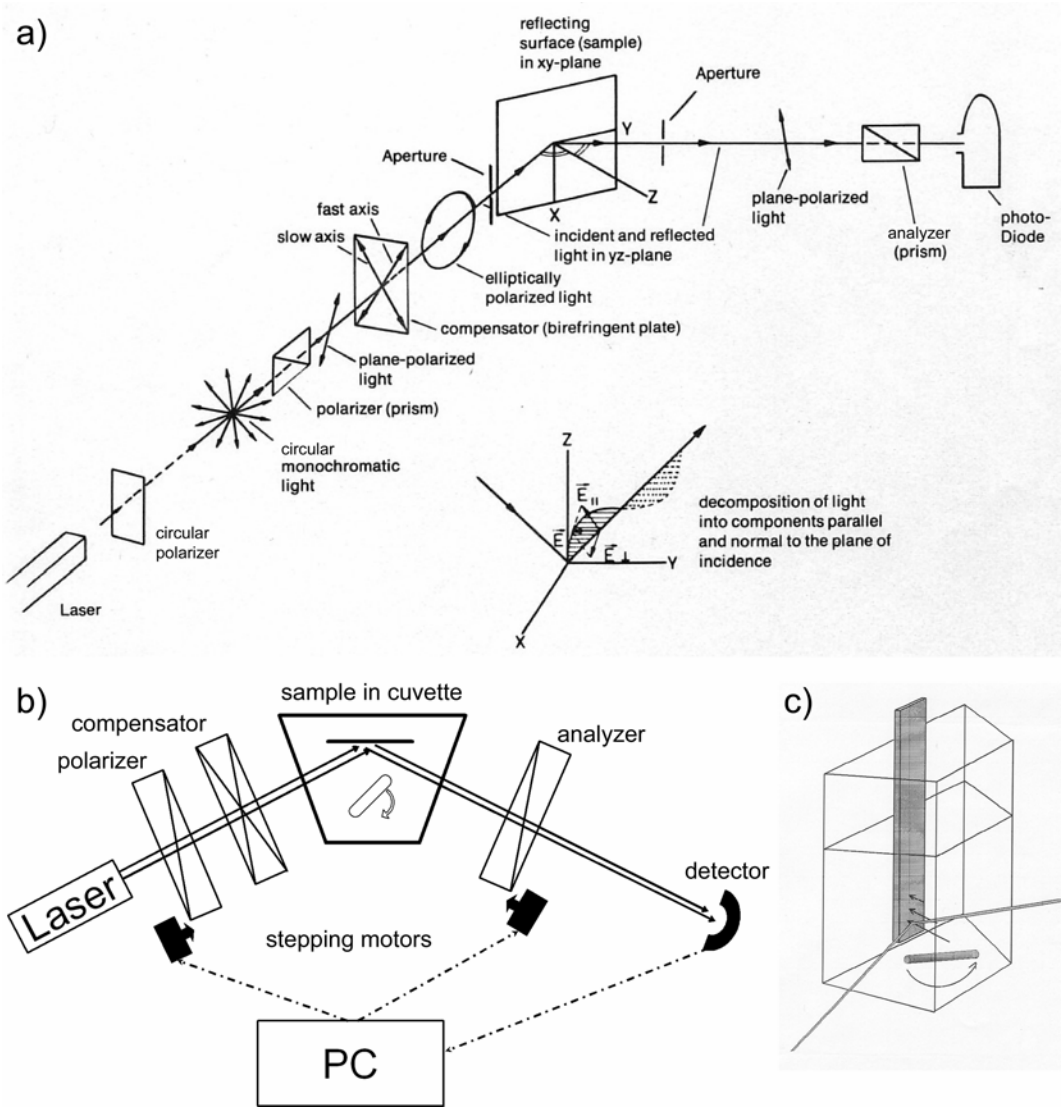

FIGURE I.13 Schematic description of the null-ellipsometer setup. (a) The polarizing prism *P* (the polarizer) generates plane-polarized light of well-defined directionality from the monochromatic light of the laser source. The compensator (usually a birefringent plate) transforms the plane-polarized light into elliptically polarized light which, by reflection on the sample surface, further changes its polarization. The orientation of the polarizer will be adjusted such that the light reflected from the sample is linearly polarized. Only in this case, the orientation of the analyzing prism *A* (analyzer) can be adjusted such that the outcoming light is extinguished. Interfacial changes on the sample will require readjustment of both polarizer and analyzer to keep the outcoming light minimized. This task is taken over by computer controlled stepping motors (b) which in this way enable to monitor the changes in *A* and *P* in real time. (c) Schematic presentation of the cuvette for measurements in liquid. Images kindly provided by Wim Hermens (University of Maastricht, The Netherlands).

I.4.3.2. Support materials

In principle, ellipsometry can be employed on any reflecting (preferably optically non-active) support. The ellipsometric response is, though, strongly interface dependent. Consequently, sensitivity varies as a function of the interface and each

type of support requires separate calibration. In particular, calibration can be obscured by surface roughness (in the nanometer range) and can add errors in case absolute adsorbed masses are to be compared. In the scope of our studies, silica (in the form of wafers) is a particularly suited material, exhibiting low roughness and high ellipsometric contrast. The feasibility of mica-ellipsometry has been demonstrated recently[250], though the determination of absolute masses has proven cumbersome.

Ellipsometry is unique in that it can be employed for measurements both at the solid-liquid and at the air-liquid interface. This property is particularly interesting for applications involving lipids as it allows linking the world of lipid monolayers (at the air-water interface)[251] with that of solid-supported lipid bilayers[252]. Further potentials of ellipsometry lie in its application at multiple wavelengths (spectroscopic ellipsometry) or with lateral resolution (microscopic ellipsometry).

I.4.3.3. Modes of operation

The ellipsometer was operated with an open cuvette system (Figure I.13c)[84] kindly made available by Wim Hermens (University of Maastricht, The Netherlands) and operated in either stirring or still mode. The solution (~3 mL) was stirred with a magnetic stirrer (~1000 rpm) placed on the bottom of the cuvette. Samples were pipetted at appropriate concentrations into the buffer. Rinses were realized by injecting ~30 mL of buffer (injection rate ~1 mL/s) while simultaneously sucking off excess liquid. Alternatively to maintaining constant stirring the stirrer could be turned off a few seconds after the injection of the sample, allowing for adsorption from still solution.

This setup has some remarkable advantages which are of particular interest for kinetic measurements. As the system is open, it allows for easy titration of sample or ions (such as Ca^{2+}) and thus enables easy acquisition of, e.g., adsorption isotherms[253]. Furthermore, the stirring setup allows for measurements with constant adsorption rates (in the case of transport limited adsorption) over a sufficiently large (compared to the size of the laser beam) uniformly accessible surface[254]. Drawbacks are a relatively large sample volume and rather ill-controlled rinsing, which renders desorption measurements cumbersome.

I.5. Solid Supports

The studies presented in this thesis may serve as an excellent demonstration of the pivotal role that the nature of the solid support can play in processes of adsorption and self-assembly. While some results were expected, such as the role of the surface charge in the process of SLB-formation[49] (see Chapter III), others, among them the observation that annexin A5 does not crystallize on silica-SLBs[188] (see Chapter IV), came as a surprise. They all stress the importance of a thorough understanding of interfacial processes in aqueous environments. Still, many questions remain open or lively debated, some of them being very fundamental, such as understanding the nature of interfacial water on the molecular level[4,5] in general and of the thin water film between an SLB and a solid support[255-257] in particular. Below, an overview over the solid supports employed in this study is given and relevant physico-chemical properties of the supports' surface are reviewed briefly.

I.5.1. Mica

Mica was already appreciated in the Middle Age. People in the region of Moscow (Russia) employed the mineral as window glass ("muscovy glass"), hence the name of mica's most common form, *muscovite* (Figure I.14). The historical use illustrates the remarkable property of mica to be cut into large, transparent and flexible sheets. Today's extended use in research stems from a need of ideally flat surfaces that enable the direct investigation of interactions between surfaces[4,7,258] or give a suitable featureless support for the immobilization and topographic investigation of (bio)molecules[129,179]. Indeed, cm^2-sized surfaces of atomic flatness can be generated with relative ease[259] and are routinely used for measurements by SFA or AFM.

FIGURE I.14 A natural sample of muscovite mica.

Muscovite mica is a layered alumina silicate of stoichiometry $K(Si_3AlO_{10})Al_2(OH)_2$. It is composed of two tetrahedral sheets of $(Si,Al)_2O_5$ that are linked by a central layer of $Al_2(OH)_2$. The net negative charge of these sandwich structures is balanced by a layer of hexagonally coordinated potassium ions (Figure I.15)[260]. Upon cleavage, the potassium layer becomes disrupted, exposing a hydrophilic surface.

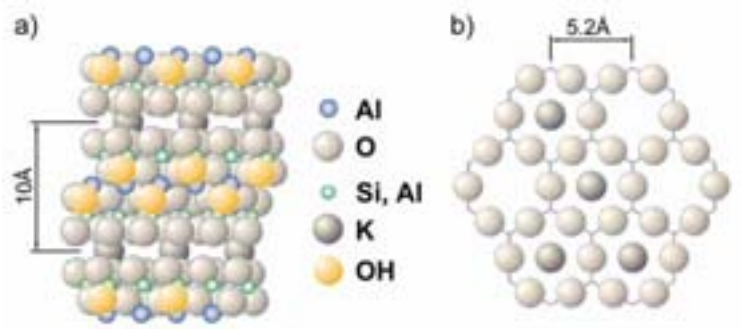

FIGURE I.15 Atomic model of the layered structure of mica. (a) A sheet of $Al_2(OH)_2$ is sandwiched by two oppositely oriented tetrahedral sheets of $(Si, Al)_2O_5$ in which O_5 forms the backbone of the tetrahedrons, that are filled with $(Si, Al)_2$. Cleavage occurs along the interlayer potassium ions, exposing the hexagonal layer of basal oxygen (b)[260]. Image adapted from ref. [179].

In aqueous solution the potassium ions dissociate and become exchanged by hydrogen or other cations[261]. The ion exchange regulates the surface charge of mica which is usually negative, though in magnitude dependent on the electrolytes in solution[262,263] (see also Chapter III). Optically, mica is a slightly birefringent material, i.e., the propagation of light is different along two directions normal to the crystalline layers.

Despite its common use in research and industry – mica is an excellent insulator, with good chemical and thermal inertness – automated cleavage has so far remained elusive. Sophisticated manual skills (and time) are required in order to create mica sheets of suitable thickness with cleavage planes of good quality. This currently imposes constraints on the use of mica for some applications, such as the deposition of mica on QCM-D sensors, an issue that will be investigated in detail in Chapter II.

I.5.2. Silicon and silica

Silicon-based materials have experienced a tremendous boost during the last 50 years, in conjunction with the development of the semiconductor industry. Large single crystals of silicon are today grown routinely with high purity and further processing (cutting, etching and polishing) generates flat decimeter sized discs (wafers) with a roughness of only a few Angstroms. Furthermore, methods have been and are currently developed to create controlled patterns in silica on the scale of micrometers or nanometers.

With the interest of patterning and nanofabrication for the design of biofunctional surfaces[61,264-266] and the relevance of connecting biology with electronics[92,267], silicon-based surfaces become increasingly used in bio(techno)logical applications. It is not to forget that silica in its colloidal form is already well established for the purification of biomolecules by liquid chromatography[268] or thin layer chromatography.

When exposed to air, a surface layer of ~1 nm thickness becomes quickly oxidized, generating an amorphous film of silica (SiO_2) on silicon surfaces. Thicker oxide layers can be grown in a controlled manner by various treatments, such as oxygen plasma, UV/ozone or baking in oxygen. Alternatively, bulk silica

materials – both amorphous (vitreous silica) and crystalline (quartz) – can be polished to obtain similarly flat surfaces. Thin films of amorphous silica are also generated by physical vapor deposition, such as evaporation or (reactive) sputtering. For example, sputtering is the method of choice to coat QCM-D sensors with silica. The intrinsic roughness of these films is usually a little higher, biased by the roughness of the underlying support.

A key characteristic of the siloxane (Si-O-Si) surface of silica is that the so-called "residual valences" react with ambient water such that the surface becomes covered with silanol (SiOH) groups. The fully hydroxylated surface is hydrophilic and accommodates 4-5 SiOH groups per nm^2, a value that is shared by both amorphous and crystalline silica[269,270]. While the silanol groups remain largely stable upon drying at 120-150°C in air, close to complete dehydroxylation can be achieved by extended thermal treatment (several hours at up to 1100°C). It is notable that the re-hydroxylation of such hydrophobic (pyrogenic) siloxane surfaces in water can be very slow, particularly at pH < 5 (in the order of years). Hydroxylation is though catalyzed at elevated temperatures and in slightly basic solution[269,271].

The surface charge of silica originates from the deprotonation of the SiOH group and is negative above pH 2. The magnitude of the charge is dependent on the hydroxylation state and generally increases with increasing pH and ionic strength[272-275] (see also Chapter III). In parallel, silica starts to dissolve above pH 8-9 [269].

Given the influence of the state of hydroxylation on the surface chemistry, its hydrophobicity and its charge, an obvious question is whether it may influence the adsorption of organic molecules from aqueous solution or the properties of adsorbed films. Indeed, such variations have been reported and may be related to the method of surface preparation, different degrees of hydroxylation as well as contaminants[269,271,276-278].

I.5.3. Other supports

Whereas the above-mentioned surfaces were chosen as model surfaces, other surfaces have important prospects in biotechnological applications, too. Some of these surfaces are titanium oxide, already intensely exploited as implant material (artificial hip-joints, dental implants)[279], polymers (such as polystyrene, the traditional support for cell-culture), glass, for applications that involve optical microscopy, hydroxyapatite[280] or gold[281]. The range of surfaces, both inorganic and organic, is growing together with the development of new materials and the demand of surface-sensitive techniques[282-284].

I. Introduction (version française)

I.1. Objectifs

Un des buts majeurs de mon travail de thèse était la caractérisation détaillée de deux processus d'auto-organisation supramoléculaire présentant un intérêt à la fois en science fondamentale et en biotechnologie : la formation de bicouches lipidiques sur support solide (SLB) et l'assemblage bidimensionnel (2D) de protéines liées à cette membrane lipidique. Un deuxième objectif était de démontrer l'intérêt de combiner plusieurs techniques de caractérisation de phénomènes de surface, permettant une description détaillée des processus d'auto-organisation 2D. Nous avons notamment utilisé la microscopie à force atomique (AFM), la microbalance à cristal de quartz avec mesure de dissipation (QCM-D) sur supports identiques et également, en partie, l'ellipsométrie.

Le Chapitre I introduira brièvement les molécules biologiques et les supports solides employés pour ces travaux, ainsi que les techniques de caractérisation utilisées. L'approche suivie pour combiner l'AFM et le QCM-D sur des supports identiques sera présentée dans le Chapitre II. Deux obstacles techniques majeurs ont dû être résolus pour pouvoir profiter pleinement de la complémentarité entre ces deux techniques : le dépôt de mica sur les capteurs QCM-D et le contrôle de l'interaction entre la pointe AFM et les lipides déposés sur support solides. Le Chapitre III traitera de la formation des SLBs par la technique d'étalement des liposomes et posera la question de la distribution des lipides entre les deux feuillets des SLBs. Le Chapitre IV présentera les résultats obtenus sur l'adsorption et l'assemblage 2D de la protéine annexine A5 au niveau de bicouches supportées.

Ce travail a abouti à plusieurs articles, publiés ou soumis à des journaux à comité de lecture. Ils forment la colonne vertébrale de cette thèse et sont insérés dans leur style original. Dans le but de donner une perspective plus large et d'adresser certains aspects du travail non couverts par les publications, ces articles seront précédés par de brèves introductions.

En unissant les aspects physiques des techniques de caractérisation, les échantillons biologiques et la science des matériaux des supports solides, cette thèse se situe dans le cadre d'une entreprise véritablement interdisciplinaire. L'étendue de ce travail rend impossible de couvrir tous ses aspects en détail et je souhaite que les spécialistes de chaque domaine ne me tiendront pas rigueur des défauts dans la présentation et m'informeront de ces erreurs ou incorrections.

I.2. Les bicouches lipidiques déposées sur supports solides

I.2.1. Les lipides et leur propriété d'auto-assemblage

Les propriétés fascinantes des lipides résultent en grande partie de l'attitude ambivalente de ces molécules en contact avec l'eau. Typiquement, les lipides sont composés d'une tête polaire et d'une ou plusieurs queues hydrophobes. Les combinaisons de la tête hydrophile et des queues hydrophobes sont déterminantes pour les propriétés de ces molécules, en particulier leur propriété d'auto organisation.

I.2.1.1. Les propriétés moléculaires des lipides

Les phospholipides constituent le groupe de lipides le plus abondant dans les membranes biologiques. Leur nom provient de la présence d'un groupement phosphate[i] au niveau de leur tête. Les têtes polaires peuvent être distinguées en fonction de leur taille et de leur charge (Figure I.1).

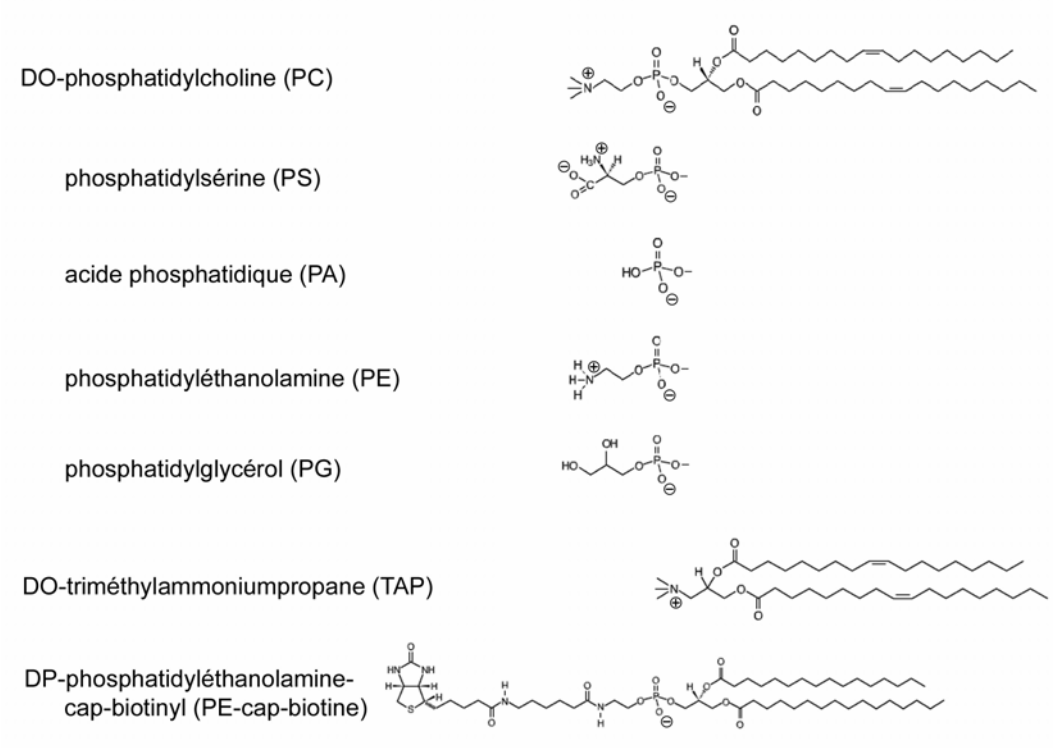

FIGURE I.1 Structure et nomenclature de quelques têtes lipidiques. Les charges à pH physiologique sont indiquées. Les groupements amines dans la PE et la PS peuvent être déprotonés à des pH plus élevés. En revanche, le groupement carboxylate dans le PS sera protoné à faible pH. Les liaisons chimiques et les queues sont ajoutées pour les DOPC, DOTAP et DPPE-lc-biotine. Les contre-ions ne sont pas présentés sur la figure pour des raisons de clarté.

[i] La présence du phosphore permet de quantifier relativement simplement la concentration d'une solution donnée en phospholipides[1].

Dans le cadre de ces recherches nous avons utilisé la phosphatidylcholine (PC), pour sa nature zwitterionique et son abondance dans les membranes biologiques, et la phosphatidylsérine (PS), portant une charge globale négative à pH neutre. Nous avons également utilisé dans nos travaux des lipides portants le triméthylammonium-propane (TAP), un groupement artificiel cationique, précédemment employé pour des études d'interaction (électrostatique) entre membranes et acides nucléiques[2,3], et la biotinoyl-aminohéxanoyl-phosphatidyléthanolamine (PE-lc-biotine), intéressante pour sa liaison spécifique avec la protéine streptavidine (Figure I.1).

Les queues sont formées par des chaînes acyles et donc non polaires. La longueur des chaînes et le nombre de doubles liaisons peuvent varier considérablement. Les chaînes les plus courantes ont une longueur entre 14 et 20 atomes de carbone. Elles sont soit saturées, ne possédant alors aucune double liaison. Elles peuvent également être insaturées et posséder une ou plusieurs doubles liaisons, induisant un coude (« kink ») dans les chaînes autrement droites. La nomenclature et la structure de quelques chaînes communes sont rassemblées dans la Table I.1. La combinaison des chaînes majoritairement employée dans notre étude est le di-oleoyl (DO), pour former les molécules de DOPC, DOPS et DOTAP. Le di-palmitoyl (DP) a été employé pour la DPPE-lc-biotine.

TABLE I.1 Nomenclature et structure de quelques chaînes acyles.

Nom	Structure	Nombre d'atomes de carbone	Nombre de doubles liaisons
Myristoyl (M)	$CH_3(CH_2)_{12}COO$-	14	0
Palmitoyl (P)	$CH_3(CH_2)_{14}COO$-	16	0
Stéaroyl (S)	$CH_3(CH_2)_{16}COO$-	18	0
Oléoyl (O)	$CH_3(CH_2)_7CH{=}CH(CH_2)_7COO$-	18	1
Linoléoyl (L)	$CH_3(CH_2)_4CH{=}CHCH_2CH{=}CH(CH_2)_7COO$-	18	2

I.2.1.2. L'auto-assemblage des lipides

La nature amphiphile des lipides est à l'origine de leur tendance de s'auto-assembler en solution aqueuse. L'organisation des molécules d'eau dans l'environnement des queues hydrophobes est associée à un coût entropique (l'effet hydrophobe[ii]) et, par conséquent, les lipides s'auto-assemblent pour former un bouclier de têtes polaires séparant les queues de l'eau environnante et permettant ainsi d'abaisser ce coût entropique[6,7].

La forme des assemblages dépend de la structure moléculaire des ses constituants. En première approximation, la forme est déterminée par le facteur de forme[7]

[ii] Le concept fondamental de la structuration de l'eau est réévalué aujourd'hui à la suite de l'émergence des nouvelles techniques permettant de sonder la structure supramoléculaire de l'eau à proximité des interfaces[4,5].

(Figure I.2, voir la légende pour plus de détails). Les lipides forment une multitude d'assemblages, entre autre des bicouches planes, des micelles, des phases hexagonales et hexagonales inverses ou des tubes (Figure I.2). L'assemblage le plus fréquent dans la nature est la bicouche lipidique. Dans cette structure, deux monocouches lipidiques sont apposées, les queues hydrophobes des lipides étant alors prises en sandwich entre les deux couches de têtes polaires (Figure I.2).

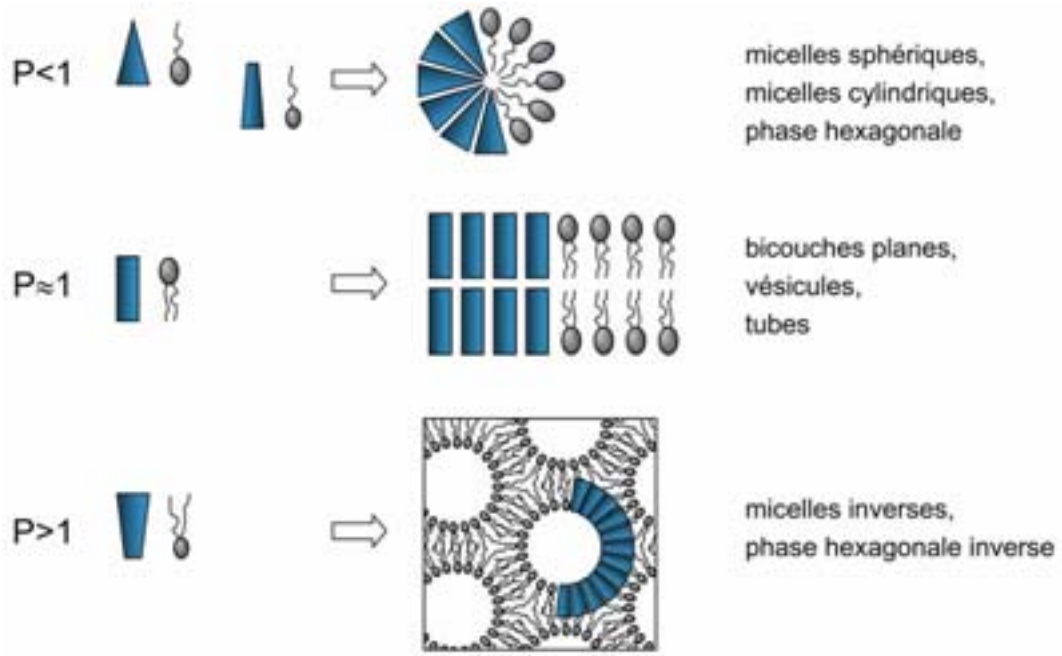

FIGURE I.2 Présentation schématique de divers assemblages lipidiques. En première approximation[7], la forme de l'ensemble est déterminée par le facteur de forme, $P = \frac{\nu}{l_c}\frac{1}{a_0}$ (ν - volume occupé par les chaînes, a_0 – surface optimale de la tête, l_c - longueur critique de la chaîne). $P = 1$ est équivalent à une forme apparente cylindrique des molécules, amenant aux assemblages de type bicouche.

La nature de la tête polaire et des queues hydrophobes a une grande influence sur quelques propriétés essentielles des bicouches lipidiques :

- Les bicouches lipidiques existent en différentes phases thermodynamiques, en particulier la phase gel, L_β, et la phase cristal liquide (également nommée la phase fluide), L_α. La température de transition, T_m, entre ces deux phases augmente avec la longueur des chaînes hydrophobes et diminue fortement avec le nombre de doubles liaisons. La nature de la tête et la présence des ions (divalents) peuvent également influencer la valeur de T_m. Le coefficient de diffusion latérale est de quelques $\mu m^2/s$ en phase fluide[6] et diminue d'au moins deux ordres de grandeur en phase gel. Dans un mélange de lipides, une séparation entre deux phases thermodynamiques peut avoir lieu.
- La charge des bicouches lipidiques est essentiellement déterminée par la charge des têtes polaires. Tous les (phospho-) lipides sont soit chargés, positivement ou négativement, soit zwitterioniques à pH neutre. Les charges et/ou la polarité des têtes peuvent influencer la nature de l'interaction avec

leur environnement, c'est-à-dire, les lipides voisins, les ions en solution et l'eau.

- L'aire moyenne occupée par molécule dans une bicouche peut varier considérablement, en fonction de la température, de la force ionique, et de propriétés de la tête et des queues des lipides (Table I.2). En règle générale, les doubles liaisons augmentent la surface moléculaire.
- Les bicouches lipidiques sont fortement sélectives dans leur perméabilité. Les molécules d'eau peuvent traverser les membranes fluides relativement rapidement (30-40 μm/s)[8], tandis que la membrane est fortement imperméable aux ions, comme le Na^+ (10^{-10} μm/s)[9] et le Cl^- (10^{-7} μm/s)[9]. La perméabilité est intermédiaire pour les ions H^+ et OH^- (de 1 à 10-4 μm/s)[10]. Elle est affectée par la charge et la taille des molécules et par la composition de la membrane, en particulier son contenu en cholestérol.
- La solubilité des monomères de lipides en solution aqueuse est en général très faible (~10^{-10}M)[10] et diminue avec la longueur des chaînes. Pour indication, la concentration totale des solutions lipidiques utilisées dans nos travaux est de l'ordre de 10^{-4} M. Le temps de résidence d'un lipide dans la bicouche est typiquement de l'ordre de quelques heures[7,11].
- En raison de la barrière énergétique associée au déplacement de la tête polaire à travers l'intérieur hydrophobe de la membrane, l'échange de lipides entre les deux feuillets d'une bicouche (le flip-flop) est difficile. La vitesse de flip-flop pour les bicouches fluides non perturbées est typiquement de l'ordre de l'heure ou du jour[11-13]. Elle dépend fortement de la nature de la tête polaire et de la température et elle augmente faiblement avec la longueur des chaînes[11,14].

TABLE I.2 Propriétés de quelques lipides typiques.

Lipide	T_m (°C)	Aire par lipide [a), e)] (Å^2)	Masse moléculaire [f)] (g/mol)
DOPC	-22[e)]	72	786.15
DPPC	41.3[e)]	44.5	734.05
PC [b)]	-15[e)]	62	760.09[h)]
DPPE	63[e)]		691.97
PE [b)]		42	744.05[h)]
DOPS	-11[f)]	67[g)]	810.04
PS [d)]		50-100[c)]	
DOTAP	~0[f)]		698.55
DPPE-CAP-biotine			1053.40

[a)] à température ambiante ; [b)] extrait du jaune d'œuf ; [c)] la surface varie en fonction du pH et de la présence des ions multivalents ; [d)] extrait du cerveau de bœuf ; [e)] ref. [6] ; [f)] ref. [15] ; [g)] dans 100 mM LiCl, pH 7.4, ref. [16] ; [h)] mass moléculaire moyenne

Les bicouches lipidiques constituent un continuum 2D dans lequel (ou auquel) des protéines peuvent être incorporées (ou associées). L'ensemble forme une assemblage à la fois complexe et dynamique : les membranes biologiques.

I.2.2. Les membranes biologiques et leur modèles

Les membranes biologiques jouent un rôle clé dans la vie cellulaire. Elles agissent en tant que barrières, transporteurs ou « centrale » de communication entre l'intérieur et l'extérieur de la cellule et elle participent à de nombreux processus intra- et extracellulaires.

L'histoire de la révélation des mystères des membranes biologiques[6,17] constitue un excellent exemple d'un travail véritablement interdisciplinaire, inspiré à la fois par la biologie, la chimie et la physique à travers le 20ème siècle. En utilisant un système développé par Langmuir[18] pour caractériser les films monomoléculaires à l'interface air-eau, Gorter et Grendl[19] déterminèrent, en 1925, que la surface couverte par une monocouche de lipides extraits de globules rouges correspondait à deux fois la surface extérieure de ces cellules. Malgré quelques erreurs dans leurs calculs, ils conclurent correctement que les cellules sont couvertes d'une bicouche lipidique. Robertson confirma cette observation par microscopie électronique et proposa que la structure de la bicouche était universelle pour toutes les cellules et organelles[20]. Plus tard, des techniques telles que la microcalorimétrie différentielle, la diffraction de rayons X, les méthodes de la résonance magnétique électronique et nucléaire, et de fluorescence[21] ont permis de caractériser et de mesurer expérimentalement les transitions de phase, la structure et la flexibilité de la bicouche et la mobilité, en deux dimensions, des lipides[22]. Ces ingrédients, conjointement à la notion de protéines membranaires (liées à la membrane de manière périphérique ou intégrale), formaient la base du modèle de mosaïque fluide proposé par Singer et Nicolson[23] (Figure I.3).

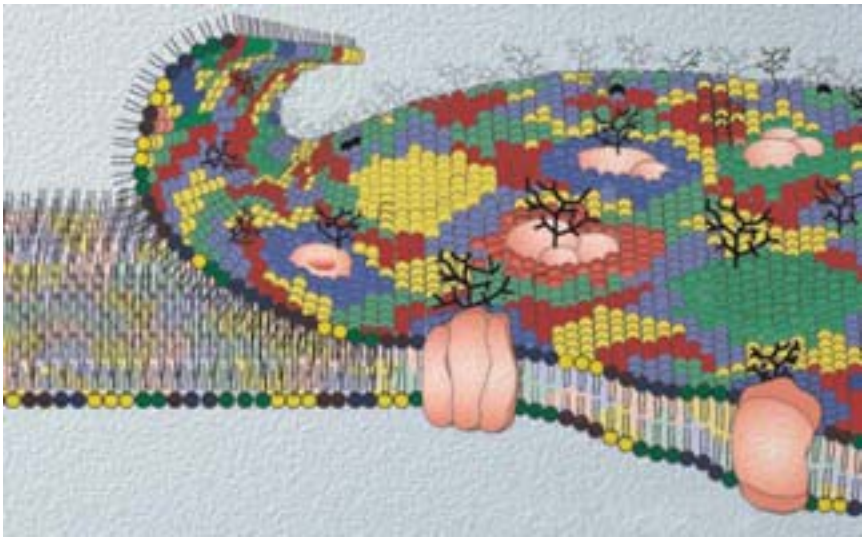

FIGURE I.3 Le modèle de mosaïques fluides de membranes biologiques initialement propose par Singer et Nicolson[23]. Image adaptée de la ref. [17].

Depuis la fin des années 1980, il est de plus en plus reconnu que les lipides et les protéines membranaires peuvent ségréger en domaines dynamiques d'une taille de quelques nm à quelques µm [25,28]. Ces domaines, appelés radeaux membranaires, accomplissent des fonctions biologiques bien distinctes, telles que le tri, le transport, et la signalisation[24,25,26,27,28]. De plus, l'aspect dynamique de la distribution asymétrique des lipides entre les deux feuillets de la membrane a été mis en evidence[29,30]. Le fait que la membrane plasmique de certaines cellules se

renouvelle en une heure[31] reflète que non seulement le comportement de la membrane mais aussi son interaction avec l'environnement est d'une nature très dynamique. Ces avancées dans la compréhension ont été rendues possible grâce aux progrès de techniques ayant une haute résolution spatiale ou temporelle, en particulier l'AFM, la résonance magnétique nucléaire ou des techniques basées sur la fluorescence.

La résolution de la structure de la membrane et de sa fonction a toujours nécessité l'interaction des recherches sur des cellules entières et sur des systèmes modèles simplifiés des membranes biologiques. Les modèles les plus courants de membranes biologiques sont : les liposomes et les vésicules géantes en solution, les monocouches lipidiques à l'interface air-eau, les membranes suspendues (« black lipid membranes »), les fragments de membranes sur pipette et les membranes supportées (Figure I.4).

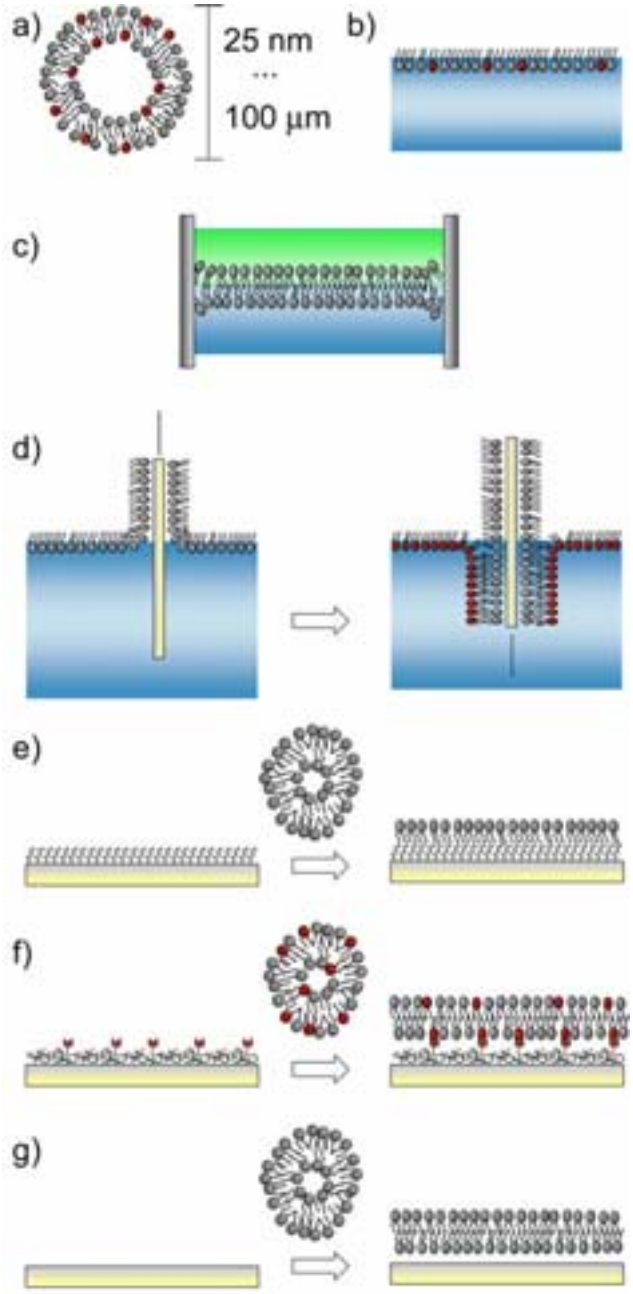

FIGURE I.4 Modèles de membranes biologiques : (a) liposomes : sphères creuses (de 20 nm à 100 µm en diamètre) entourées d'une bicouche lipidique; (b) monocouche lipidique à l'interface air-eau; (c) membrane lipidique suspendu sur un orifice entre deux phases aqueuses (« black lipid membranes »); (d) film de Langmuir-Blodgett (la méthode de Langmuir-Blodgett permet le transfert de mono- ou multicouches lipidiques de l'interface air-eau sur support solide); (e) monocouches auto-assemblées (SAM, par exemple, thioalkanes sur Au ou alkoxysilanes fonctionnalisés sur verre ou sur silice), une deuxième couche lipidique peut être déposée par rupture spontanée de liposomes; (f) déposition d'un polymère avec encrage (« tether ») suivie par l'étalement spontané de liposomes, le polymère crée un coussin mou entre support et bicouche; (g) étalement spontané de liposomes ou de membranes sur mica, verre et silice.

I.2.2.1. Les vésicules unilamellaires

Depuis l'introduction des vésicules (ou liposomes) comme système modèle dans les années 1960, plusieurs techniques de préparation[32-34], telles que la sonication,

l'extrusion[35], la dialyse de détergent, l'évaporation en phase reverse[36], l'injection en présence de solvant[37,38], ou l'électroformation[39], ont été mises au point pour créer des vésicules unilamellaires. L'ensemble de ces méthodes permet la préparation de vésicules avec un rayon de ~10 nm (par sonication) jusqu'à ~50 μm (par électroformation) et avec une distribution de taille plus ou moins étroite[iii].

Les vésicules unilamellaires, dans leur forme la plus simple, sont constituées d'une bicouche sphérique fermée qui sépare un compartiment intérieur de l'extérieur. Ces systèmes ont permis, conjointement avec des méthodes théoriques, d'étudier les propriétés principales des bicouches lipidiques, telles que leur comportement mécanique[42-46], les phénomènes d'adhésion et de fusion[43,47], la perméabilité des membranes[48] ou la diffusion des lipides dans les membranes.

Les vésicules unilamellaires que nous avons utilisées pour l'ensemble de nos travaux ont été préparées par sonication (SUV, pour « sonicated unilamellar vesicles » ou pour « small unilamellar vesicles ») (la procédure de préparation est décrite dans l'article [49]). Chacune de ces vésicules a un diamètre compris entre 20 et 30 nm et contient environ 3000 molécules de lipides. La courbure élevée des SUVs contraint l'arrangement des lipides, ce qui conduit à une distribution asymétrique des molécules entre les feuillets internes et externes, à la fois en nombre (60-75% du contenu total en lipides réside dans le feuillet extérieur[6,34]) et en espèce[34,50]. De plus, le volume d'eau confiné est faible et représente moins de 30% du volume total des vésicules. Les SUVs ne sont probablement pas thermodynamiquement stables. Cependant, la barrière s'opposant à la fusion spontanée des vésicules est suffisamment élevée pour maintenir les SUVs dans leur phase métastable pour des semaines et des mois sous conditionnement appropriées.

I.2.2.2. Les bicouches lipidiques supportées

Depuis les travaux pionniers de McConnell et coll.[51], les (modèles de) membranes biologiques déposées sur support solide sont devenus très populaires[52,53], aussi bien pour l'étude fondamentale des membranes que pour des applications potentielles dans le domaine de la nano-bio-technologie[54-56]. L'intérêt croissant dans le confinement des membranes sur des surfaces a été alimenté par l'émergence d'une multitude de techniques de caractérisation de phénomènes de surface (voir ci-dessous), des méthodes avancées de nano-structuration « patterning »[55,57-60] et des techniques microfluidiques[61].

Une multitude de méthodes a été proposée pour créer des bicouches lipidiques supportées (SLB) ou d'autres types de membranes hybrides supportées. Les approches les plus communes sont les méthodes de type Langmuir (déposition de type Langmuir-Blodgett ou Langmuir-Schäfer)[62-65], la méthode de dilution des micelles[66,67] et, principalement, la méthode de l'étalement des vésicules sur des supports preconditionnés (Figure I.4)[57,64,68-72]. Chaque méthode induit des

[iii] Il est souvent négligé que la distribution de taille peut être assez large et que sa détermination n'est pas une tâche triviale[40,41].

caractéristiques propres dans la capacité des membranes modèles ainsi formées de mimer certains paramètres de la membrane biologique, sa qualité et sa stabilité. En conséquence, les applications peuvent varier entre ces différentes approches.

Il est remarquable que différentes techniques ont traditionnellement été employées pour caractériser les propriétés physico-chimiques et structurales des divers types d'assemblages lipidiques mentionnés ci-dessus. Les paramètres physiques fournis par des techniques différentes ne sont souvent pas comparables de manière directe. Ainsi, d et la méthode du retour de fluorescence après photoblanchiment (FRAP) sont communément utilisés pour caractériser la formation des SLBs. Alors que la présence de vésicules résiduelles dans une membrane est facilement détectée par AFM (sous certains conditions d'imagerie, voir Chapitre II), la détection de défauts aussi petits est difficile par FRAP. Des études comparatives, (i) soit de la caractérisation de la qualité d'une bicouche par une multitude de techniques, (ii) soit de la caractérisation des différentes types de membranes supportées par une même technique[64,68], sont rares. Ceci rend difficile la corrélation des résultats publies dans ce domaine.

La formation spontanée de SLBs par dépôt de vésicules sur des supports solides hydrophiles est attrayante par sa simplicité. Des SLBs contenant peu de défauts peuvent être fabriquées par cette méthode en une seule étape (voir Chapitre III). Les SLBs constituent un espace fluide 2D, qui permet aux lipides et aux protéines associées de diffuser, en translation et en rotation. Cette propriété rend les SLBs bien adaptés pour l'analyse de la formation des domaines lipidiques[73-81], des interactions entre membranes[82,83] ou des processus membranaires, tels que l'adsorption des protéines[84,85] et leur auto-assemblage[74,77,86], la localisation des protéines sur les bords des phases lipidiques[87] et la fonction des protéines[63].

Une compréhension physique des forces motrices et des étapes intermédiaires de la formation des SLBs n'a émergé que récemment. Les études théoriques et expérimentales pendant la dernière décennie ont considérablement amélioré la compréhension des mécanismes sous-jacents à la formation des SLBs. Il est intéressant de noter que le choix du support est critique pour la formation des SLBs. Tandis que les SLBs de DOPC se forment sur des surfaces de silice, de verre ou de mica, elles ne se forment pas sur l'or ni sur TiO_2 dans des conditions de salinité et de pH identiques[69,152,216]. Une meilleure compréhension des mécanismes de formation des SLBs devrait améliorer la préparation des bicouches déposées sur support solide et d'autres membranes confinées à des surfaces, telles que les « tethered »-SLBs[88,89], les SLBs supportées sur coussin de polymères[64,72,90] ou les membranes suspendues[91,92]. La formation des SLBs a constitué un enjeu majeur du travail présenté dans cette thèse. L'ensemble des résultats concernant la formation des SLBs et la description des mécanismes et des paramètres influençant leur formation seront présentées dans le Chapitre III.

I.3. L'annexine A5

I.3.1. Propriétés fondamentales et fonction biologique

La protéine annexine A5 est un membre de la superfamille des annexines (revue dans les références [93,94]). Ces protéines partagent la propriété d'interagir avec des phospholipides négativement chargés sous l'influence des ions calcium. Le domaine C-terminal, responsable de la liaison à la membrane, est conservé parmi les annexines. L'extrémité N-terminale confère l'individualité des annexines. Dans le cas de l'annexine A5, l'extrémité N-terminale est réduite, conférant à cette protéine une propriété prototype des annexines.

Bien qu'il soit communément admis que les annexines sont impliquées dans divers processus transmembranaires, comme l'exocytose, la régulation de la coagulation sanguine ou de l'inflammation, leurs fonctions physiologiques précises sont encore mal définies. L'annexine A5 pourrait être impliquée dans des processus d'inhibition de la coagulation sanguine[95,96], agissant comme écran de processus thrombotiques[97,98].

Hormis l'aspect de fonction biologique, l'annexine A5 est particulièrement intéressante pour ses applications biotechnologiques potentielles grâce à une combinaison de plusieurs propriétés : (i) sa liaison avec la membrane est réversible et peut être contrôlée par la concentration en ions calcium en solution et par le taux de DOPS dans la membrane ; (ii) une fois liée à la membrane, l'annexine A5 a la capacité de former des assemblages 2D de structure contrôlée ; (iii) enfin, la protéine présente une stabilité remarquable.

I.3.2. La structure moléculaire et la liaison de l'annexine A5 aux membranes

Le monomère d'annexine A5 est composé de quatre domaines homologues en séquence et en structure[100]. Chaque domaine contient environ 70 acides aminés arrangés sous forme de cinq hélices α. Vue du coté, l'annexine A5 présente une forme plate, légèrement courbée (Figure I.5). Les donnés de cristallographie des rayons X ont mis en évidence un nombre (variable) d'ions calcium au niveau de boucles localisés sur la face convexe de la molécule[93,99,100]. L'annexine A5 s'associe à la membrane par sa face convexe, et les sites de liaison du calcium ont été impliqués dans cette interaction[93]. La nature exacte de la liaison et la stœchiométrie de sites de liaison reste pourtant mal connue. La structure globale d'annexine A5 change peu lors de l'interaction de la protéine avec la membrane[101] (voir ci-dessous). Les géométries de la membrane et de la protéine suggèrent une forte proximité entre une grande partie de la surface convexe de l'annexine A5 et les têtes polaires des lipides[102]. Cependant, des mesures de fluorescence ont mis en évidence un changement de conformation d'une boucle dans le domaine III, contenant l'unique résidu tryptophane de la molécule (Trp-187)[103,104]. Deux structures 3D, avec une forte similitude globale mais avec une différence dans le positionnement de cette boucle, ont été résolues. Dans une structure[100,105], la boucle est située à l'intérieur du domaine III et la protéine ne présente pas de site

de liaison de calcium à cet endroit. Dans l'autre structure[106,107], la boucle est exposée et présente un ion calcium lié. L'annexine A5 peut également s'associer aux membranes de DOPC pur et aux monocouches de cholestérol pur en présence de concentrations élevées de calcium[108].

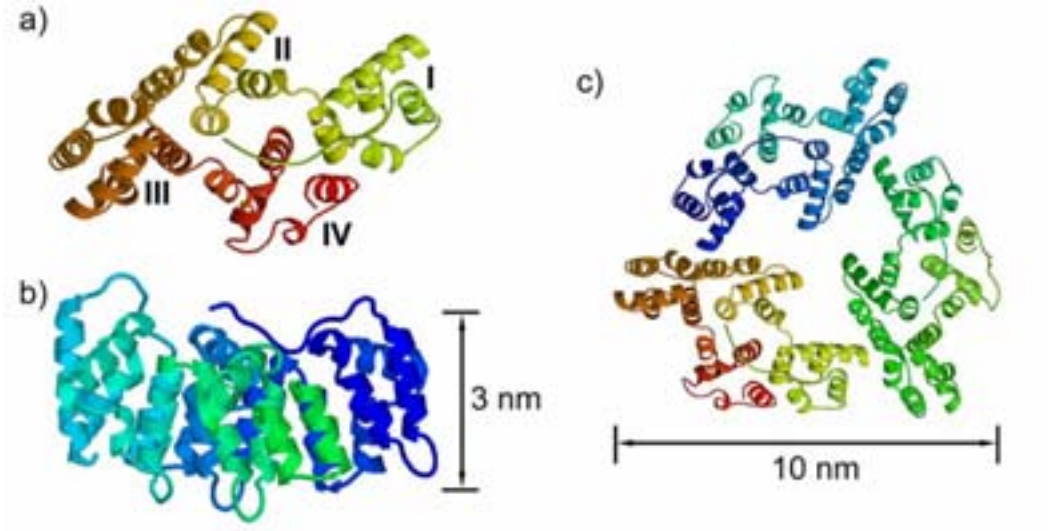

FIGURE I.5 Modèle atomique de l'annexine A5. (a) Monomère, vue révélant l'organisation symétrique en quatre domaines de la molécule. Les domaines de la protéine sont annotés[100]. (b) Vue de côté d'un monomère. La face inférieure, convexe, s'associe à la membrane. (c) Le trimère crystallographique[106], observé selon l'axe de symétrie d'ordre trois. Adapté de la réf. [101].

I.3.3. L'auto-assemblage de l'annexine A5

Une fois confinée en deux dimensions, suite à la liaison aux bicouches (SLBs sur mica[109]) ou aux monocouches (à l'interface air-eau[110]) lipidiques, l'annexine A5 présente la propriété de s'auto-assembler[111]. Les étapes de l'auto-assemblage sont présentées schématiquement sur la Figure I.6.

Les phases cristallines les plus communes de l'annexine A5 présentent une symétrie p3 ou p6, mais d'autres formes ont également été observées[113]. Reviakine et coll. ont utilisé l'AFM et des SLBs sur mica contenant du DOPS pour étudier la transition entre la forme cristalline p6 (avec une densité relativement faible des protéines) et la forme p3 (avec une densité plus forte). Ils ont trouvé que la transition est réversible, amenant à la conclusion qu'il s'agit d'une transition de phase de première ordre entre les deux phases solides[112]. Remarquablement, le trimère d'annexine A5 (Figure I.5) a été identifié comme structure de base non seulement dans tous les cristaux 2D de la protéine associés à la membrane[113], mais aussi dans tous les cristaux 3D de la protéine[99].

Des trimères isolés, liés à la membrane, ont fréquemment été observés sous forme non cristalline, ce qui souligne la stabilité de cet oligomère associé à une bicouche. Par contre, la forme trimèrique n'a encore pas pu être mis en évidence en solution sous conditions physiologiques[108]. Comme les différences structurales entre la forme immobilisé en 2D et la forme soluble sont faibles, il est tentant d'attribuer la propension de l'annexine A5 de former des trimères et des cristaux à des interactions attractives de courte portée avec une forte dépendance de

l'orientation, c'est-à-dire à des interactions qui ne peuvent prendre effet que lorsque la protéine est pré-orientée de manière appropriée, par exemple par interaction avec la membrane. Les caractéristiques principales de la transition de phase entre les états cristallins d'annexine A5 ont pu en effet être reproduites avec un simple modèle basé sur ce type d'interaction[114].

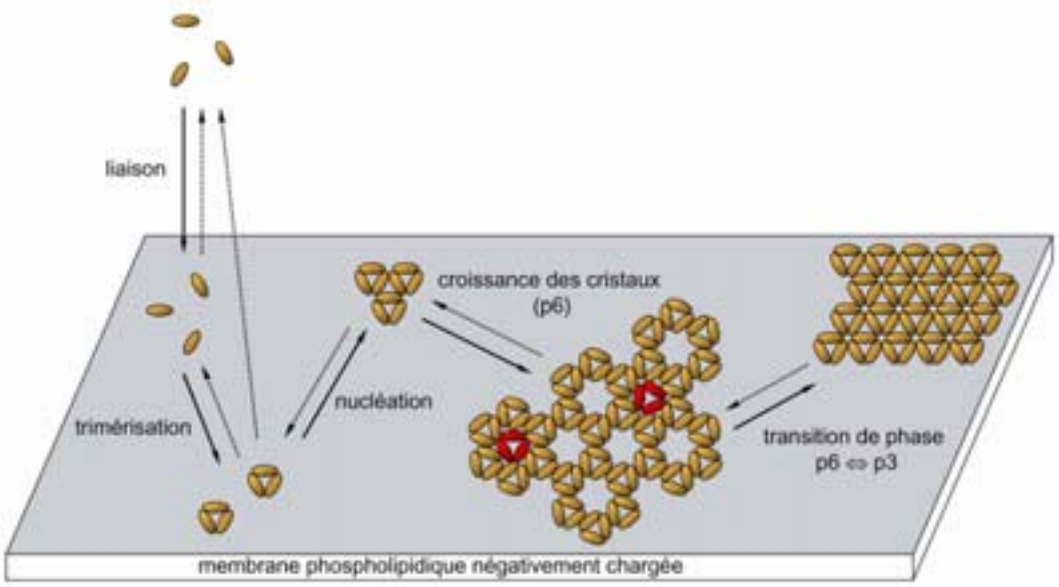

FIGURE I.6 Présentation schématique de l'auto-assemblage 2D de l'annexine A5 sur une membrane phospholipidique de charge négative[108,112]. L'annexine A5 existe sous forme monomérique en solution. La protéine s'associe à la membrane de manière calcium dépendante, puis forme des trimères. Les trimères cristallisent en 2D. La symétrie p6 du cristal ressemble à une structure en nid d'abeilles. Les vacances dans ce nid d'abeilles peuvent être remplis par des trimères supplémentaires non cristallins (les « trimères centraux », marqués en rouge). A couverture élevée de la protéine, la transition en une phase cristalline plus dense (p3) peut se produire.

Alors que les états intermédiaires et finaux du processus d'adsorption et de l'auto assemblage d'annexine A5 ont été étudiés de manière extensive[108], peu de données existent sur la cinétique de ce processus. La connaissance de cette cinétique est cependant importante dans le contexte de la fonction biologique et des applications biotechnologiques de cette protéine. La caractérisation de la cinétique de la liaison de l'annexine A5 à la membrane constitue un deuxième enjeu dans ce travail, et est présentée dans le Chapitre IV. Nos études ont abouti à quelques résultats surprenants concernant la nature de l'auto-assemblage de l'annexine A5 sur des SLBs supportées par des solides autres que le mica. Nos résultats indiquent, que la formation de cristaux 2D est fortement contrainte sur silice et sur verre.

I.4. Les techniques de caractérisation

L'émergence des domaines de recherche périphrasés par les termes "nanotechnologie" et "biotechnologie" n'aurait pas été possible sans le développement de techniques de caractérisation avancées, qui relient les mondes nanoscopique, microscopique et macroscopique. L'idéal d'un outil analytique qui est capable de voir tout, de la taille d'un atome jusqu'a la taille d'une cellule vivante, restera vraisemblablement un but lointain pour encore longtemps. Chaque technique présente des avantages et des limitations en ce qui concerne les paramètres caractérisés, le milieu nécessaire, la perturbation de l'échantillon, et la résolution spatiale et temporelle. Par conséquent, une multitude de méthodes est requise pour donner une image détaillée des paramètres pertinents et pour permettre d'identifier d'éventuels artefacts. Les aspects complémentaires de différentes méthodes et/ou une combinaison *in situ* sur un même échantillon promettent plus de résultats que la somme des résultats obtenus par les techniques constituantes.

Les interfaces, en particulier l'interface solide-liquide, constituent par leur nature un terrain d'exploration pour beaucoup d'effets physiques. Une multitude de techniques de caractérisation de phénomènes de surface exploitant ces effets, a émergé au cours du 20ème siècle. Quelques méthodes exploitent l'interface (i) pour la génération d'un signal (telles que la résonance plasmonique de surface (SPR)[115], l'ellipsometrie[116], la génération de fréquence somme (SFG)[117], la microscopie de fluorescence interférentielle (FLIC)[118,119], la microscopie interférentielle par réflexion (RICM)[120] ou l'appareil de force (SFA)[7]), (ii) pour son confinement (microscopie de fluorescence à réflexion totale interne (TIRFM)[121], microscopie à réflexion totale interne (TIRM)[122], spectroscopie de fluorescence par plasmons de surface (SPFS)[123]) et (iii) pour son amplification (diffusion Raman amplifiée par la surface (SERS)). D'autres techniques utilisent l'interface pour l'immobilisation de l'échantillon et/ou pour son confinement en deux dimensions (microscopie à force atomique (AFM), microbalance a cristal de quartz avec mesure de dissipation (QCM-D))[iv].

Pour les travaux présentés dans ce manuscrit, nous avons employé de manière extensive plusieurs techniques de caractérisation de phénomènes de surface, principalement l'AFM et la QCM-D. La combinaison de ces deux techniques (voir Chapitre II) a constitué un enjeu majeur de ce travail. Les résultats ont été complétés par l'ellipsométrie. Un dénominateur commun de ces techniques est leur utilisation en milieu aqueux, proche des conditions physiologiques. Par contre, les principes de la mesure et, par conséquent, les paramètres extraits diffèrent de manière substantielle. Les trois techniques sont introduites brièvement ci-dessous avec une mise en perspective de leurs complémentarités.

[iv] La liste des techniques énumérées, utilisables en milieu liquide, est complémentée par une gamme de techniques de caractérisation de surface dans l'air ou sous vide, telles que la microscopie à effet tunnel (STM), la microscopie électronique de balayage (SEM) ou la spectroscopie de photo-électrons induits par rayons X (XPS).

I.4.1. La microscopie à force atomique (AFM)

Depuis l'invention de la microscopie à effet de tunnel[124], une multitude de méthodes basées sur le principe de sonde locale a vu le jour. Le principe de fonctionnement est identique pour toutes : une petite sonde balaye la surface d'un échantillon avec une précision de l'ordre d'un nanomètre (ou mieux) pour sonder les propriétés locales physiques ou chimiques (ou biologiques). La microscopie à force atomique (AFM)[125,126] occupe une place prédominante parmi ces techniques. Cette technique permet de voir et de toucher, en direct, des objets à l'échelle de nanomètre dans virtuellement tout milieu.

I.4.1.1. Le principe de fonctionnement

Dans l'AFM, une sonde microscopique (la pointe) est montée à l'extrémité d'un levier. La déflection de ce levier est mesurée avec haute précision par un système optique de détection (Figure I.7). L'échantillon est balayé par la pointe grâce à des éléments piézo-électriques (le scanner) et les interactions entre l'extrémité de la pointe et l'échantillon sont contrôlées par une boucle de rétro-contrôle. Le système permet donc d'obtenir des informations sur la topographie de l'échantillon, et permet de caractériser les forces d'interaction entre pointe et échantillon (les forces normales et les forces de friction).

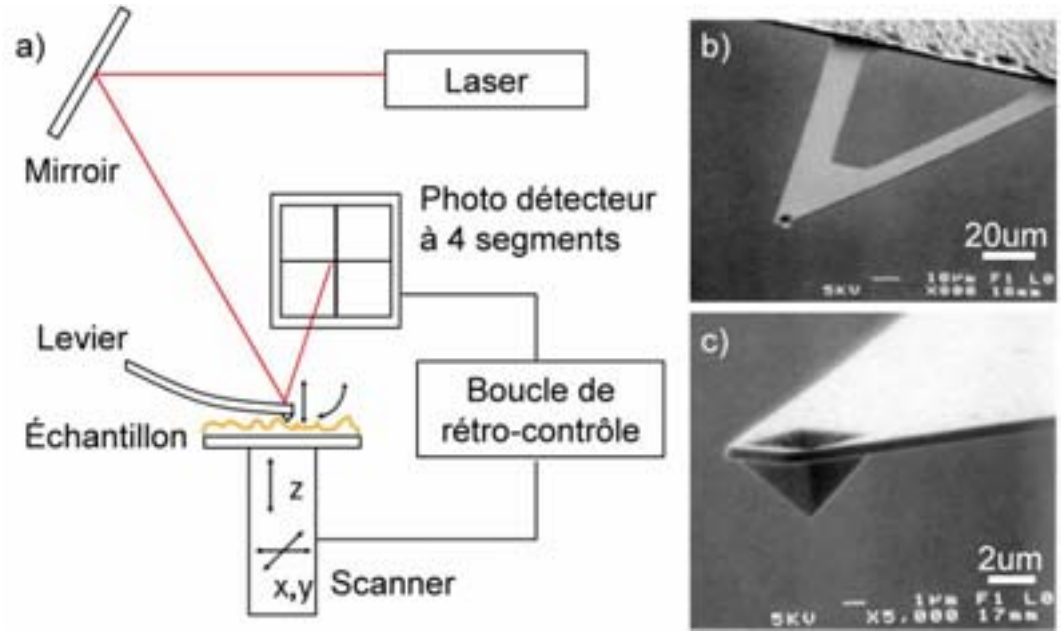

FIGURE I.7 (a) Présentation schématique de l'AFM. (b) Micrographie (par microscopie électronique à balayage) d'un levier utilisé pour les mesures en milieu liquide. La pointe se situe à l'extrémité du levier (c).

Pour illustrer la sensibilité et la géométrie de l'AFM, imaginons qu'une molécule de la taille d'une protéine ait la largeur d'une fraise de taille moyenne. Cela impliquerait l'utilisation d'une pointe de la taille et de la forme de la pyramide du Louvre à Paris pour sonder les contours du fruit. De plus, avec la résolution actuelle il serait (presque) possible de détecter les grains sur la surface de la

fraise![v] Avec une constante de raideur k du levier de quelques 10 mN/m et une sensibilité de la mesure de la déflection x de mieux d'un Angstrom, des forces $F = k \cdot x$ de l'ordre de pN peuvent en principe être détectées.

Dans le mode traditionnel et le plus direct d'opération, la pointe est maintenue en contact permanent avec l'échantillon pendant le balayage (*mode contact*) (Figure I.8a). En ajustant la déflection du levier par la boucle de rétro-contrôle, les forces normales peuvent être maintenues à un niveau faible (50-100 pN). Toutefois, les forces latérales peuvent atteindre des valeurs considérablement plus élevées[127], en particulier pour les échantillons rugueux (« high aspect ratio »). Par conséquent, la pointe peut perturber, de manière significative, les échantillons « mous ».

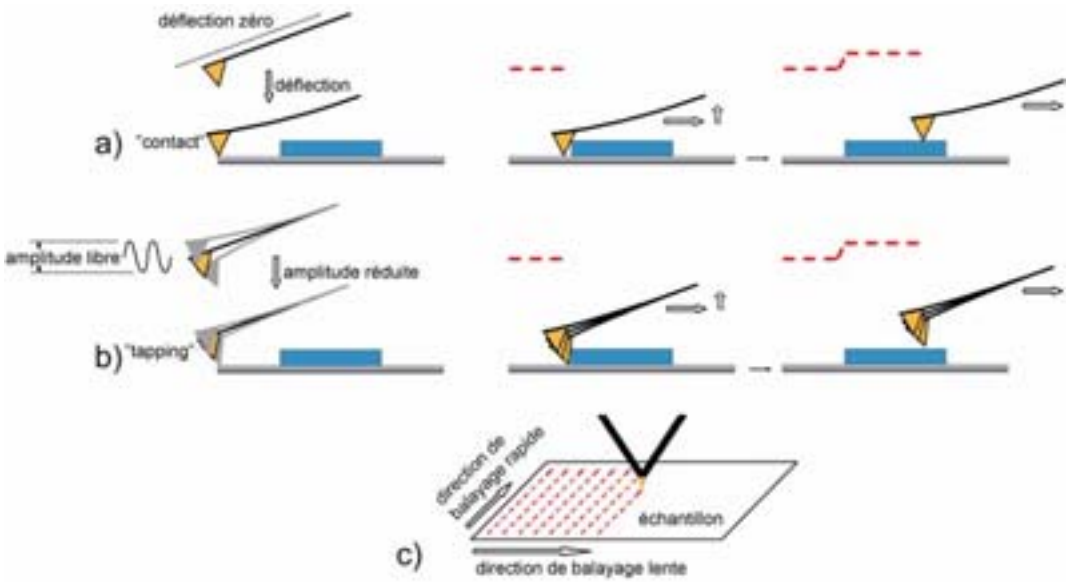

FIGURE I.8 Présentation schématique des deux modes d'imagerie par AFM. (a) Mode contact : la pointe est approchée vers l'échantillon jusqu'à ce que la déflection du levier atteigne un seuil défini à l'avance. Pendant le balayage, la déflection (la force) est maintenue constante par ré-ajustement de la distance entre pointe et échantillon. Le déplacement, vertical et horizontal, de la pointe par rapport à l'échantillon est équivalent à la topographie de l'échantillon (image de hauteur, *ligne rouge discontinue*). (b) Mode tapping : la pointe est approchée de l'échantillon jusqu'à ce que l'amplitude de vibration du levier atteigne un niveau inférieur à un seuil défini à l'avance. Pendant le balayage l'amplitude est maintenue constante. Le mouvement normal de la pointe par rapport de l'échantillon donne l'information topographique (image de hauteur, *ligne rouge discontinue*). (c) Le balayage se fait ligne par ligne (*flèches rouges discontinues*). La direction de balayage rapide correspond à l'orientation d'avancement d'une ligne. La direction de balayage lent est définie par l'orientation d'avancement de l'ensemble des lignes.

Cette limitation a été surmontée avec l'avènement du mode basé sur l'oscillation du levier (*mode tapping*). Dans ce mode, la variation de l'amplitude de l'oscillation induite par la proximité de l'échantillon est mesurée à la place de la déflection statique de levier (Figure I.8b). Le mode tapping est mieux adapté pour l'imagerie des molécules ayant une hauteur élevée par rapport à leur environnement, telles que les protéines isolées, les fibres ou les fragments

[v] Pour être en accord avec la pression exercé entre la pointe et l'échantillon, la fraise devrait cependant supporter la pression exercée par une lourde moto stationnée sur elle.

d'acides nucléiques (ADN). La résolution intrinsèque du mode tapping est cependant sensiblement inférieure à celle du mode contact[128] et le mode contact est mieux adapté pour l'imagerie à haute résolution des échantillons de faible rugosité, tels que les cristaux 2D de protéines[109,129-131].

I.4.1.2. L'AFM en biologie

Le potentiel de l'AFM en milieu aqueux est devenu apparent peu de temps après l'introduction de l'AFM, grâce à des images de résolution moléculaire d'échantillons biologiques[132,133]. Depuis, une grande variété de molécules biologiques –protéines, lipides, acides nucléiques, leurs assemblages, même des organelles[135] ou des cellules[134], ont été touchées « par la pointe » pour être imagés, bougés ou étirés.

En raison de leur importance biologique et de leur potentiel pour des applications biotechnologiques, les assemblages lipidiques ont été des objets attrayants pour des études par AFM. La possibilité de former de membranes planes à l'échelle du nanomètre, de composition variée, a permis des études détaillées des phénomènes de transition de phase[127,136-138], de la formation de domaines[74,75,77-80,139-141] et de l'interaction de protéines[73,87,142,143] ou de peptides[77,144] avec des membranes. Des nombreuses études ont portée sur les propriétés physiques des SLBs et des fragments de SLBs[75,145-148] ou des vésicules immobilisées[137,149-151]. Toutefois, jusqu'à très récemment, peu d'études ont été dédiées aux aspects cinétiques de la formation des SLBs[152-154]. Les difficultés expérimentales associées à l'imagerie des structures lipidiques hétérogènes expliquent cette lacune (voir les Chapitres II et III).

Des assemblages 2D de protéines membranaires et de protéines associées à des membranes ont été identifiés rapidement comme des objets prometteurs pour l'imagerie à haute résolution, à l'échelle du nanomètre ou mieux[127,133,155]. En conjonction avec d'autres méthodes de détermination de structure (cristallographie de rayons X et microscopie électronique à transmission), des questions pertinentes sur la structure des protéines, telles que la stœchiométrie de leurs sous unités[156], leur « handedness »[157] ou leur inclinaison par rapport à la membrane[158], ont été clarifiées. Grâce à l'application *in-situ* de l'AFM, des aspects dynamiques de la structure moléculaire et de la fonction des protéines ont pu être cartographiés[159,160]. Le suivi de l'auto-assemblage de la protéine annexine A5 en cristaux 2D, en temps réel[112,142], constitue un événement marquant, en particulier par rapport aux études présentées dans le Chapitre IV.

Par comparaison aux cristaux bidimensionnels, l'imagerie à haute résolution des assemblages moins ordonnés s'est avérée plus difficile. Cependant, quelques succès ont été rapportés récemment[161-163]. Avec la reconnaissance du rôle important de l'agrégation de peptides sous forme de structures fibreuses dans des nombreuses maladies (la maladie d'Alzheimer, la maladie de Parkinson et d'autres maladies liées aux prions, la diabète de type II), l'AFM est devenue attractive pour étudier la structure et la formation des fibres amyloïdes[164,165]. Au niveau de la molécule unique, des question concernant la structure des acides nucléiques ont été abordés[2,166] et des changements dans leur enroulement et dans l'activité des polymérases ont pu être suivis en temps réel[167-169]. Malgré quelques

exceptions remarquables[73], l'imagerie de molécules uniques des protéines reste difficile[127,170].

Outre l'imagerie, l'AFM à fourni des contributions importantes sur la caractérisation des propriétés mécaniques des molécules biologiques par l'approche de la spectroscopie de force moléculaire[171]. En appliquant une force d'étirement sur des molécules uniques, l'AFM permet d'explorer les propriétés mécaniques et thermodynamiques, telles que la résistance des protéines aux forces externes[172,173], le dépliement des protéines[174] ou des acides nucléiques[175] ou l'extraction de protéines des membranes[176]. La Figure I.9 dresse un tableau des forces observées pour quelques interactions biologiques et de la gamme des forces accessible par AFM et par d'autres techniques.

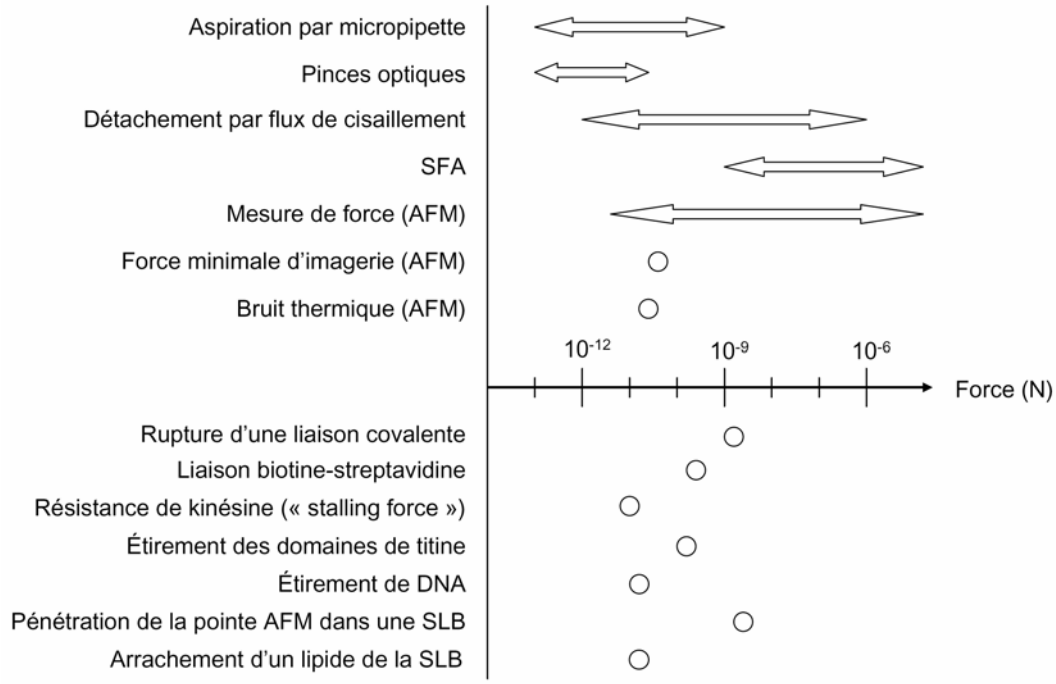

FIGRUE I.9 Forces typiquement observées pour l'interaction des biomolécules et leurs assemblages (tableau inférieur). Le tableau supérieur montre les gammes de force accessibles par AFM et par d'autres techniques.

I.4.1.3. La complexité de l'interaction entre pointe et échantillon

La littérature est riche en exemples d'une multitude d'effets qui peuvent intervenir quand une pointe AFM touche des échantillons (mous) en milieux aqueux. Quelques exemples illustratifs sont le rôle délicat des ions en solution pour l'immobilisation et l'imagerie à haute résolution des acides nucléiques[166,168,177] et des protéines[178-181], la surestimation notoire de la largeur des acides nucléiques[127], la facilité avec laquelle des cristaux 2D peuvent être imagés par rapport de l'imagerie des protéines sous forme d'assemblages non ordonnés ou de molécules uniques[170], l'effet des interactions électrostatiques sur la hauteur apparente des bicouches lipidiques[180] et des protéines[182], la réorganisation des lipides induite par la pointe[183] ou bien les effets de type « ski nautique »[145] et d'inversion de contraste[75,146] qui peuvent se produire sur des bicouches lipidiques en changeant la vitesse ou la force de balayage.

Des approches originales de caractérisation des échantillons à l'échelle du nanomètre ont émergé de la compréhension de tels effets. La cartographie des charges surfaciques[184-186] jusqu'au niveau submoléculaire[187], la mesure des changements de conformation des protéines[129] et des assemblages lipidiques[148,188] induites par la pointe ou le développement des pointes et des supports fonctionnalisés[189] en sont quelques exemples.

Tandis que ces développements élargissent les possibilités d'application de l'AFM, ils démontrent aussi la complexité de l'imagerie par AFM[127]. De nombreux paramètres doivent être ajustés et contrôlés pour obtenir de « bonnes » images d'échantillons biologiques. Particulièrement importants sont : (i) l'immobilisation adéquate de l'échantillon, (ii) la forme de la pointe bien définie et appropriée et (iii) le contrôle de l'interaction entre pointe et échantillon. Malgré beaucoup d'avancées technologiques et une reconnaissance de longue date de ces aspects, les contraintes restent importantes et des approches générales pour s'attaquer aux limitations sont rares. En conséquence, l'imagerie par AFM des échantillons biologiques reste un travail demandant de l'expérience, de la patience et une grande attention envers l'interaction entre pointe et échantillon (pour des exemples illustratifs voir les Chapitres II et III).

Grâce à son application *in situ*, l'AFM a le potentiel unique de suivre, avec une résolution spatiale de l'ordre d'un nanomètre, la cinétique de processus en temps réel. Toutefois, un facteur limitant aujourd'hui est le temps d'acquisition des images, qui est de l'ordre d'une minute pour les AFM commercialement disponible. Avec l'avènement des leviers courts[190] et des modifications dans la construction et le contrôle de l'appareillage[191,192,193], une vitesse d'acquisition de l'ordre d'une seconde est devenue possible[191], conjointement avec une augmentation de la sensibilité en mesure de force[190]. Tandis que ces avancées sont fort prometteuses, il reste à démontrer qu'elles peuvent être combinées avec une haute résolution latérale.

I.4.2. Microbalance à cristal de quartz avec mesure de dissipation (QCM-D)

La méthode QCM-D a été développée dans les années 1990 par Rodahl et coll.[194] à partir de la méthode classique de la microbalance à cristal de quartz (QCM). Elle est aujourd'hui établie comme outil de caractérisation des surfaces et des couches minces molles, permettant de mesurer la masse déposée sur une surface et de caractériser les propriétés viscoélastiques de couches minces.

L'adsorption des protéines sur supports solides[195-198] a été une des premières applications de la QCM(-D). Depuis, de nombreux questions de pertinence biologique ont été étudiées, telles que l'action d'enzymes[199], l'hybridation de brins d'acides nucléiques (DNA)[200,201]; des aspects fonctionnels des bicouches lipidiques supportées[202-206], les interactions drogue/DNA[207], la réticulation des protéines[208,209], l'adhésion et l'étalement des cellules[210,211].

Grâce à la mesure de la dissipation (*D*), la QCM-D est plus qu'un capteur de masse. Elle fournit également des informations sur la structure des films adsorbés.

Cela rend la technique particulièrement prometteuse comme outil de caractérisation pour le développement et pour la validation des surfaces bio-fonctionnalisées[59,212,213] pour des applications biomédicales, des capteurs[214] ou des bio-puces. Outre les SLBs[49,69,206,215-220], les multicouches des polyélectrolytes[221-224], des couches minces de polymères[225] ou les couches anti-coagulantes[226-228] ont également été étudiées.

I.4.2.1. Le principe de fonctionnement

La méthode QCM-D est basée sur la mesure du comportement de résonance d'un oscillateur à cristal de quartz en mode de cisaillement. Grâce à ses propriétés piézo-électriques, les oscillations mécaniques du quartz peuvent être excitées par l'application d'un champ électrique oscillatoire à travers le cristal. Une fois excité, l'oscillation libre (et décroissante) mécanique peut être suivie par mesure du champ électrique correspondant. A partir de la courbe de résonance, la fréquence, f, et la dissipation, D, sont déduites (Figure I.10, voir la légende pour de plus amples détails). Le suivi des variations, Δf et ΔD, des deux paramètres, induites par le matériel déposé, permet la caractérisation en temps réel des processus d'adsorption et des changements structuraux des couches déposées. La résolution temporelle de la méthode est en principe limitée par le temps de décroissance de l'oscillation (à l'échelle de la milliseconde). Actuellement les instruments communs permettent une résolution inférieure à une seconde, une différence importante par rapport à la résolution temporelle de l'AFM (voir Chapitre II).

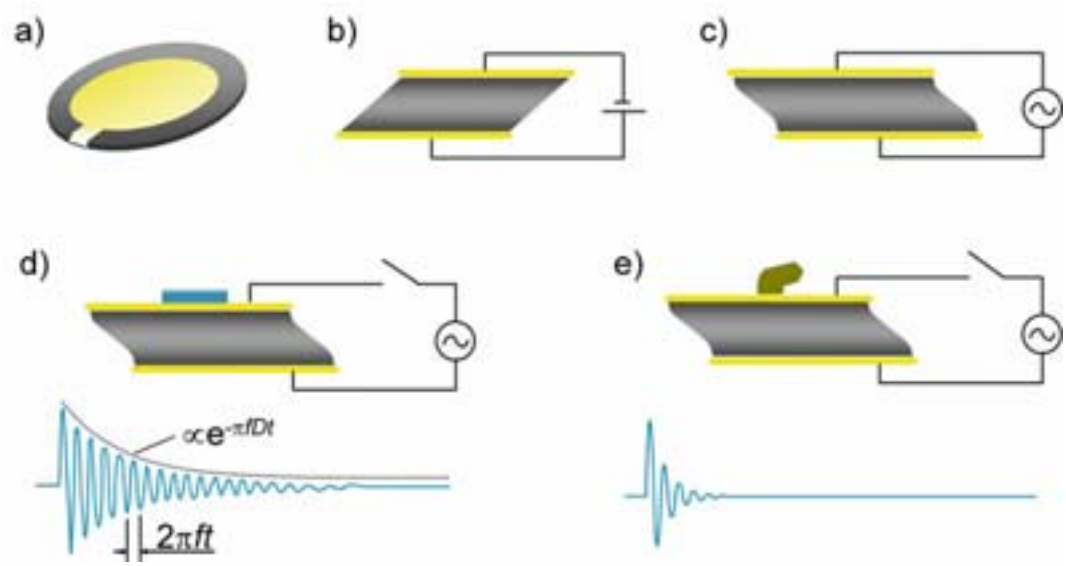

FIGURE I.10 Présentation schématique du principe de fonctionnement de la technique QCM-D. Le cristal de quartz piézo-électrique est pris en sandwich entre deux électrodes en or (a). L'application d'un champ électrique à travers le cristal induit son cisaillement (b). La résonance du mouvement de cisaillement peut être obtenue par un champ oscillatoire électrique de fréquence adaptée (c). Après arrêt de l'excitation, l'amortissement de l'oscillation du cristal est suivi (d, e). La variation temporelle de l'élongation, $A(t)$, est caractérisée par la relation $A(t) = A_0 \exp(-\pi f D t)\sin(2\pi f t + \phi)$ pour extraire la fréquence propre de résonance, f, et la dissipation, D (D est le la réciproque du facteur de qualité, Q). La déposition d'une masse rigide (d) sur la surface du cristal conduit à une diminution de f, tandis qu'une masse molle (et viscoélastique) affecte également D. La mesure des variations de f et D permet de suivre des processus à l'interface, tels que l'adsorption, en temps réel.

I.4.2.2. La détermination de la masse adsorbée

Dans les années 1950, Sauerbrey[229] a déduit une relation simple entre la masse adsorbée, Δm, et le changement en fréquence, Δf :

$$\Delta m = -\frac{\nu_q \rho_q}{2 f_0^2} \frac{\Delta f_n}{n} = -C \frac{\Delta f_n}{n}. \qquad (1)$$

Cette formule constitue le fondement de l'utilisation de la technique QCM comme capteur de masse. La vitesse de propagation du son, $\nu_q = 3340$ m·s^{-1}, et la densité, $\rho_q = 2.65$ g·cm^{-3} sont des propriétés intrinsèques du quartz. La fréquence fondamentale, f_0, est déterminée par l'épaisseur, t_q, du cristal (en première approximation, $f_0 = \upsilon_q / 2t_q$) qui peut être reproduite avec une précision meilleure que 1%. La constante de sensibilité de masse, C, est alors indépendante du matériel adsorbé et ne nécessite aucune calibration supplémentaire. Pour des capteurs communs ($f_0 = 5$ MHz), $C = 17.7$ ng·cm^{-2}·Hz^{-1}. La résolution en fréquence est actuellement d'environ 0.2 Hz (en milieu liquide), ce qui correspond à une résolution massique de quelque ng·cm^{-2}. Hormis l'oscillation en mode fondamental ($n = 1$), d'autres harmoniques peuvent également être excitées ($f_n \approx nf_0$, $n = 3, 5, 7$ étant l'ordre de l'harmonique).

Alors que les capteurs de masse basés sur l'équation de Sauerbrey fonctionnent pour des nombreuses applications à l'air ou sous vide, il est important de noter que l'équation n'est valide que pour des masses adsorbées qui sont (i) faibles (par rapport de la masse du cristal), (ii) rigides, (iii) distribuées de manière homogène et (iv) couplées au cristal sans glissement (« slip »). Parmi les limitations énumérées, la contrainte sur la rigidité est particulièrement sévère pour des applications biologiques. Le milieu aqueux et la plupart des biomatériaux sont en effet des matières molles et, par conséquent, l'équation (1) devient une approximation avec une précision *per se* inconnue.

I.4.2.3. La dissipation

Par opposition aux films rigides, les propriétés viscoélastiques de la matière molle donnent lieu à une dissipation d'énergie ($\Delta D > 0$). La mesure de la dissipation a conduit à un nombre d'améliorations dans la caractérisation d'échantillons – polymères, échantillons biologiques, sur le plan qualitatif mais aussi sur le plan quantitatif.

Qualitativement, la dissipation permet de détecter des transitions de phase, i.e. de distinguer les états différents d'un matériel déposé. Ceci est particulièrement bien illustré par la capacité de la dissipation de distinguer entre des vésicules intactes et des bicouches lipidiques déposées sur un support solide. Cette distinction, mise en évidence par Keller et Kasemo[69], a été à la base d'un progrès significatif dans la compréhension du processus de la formation des SLBs[49,215,218]. La rigidification d'une couche de protéines par cross-linking[208] ou l'hybridation de brins d'acides nucléiques[200] en sont d'autres exemples. Des faibles variations dans le comportement d'adsorption, en particulier en fonction de la couverture, peuvent être mises en évidence au niveau du graphe ΔD-Δf. L'utilisation de ce mode de

représentation nous à permis d'identifier un comportement « anormal » d'adsorption de protéines (un exemple est donné dans l'article II - figure 2).

L'analyse quantitative de processus d'adsorption par QCM-D a été rendue possible grâce au développement de modèles qui prennent en compte les propriétés viscoélastiques des couches déposées et des milieux liquides[230-233]. En particulier, le modèle de Voinova et coll.[230] établit une relation entre, d'un côté, les propriétés de la couche déposée (son épaisseur, sa densité, sa viscosité et son module de cisaillement) et immergé dans un milieu liquide et, de l'autre côté, les variations de fréquence et de dissipation (sur plusieurs harmoniques) (Figure I.11).

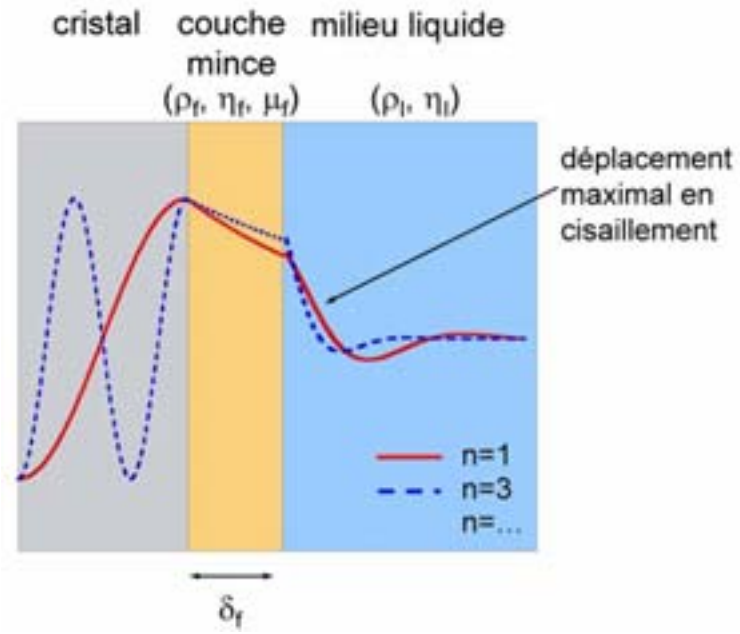

FIGURE I.11 Le modèle viscoélastique de Voinova et coll.[230]. Une onde cisaillante créée dans le cristal de quartz se propage et se dissipe dans le matériel adjacent. Le modèle décrit la relation entre, d'un côté, les propriétés viscoélastiques (la viscosité, η_f et le module de cisaillement, μ_f) d'une couche d'épaisseur homogène, δ_f et de densité ρ_f, immergée dans un milieu liquide de type Newtonien (de densité ρ_l et de viscosité η_l) et, de l'autre côté, les changements correspondants en fréquence, Δf_n, et en dissipation, ΔD_n, pour de multiples harmoniques (n = 1, 3, 5, 7). Une routine numérique, implémentée dans le logiciel QTools (Q-Sense, Suède), permet, à partir de la réponse QCM-D, de remonter aux propriétés de la couche déposée[212].

Ce modèle a permis d'évaluer la validité d'application de l'équation de Sauerbrey[212] : en première approximation, l'équation de Sauerbrey n'est pas valide pour des couches minces (en milieu aqueux) caractérisées par un rapport $\Delta D/\Delta f < 0.2 \cdot 10^{-6} \mathrm{Hz}^{-1}$. Le modèle à été utilisé avec succès dans le cas de différents types de couches[212,234], telles que des couches de protéines[208,209,212], de vesicules[216], ou des couches de brins d'ADN immobilisés[201], permettant de déterminer la masse exacte de ces couches fortement dissipatives et/ou de déduire leurs propriétés viscoélastiques, le modèle a été appliqué avec succès pour. Cependant, ce modèle constitue certainement une représentation simplifiée de la réalité. En particulier, l'approximation d'une couche mince homogène dont les propriétés viscoélastiques obéissent au modèle de Voigt-Kelvin (ou de Maxwell) n'est valable que pour certains systèmes.

I.4.2.4. Le rôle de l'eau en QCM-D

La méthode QCM-D est sensible pour toute matière mécaniquement excitée par l'oscillation du cristal de quartz. Une caractéristique essentielle de signal QCM-D est que la masse mesurée inclut l'eau associée à la couche adsorbée. Ceci est une différence notable par rapport aux techniques optiques. En effet, des techniques comme le SPR, l'ellipsométrie, la réflectométrie ou la spectroscopie à guide d'onde (OWLS) sont sensibles aux changements de l'indice de réfraction (de la densité optique) entre l'adsorbat et le milieu aqueux. Ainsi, essentiellement la masse sèche de l'adsorbat contribue au signal pour autant que l'eau associée ait le même indice de réfraction que l'eau « bulk ». Cette différence rend les techniques optiques et la méthode QCM-D complémentaires, leur combinaison permettant de déduire l'état d'hydratation d'une couches déposée[198,209,219,235]. Dans certains cas, comme celui de polymères immobilisés dans la conformation « brosse » ou pour des brins de nucléotides immobilisés, l'eau peut contribuer pour plus de 90% de la masse totale[201]. Ceci peut être utilisé pour augmenter considérablement la sensibilité de la méthode QCM-D[201]. En outre, la fraction d'eau détectée par unité de masse sèche peut varier en fonction de la couverture de surface, et ainsi influencer la cinétique apparente des processus d'adsorption ou de désorption[236] et rendre l'analyse du signal complexe.

Le rôle de l'eau dans les processus dissipatifs n'est actuellement pas compris en détails. En fonction de l'environnement, l'eau peut présenter des propriétés apparentes très différentes : confinée dans les interstices d'une couche rigide, l'eau apparaît comme une masse rigide[237,238], alors qu'elle apparaît fortement viscoélastique dans une matrice viscoélastique[201]; en absence de confinement, l'eau exhibe ses propriétés ordinaires macroscopiques[232,238].

I.4.2.5. L'influence des oscillations sur l'interface solide-liquide

Étant donné que l'interface solide-liquide est agitée mécaniquement, il est logique de se demander si l'oscillation du cristal de quartz peut avoir une influence sur les processus à l'interface, comme par exemple la production de phénomènes de « glissement »[239]. Dans les conditions habituelles d'utilisation, l'amplitude de l'oscillation est inférieure à 1 nm en milieu aqueux[vi]. Alors qu'il a été mis en évidence que des oscillations d'amplitudes élevées (10 nm et plus) peuvent influencer des processus d'adsorption ou de désorption ou induire une agitation locale[241-243], aucun effet (ou des effets mineurs) n'a été observé pour des amplitudes faibles[243] sur des surfaces hydrophiles. Par conséquent, la technique est essentiellement non perturbante et la condition de « non-glissement » mentionnée ci-dessus est considérée valable pour les mesures de QCM-D.

[vi] Borovsky et coll.[240] proposent la formule empirique : $A = 1.4\ Q\ V$ pour l'amplitude, A (en pm). $Q = 1/D$ et V sont, respectivement, le facteur de qualité et la tension appliquée au cristal (en V). Les valeurs habituelles de $V = 0.14$ mV (correspondant à une « driving voltage » de 1.0 en QSoft (Q-Sense, Suède)) et de $D = 350 \cdot 10^{-6}$ en milieux aqueux ($20 \cdot 10^{-6}$ dans l'air) donnent une amplitude de $A = 0.6$ nm (10 nm).

I.4.2.6. Les supports utilisables

En contraste avec la plupart des techniques optiques qui dépendent fortement des propriétés de l'interface, les capacités de mesure de la méthode QCM-D ne dépendent que du cristal de quartz. Le cristal peut être couvert d'une multitude de supports sans perturber le signal. Les exemples les plus courants sont des couches minces de métal (Au), d'oxydes (SiO_2, TiO_2) ou de polymères qui peuvent être déposées, respectivement, par évaporation, la pulvérisation ou « spin-coating ». L'épaisseur de la couche déposée est un paramètre limitant. Des couches rigides peuvent atteindre des épaisseurs de plus que 10 μm sans trop perturbé le signal, comme ceci a été mis en évidence pour des feuilles de métal[244] ou du mica[219] collés sur le cristal de quartz (cette question est abordée au Chapitre II).

I.4.2.7. Les modes d'utilisation

Dans le contexte de nos travaux, la méthode QCM-D a été utilisée dans deux modes différents de manipulation des liquides : le mode « échange » et le mode « flux » (Figure I.12). Le mode échange constitue la manière la plus simple et la plus robuste d'utilisation. Le mode flux est par contre mieux approprié dans le cas d'échantillons de concentrations relativement faibles (moins de 5 μg/mL), la déplétion du milieu liquide associée à l'adsorption de l'échantillon étant limitée. Le flux limite également l'enrichissement du milieu liquide avec l'échantillon (de la surface active ou des parois de la cellule) pendant le rinçage.

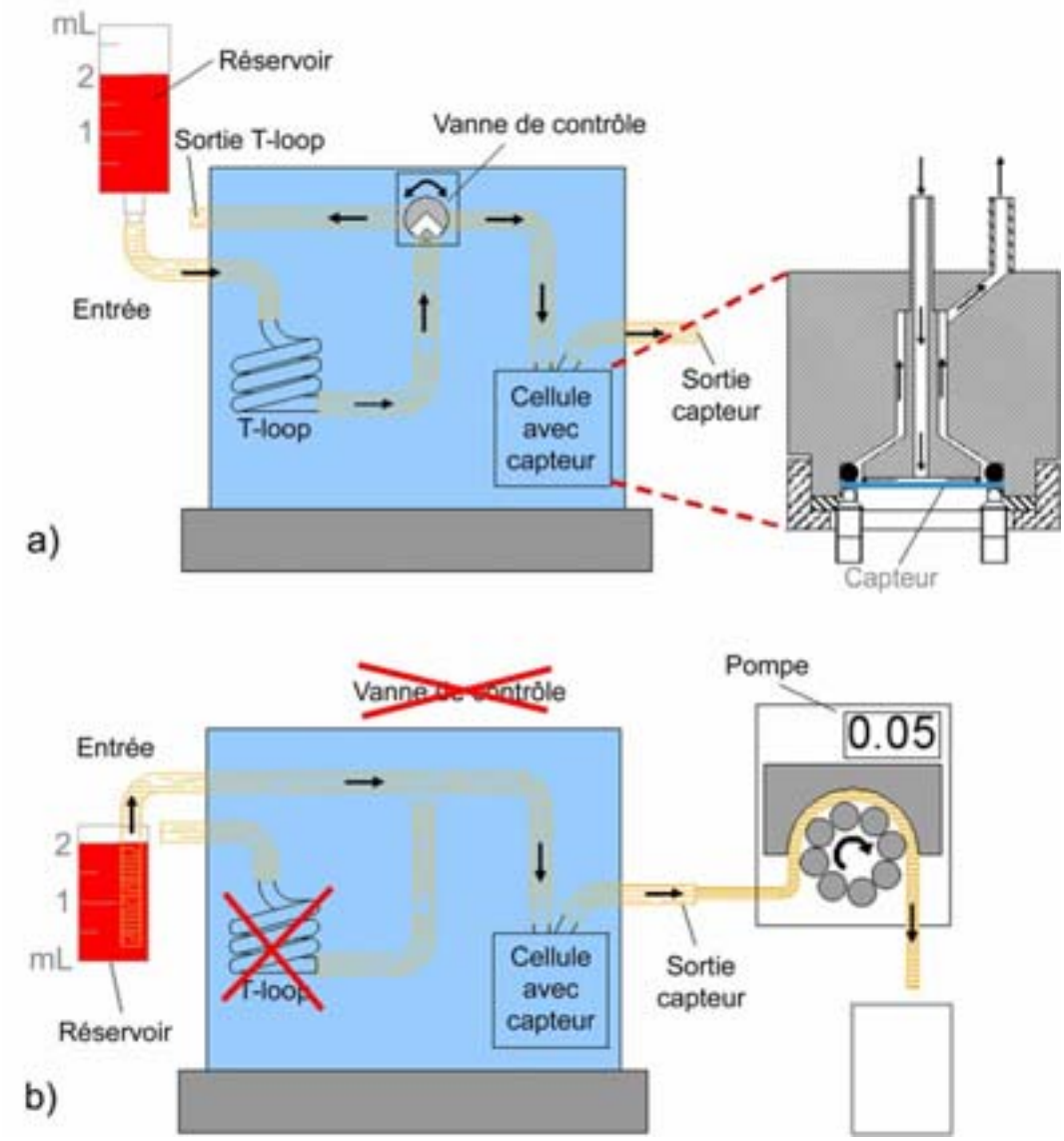

FIGURE I.12 Description schématique de la manipulation de liquides en QCM-D. La direction du transport du liquide est indiquée par des flèches. (a) Le mode « échange » permet l'échange rapide de solutions. La vanne de contrôle est en position fermée par défaut et ouverte uniquement pendant le transfert rapide de liquide. La solution est (i) transférée du réservoir à la boucle de stabilisation en température (*T-loop*) où (ii) elle réside pendant 2 min, (iii) avant d'être délivrée à la cellule de mesure contenant le capteur (*Cellule avec capteur*). Les étapes (i) à (iii) sont répétées pour chaque échantillon et chaque étape de rinçage. La coupe à travers la cellule (à droite) révèle la géométrie symétriquement axiale du flux. Le liquide est injecté au dessus du centre du cristal (mode « impinging jet ») et sort par la périphérie. Le volume de la cellule et de ~50 µL. 1.5 mL et 0.5 mL de liquide sont respectivement nécessaires pour un échange complet du liquide dans la T-loop et dans la cellule. Chaque échange prend quelques secondes. (b) Mode « flux » : le liquide est injecté à travers la cellule en continu, au moyen d'une pompe péristaltique. Le débit habituel est de 1 µL/s, environ. La T-loop et la vanne sont hors circuit.

I.4.3. L'ellipsométrie

Le principe de l'ellipsométrie à été élucidé il y a plus d'un siècle[245-247]. La technique est basée sur la mesure du changement de l'état de polarisation d'une lumière incidente elliptiquement polarisée pendant sa réflexion sur une interface. Les angles ellipsométriques sont sensibles à la présence de couches minces

organiques déposées sur la surface réfléchissante, permettant de détecter des dépôts de l'ordre de quelques ng·cm^{-2}. Plusieurs types d'ellipsomètre sont disponibles, l'ellipsomètre à méthode de zéro étant probablement le plus robuste.

I.4.3.1. Le ellipsomètre à méthode de zéro

Dans l'ellipsométrie à méthode de zéro, les angles de polarisation de deux prismes, le polariseur, *P*, et l'analyseur, *A*, sont ajustés par de moteurs pas-à-pas, de sorte que l'intensité de la lumière émise soit minimale (« null ellipsometer »[vii]) (figure I.13a-b, voir la légende pour de plus amples détails). La résolution temporelle est limitée par les moteurs pas-à-pas et est de plusieurs secondes. Les angles ellipsométriques, Δ et ψ, sont déterminés à partir des angles *P* et *A*, respectivement, en utilisant quelques simples règles de sélection[247]. Les coefficients (complexes) de réflexion de la lumière polarisée parallèle, $r_{p,}$ et perpendiculaire, r_s, par rapport au plan d'incidence, sont liés aux angles ellipsométriques par

$$\frac{r_p}{r_s} = \tan\Psi \exp(i\Delta). \qquad (2)$$

La relation entre les propriétés de la couche déposée et les angles ellipsométriques est en général non linéaire. L'épaisseur, *d*, et l'indice de réfraction, *n*, de la couche peuvent, en principe, être déterminés par modélisation à partir d'une modèle approprié de l'adsorbat[247,248]. La masse (sèche) adsorbée, *m*, peut alors être déterminée, à condition que la relation de Lorentz-Lorenz s'applique à la couche contenant les molécules adsorbées et la solution,

$$m = 3\left(\frac{A_p}{M_p}\left(n_b^2+2\right) - V_p\left(n_b^2-1\right)\right)^{-1} \frac{n+n_b}{n^2+2} d\left(n-n_b\right), \qquad (3)$$

où A_p, M_p, V_p et n_b sont, respectivement, la réfractivité molaire par unité de volume, la masse moléculaire, le volume partiel spécifique de l'échantillon et l'indice de réfraction de la solution[248]. En pratique, les erreurs associées à d et n-n_b peuvent être élevées, en particulier pour des couches très minces (d'une épaisseur de l'ordre de 1 nm). Etant donné que les erreurs sont covariantes, le produit $d(n\text{-}n_b)$ et donc la masse adsorbée peuvent être déterminés avec une meilleure précision.

Il est notable que la relation entre les propriétés de la couche déposée et les angles ellipsométriques, outre sa non linéarité, dépend fortement de l'angle d'incidence et des supports employés. Le scénario se complique encore pour des applications en milieu liquide, parce que la lumière traverse des interfaces et de la matière supplémentaires, telles que la solution ou les parois de la cellule. Ceci explique l'importance d'utiliser des surfaces contrôlées, une cellule expérimentale adaptée

[vii] Idéalement, l'intensité de la lumière sortante devrait être nulle, « null » en allemand, d'où le nom de ce mode d'utilisation.

et une calibration adéquate pour pouvoir aboutir à une détermination, absolue, de *m* (ou également de *d* et de *n*). Si une telle calibration n'est pas disponible, l'évolution de l'angle Δ (ou ψ) permet de déterminer la variation de la masse déposée, par exemple, lors d'une analyse cinétique d'une processus d'adsorption[249]. Les résultats obtenus par ellipsométrie doivent être considérés avec précaution car l'hypothèse sous-jacente d'une relation linéaire entre *m* et Δ, n'est pas garantie pour tout type d'échantillon.

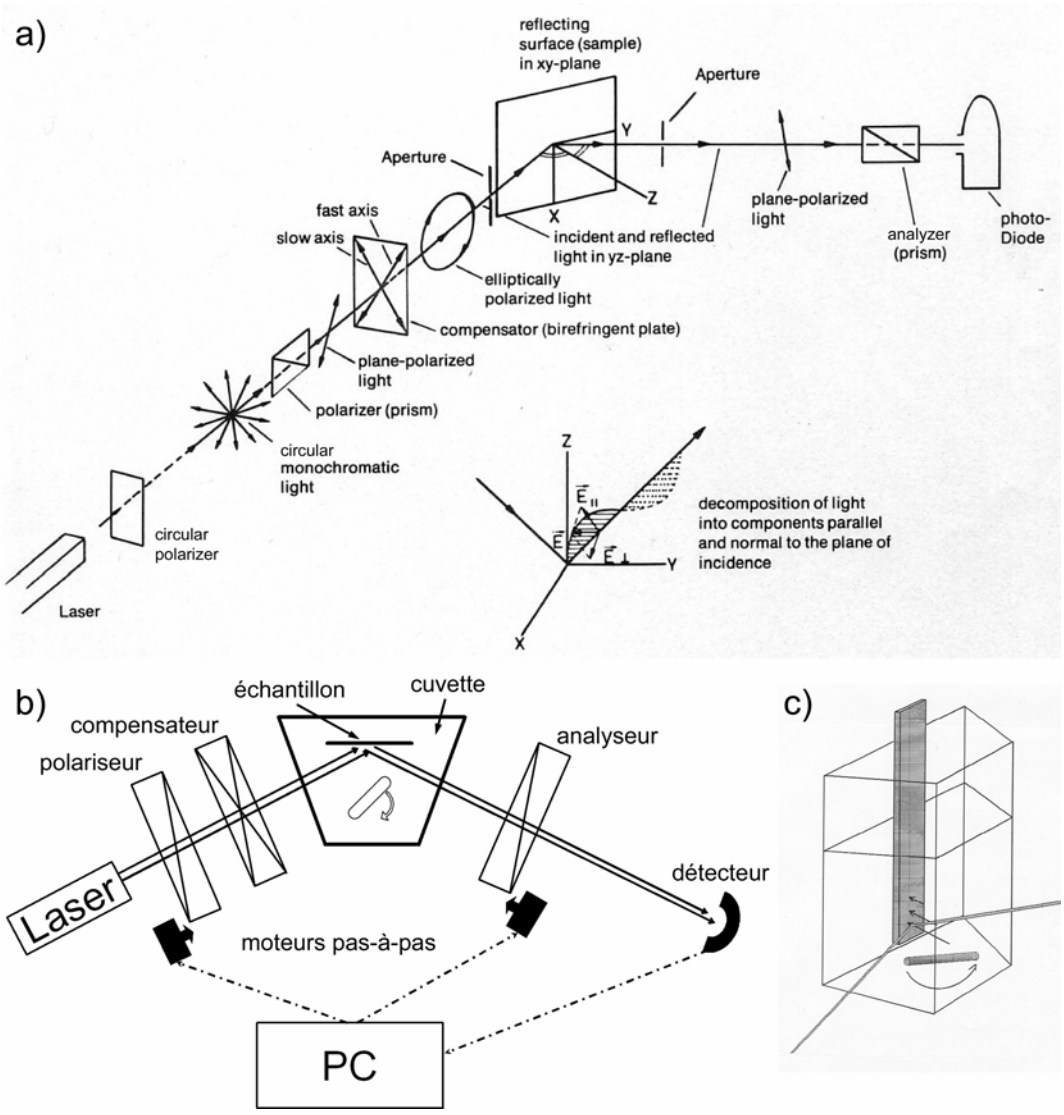

FIGURE I.13 Description schématique de l'ellipsomètre à méthode de zéro. (a) Le prisme polariseur *P* génère une lumière plane polarisée d'orientation définie de la lumière monochromatique d'une source laser. Le compensateur (habituellement une plaque biréfringente) transforme la lumière polarisée plane en lumière elliptiquement polarisée. La traversée de l'échantillon induit une variation de la polarisation de la lumière incidente. L'orientation du polariseur est ajustée de sorte que la lumière réfléchie par l'échantillon soit linéairement polarisée. L'orientation du prisme analyseur *A* est alors ajustée de manière à ce que l'intensité de la lumière sortante soit proche de zéro. Les changements des propriétés de l'interface nécessitent un ajustement concerté du polariseur et de l'analyseur pour maintenir l'intensité de la lumière sortante minimale. L'ajustement est assuré par deux moteurs pas-à-pas, contrôlés par un ordinateur (b), qui assure la mesure des variations de *A* et *P*, lors de l'adsorption à l'interface, en temps réel. (c) Présentation schématique de la cuvette utilisée pour la mesure en milieu liquide. Images fournies par le Prof. Wim Hermens (Université de Maastricht, Pays Bas).

I.4.3.2. Les support utilisables

En principe, l'ellipsométrie peut être employée sur toute surface (de préférence optiquement non active). Cependant, la réponse ellipsométrique est fortement dépendante de la surface. En conséquence, la sensibilité varie en fonction de l'interface et chaque type de support nécessite une nouvelle calibration. En outre, la calibration peut être rendu difficile par la rugosité de la surface (à l'échelle du nanomètre), ce qui peut induire des erreurs de détermination de masses absolues. Dans le cadre de nos travaux, nous avons utilisé des supports de silice (sous forme de « wafer ») qui sont particulièrement bien adaptés, en raison de leur faible rugosité et de leur fort contraste ellipsométrique. La possibilité d'utiliser des supports de mica en ellipsométrie a récemment été démontrée[250]. Cependant, la détermination absolue de la masse déposée sur mica est plus difficile.

L'ellipsométrie présente la propriété unique de pouvoir être employée pour des mesures à l'interface solide-liquide aussi bien qu'à l'interface air-eau. Cette propriété est particulièrement intéressante pour les membranes lipidiques car elle permet une corrélation entre le monde des monocouches lipidiques (à l'interface air-eau)[251] et le monde des bicouches déposées sur support solide[252]. L'ellipsométrie présente d'autres potentiels comme l'application à multiples longueurs d'onde (l'ellipsométrie spectroscopique) et l'imagerie par ellipsométrie.

I.4.3.3. Les modes d'utilisation

L'ellipsomètre que nous avons utilisé est un système de cuvette ouverte (Figure I.13c)[84], qui nous a été rendu accessible gracieusement par le Prof. Wim Hermens (Université de Maastricht, Pays Bas). La solution (~3 mL) est agitée par un barreau magnétique (~1000 rpm) situé au fond de la cuvette. Les échantillons sont injectés dans la solution à une concentration désirée. Des rinçages sont réalisés par injection de ~30 mL de solution (débit de ~1 mL/s) en aspirant l'excès de liquide simultanément. Un autre mode de fonctionnement consiste à stopper l'agitation pendant quelques secondes après l'injection de l'échantillon, de manière à suivre l'adsorption en absence d'agitation.

Le système présente des avantages remarquables, en particulier pour les mesures de cinétique. Etant donné que la cuvette est ouverte, le système permet de modifier à volonté le milieu ou les ions (tels que le Ca^{2+}) et rend possible l'acquisition des d'isothermes d'adsorption[253]. En outre, le mode d'agitation génère une vitesse d'adsorption constante (à condition que l'adsorption soit limitée par le transport des molécules vers l'interface) sur une surface uniformément accessible d'une taille suffisamment grande (c'est-à-dire par rapport à la taille du faisceau laser)[254]. Les inconvénients du système « cuvette ouverte » sont le volume relativement élevé et le rinçage relativement mal contrôlé, ce qui rend la mesure de la désorption et l'échange de l'échantillon difficilement contrôlable.

I.5. Les supports solides

Les travaux présentés dans ce manuscrit pourraient servir comme une excellente démonstration du rôle essentiel de la nature du support solide dans les processus d'adsorption et d'auto-organisation. Tandis que certains résultats était attendus, tels que le rôle de la charge surfacique sur le processus de formation des SLBs[49] (voir Chapitre III), d'autres ont été surprenants, tels que l'absence de cristallisation de la protéine annexine A5 sur des SLBs déposées sur silice[188] (voir Chapitre IV). Dans leur ensemble, les résultats soulignent l'importance d'une bonne compréhension des processus à l'interface entre un support solide et le milieu aqueux. Beaucoup de questions restent encore ouvertes ou vivement débattues. Certaines sont fondamentales, telles que la compréhension, à l'échelle moléculaire, de la nature de l'eau à l'interface[4,5] et, en particulier, de la couche mince d'eau entre les SLB et le support solide[255-257].

I.5.1. Le mica

Le mica a déjà été utilisé au Moyen Age. Le peuple de la région de Moscou en Russie a employé ce minéral comme base pour les fenêtres ("le verre de Moscou"), d'où le nom de la forme la plus courante du mica, le *muscovite* (Figure I.14). Cette utilisation historique illustre la propriété remarquable du mica de se cliver en feuillets transparents, flexibles et de tailles relativement grandes. Aujourd'hui, son utilisation extensive en recherche provient d'un besoin de surfaces idéalement planes pour l'étude des forces d'interactions entre surfaces[4,7,258] ou comme support non contrasté pour l'immobilisation et l'étude des propriétés topographiques de molécules (biologiques)[129,179]. En effet, des surfaces planes à l'échelle atomique sur une aire de quelques cm^2 peuvent être générées de manière relativement facile[259] et sont utilisées en routine pour des mesures par SFA ou par AFM.

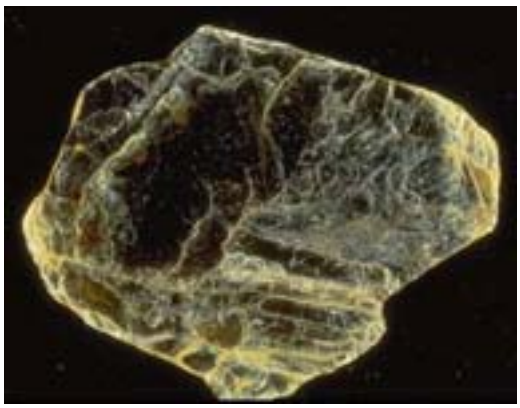

FIGURE I.14 Un échantillon naturel de mica de type muscovite.

Le mica de type muscovite est un silicate d'aluminium de structure stratifiée avec la composition chimique suivante $K(Si_3AlO_{10})Al_2(OH)_2$. Il est composé d'un empilement de couches, chacune d'entre elles constituée de deux feuillets tétraédriques de $(Si,Al)_2O_5$, liées par un feuillet central d'$Al_2(OH)_2$. La charge globale négative de ce sandwich est contrebalancée par une couche d'ions

potassium coordonnés sous forme d'hexagones (Figure I.15)[260]. Le clivage se fait au niveau de la couche de potassium, exposant une surface hydrophile.

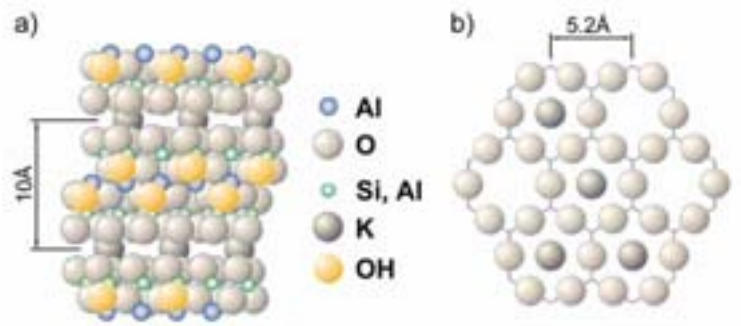

FIGURE I.15 Modèle atomique de la structure stratifiée du mica. (a) Un feuillet d'$Al_2(OH)_2$ est pris en sandwich entre deux feuillets de structures tétraédriques de $(Si, Al)_2O_5$, orientés de manière opposés. O_5 forme des tétraèdres, qui sont rempli par un atome de Si ou d'Al. Le clivage se produit au long de la couche des ions potassium, exposant la couche des oxygènes basales en forme d'hexagones (b)[260]. Image adaptée de la réf. [179].

En milieu aqueux les ions potassium se dissocient et ils sont échangés par des protons ou par d'autres cations[261]. L'échange d'ions détermine la charge de la surface du mica. La charge est habituellement négative et sa grandeur dépend de la concentration d'électrolytes en solution[262,263] (voir Chapitre III). Optiquement, le mica est un matériel faiblement biréfringent, c'est-à-dire que la propagation de la lumière est différente selon deux axes normaux aux couches cristallines.

Malgré son utilisation courante dans la recherche et dans l'industrie – le mica est un excellent isolant avec des propriétés chimiques et thermiques intéressantes – l'automatisation de processus de clivage reste difficile. La production de feuillets d'une épaisseur convenable avec deux surfaces de bonne qualité nécessite une expérience manuelle sophistiquée et demande beaucoup de temps. Cela impose de contraintes sur l'utilisation du mica pour certaines applications, telle que le dépôt du mica sur les capteurs QCM-D, une question étudiée en détail au Chapitre II.

I.5.2. Le silicium et la silice

L'utilisation des matériaux basés sur le silicium a connue une croissance énorme lors des dernières 50 années, en conjonction avec le développement de l'industrie des semi-conducteurs. Des larges cristaux monolithiques de silicium sont aujourd'hui produits en routine avec une haute pureté. De procédés supplémentaires (coupe, gravure à l'eau forte, polissage) permettent de générer de disques d'une taille de plusieurs décimètres (les wafers) avec une très faible rugosité (quelques Angstrom). De plus, des méthodes pour créer des nano-structures de géométrie contrôlée sur silicium, à l'échelle micrométrique ou nanométrique, ont été développées, ou sont en cours de développement.

Avec l'attraction du patterning et de la nano-fabrication pour le développement de surfaces biofonctionnalisées[61,264-266] et l'intérêt de lier la biologie à l'electronique[92,267], les surfaces basées sur le silicium deviennent de plus en plus utilisées dans des applications bio(techno)logiques. De plus, l'utilisation de la silice sous forme des particules colloïdales est déjà établie pour la séparation et la

purification des biomolécules par chromatographie en liquide[268] ou en couche mince.

Suite à l'exposition à l'air des surfaces de silicium, une couche mince d'une épaisseur de ~1 nm est rapidement oxydée, générant ainsi une couche amorphe de silice (SiO_2). Des couches d'oxyde plus épaisses peuvent être produites de manière contrôlée par différentes méthodes, telles que le traitement de plasma d'oxygène, le traitement par lumière ultraviolette et ozone ou le traitement thermique. Des blocs de silice – sous forme amorphe (la silice vitreuse) et cristalline (le quartz) – peuvent également être polis pour obtenir des surfaces avec une rugosité similaire à celle des wafers de silicium. Des couches minces de silice amorphe sont aussi créées par déposition de vapeur de plasma, telle que l'évaporation ou la pulvérisation de type réactif. La pulvérisation est la méthode de choix pour déposer de la silice sur les capteurs QCM-D. La rugosité intrinsèque de ces couches est souvent légèrement plus élevée, induite par la rugosité du support.

La silice avec ses groupements siloxanes (Si-O-Si) possède une propriété clé, les « valences résiduelles » qui réagissent avec l'eau environnante pour couvrir la surface avec des groupements silanol (SiOH). Une surface complètement hydroxylée est fortement hydrophile et contient 4-5 groupements SiOH par nm^2, une valeur partagée par des silices amorphes et cristallines[269,270]. Le groupement silanol résiste à un séchage à l'air à 120-150°C. Pourtant, la surface peut être dé-hydroxylée de manière presque totale par un traitement thermique de quelques heures à 1100°C. Il est notable, que la ré-hydroxylation d'une telle surface hydrophobe de siloxanes (la silice pyrogénique) dans l'eau peut être excessivement lente, en particulier à $pH < 5$ (à l'échelle de quelques années). L'hydroxylation est cependant catalysée à température élevée et dans des solutions légèrement basiques[269,271].

La charge surfacique de la silice est négative à $pH > 2$ et provient de la déprotonation des groupements SiOH. La magnitude de la charge dépend de l'état d'hydroxylation et augmente généralement avec le pH et la force ionique[272-275] (voir aussi Chapitre III). En parallèle, la silice commence à se dissoudre à $pH > 8$-9[269].

Étant donné l'influence de l'état d'hydroxylation sur la chimie, l'hydrophobicité et la charge de la surface, on peut se demander si l'hydroxylation peut aussi influencer l'adsorption des molécules organiques du milieu aqueux et les propriétés des couches organiques déposées. En effet, de telles variations ont été observées et peuvent être liées à la méthode de la préparation de la surface, à l'état d'hydroxylation et à la présence de contaminations[269,271,276-278].

I.5.3. D'autres supports

Pendant que les surfaces décrites ci-dessus ont été choisies comme surfaces modèles dans nos travaux, d'autres supports offres de possibilités aussi importantes pour les applications biotechnologiques. L'oxyde de titane, déjà couramment utilisé comme matériel pour la fabrication des implants (articulations artificielles, implants dentaires)[279], les polymères (le polystyrène et le support

traditionnel pour la culture de cellules), le verre, pour des applications en microscopie optique, l'hydroxyapatite[280] ou l'or[281] sont quelques exemples. La gamme des surfaces, inorganiques aussi bien qu'organiques, accroît avec le développement de nouveaux matériaux et avec les exigences des techniques de caractérisation de phénomènes de surface[282-284].

.

II. New tools to characterize the process of 2D supra-molecular self-organization

Investigating supra-molecular self-organization requires the ability to focus equally well on the growing assembly as on the molecular entities it is made of. Tools that allow such a "split vision"[i] are not readily available. The coming chapter briefly describes some of the technical challenges that we encountered in the course of our studies. Some of them have led to rather interesting findings and original developments, as witnessed by the included papers; others may be of help to rationalize our experimental approach. It should not stay unmentioned that a part of the work presented here originated from artifacts that bothered a seemingly certain world. I hope that the results demonstrate that it was worth trying to understand them, in many cases.

II.1. The interactions between the AFM-tip and solid-supported soft molecules

II.1.1. Understanding the interaction between the AFM-tip and surface-bound lipid assemblies

A crucial part of each scanning probe technique is the scanning probe itself. The probes for AFM investigations in liquid are commonly made of silicon-nitride, the surface layer of which becomes similar to silica upon exposure to air (or treatment by UV/ozone)[285]. It appears generally little acknowledged that, given its surface chemistry, the tip is prone to become covered with lipid material, either from lipids in solution or upon first contact with the lipid-covered support.

Paper I provides evidence that this is indeed the case and exploits this circumstance to investigate the interaction of two lipid-covered solid objects. The experimental results strongly suggest that both hemifusion and fusion can occur between a planar solid-supported lipid bilayer and a bilayer-like structure on the nanometer-sized tip (Scheme II.1). Interestingly, the interaction between SLBs had been studied previously by SFA, though using two supports of macroscopic curvature. While hemifusion was frequently observed[286], fusion was only obtained

[i] This term was, to my knowledge, initially coined by Prof. Bengt Kasemo, though in a rather different context.

for bilayers that were lifted from the solid support by a polymer cushion[287]. This illustrates the effects that membrane curvature and the solid support can have on the interaction of membranes. In addition to fusion events, Paper I also reports on a constant force of ~60 pN upon retraction of the AFM-tip from the (hemi-)fused state, that was maintained over distances of more than 100 nm. We interpreted these observations tentatively as the formation of tube-like structures, as investigated by others with AFM[288] and other techniques[43,289-291].

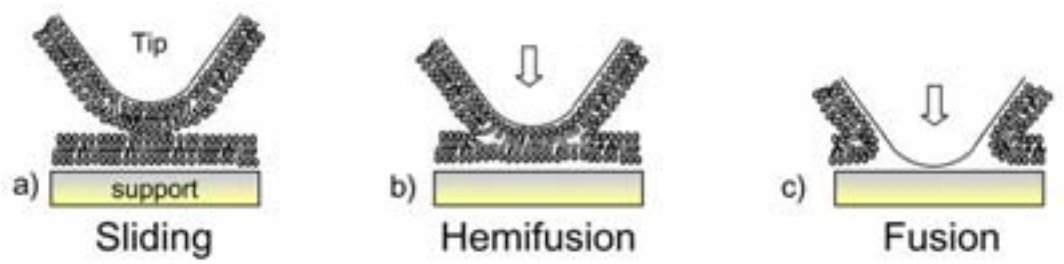

SCHEME II.1 The three different regimes of interaction between the lipid-coated AFM-tip and a bilayer-coated planar support, according to Paper I. In the sliding regime, the lipid structures on both tip and support remain intact. A dynamic connection is established across one or both lipid monolayers in the regimes of hemifusion and fusion, respectively.

Lipid structures such as surface-bound vesicles and bilayer patches are known to be easily modified by the AFM-tip[49,151-153], and observed artifacts were mostly attributed to the soft and fragile nature of lipid assemblies or to rather weak immobilization. The results presented in Paper I suggest the specific interactions between the lipid-covered tip and the sample as another important source of artifacts.

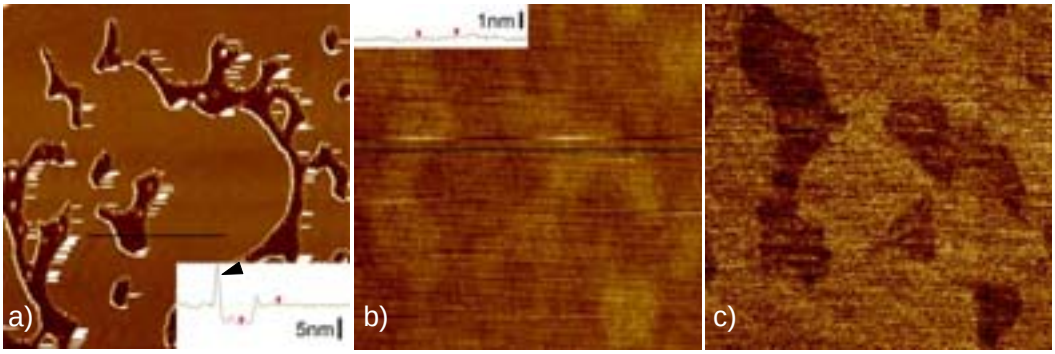

FIGURE II.1 Examples of artifacts in the AFM-imaging of lipid bilayer patches. All images were obtained after incubation of SUVs made of DOPC/DOPS (molar ratio 4:1) in 10 mM $CaCl_2$ on a silicon wafer. (a) Tapping mode (height image). Two plane levels, separated by ~4.5 nm (c.f. cross-section in inset) are likely to correspond to the solid support and the top of a bilayer. Accordingly, an incomplete bilayer covers most of the surface. Close to the bilayer edges, anomalous transients in the height are evidenced (*arrowhead* in inset), indicating instabilities of the imaging at this location. Image size (z-limit): 2.5 µm (20 nm). (b-c) Contact mode images on the same sample at another location. The height between the two features differs by only a few Angstroms (inset in b) and the contrast appears inversed. A slightly better contrast is revealed in the friction image (c). Image size (z-limit/friction limit): 2.5 µm (2 nm/5 mV).

We have indeed observed effects such as tip-instabilities (Figure II.1a) or the disappearance (and inversion) of contrast (Figure II.1b) that may be explained by such interactions (Scheme II.2b). A strong (undesired) attraction of the lipid-

covered tip may in particular be promoted on incomplete bilayers, as the barrier for (hemi-)fusion is expected to be substantially lowered in the vicinity of freely accessible bilayer edges. This rationalizes our initial difficulties to reproducibly image intermediates in the process of SLB-formation.

In order to remedy this shortcoming, we attempted to coat the tip with a lipid repelling polymer. The simple physisorption of poly(ethylene glycol) (PEG) to the tip proved in principle successful, as demonstrated in Paper III. Very careful operation in tapping mode at minimum forces was though required to maintain the functionality of the tip-coating. A more resistant coating could be obtained by grafting PEG to a backbone of poly(L-lysine) (PLL), that adsorbs to the tip by electrostatic interactions[292] (Scheme II.2b)[ii]. The success of this method to obtain reliable images of surface-confined lipid structures is demonstrated in Paper IV.

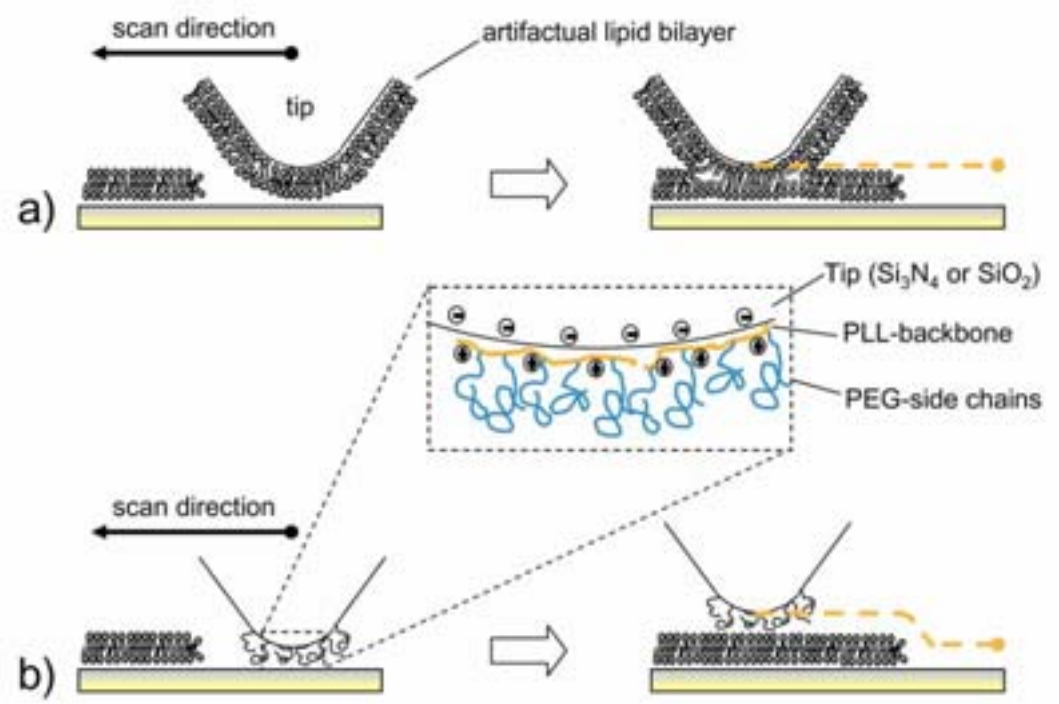

SCHEME II.2 The possible influence of lipid-mediated tip-sample interactions on the imaging of lipid assemblies. (a) Lipid material is likely to be present on a common AFM-tip. The interactions between the lipid-covered tip and the lipid sample can induce reassembly of the lipid material, in particular in the vicinity of bilayer edges, thus prohibiting proper tracking (*thick dotted line*) of the lipid sample. (b) By coating the tip with a lipid-repelling polymer, such as PLL-*g*-PEG, such unwanted interactions can be circumvented and the lipid patch is traced correctly (*thick dotted line*).

II.1.2. AFM-imaging and lateral mobility of surface-bound molecules - the quest for non-crystalline annexin A5

While it is well established that the immobilization of the sample is one of the crucial aspects for successful AFM-imaging of biological specimens[127], it is

[ii] Covalent binding of PEG groups to a surface is another interesting approach to achieve resistance to lipid or protein adsorption[293].

sometimes overlooked that the 2D movement of surface-confined molecules can be considerable.

A simple but illustrative example may be proteins, such as annexin A5, that bind to one or a few lipid molecules in a fluid membrane. Providing that the coverage is low, protein molecules diffuse in two dimensions with about the same speed as the lipids, covering an area of several square micrometers within one second. In comparison, for an image size and an imaging speed adapted to resolve a protein, the scanning AFM-tip covers less than 0.1 μm^2 over this time. Thus the tip is much to slow to image a freely diffusing protein and the molecules, although present, may not be visible.

While *imaging* is effectively inhibited, a random encounter of the tip with diffusing molecules, their oligomers or small clusters may in some cases be sufficient to *track* their presence, as is illustrated in Figure II.2. Whether molecules are effectively tracked, is determined by a rather intricate interplay of the scanning speed, the applied force, the diffusion speed of the molecules and their 2D concentration. In particular, tracking will be improved with increasing coverage as the diffusion speed decreases and the probability of encounter increases. As an example, the effect of mobility on AFM-imaging was exploited in Paper I, in order to ascertain the presence of a layer of non-crystalline (and thus mobile) annexin A5 oligomers on silica-SLBs in contrast to the solid 2D-crystals that are commonly formed on mica-SLBs.

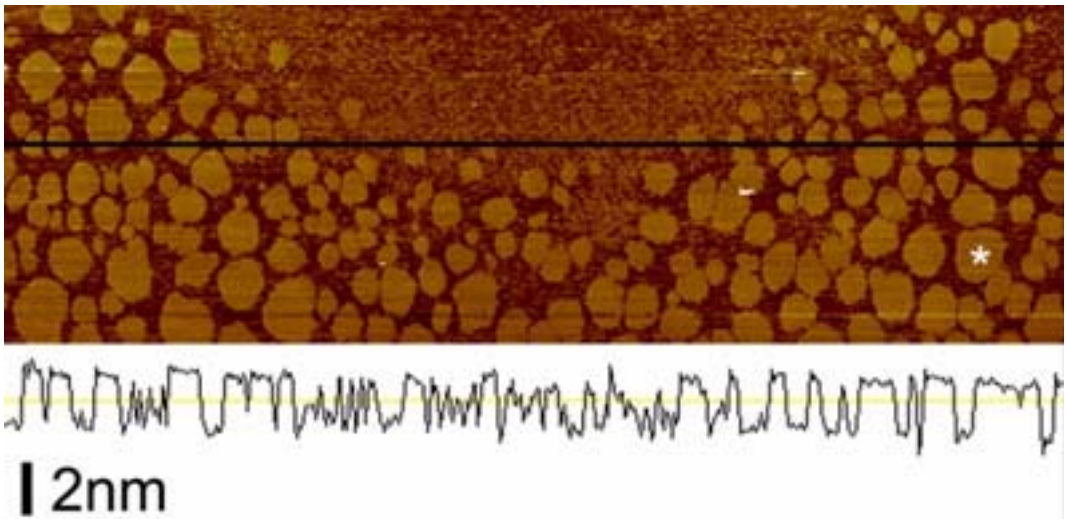

FIGURE II.2 Following the formation of annexin A5 crystals. The image (contact mode) was acquired a few minutes after the injection of 20 µg/mL annexin A5 into the AFM-cell. Prior to exposure to annexin A5 the mica support had been covered with an SLB formed from SUVs containing DOPC/DOPS (1:2). Bright flat spots (*white asterisk*) with diameters of ~100 nm and more and a height of ~2.2 nm (*cross section*) cover the lower, left and right part of the image. These are (growing) 2D crystals of annexin A5[142]. Crystals are not clearly discernible in the image's middle-upper part, though smaller objects of various heights (*cross section*) are detected that generate a rough overall aspect of this zone. These objects are likely to be diffusing molecules, oligomers or clusters of annexin A5. Notably, such objects are less frequently observed in the space between the crystalline patches. Image size (z-limit): 20 µm (8 nm). Slow scan direction: downwards.

II.1.3. Surface roughness: effects on AFM-imaging and self-assembly

Roughness limits the quality of AFM-imaging as it enhances both tip-convolution effects[127] and tip-sample interactions (c.f. Paper I) and, therefore, smooth surfaces are in demand. Besides mica, silica-wafers or glass, exhibiting a roughness of a few Angstroms[iii], are attractive. Template stripping methods have been developed during the last decade to generate surfaces of gold[294-296] or titanium[297] with a roughness well below 1 nm. Furthermore, thin polymer-coatings (spin-coated or plasma-treated) present an alternative, yet little explored way to generate smooth surfaces.

By far the most commonly used surface for high-resolution imaging, however, is mica. Due to the ease of preparing clean surfaces with atomic flatness over large areas, it is the ideal support for applications that require a hydrophilic surface. This and the promises of mica to study the formation of SLBs[152] and the 2D crystallization of annexin A5[112,142] constituted the principal driving forces for the development of mica-coated QCM-D sensors, presented in Paper II, for combined QCM-D – AFM studies.

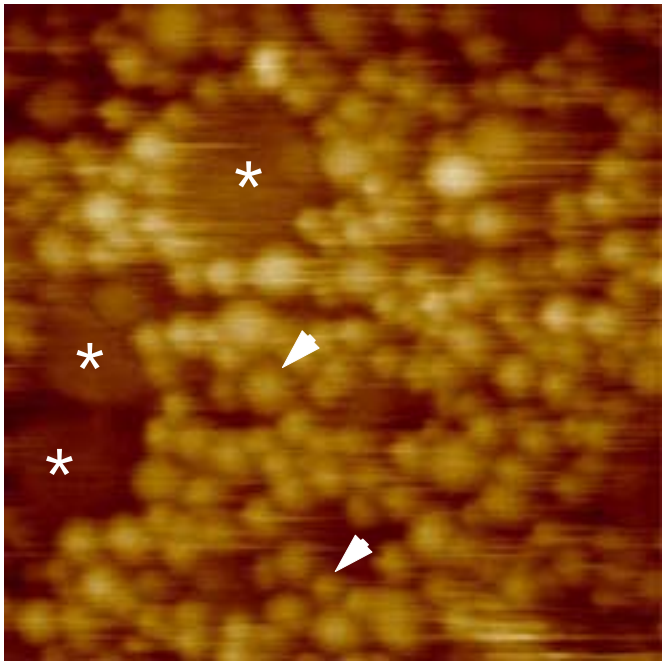

FIGURE II.3 Imaging vesicles and bilayer patches on a rough silica surface as it is present on standard QCM-D sensors. Image size (z-limit): 750 nm (40 nm). The adsorption of SUVs of DOPC/DOPS (4:1) was followed by QCM-D and interrupted at an intermediate surface coverage corresponding to a frequency shift of -37 Hz before transfer of the sample to the AFM. Both vesicles (*arrowheads*) and bilayer patches (*asterisks*) can be discerned, despite the support's corrugations in the nanometer range (c.f. Paper I).

Although it may be undesired for many applications, roughness is a relevant parameter that can influence the adsorption of biomolecules[298]. Surface

[iii] The given numbers are root mean square (rms) values measured over a surface area of a few μm^2.

corrugations impose local geometrical constraints on the adsorbents which may be crucial for self-assembly processes, such as SLB-formation or 2D protein crystallization. In addition, supports of biotechnological interest frequently exhibit some degree of roughness[91] and surface-sensitive techniques, complementary to AFM, often impose constraints on the support's smoothness. This motivates the desire to push the limits of AFM-imaging on rough supports.

In this context, it is interesting to note that 2D protein crystals can, in principle, be resolved on glass[155] and even on rougher surfaces such as sputtered gold[299], the ultimate success is though expected to be very dependent on the proteins under study. Figure II.3 demonstrates that also vesicles and bilayer patches can be imaged with acceptable quality on a silica-coated QCM-D sensor, which has a roughness of 1.4 nm. Paper I further explores the impact of roughness on AFM-imaging, SLB-formation and protein 2D crystallization.

II.2. Combining AFM and QCM-D

II.2.1. Promises

Considering today's technical state of the art, AFM and QCM-D are highly complementary in many respects, as may be appreciated from the comparison in table II.1.

TABLE II.1 An overview of complementary aspects of AFM and QCM-D.

QCM-D	**AFM**
information of the adsorbent's mass and of its average structural state	local structural information (nm-range, single molecule imaging)
average viscoelastic information	local viscoelastic information
temporal resolution of better than a second	temporal resolution in the minute range
can be operated in liquid	can be operated in liquid
applicable on various (thin) supports	applicable on various (smooth) supports
easy to use	time consuming and prone to artifacts

Of particular interest for our studies is the complementarity in the spatial and temporal resolution. The combination of both techniques provides information on the ensemble - with high temporal resolution – together with a very local picture - of a spatial resolution down to the level of the basic entities of interest – a duality of focus that is advantageous for the characterization of self-assembly processes.

QCM-D provides information about *all* adsorbed material (including trapped water), while AFM can sometimes be selective in its perception, as we have demonstrated for non-crystallized annexin A5 molecules. In the light of numerous potential imaging artifacts on soft specimens, QCM-D provides a valuable control for the interpretation of AFM data. Furthermore, the ease of use of QCM-D and the overall structural information that it provides, enables screening for relevant experimental conditions which allow for optimized, yet more laborious, structural investigations by AFM.

While the dissipation contains valuable information about the viscoelastic properties of the adsorbed layer and indications about its structural state, an unambiguous interpretation of this parameter in terms of the adsorbent's supramolecular structure is often difficult, in particular for biological systems that can exhibit a significant degree of complexity. In this respect, the spatially resolved information from a few AFM-images can confirm the interpretation of QCM-D data and/or improve the interpretation of many QCM-D measurements.

The nature of the support can considerably influence processes of adsorption and self-assembly. Thus only the use of identical supports for both techniques guarantees a comparability of the results. The synergy-effects, described above and summarized in Scheme II.3, can thus only be fully exploited if identical supports are used for both AFM and QCM-D.

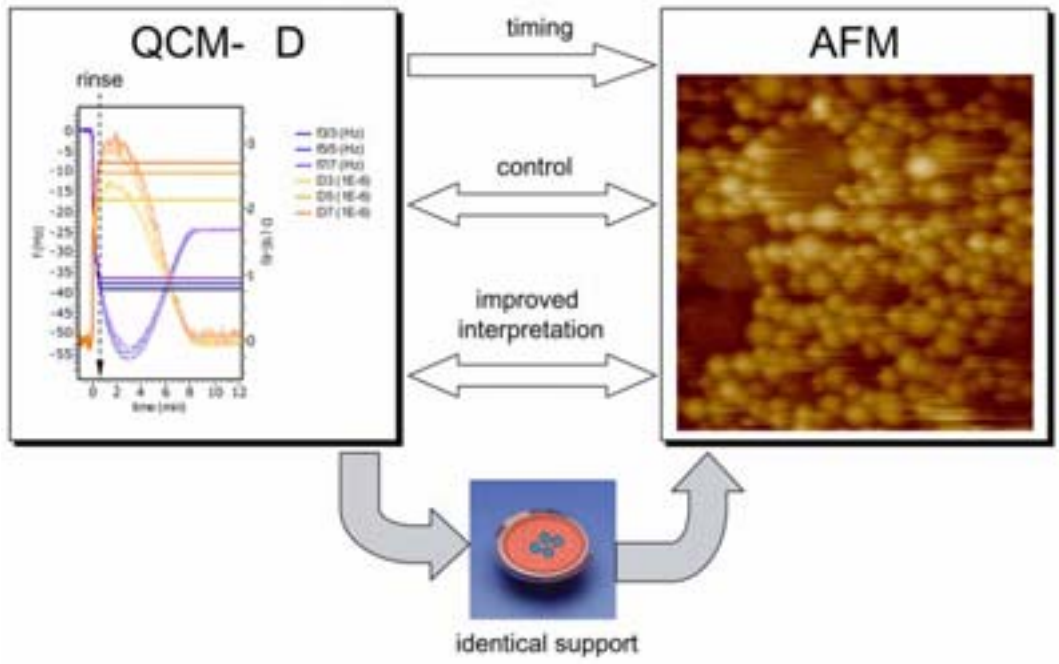

Scheme II.3 Some synergy effects of combining QCM-D and AFM on identical supports.

II.2.2. Challenges

A successful combination of QCM-D and AFM should exploit the potential of both techniques, without inducing severe constraints. As described previously, the possibilities of AFM-imaging can be best used on smooth surfaces. In contrast, the most common coatings on QCM-D sensors, such as evaporated gold or sputtered silica, exhibit a roughness that would constrain, in particular, the imaging of proteins. Fortunately, the QCM-D sensors can be coated with various thin films while maintaining their sensitivity. A rarely used, but not unknown[244,300] deposition method is to glue sheets, a few μm thin, onto the sensor. Concerns were though raised whether the thickness and the heterogeneity of the resulting glue-sheet compound would affect the sensitivity of the QCM-D sensor.

In Paper II we demonstrate that it is possible to glue mica on QCM-D sensors and that, indeed, a sensitivity close to that of common surfaces can be obtained. Importantly, we could show that the QCM-D response of the coated crystal, exposed to air and immersed in aqueous solution provides good indications about the sensor's reliability *prior* to the measurement. The successful mica-coating marks a milestone in our study, without which much of the work in Papers IV, V and VI would not have been possible.

While the gluing procedure is now fairly reproducible and well controlled, the cleavage of mica remains an obstacle for the large-scale preparation of mica-coatings of good quality. Advances in the reproducible cleavage of mica into ~5 μm thin sheets of perfect flatness on both sides of the sheet would constitute considerable potential not only for mica-QCM-D but also for other techniques such as SFA.

It should be noted that the developed deposition method can be generalized for other thin films, such as template stripped gold or titanium, making a wider range of flat supports accessible for QCM-D studies. In these cases the critical step of mica-cleavage is omitted and such a deposition is expected to be straightforward.

II.2.3. Limits in combining AFM and QCM-D: AFM and kinetics

Papers II to VI illustrate that many of the above-mentioned expectations in combining QCM-D and AFM-imaging for studying self-assembly processes have been fulfilled. Our technical approach was, though, rather simple: measurements by QCM-D and AFM, respectively, were performed in physically separated instruments, and the samples were either prepared independently for both measurements or transferred from the QCM-D to the AFM. The nature of our studies may suggest a combination *in situ* of AFM and QCM-D as the next promising step in instrumental development. While such a combination seems technically feasible, one important constraint is imposed by AFM for combined kinetic studies.

Various examples (Figure II.4) provide evidence that the bulk transport conditions can be considerably modified in the vicinity of the cantilever-mounted AFM-tip as compared to the rest of the measurement chamber[301]. This can be readily rationalized by the fact that the thickness of the depletion layer, i.e., the solution layer next to an adsorbing surface that becomes depleted in sample, can easily reach 10 μm under common experimental conditions[254]. In comparison, the AFM-tip has a height of ~3 μm and thus, the tip and a substantial part of the cantilever that hold it will induce heterogeneities in the depletion layer, and in this way affect the local adsorption rate.

This effect currently limits the use of AFM for the quantitative analysis of adsorption kinetics. In particular, a reliable correlation of the local adsorption kinetics under the AFM-tip with the overall kinetics measured over the QCM-D sensing area is rendered difficult. This constraint is of general character for the combination of AFM with other surface-sensitive techniques, as many of them rely on the averaging of a signal over a more or less extended surface area. It should, however, be noted that notwithstanding this constraint, the *in-situ* combination of QCM-D and AFM has important prospects for other applications, such as tribology[258,302] or the investigation of viscoelastic properties of thin films.

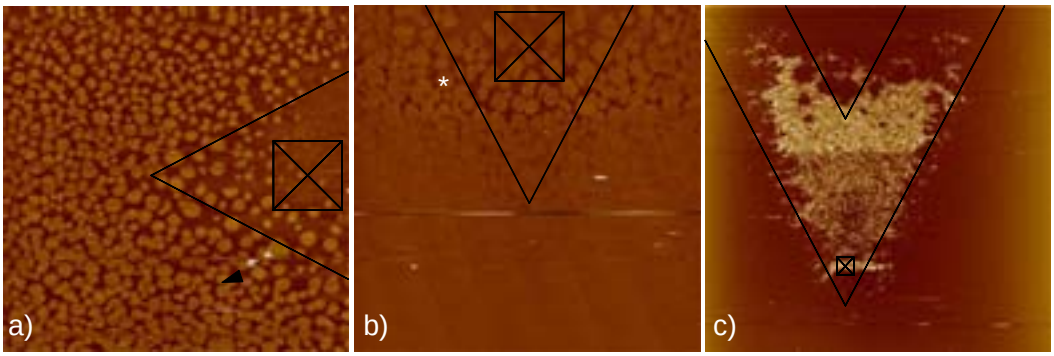

FIGURE II.4 Examples of the influence of the AFM-cantilever on adsorption kinetics. The position of the tip and the cantilever relative to the imaged surface is indicated schematically with solid lines. (a-b) The images were acquired a few minutes after the injection of 20 μg/mL annexin A5 into the AFM-cell. Prior to exposure to annexin A5 the mica support had been covered with an SLB formed from SUVs containing DOPC/DOPS (1:2). Bright flat spots (*white asterisk* in b) with diameters of ~100 nm and more represent growing 2D crystals of annexin A5[142]. Crystallization is appreciably slowed down under the tip and the cantilever, suggesting that the cantilever limits the access of annexin A5 to the surface. This effect persists for different scan angles (90° in A, 0° in B). Image size (z-limit): 20 μm (15 nm). Slow scan direction: downwards. (c) 100mg/L of SUVs of DOPC were injected in the AFM-cell in 2 mM EDTA on mica, followed by successive rinses in buffers solution containing 2 mM EDTA and 2 mM $CaCl_2$, respectively. As a result, (incomplete) bilayers are formed over a large area of the surface, while the brighter zone in the centre hosts vesicles as identified by imaging at lower image size (not shown). Size and shape of the vesicle rich zone correlate well with that of the cantilever. Again, the surface heterogeneity is likely due to the restrained access of vesicles to the zone under the cantilever (c.f. Paper IV). Image size (z-limit): 80 μm (30 nm).

Paper I

Ralf P. Richter and Alain Brisson

Characterization of lipid bilayers and protein assemblies supported on rough surfaces by atomic force microscopy.

Langmuir, **19** (2003), p. 1632-1640

Characterization of Lipid Bilayers and Protein Assemblies Supported on Rough Surfaces by Atomic Force Microscopy†

Ralf P. Richter and Alain Brisson*

Laboratoire d'Imagerie Moléculaire et Nano-Bio-Technologie, IECB, Université Bordeaux I, 16 Avenue Pey Berland, 33607 Pessac Cedex, France

Received August 19, 2002. In Final Form: November 12, 2002

Supported lipid bilayers (SLBs) and two-dimensional protein assemblies formed on solid supports of various roughnesses were characterized by atomic force microscopy (AFM). The presence of SLBs was detected reliably by force measurements and by imaging. Three types of responses could be distinguished depending on the applied loads. These responses are interpreted as due to transient restructuration of the lipid assembly in the region of contact between lipid-covered support and AFM tip, driven by hydrophobic/hydrophilic interactions. Two-dimensional crystals of streptavidin could be resolved on SLBs formed on silicon wafers, whereas annexin A5, previously shown to crystallize on mica-SLBs, formed a close-packed noncrystalline assembly on lipid bilayers supported by silicon wafers.

Introduction

Atomic force microscopy (AFM) is recognized for its potential in providing a diversity of information such as topography, elastic properties, and interaction forces, in liquids, at supramolecular and submolecular levels. An important limitation of topography studies by AFM is its requirement for flat surfaces. The resolution of AFM images is indeed limited due to tip-convolution effects.[1,2] The use of rough surfaces would increase the difficulties in extracting the signal of the adsorbent in the recorded topography. In addition, increased tip−sample interactions would risk enhancing mechanical damage on soft samples. This explains why AFM imaging studies are usually performed on atomically flat surfaces, such as mica or highly oriented pyrolytic graphite (HOPG).[3−6] The characterization of biomolecules by force spectroscopy[7,8] is though not limited to flat surfaces.

On the other hand, most substrates with (bio)chemical properties of interest for fundamental research and biotechnological applications are difficult or impossible to render atomically flat. In particular, surface sensitive methods such as quartz crystal microbalance with dissipation monitoring (QCM-D), surface plasmon resonance, or ellipsometry, commonly used to investigate adsorption processes, require surfaces that are not atomically flat, for example, gold, sputtered silica, or silicon wafers (despite some recent progress[9]).

Next to other physicochemical properties of surfaces which are determinants for the adsorption of biomolecules and the conformational state of the adsorbent, such as their chemical nature, charge, hydrophilicity, or structure, the role of surface roughness in adsorption phenomena is poorly characterized. Roughness imposes local geometrical constraints on the adsorbents which can be crucial for self-assembly processes, particularly when the sizes of self-assembled domains exceed the characteristic dimensions of the surface features. Thus, roughness is expected to influence the formation and organization of self-assembled biomolecular systems such as supported lipid bilayers (SLBs)[10] or two-dimensional (2D) crystals of proteins.[11]

The objective of this study was to evaluate the possibilities of the AFM technique to characterize adsorption phenomena on solid supports of various roughnesses. We focused on two model systems, SLBs and 2D crystals of proteins, grown on SLBs, for their potential interest as biocompatible surfaces. Vesicles with a lipid composition of dioleoylphosphatidylcholine (DOPC)/dioleoylphosphatidylserine (DOPS) (molar ratio 4:1) were chosen as they form essentially defect-free SLBs as shown by AFM on flat mica surfaces[12] and by QCM-D on rough surfaces.[13] The proteins streptavidin[14] and annexin A5[6,15] were also previously shown to self-assemble into 2D crystals on mica-SLBs.

The literature on lipid assemblies deposited on solid supports and investigated by AFM is extensive.[2,16] While

* Corresponding author. Phone: +33 5 57 96 34 58. Fax: +33 5 57 96 34 84. E-mail: a.brisson@iecb-polytechnique.u-bordeaux.fr.

† Part of the *Langmuir* special issue entitled The Biomolecular Interface.

(1) Engel, A.; Schoenenberger, C.-A.; Müller, D. J. *Curr. Opin. Struct. Biol.* **1997**, *7*, 279−284.
(2) Shao, Z.; Mou, J.; Czajkowsky, D. M.; Yang, J.; Yuan, J.-Y. *Adv. Phys.* **1996**, *45*, 1−86.
(3) Scheuring, S.; Müller, D. J.; Ringler, P.; Heymann, J. B.; Engel, A. *J. Microsc.* **1999**, *193*, 28−35.
(4) Müller, D. J.; Fotiadis, D.; Engel, A. *FEBS Lett.* **1998**, *430*, 105−111.
(5) Scheuring, S.; Stahlberg, H.; Chami, M.; Houssin, C.; Rigaud, J.-L.; Engel, A. *Mol. Microbiol.* **2002**, *44*, 675−684.
(6) Reviakine, I.; Bergsma-Schutter, W.; Brisson, A. *J. Struct. Biol.* **1998**, *121*, 356−361.
(7) Rief, M.; Gautel, M.; Oesterhelt, F.; Fernandez, J. M.; Gaub, H. E. *Science* **1997**, *276*, 1109−1112.
(8) Rief, M.; Clausen-Schaumann, H.; Gaub, H. E. *Nat. Struct. Biol.* **1999**, *6*, 346−349.
(9) Benes, M.; Billy, D.; Hermens, W. T.; Hof, M. *Biol. Chem.* **2002**, *383*, 337−341.
(10) Rädler, J.; Strey, H.; Sackmann, E. *Langmuir* **1995**, *11*, 4539−4548.
(11) Brisson, A.; Bergsma-Schutter, A.; Oling, F.; Lambert, O.; Reviakine, I. *J. Cryst. Growth* **1999**, *196*, 456−470.
(12) Reviakine, I.; Brisson, A. *Langmuir* **2000**, *16*, 1806−1815.
(13) Richter, R.; Mukhopadhay, A.; Brisson, A. *Biophys. J.* **2002**, submitted.
(14) Reviakine, I.; Brisson, A. *Langmuir* **2001**, *17*, 8293−8299.
(15) Reviakine, I.; Bergsma-Schutter, W.; Mazères-Dubut, C.; Govorukhina, N.; Brisson, A. *J. Struct. Biol.* **2000**, *131*, 234−239.
(16) Dufrêne, Y. F.; Lee, G. U. *Biochim. Biophys. Acta* **2000**, *1509*, 14−41.

10.1021/la026427w CCC: $25.00
Published on Web 01/09/2003

many studies performed on mica were mostly descriptive and information on the distribution of fluid-phase and solid-phase domains in lipid mixtures[2,17,18] or the transition from vesicles to bilayer disks[12] could be obtained by using contact mode AFM at lowest force, the critical influence of the tip−sample interactions in the case of lipid systems has been identified with the exemplary water-skiing effect reported by Rädler et al.[19] Mechanical interactions between tip and SLBs and their influence on the imaging of SLBs has since been addressed in several publications measuring normal[20,21] and lateral (friction)[22,23] forces. Jumps on bilayers have frequently been reported and have been interpreted as a breakthrough of the tip in the bilayer.[21,22]

In this paper, tools to characterize SLBs on rough surfaces are presented. As for studies with flat surfaces, an understanding of the interaction between tip and bilayer is important for the interpretation of the data.

Materials and Methods

Materials. DOPC and DOPS were purchased from Avanti Polar Lipids (AL). *N*-(6-((Biotinoyl)aminohexanoyl-dipalmitoylphosphatidylethanolamine, triethylammonium salt (DPPE-lc-biotin), was purchased from Pierce (IL). Recombinant rat annexin A5 was overexpressed in *Escherichia coli*.[15] Lyophilized streptavidin and other chemicals were purchased from Sigma. Ultrapure water with a resistivity of 18.2 MΩ was used, prepared with a Maxima system (USF ELGA, France).

Muscovite mica plates of 11 mm diameter were purchased from Metafix (Montdidier, France). Plates of (11 × 11) mm^2 of pure silicon wafer and wafers thermally coated with 500 nm of silica were provided by the CEA (Grenoble, France). QCM-D sensor crystals, covered with 100 nm of evaporated gold and reactively sputter-coated with 50 nm silicon oxide, were purchased from Q-Sense (Gothenburg, Sweden).

A buffer solution made of 150 mM NaCl, 2 mM NaN_3, and 10 mM HEPES, pH 7.4, was prepared in ultrapure water, and 2 mM EDTA or $CaCl_2$ was added as indicated in the text. Streptavidin was resuspended in EDTA-containing buffer at 1 mg protein per mL.

Lipid Vesicle Preparation. Lipids were dissolved in chloroform, mixed in desired amounts, dried under a stream of nitrogen followed by drying in a vacuum desiccator overnight, resuspended at 1−2 mg/mL final concentration, and vortexed in EDTA-containing buffer. Lipid mixtures were homogenized by five cycles of freeze−thawing and subsequent vortexing. Small unilamellar vesicles (SUVs) were obtained by sonication with a tip-sonicator (Misonix, NY) operated in a pulsed mode at 30% duty cycle for 30 min with refrigeration, followed by centrifugation in an Eppendorf centrifuge (10 min at 16 000*g*) to remove titanium particles. SUV suspensions were stored at 4 °C under nitrogen and used within 4 weeks.

Support Preparation. Mica disks were glued to Teflon-coated (Bytac, Norton) metal disks using a two-component epoxy glue. Uniform surfaces were obtained by cleavage with Scotch tape and immediately covered with buffer solution.

Silica and silicon substrates were cleaned by two cycles of exposure to 2% sodium dodecyl sulfate (SDS) solution for 15 min, rinsing with ultrapure water, blow-drying with nitrogen, and exposure to UV/ozone for 10 min. For UV/ozone treatment, the substrates were placed in the vicinity of a mercury grid lamp (BHK, CA), mounted into a home-built chamber and driven by a suitable power source (BHK). Ozone is produced from the oxygen present in ambient air by the emitted UV light of wavelength 185 nm. By this treatment, the surface is cleaned from traces of organic contaminants[24] and rendered hydrophilic.[25] Substrates cleaned in this way were stored in air. Prior to use, they were re-exposed to UV/ozone for 10 min, attached to Teflon-coated metal disks using double-sided tape (Tesa, Hamburg, Germany), and immediately covered with buffer solution.

For simplicity, UV/ozone-treated silicon wafers will hereafter be referred to as "silicon wafers". Note, however, that due to exposure to oxygen in ambient air and due to the UV/ozone treatment, these wafers are covered by an oxide layer that is several nanometers thick.[24] Thermally silica-coated wafers and silica-coated QCM-D sensor crystals will be referred to as "silica-coated wafers" and "silica-coated quartz crystals", respectively.

Sample Preparation. If not stated otherwise, substrates were covered by 100 μL of calcium-containing buffer to which a SUV suspension was added at 0.1 mg/mL final concentration. After 30 min of exposure, vesicles present in solution were removed by cycles of exchange of the lipid solution with buffer solution, by pipetting.

Atomic Force Microscopy. AFM measurements were performed in liquid using a Nanoscope IV-Multimode (Veeco, Dourdan, France), equipped with a J-scanner (120 μm). The contact mode fluid cell was washed by sonication in subsequent baths of ethanol and ultrapure water, followed by extensive rinsing in ethanol and blow-drying in a stream of argon. Tubings were sonicated in ethanol and water and rinsed with water. The O-ring was rinsed with water. Oxide-sharpened silicon nitride cantilevers with nominal spring constants of 0.06 and 0.32 N/m (Digital Instruments, CA) were exposed to UV/ozone (BHK) for 10 min prior to use. The spring constants were recalibrated using the unloaded resonant frequency.[26]

The liquid-covered substrates were installed in the AFM cell using the O-ring and rinsed with 1 mL of buffer. The AFM was equilibrated for 1 h prior to imaging. Sample solution or buffer was injected with a syringe when necessary.

Images acquired in constant force contact mode were recorded at a scanning rate of 4−8 Hz and a scan angle of 90°. Images were flattened and plane-fitted except when otherwise stated. Roughness values given are root-mean-square (rms) values determined from (500 × 500) nm^2 images, if not otherwise stated.

Contact mode force−displacement curves were acquired at approach and retraction speeds of 350 nm/s (unless otherwise stated) and converted to force−distance plots.[27] Repulsive and adhesive forces are denoted with positive and negative signs, respectively. Friction data were obtained by subtracting friction images recorded in trace and retrace, which averages out irregularities due to surface roughness.[23] Values are given in millivolts corresponding to the response of the photodiode, which is assumed to be proportional to the friction force.

Results

Lipid Bilayers on Solid Supports. Solid supports and substrates covered with SLBs of DOPC/DOPS (molar ratio 4:1) were characterized in calcium-containing buffer by imaging in contact mode and by force−distance curves.

Imaging Solid Supports. The surface roughness of the solid supports used in this study (mica, silicon wafer, silica-coated wafer, and silica-coated quartz crystal) was characterized by contact mode AFM. On mica, no corrugations were discernible, the surface being flat over areas larger than (10 × 10) μm^2 (not shown) and exhibiting a surface roughness of less than 0.05 nm, considered as the noise limit of our equipment. Silicon wafers (Figure 1A) were essentially flat on scales of 50 nm and larger but showed surface features of subnanometer height and lateral

(17) Rinia, H. A.; Kruijff, B. D. *FEBS Lett.* **2001**, *504*, 194−199.
(18) Reviakine, I.; Simon, A.; Brisson, A. *Langmuir* **2000**, *16*, 1473−1477.
(19) Rädler, J.; Radmacher, M.; Gaub, H. E. *Langmuir* **1994**, *10*, 3111−3115.
(20) Franz, V.; Loi, S.; Müller, H.; Bamberg, E.; Butt, H.-J. *Colloids Surf., B* **2002**, *23*, 191−200.
(21) Müller, H.; Butt, H.-J.; Bamberg, E. *J. Phys. Chem. B* **2000**, *104*, 4552−4559.
(22) Schneider, J.; Dufrêne, Y. F.; Barger, W. R., Jr.; Lee, G. U. *Biophys. J.* **2000**, *79*, 1107−1118.
(23) Grant, L. M.; Tiberg, F. *Biophys. J.* **2002**, *82*, 1373−1385.
(24) Vig, J. R. In *Treatise on Clean Surface Technology*; Mittal, K. L., Ed.; Plenum Press: New York, 1987; Vol. 1, p 1−26.
(25) Keller, C. A.; Kasemo, B. *Biophys. J.* **1998**, *75*, 1397−1402.
(26) Cleveland, J. P.; Manne, S.; Bocek, D.; Hansma, P. K. *Rev. Sci. Instrum.* **1993**, *64*, 403−405.
(27) Mueller, H.; Butt, H.-J.; Bamberg, E. *Biophys. J.* **1999**, *76*, 1072−1079.

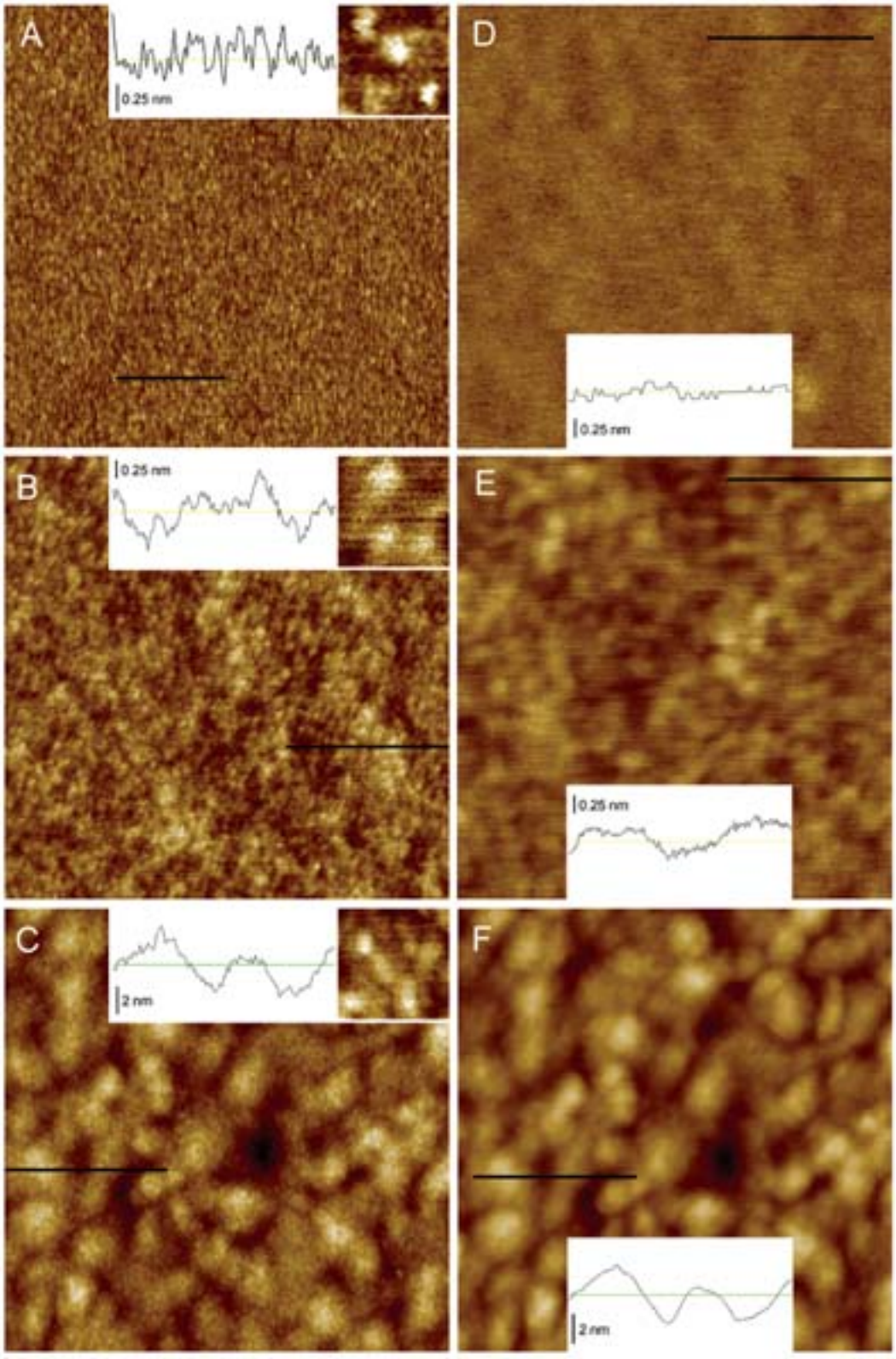

Figure 1. AFM images of UV/ozone-treated solid supports (A−C) and of DOPC/DOPS SLBs deposited on respective supports (D−F). Cross sections measured along the black lines are presented for each image. Image size, 500 nm. (A) Silicon wafer. *Z*-scale, black-to-white: 2 nm. Inset: 10× magnified view of protrusions of 3−6 nm diameter and subnanometer height (*Z*-scale, 1 nm). (B) Silica-coated wafer. Undulations of subnanometer height and lateral dimensions of ∼50 nm are observed (cross section). *Z*-scale, 2 nm. Inset: 5× magnified, showing protrusions with a diameter of 5−15 nm. Note that tip-convolution effects might enhance the lateral size of small features. (C) Silica-coated quartz crystal. Grains of 30−70 nm diameter and up to ∼5 nm height are observed, reflecting the roughness of the underlying template of evaporated gold. *Z*-scale, 10 nm. Inset: 5× magnified, revealing a subgrain structure of 3−6 nm diameter (*Z*-scale, 2 nm). (D) Silicon wafer with an SLB. Protrusions are no longer visible. *Z*-scale, 2 nm. (E) Silica-coated wafer, covered by an SLB. The surface undulations of 50 nm lateral size are still apparent, while the smaller protrusions have disappeared. *Z*-scale, 2 nm. (F) Silica-coated quartz crystal, covered by an SLB. Subgrain structures are smoothened, whereas the grains remain visible. *Z*-scale, 10 nm.

dimensions of 3−6 nm (Figure 1A, inset), the surface roughness being small (0.14 ± 0.01 nm). On silica-coated wafers (Figure 1B), both small features of 5−15 nm lateral extension (Figure 1B, inset) and faint undulations of ∼50 nm lateral scale (Figure 1B, cross section) contributed to a slightly increased roughness of 0.19 ± 0.02 nm. The surface roughness was considerably larger for silica-coated quartz crystals used for QCM-D (1.2 ± 0.1 nm). Grains with lateral dimensions of 30−70 nm and heights of 5 nm and larger could be discerned, likely to originate from the underlying template of evaporated gold (Figure 1C). In addition, a substructure with a characteristic lateral extension of 3−6 nm was resolved (Figure 1C, inset).

Imaging SLBs. We have demonstrated previously by AFM on mica[12] and by QCM-D on silica-coated quartz crystals[13] that SLBs made of DOPC/DOPS (4:1) were continuous and essentially devoid of defects. When the images at low scanning force, $F^{scan} \sim 200$ pN,[28] taken on SLB-covered substrates (Figure 1D−F) are compared with those of the bare substrates (Figure 1A−C), an important difference is revealed. Surface features of lateral dimension comparable to the thickness of a bilayer disappear (Figure 1D,E) or remain only faintly resolved (Figure 1F). The smoothening effect is manifested in decreased values for the surface roughness, being 0.06 ± 0.01 nm, 0.14 ± 0.01 nm, and 1.0 ± 0.1 nm for the silicon wafer, the silica-coated wafer, and the silica-coated quartz crystal, respectively. However, grain structures (Figure 1F) or surface undulations (Figure 1E) with lateral dimensions larger than the bilayer thickness are reproduced. The appearance of the mica surface in the presence of a bilayer did not change (not shown).

Force Measurements on Solid Supports. Force−distance curves recorded on clean supports (Figure 2A) are characteristic of solid substrates under the buffer conditions applied here.[29] Van der Waals forces and electrostatic forces are essentially balanced, resulting in small forces (<50 pN) of repulsion upon tip approach and adhesion upon tip retraction. Force curves were reproducible and independent of lateral position, tip, and applied load (up to 15 nN).

Force Measurements on SLBs. Force−distance curves on SLB-coated supports differed from what was observed on bare substrates. Typical curves are shown in Figure 2B−D for a silica-coated wafer. Three distinctive responses were obtained, depending on the load, F^{stat}, applied: (i) At low load, a first repulsive regime upon approach and no or small rupture forces ($|F^{stat}_{off}| < 0.6$ nN) upon retraction were measurable (Figure 2B). (ii) Above a threshold load, $F^{stat}_{in1} \sim 4.9$ nN in Figure 2C, the repulsive regime was followed by a jump, $d^{scan}_{in1} = 3.9$ nm (Figure 2C, arrowhead), and a second repulsive regime. Considerable pull-off forces, $F^{stat}_{off1} \sim -2.2$ nN in Figure 2C, were measured upon retraction. (iii) At loads larger than a second threshold load, $F^{stat}_{in2} \sim 12.2$ nN in Figure 2D, a second jump, $d^{scan}_{in2} = 1.5$ nm (Figure 2D, arrowhead), occurred, followed by hard-wall contact. Upon retraction, two pull-off events, $F^{stat}_{off2} \sim 1.1$ nN and $F^{stat}_{off1} \sim -1.6$ nN (Figure 2D, asterisks), could be observed.

The onset of the first repulsive regime occurs at a separation of ∼9 nm from hard-wall contact (cf. Figure 2D). This distance is close to the thickness of two lipid bilayers, indicating that apart from the bilayer on the solid support, a second bilayer must be present on the tip.

(28) The index "scan" refers to forces applied during scanning; in contrast, the index "stat" is used for forces applied in static lateral positioning of the tip with respect to the sample.

(29) Müller, D. J.; Engel, A. *Biophys. J.* **1997**, *73*, 1633−1644.

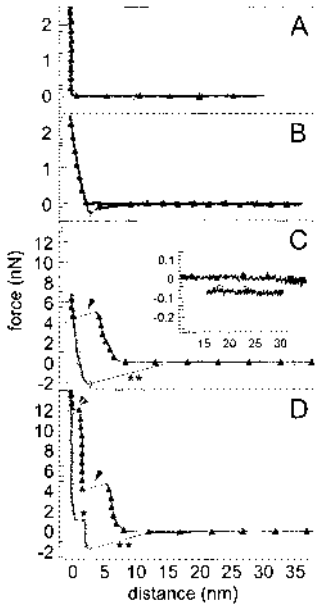

Figure 2. Force−distance curves on a silica-coated wafer without (A) and with (B−D) an SLB present, recorded in calcium-containing buffer (▲, approach; ○, retraction). No (B), one (C), or two (D) jump-in (arrowheads) and pull-off (asterisks) events can be observed, depending on the applied load. According to our interpretations, the onset of the first repulsive regime at a distance of ∼9 nm (D) is due to the presence of a second bilayer on the tip. With increasing load, the lipid material between tip and support is compressed and displaced in two sequential steps, each of them corresponding to the displacement of one bilayer. Upon retraction, a small constant negative force (C, inset) was often observed at separations beyond 10 nm, extending over several tens of nanometers, indicating that the tip can maintain some form of contact with the sample over distances exceeding the thickness of two bilayers.

The most direct interpretation of the force−distance curves presented here is that they reflect the interaction between solid supports coated by an SLB and that with increasing load, the lipid material between tip and support is compressed and displaced in two sequential steps, each of them corresponding to the displacement of one bilayer. A distance of ∼7 nm is measured between the onset of the first repulsive regime and the position after the first jump (cf. Figure 2D) corresponding to the displacement of one bilayer and subsequent compression of the remaining bilayer between tip and support.

Note that upon retraction a small constant negative force, $F^{stat}_{tub} \sim -0.06 \pm 0.05$ nN, was often observed at separations beyond 10 nm (cf. Figure 2C, inset). This force extended sometimes over distances of several tens of nanometers, indicating that the tip can maintain some form of contact with the sample far beyond separations corresponding to the thickness of two bilayers.

It was possible to switch between the three responses described above by varying F^{stat} below or above the characteristic threshold values, F^{stat}_{on1} and F^{stat}_{on2}. The qualitatively different responses persisted at varying velocities of approach and retraction (20−1600 nm/s). Forces and distances of jump-in and pull-off were reproducible with some statistical spreading (in the order of 10%).

Qualitatively similar force curves were obtained on all solid supports investigated. On mica, silicon wafers, and silica-coated wafers, the response was laterally invariant, but measured forces could vary considerably (in the order of 100%) upon exchange of the tip. Since the response was laterally invariant, we attribute these changes to the exact nature of the lipid deposit present on the tip apex and not

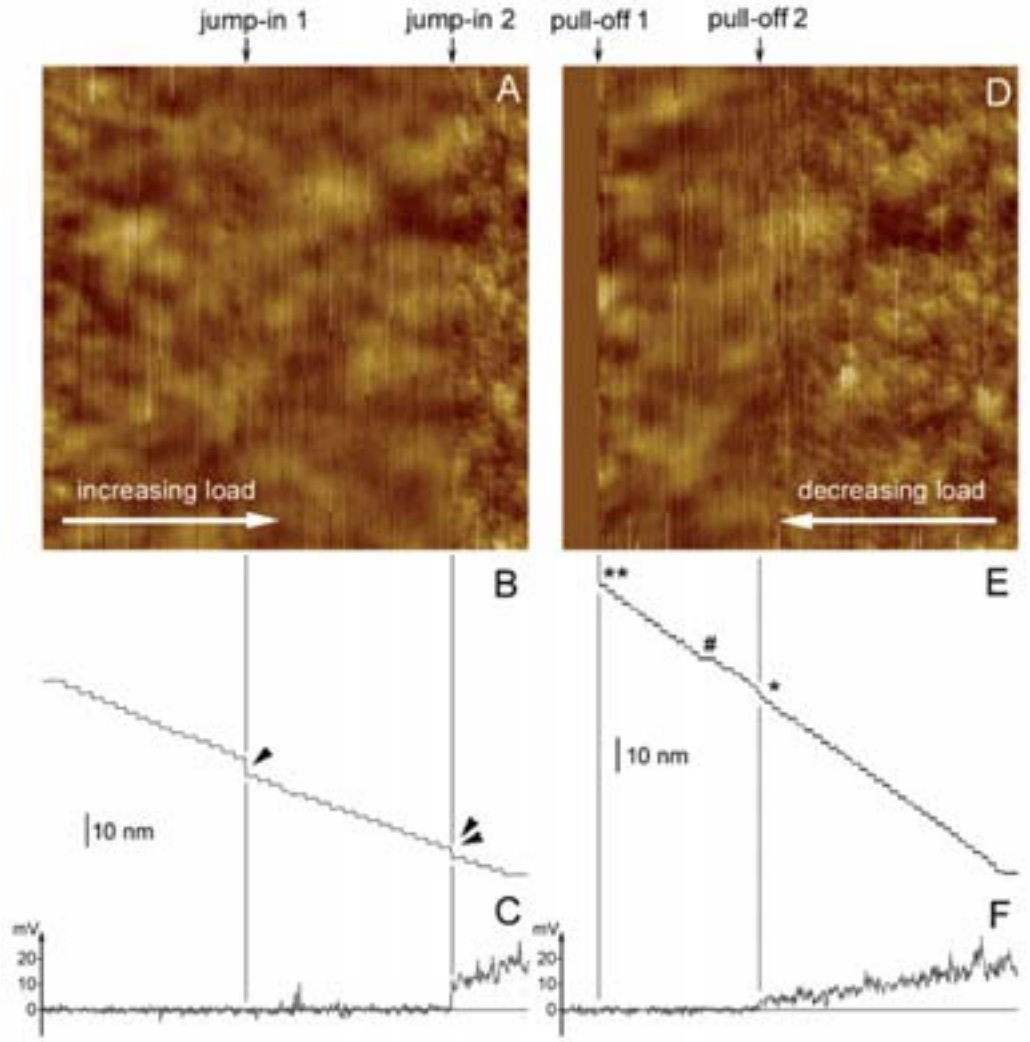

Figure 3. Effect of applied scanning force on AFM images of a lipid bilayer supported by a silica-coated wafer. The force was increased stepwise in intervals of 0.3 nN per 12 scan lines from ~100 pN to ~11 nN (A−C) and subsequently decreased in intervals of 0.3 nN per 8 scan lines until retraction of the tip (D−F). Flattened height images (A,D) were rotated by 90° with the slow scan axis as indicated by the white arrows. Cross sections of the nonflattened height images (B,E) show the *z*-movement of the scanner. The apparent regular steps of $d_{cant} = 1.6$ nm height are due to the change of the scanning force, as the scanner movement compensates for the cantilever deflection. To determine effective jump heights of the tip with respect to the substrate, d_{cant} was subtracted from heights apparent in (B) and (E). As the force was ramped manually, some irregularities did occur (# in E). (C) and (F) show friction data. (A−C) At low forces, the smooth bilayer was revealed (A) with friction below the detection limit. A first jump-in (arrowhead) of 4.0 nm at $F_{in1}^{scan} \sim 4.9$ nN did not change the appearance either of the height image or of the friction. After a second jump-in (double arrowhead) of 1.8 nm at $F_{in2}^{scan} \sim 10.2$ nN, the height image resembled that of the silica substrate and friction increased abruptly. (D,E) The friction decreased proportionally to the applied load. After a first pull-off event (asterisk) of −1.7 nm at $F_{off2}^{scan} \sim 2.6$ nN, the height image again resembled a smooth bilayer and friction was below the detection limit. The second pull-off (double asterisk) at $F_{off1}^{scan} \sim -2.8$ nN retracted the tip from the surface.

to a (permanent) reorganization of the lipid assembly induced by the tip. On silica-coated quartz crystals, however, measured forces varied laterally (in the order of 100%), likely due to geometrical constraints on the interaction between tip and substrate, imposed by the elevated surface roughness.

Force Measurements upon Scanning. To investigate dynamic aspects of the tip−sample interaction, images were recorded while the load was varied upon scanning, and responses were compared to force−distance curves acquired under static conditions.

At scanning forces, F^{scan}, used to record the images described in the above section (Figure 1), the tip immediately lost contact when decreasing the scanning force to zero. Correspondingly, force curves recorded before and after the acquisition of the images ($F^{stat} = F^{scan}$) were similar to those in Figure 2B.

To study the effect of the scanning force on the appearance of the image, F^{scan} was first increased in small regular intervals from ~100 pN to ~11 nN and then decreased until detachment of the tip from the sample, while imaging a lipid bilayer supported on a silica-coated wafer (Figure 3). Together with the height images (Figure 3A,D), friction data were also recorded (cross sections shown in Figure 3C,F) to provide complementary information about the interaction between tip and sample.

With increasing load, two steps showed up in cross sections of untreated[30] height images (Figure 3B, arrowheads), indicating abrupt approaches of the tip toward

(30) The cross sections of the untreated height image show the *z*-movement of the scanner, which can reveal jumps of the tip with respect to the distance from the substrate (Figure 3B,E, see figure legend for details); the common flattening treatment removes this information.

the substrate. The first jump-in of $d_{in1}^{scan} = 4.0$ nm occurred at $F_{in1}^{scan} \sim 4.9$ nN without significant changes in the appearance of the treated or nontreated height image, resembling an SLB (Figure 3A). The friction remained insignificant (Figure 3C). The second jump-in of $d_{in2}^{scan} = 1.8$ nm occurred at $F_{in2}^{scan} \sim 10.2$ nN. The appearance of the height image changed abruptly, resembling the underlying substrate, and the friction increased significantly. Upon further increased load, the friction increased proportionally to the applied load, whereas the topography remained unchanged.

With decreasing load, the friction decreased proportionally to the applied load. A first pull-off event of $d_{off2}^{scan} = -1.7$ nm occurred at $F_{off2}^{scan} \sim 2.6$ nN (Figure 3E, asterisk), upon which the appearance of the height image changed back to that of an SLB and the friction diminished to insignificant values. Height images and friction did not change until the tip detached entirely from the surface (Figure 3E, double asterisk), at a negative load of $F_{off1}^{scan} \sim -2.8$ nN. Correspondingly, force curves recorded with $F^{stat} > F_{in1}^{scan}$ ($F^{stat} > F_{in2}^{scan}$) were similar to those in Figure 2C (Figure 2D) showing one (two) jumps upon approach and one (two) pull-off events upon retraction. Also, friction forces measured after the second jump-in and before the first jump-off were similar to forces measured on the bare surface at comparable loads (not shown), in agreement with observations by Grant and Tiberg.[23]

When, after scanning with high loads, the tip was reapproached at low scanning force, the original image of a smooth bilayer was obtained without visible damage (not shown). Responses were reproducible upon repeated variation of the scanning force on the same area, indicating that changes in the bilayer assembly are transient. Threshold forces for jump-in (F_{in1}^{scan}, F_{in2}^{scan}) and pull-off (F_{off1}^{scan}, F_{off2}^{scan}) could deviate by 10% and 50%, respectively, whereas the jump heights could deviate by 10−20% ($n = 6$) with the same tip on the same surface. Variations were larger after tip exchange, though the qualitative response remained the same.

Taken together, three types of responses could be observed, depending on F^{scan}, which are interpreted as follows: (i) When scanning below a threshold force ($F^{scan} < F_{in1}^{scan}$) the (lipid-covered) tip is close to the SLB, following its topography, exhibiting low friction, and immediately losing contact upon decrease of F^{scan} to zero. (ii) When scanning above a threshold force ($F^{scan} > F_{in1}^{scan}$), topography and friction responses remain essentially unchanged but a jump-in event indicates that lipid material corresponding to one bilayer is displaced between tip and substrate. A negative force is required to pull the tip off the sample. (iii) When imaging above a second, yet higher threshold force ($F^{scan} > F_{in2}^{scan}$), the aspect of the height image and the friction measured indicate that the tip is close to the underlying substrate, revealing its structural details and exhibiting enhanced friction. Additional lipid material is displaced upon a second jump-in.

A remarkable adhesion mechanism keeps the tip in contact with the SLB-covered substrate in cases ii and iii. First, the adhesion does not fatigue when pulling the tip off the surface at $F_{off1}^{scan} < F^{scan} < 0 < F_{in1}^{scan}$ and $F_{off2}^{scan} < F^{scan} < F_{in2}^{scan}$, respectively. Second, the adhesion is maintained while scanning; that is, rearrangements of the lipids in the vicinity of the tip do not perturb its adhesion.

Qualitatively similar responses were obtained for SLBs on silicon wafers and mica. On silica-coated quartz crystals, some of the responses could coexist depending on the scanning force and the scanned substrate geometry. The appearance of the height image was irregular, fluctuating between SLB and substrate during one scan line and for subsequent scan lines (not shown).

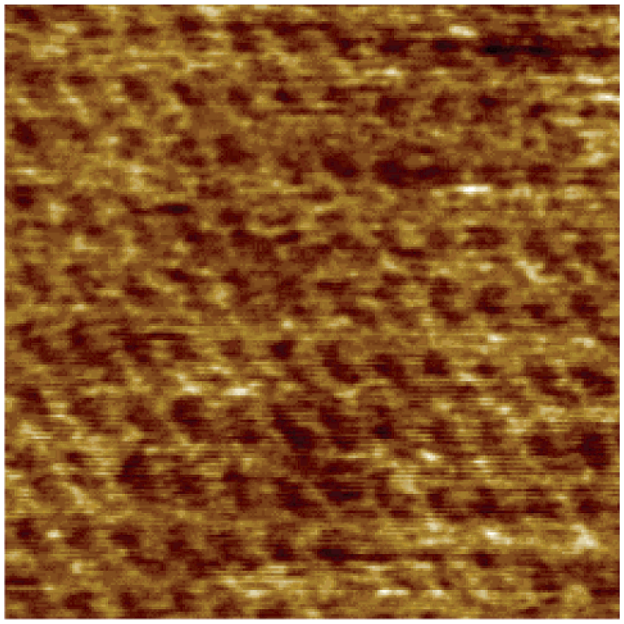

Figure 4. AFM image of a 2D crystal of streptavidin grown on an SLB of DOPC/DOPS/DPPE-lc-biotin (7:2:1) on a silicon wafer. The Fourier transform (not shown) shows diffraction peaks up to 1/2.5 nm^{-1} and confirms the c222 symmetry of the crystalline assembly as described by Reviakine and Brisson (ref 14). Image size (*z*-scale), 100 (2.5) nm.

Protein Assemblies on SLBs. The possible influence of the support roughness on the property of 2D organization of proteins on SLBs was investigated by using two model systems, streptavidin and annexin A5, which have previously been shown to form 2D crystals on mica-supported SLBs.[6,14,15,18]

2D Crystalline Assembly of Streptavidin. For streptavidin, a silicon wafer was first coated with an SLB made of DOPC/DOPS/DPPE-lc-biotin (7:2:1) in calcium-containing buffer. AFM characterization by force curves and imaging in contact mode gave responses typical of an essentially defect-free SLB (not shown). This is in contrast with results obtained on mica where numerous defects have been observed in SLBs containing biotinylated lipids.[14]

2D crystalline domains of streptavidin were observed to cover the entire surface 1 h after addition of streptavidin (40 μg/mL). Grain boundaries could be resolved (not shown). The crystalline organization was readily apparent (Figure 4) and was similar to that reported before on mica-SLBs.[14] This demonstrates that protein 2D crystals can be resolved unambiguously on bilayers formed on a support with small corrugations.

Close-Packed Assembly of Annexin A5. In the case of annexin A5, while 2D crystals form reproducibly on mica-SLBs containing 15−20% DOPS,[6,18] no 2D crystals were observed on silicon wafers or silica-coated wafers under otherwise identical conditions. Instead, a close-packed assembly of annular objects with a diameter of around 14 nm was resolved (Figure 5), the global appearance of which was stable for several hours. The annular objects can be unambiguously identified as trimers of annexin A5, which are the building blocks of annexin A5 2D crystals.[31] The

(31) Oling, F.; Bergsma-Schutter, W.; Brisson, A. *J. Struct. Biol.* **2001**, *133*, 55−63.

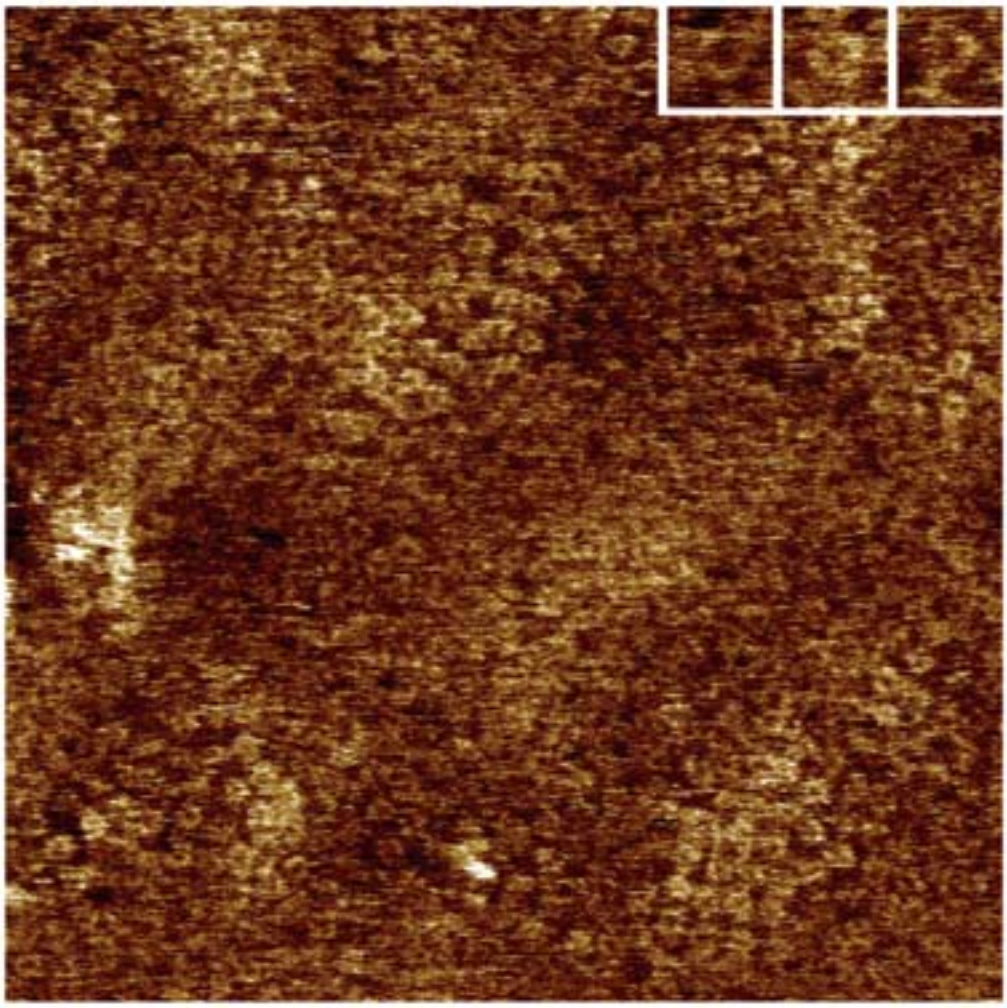

Figure 5. AFM image of the annexin A5 close-packed assembly formed on an SLB of DPPC/DOPC/DOPS (3:3:1) on a silicon wafer. The annular objects (insets) with a diameter of 14 ± 2 nm ($n = 5$) are trimers of annexin A5. No long-range order is revealed. Scan size (z-scale), 500 (2) nm.

difference in diameter of the objects measured here (14 nm) and by electron microscopy (10 nm)[31] is attributed to tip convolution and drifts due to the use of an O-ring. The trimers disappeared after rinsing with EDTA-containing buffer, as expected (not shown).

To investigate whether this difference originated from a lack of mobility of annexin A5 molecules on silica-SLBs, defects were created in the 2D close-packed assembly of annexin A5 trimers and the kinetics of healing of these defects was followed (Figure 6). To make defects in the protein assembly, the AFM tip was used to scan an area of (500 × 500) nm^2 of the surface with an elevated force (~5 nN). Zoom-out images recorded at minimum force immediately afterward revealed a hole with a depth of 2.1 nm (Figure 6A). The defect was found to heal within seconds (Figure 6B,C). A subsequent zoom-in resolved the close-packed assembly of annular objects (not shown). These observations confirm that (i) the distortion of the protein−lipid assembly by the tip does not disturb the functionality of the bilayer as a *fluid* matrix for bound proteins and (ii) bound proteins can diffuse laterally in a rapid manner. Note also that a transient thin-out of the protein layer close to the defect area (arrowhead in Figure 6A) occurs immediately after scratching, which is a further indication of the high lateral mobility and thus noncrystallinity of the protein layer.

Discussion

To characterize SLBs formed on various solid supports, two types of AFM measurements were combined: force−distance curves, referred to as "static mode" as they do not involve lateral movement of the tip with respect to the support, and AFM images, referred to as "scanning mode". We show that both in static mode and in scanning mode three regimes of interaction between tip and SLBs can be obtained by operating below or above certain threshold loads, F_{in1}^{stat}, F_{in2}^{stat} and F_{in1}^{scan}, F_{in2}^{scan}, respectively. These results are interpreted according to a schematic model presented in Figure 7.

In the first regime, the tip interacts with the bilayer with little or no adhesion and slides over the bilayer (Figure 7A). In the second and third regimes, the tip indents the bilayer(s) (Figure 7B,C). These regimes are thus termed "sliding regime" (Figure 7A), "first indentation regime" (Figure 7B), and "second indentation regime" (Figure 7C), respectively. In the indentation regimes, forces, F_{off1}^{stat} (F_{off2}^{stat}) and F_{off1}^{scan} (F_{off2}^{scan}), respectively, of several nanoNewtons are necessary to pull the tip off the lipid layer. The adhesion between tip and SLB does not fatigue over time and remains upon local distortion of the bilayer induced by the movement of the tip through the bilayer. At the same time, the SLB is not permanently perturbed since the effects are reproducible. The rupture forces are expected to originate from the cohesion of the lipid

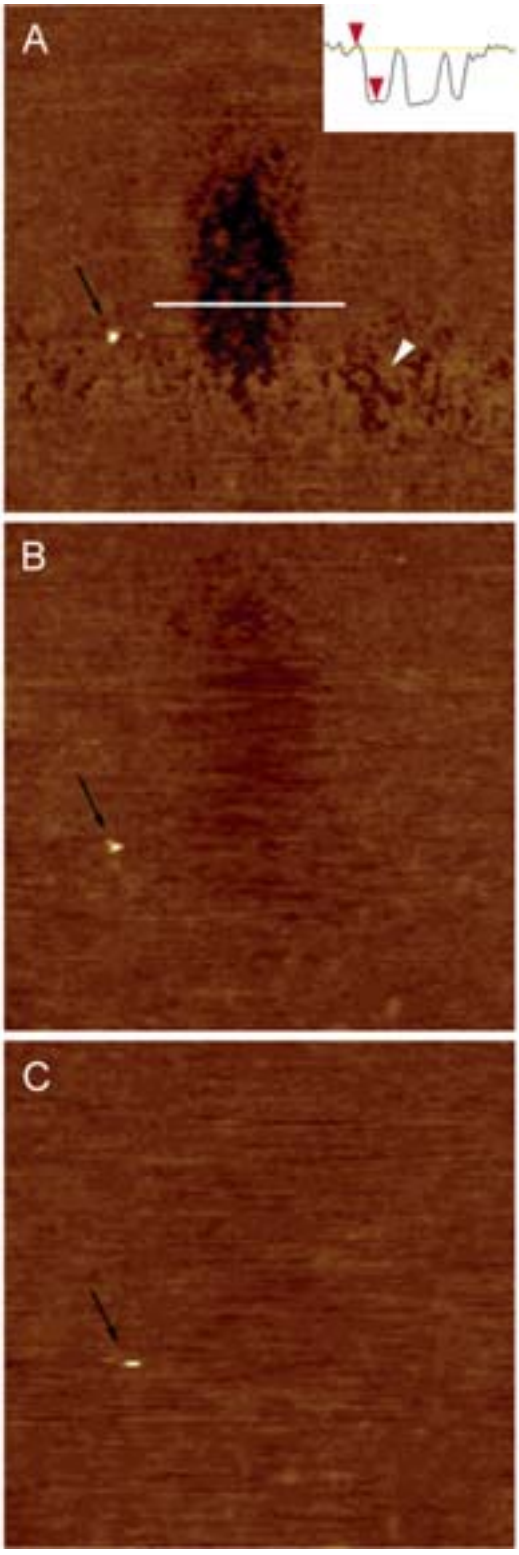

Figure 6. Healing of a defect created in a close-packed assembly of annexin A5 trimers on a lipid bilayer of DOPC/DOPS (4:1) supported on a silicon wafer. Successive images were acquired immediately (A), 20 s (B), and 40 s (C) after scratching a central area of (500 × 500) nm^2 with a force of 5 nN. The defect shows a maximum depth of 2.1 nm (cross section in (A)) and heals within seconds. As annexin A5 molecules in solution were rinsed away before scratching, healing must result from the lateral diffusion of lipid-bound annexin A5. Note a temporary thin-out of the protein layer close to the defect (white arrowhead in (A)). The contamination (black arrow) provides a reference for the lateral position. The resolution was limited to 128 × 128 pixels per image in order to decrease the image acquisition time to about 20 s. Scan size, 3 μm. *Z*-scale, 5 nm.

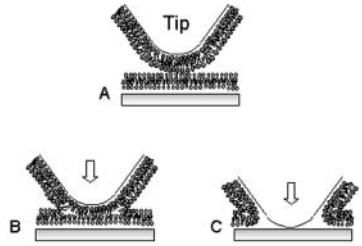

Figure 7. Schematic model representing the three regimes of tip−sample interactions described in this paper. (A) In the sliding regime, the lipid structures covering both tip and solid support remain intact. (B) A continuous lipid film with a hydrophobic interior is formed between the (moving) tip and the solid support in the first indentation regime. (C) Contact between tip and solid support is established in the second indentation regime while a continuous lipid structure is maintained around the interface of tip and support. The lipid structures are thought to be dynamic, continuously reforming upon lateral movement of the tip and stabilized by hydrophobic interactions of the lipid film.

assembly around the tip since the interaction between tip and solid support is too small to account for the measured forces.

We propose that the described regimes are associated with molecular rearrangements of the highly mobile lipids in the vicinity of the tip driven by hydrophobic/hydrophilic interactions. The simple model in Figure 7 explains our results and helps to interpret previous studies.[21,23,32] In the indentation regimes, a hydrophobic continuum is formed by the tails of the lipids, which links the tip and the substrate together (Figure 7B,C). Upon scanning, this hydrophobic continuum can move with the tip due to rapid rearrangements of the lipids, leaving an intact bilayer behind. A barrier needs to be overcome to switch between the different molecular organizations, as reflected by the threshold forces upon approach and retraction of the tip.

In addition to the molecular rearrangements driven by hydrophobic interactions, a component of mechanical compression cannot be neglected in the tip−bilayer interaction as indicated in the repulsive zones and by the fact that the jump distances do not correspond exactly to a bilayer thickness.

The mechanism proposed here is analogous to what can be observed for a hydrophilic tip interacting with a hydrophilic substrate via a water film formed by capillary forces in ambient air.[2,33] In the present case, a hydrophobic continuum is formed in a hydrophilic surrounding, held together by hydrophobic interactions, whereas the water meniscus constitutes a hydrophilic continuum in a hydrophobic surrounding (air).

The hypothesis that the silicon nitride tip is covered with lipid structures is supported by the fact that it is expected to be hydrophilic, as already reported by others.[20,23] It is thus reasonable to expect the tip apex to become covered with lipid structures once exposed to it. In the present model, the lipid assembly on the AFM tip is represented as an ideal SLB following the tip topography, although the exact organization of the lipid layer is not known and is likely to be more complex. As the tip shape and the lipid deposition are ill controlled, the conformation of the lipid assembly on the tip apex is expected to vary from tip to tip, which readily explains the variations observed for the jump-in and pull-off forces.

Double jumps or single jumps have been reported before to occur over distances corresponding to one or two

(32) Dufrêne, Y. F.; Boland, T.; Schneider, J. W.; Barger, W. R.; Lee, G. U. *Faraday Discuss.* **1998**, *111*, 79−94.
(33) Cappella, B.; Dietler, G. *Surf. Sci. Rep.* **1999**, *34*, 1−104.

bilayers, depending on the size of the AFM tip.[20,23] In addition, the hysteresis between jump-on and pull-off events has been reported previously and has received several interpretations.[21,23,32] Grant and Tiberg[23] speculate about energy dissipation during the squeeze-out of the bilayer from the contact zone, kinetically limited healing, or material trapped irreversibly in the contact zone for bilayers of DOPC and a silica tip. These reasons alone would make it unlikely for the tip to stay in the first indentation regime upon scanning at negative loads. We propose lipid rearrangements in the vicinity of the tip due to hydrophobic/hydrophilic interactions as an explanation of the observed response.

On the same lines, the formation of tubelike structures might give an explanation for forces present after retraction at distances by far exceeding the thickness of two bilayers. It is known that lipid tubes can be drawn from lipid vesicles,[34,35] and corresponding force measurements by AFM have recently been reported.[36]

The proposed mechanism is expected to occur for fluid SLBs that adsorb to support and tip. SLBs made of DOPC/DOPS (4:1) used here are indeed liquidlike as supported by the facts that (i) scratches in adsorbed noncrystalline protein assemblies heal quickly and (ii) the SLBs are defect-free and defects cannot be induced by scratching with the tip. Also, diffusion constants of $2-2.8 \times 10^{-12}$ m^2 s^{-1} [9] and $0.7-1 \times 10^{-12}$ m^2 s^{-1},[37] characteristic for fluid bilayers, have been reported for similar lipid mixtures on mica and glass, respectively. It remains to be elucidated whether a similar interaction between SLB and tip will occur with gel-phase bilayers as constrained lipid diffusion might prevent the dynamic lipid structure in the vicinity of the tip from being maintained upon scanning. However, the tip may create a local environment such that the global diffusion constant of the SLB is not the determining factor. Also the tip material used, in particular its hydrophilicity, is expected to have an influence on the interaction between tip and SLB.

The characterization of tip−sample interactions as reported here, whether in static mode (with its potential application in force mapping[29,38,39]) or scanning mode, could be particularly useful for a simple and unambiguous detection of the presence of lipid bilayers on rough supports, as standard imaging conditions involving low loads might make the detection of bilayers ambiguous. However, it was shown that the bilayer-covered silica-coated quartz crystal creates a rather complex response due to its large roughness, likely to impose geometrical constraints on the lipid-mediated tip−support interaction.

It is not entirely clear whether the images at low loads reflect the true topography of the bilayer, shown to intimately track support features larger than the bilayer thickness. It cannot be excluded that the bilayer spans over larger valleys being suspended over a limited number of protrusions but that even minimized forces exerted by the tip press the bilayer into the valley. Investigations are under way to answer this question.

Protein crystals can clearly be imaged with submolecular resolution on surfaces with small roughness such as silicon wafers and silica-coated wafers.[40,41] For rougher surfaces, for example, the silica-coated quartz crystal, this could not be done successfully. Somewhat surprisingly, the annexin A5 trimers did not crystallize on lipid bilayers supported by a silicon wafer or a silica-coated wafer under conditions where they do crystallize on a mica-SLB. This suggests that the support properties have an influence on the bilayer, which in turn has an influence on the protein crystallization process. Factors changed are the roughness of the support, even though to a small extent, and possibly the fluidity of the bilayer. The SLB clearly remains in the fluid phase, but it can be speculated that a minor change in the lipid diffusion coefficient[9,37] might influence the 2D rearrangement of membrane-bound annexin A5. Further work will aim to elucidate the origin of such variations in the 2D crystallization behavior of proteins.

Conclusions

It was shown that the AFM is a versatile tool to investigate SLBs and protein assemblies on rough surfaces. Due to a combination of imaging modes and force measurements, local properties of SLBs such as roughness or mechanical properties can be characterized. The understanding of the interactions between the SLB and the lipid-covered tip, proposed to be driven by hydrophobic/hydrophilic interactions, is crucial in order to correctly interpret the observed responses.

It could be shown that the properties of the solid support, mediated by the bilayer, can have a crucial impact on the self-organization of proteins on SLBs. This can have important consequences for the use of these systems as building blocks in biofunctional surfaces.

Acknowledgment. Discussions with Jean-Pierre Aimé and Touria Cohen-Bouhacina (University Bordeaux I, Bordeaux, France) are acknowledged. We thank Natalia Govorukhina (University of Groningen, Groningen, The Netherlands) for providing annexin A5 and Patrice Caillat and Claude Vauchier (CEA-LETI, Grenoble, France) for the gift of silicon and silica-coated wafers. Ralf Richter is the recipient of a Ph.D. fellowship from the Conseil Régional d'Aquitaine, France. This research was supported by the Conseil Régional d'Aquitaine, the Fonds Européen de Développement Régional, and EC Grants QLK2-CT2001-01339 and QLG3-CT2001-00902.

LA026427W

(34) Karlsson, M.; Sott, K.; Cans, A.-S.; Karlsson, A.; Karlsson, R.; Orwar, O. *Langmuir* **2001**, *17*, 6754−6758.
(35) Evans, E.; Yeung, A. *Chem. Phys. Lipids* **1994**, *73*, 39−56.
(36) Maeda, N.; Senden, T. J.; Meglio, J.-M. D. *Biochim. Biophys. Acta* **2002**, *1564*, 165−172.
(37) Cézanne, L.; Lopez, A.; Loste, F.; Parnaud, G.; Saurel, O.; Demange, P.; Tocanne, J.-F. *Biochemistry* **1999**, *38*, 2779−2786.
(38) Dufrêne, Y. F.; Barger, W. R.; Green, J.-B. D.; Lee, G. U. *Langmuir* **1997**, *13*, 4779−4784.
(39) Rotsch, C.; Radmacher, M. *Langmuir* **1997**, *13*, 2325−2832.
(40) Karrasch, S.; Hegerl, R.; Hoh, J. H.; Baumeister, W.; Engel, A. *Proc. Natl. Acad. Sci. U.S.A.* **1994**, *91*, 836−838.
(41) Wetzer, B.; Pum, D.; Sleytr, U. B. *J. Struct. Biol.* **1997**, *119*, 123−128.

Paper II

Ralf P. Richter and Alain Brisson

QCM-D on mica for parallel QCM-D – AFM studies.

Langmuir, **20** (2004), p. 4609-4613

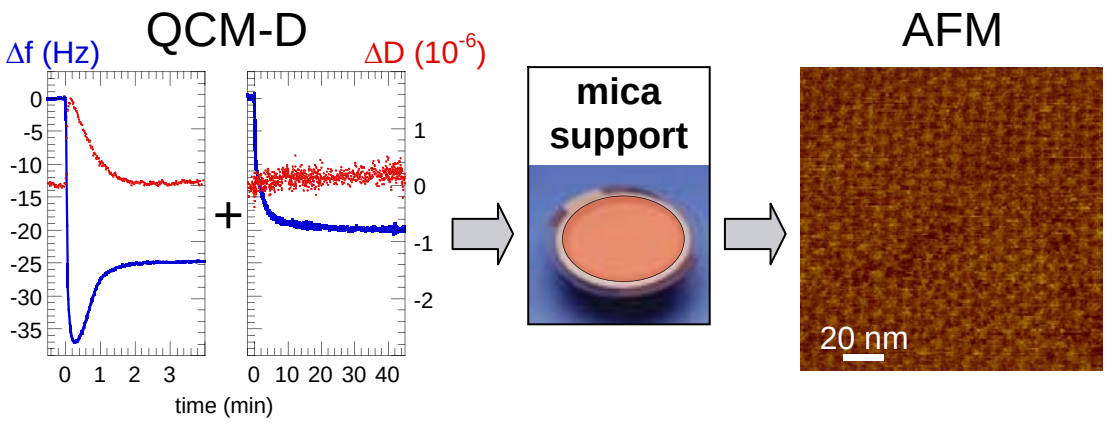

QCM-D on Mica for Parallel QCM-D−AFM Studies

Ralf P. Richter and Alain Brisson*

Laboratoire d'Imagerie Moléculaire et Nano-Bio-Technologie, IECB, UMR-CNRS 5471, Université Bordeaux I, 2 Rue Robert Escarpit, 33607 Pessac Cedex, France

Received January 19, 2004. In Final Form: March 18, 2004

Quartz crystal microbalance with dissipation monitoring (QCM-D) has developed into a recognized method to study adsorption processes in liquid, such as the formation of supported lipid bilayers and protein adsorption. However, the large intrinsic roughness of currently used gold-coated or silica-coated QCM-D sensors limits parallel structural characterization by atomic force microscopy (AFM). We present a method for coating QCM-D sensors with thin mica sheets operating in liquid with high stability and sensitivity. We define criteria to objectively assess the reliability of the QCM-D measurements and demonstrate that the mica-coated sensors can be used to follow the formation of supported lipid membranes and subsequent protein adsorption. This method allows combining QCM-D and AFM investigations on identical supports, providing detailed physicochemical and structural characterization of model membranes.

Introduction

Besides the potential application of supported lipid bilayers (SLBs) and two-dimensional (2D) ordered protein assemblies as building blocks in biofunctional surfaces,[1−4] the self-assembly mechanisms driving the formation of these structures are of fundamental scientific interest.[5−12] From previous studies on the formation of SLBs by spreading of vesicles on hydrophilic supports[5,6,9,12−23] and on the 2D crystallization of proteins on lipid membranes,[3,7,10,24−26] a qualitative picture of structural intermediates and driving forces is emerging, whereas a quantitative characterization of the self-assembly kinetics is still largely lacking. These studies have also shown that combining information from various surface-sensitive methods is required to get a detailed description and understanding of such processes. However, a direct correlation of results obtained from different surface-sensitive methods is hampered by the fact that they use various types of support materials, which play a determining role in the adsorption process investigated. In particular, we have shown recently that the nature of the surface can influence the pathways of SLB formation as well as the nature—order versus disorder—of protein assemblies.[6,7,12,27]

In this study, we present a method to deposit mica sheets on QCM-D sensors for measurements in liquid. Our objective is to perform studies of adsorption processes, by QCM-D and AFM, allowing parallel physicochemical and structural analysis on identical supports.

Quartz crystal microbalance with dissipation monitoring (QCM-D), a technique that provides information of bound mass, water content, and viscoelastic properties of surface-bound material,[28] has become popular to investigate the formation of SLBs[12−16] as well as interactions of SLBs with proteins and other biomolecules.[29−35]

Among materials currently used in surface-sensitive methods, which include glass, gold, graphite, mica, silica,

* Corresponding author. E-mail: a.brisson@iecb.u-bordeaux.fr.

(1) Sackmann, E. *Science* **1996**, *271*, 43−48.
(2) Wetzer, B.; Pum, D.; Sleytr, U. B. *J. Struct. Biol.* **1997**, *119*, 123−128.
(3) Reviakine, I.; Bergsma-Schutter, W.; Brisson, A. *J. Struct. Biol.* **1998**, *121*, 356−361.
(4) Reviakine, I.; Brisson, A. *Langmuir* **2001**, *17*, 8293−8299.
(5) Seifert, U. *Adv. Phys.* **1997**, *46*, 13−137.
(6) Reviakine, I.; Brisson, A. *Langmuir* **2000**, *16*, 1806−1815.
(7) Reviakine, I.; Bergsma-Schutter, W.; Mazères-Dubut, C.; Govorukhina, N.; Brisson, A. *J. Struct. Biol.* **2000**, *131*, 234−239.
(8) Reviakine, I.; Bergsma-Schutter, A.; Morozov, A. N.; Brisson, A. *Langmuir* **2001**, *17*, 1680−1686.
(9) Zhdanov, V. P.; Keller, C. A.; Glasmästar, K.; Kasemo, B. *J. Chem. Phys.* **2000**, *112*, 900−909.
(10) Zhdanov, V. P.; Höök, F.; Kasemo, B. *Proteins: Struct., Funct., Genet.* **2001**, *43*, 489−498.
(11) Noro, M. G.; Bates, M. A.; Brisson, A.; Frenkel, D. *Langmuir* **2002**, *18*, 2988−2992.
(12) Richter, R.; Mukhopadhay, A.; Brisson, A. *Biophys. J.* **2003**, *85*, 3035−3047.
(13) Keller, C. A.; Glasmästar, K.; Zhdanov, V. P.; Kasemo, B. *Phys. Rev. Lett.* **2000**, *84*, 5443−5446.
(14) Keller, C. A.; Kasemo, B. *Biophys. J.* **1998**, *75*, 1397−1402.
(15) Reimhult, E.; Höök, F.; Kasemo, B. *Phys. Rev. E* **2002**, *66*, 051905−1−4.
(16) Reimhult, E.; Höök, F.; Kasemo, B. *J. Chem. Phys.* **2002**, *117*, 7401−7404.
(17) Johnson, J. M.; Taekijp, H.; Chu, S.; Boxer, S. G. *Biophys. J.* **2002**, *83*, 3371−3379.
(18) Cremer, P. S.; Boxer, S. G. *J. Phys. Chem. B* **1999**, *103*, 2554−2559.
(19) Jass, J.; Tjärnhage, T.; Puu, G. *Biophys. J.* **2000**, *79*, 3153−3163.
(20) Nollert, P.; Kiefer, H.; Jähnig, F. *Biophys. J.* **1995**, *69*, 1447−1455.
(21) Rädler, J.; Strey, H.; Sackmann, E. *Langmuir* **1995**, *11*, 4539−4548.
(22) Lipowsky, R.; Seifert, U. *Mol. Cryst. Liq. Cryst.* **1991**, *202*, 17−25.
(23) Zhdanov, V. P.; Kasemo, B. *Langmuir* **2001**, *17*, 3518−3521.
(24) Yatcilla, M. T.; Robertson, C. R.; Gast, A. P. *Langmuir* **1998**, *14*, 497−503.
(25) Wang, S.-W.; Robertson, C. R.; Gast, A. P. *Langmuir* **1999**, *15*, 1541−1548.
(26) Oling, F.; Bergsma-Schutter, W.; Brisson, A. *J. Struct. Biol.* **2001**, *133*, 55−63.
(27) Richter, R.; Brisson, A. *Langmuir* **2003**, *19*, 1632−1640.
(28) Höök, F.; Larsson, C.; Fant, C. In *Encyclopedia of Surface and Colloid Science*; Somasundaran, P., Ed.; Marcel Dekker: New York, 2002; pp 774−791.
(29) Glasmästar, K.; Höök, F.; Kasemo, B. *J. Colloid Interface Sci.* **2002**, *246*, 40−47.
(30) Kastl, K.; Ross, M.; Gerke, V.; Steinem, C. *Biochemistry* **2002**, *41*, 10087−10094.
(31) Govorukhina, N.; Bergsma-Schutter, A.; Mazères-Dubut, C.; Mazères, S.; Drakopoulou, E.; Bystrykh, L.; Oling, F.; Mukhopadhyay, A.; Reviakine, I.; Lai Kee Him, J.; Brisson, A. In *Annexins: Biological importance and annexin-related pathologies*; Bandorowicz-Pikula, J., Ed.; Landes Bioscience/Eurekah.com: Georgetown, TX, 2003; pp 37−55.
(32) Larsson, C.; Rodahl, M.; Höök, F. *Anal. Chem.* **2003**, *75*, 5080−5087.
(33) Richter, R.; Lai Kee Him, J.; Brisson, A. *Mater. Today* **2003**, *6*, 32−37.
(34) Fant, C.; Elwing, H.; Höök, F. *Biomacromolecules* **2002**, *3*, 732−741.
(35) Höök, F.; Ray, A.; Nordén, B.; Kasemo, B. *Langmuir* **2001**, *17*, 8305−8312.

10.1021/la049827n CCC: $27.50
Published on Web 04/30/2004

silicon, or titanium oxide, mica is unique for its intrinsic hydrophilicity and because it is easily cleaved into large (cm^2) atomically flat areas, making it an ideal surface for imaging by AFM.[27,36,37] Previous attempts to develop mica-coated sensors for QCM so far focused on applications in gaseous environment[38−40] or, when applied in liquid, resulted in limited stability, preventing quantitative evaluation.[41]

The objectives of this work are (i) to demonstrate the feasibility of performing QCM-D experiments in liquids on mica with high stability and sensitivity, (ii) to evaluate how the reliability of mica-QCM-D can be ensured on the quantitative level, (iii) to demonstrate that mica-QCM-D allows to follow self-assembly processes such as SLB-formation or protein 2D crystallization, and (iv) to demonstrate the potential of a combination of AFM and QCM-D on identical supports.

Materials and Methods

Materials. Dioleoylphosphatidylcholine (DOPC) and dioleoylphospatidylserine (DOPS) were purchased from Avanti Polar-Lipids (AL). Recombinant rat annexin A5 was overexpressed in *Escherichia coli* and purified as previously described.[7] Other chemicals were purchased from Sigma. Ultrapure water with a resistivity of 18.2 MΩ was used (Maxima, USF ELGA, France).

Muscovite mica disks of 12-mm diameter were purchased from Metafix (Montdidier, France). QCM-D sensor crystals (5 MHz) with gold electrodes, reactively sputter coated with 50 nm silicon oxide, were purchased from Q-SENSE (Gothenburg, Sweden). Low viscosity epoxy glue (EPOTEK 377) was purchased from Gentec Benelux (Waterloo, Belgium).

A buffer solution made of 150 mM NaCl, 2 mM NaN_3, and 10 mM HEPES, pH 7.4, was prepared in ultrapure water, and either 2 mM EDTA or $CaCl_2$ was added as indicated in the text. Small unilamellar vesicles (SUVs) of desired lipid mixture were prepared by sonication as described earlier.[12] Before use, vesicle suspensions were diluted at 0.1 mg/mL. Annexin A5 was used at a concentration of 20 μg/mL.

Preparation of Mica-Coated QCM-D Sensors. Prior to the mica deposition, the QCM-D sensor crystals were rinsed in water and ethanol, blow-dried with nitrogen, and exposed to UV/ozone (BHK, CA) for 10 min.[27] Mica disks were cleaved with Scotch tape, until a thin sheet (<100 μm thickness) devoid of cleavage steps—as checked by eye—remained on the tape. The tape−mica sheet was subsequently cut into disks of 9.5-mm diameter using a punch and die set (Precision Brand, IL).

QCM-D sensors were coated with mica as schematically described in Figure 1. Mica was applied in an oven at 50 °C at low humidity (RH < 0.2). A droplet of ∼0.2 μL undiluted epoxy glue was deposited in the center of the active electrode of the QCM-D sensor. The tape−mica sheet was placed concentrically on top of the droplet, the mica side facing the glue. Capillary forces ensured spreading of the glue along the interface without entrapment of bubbles. The resin was polymerized under pressure (using a home-built press) at 150 °C for 1 h, after which the system was cooled overnight to room temperature and stored until use.

Before use, excess of glue was scratched off around the mica sheet. The tape was peeled off, uncovering a surface of freshly cleaved mica (Figure 1B). If necessary, the mica sheet was subsequently thinned by tape peeling until a stable oscillation

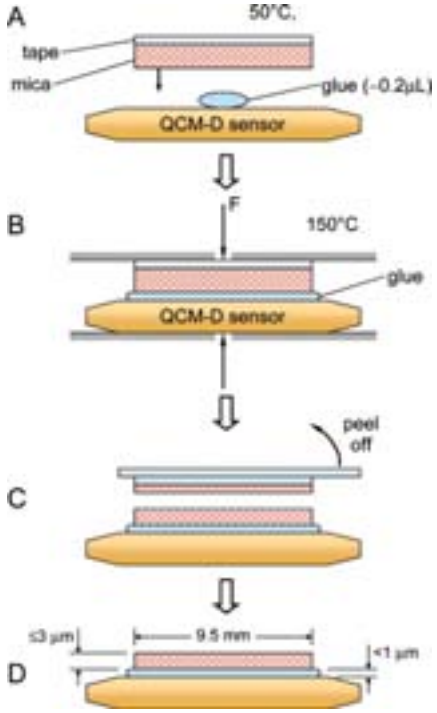

Figure 1. Schematic presentation of the preparation of a mica-coated QCM-D sensor: (A) A droplet of glue is sandwiched between the QCM-D sensor and a mica sheet covered with adhesive tape. (B) Hardening of the glue under press. (C) The tape is peeled off uncovering a surface of freshly cleaved mica, (D) resulting in a mica disk of a few micrometer thickness glued on the QCM-D sensor.

of the mica-coated QCM-D sensor could be obtained at several overtones in air (see below). A stably operating mica-coated sensor was immediately covered with buffer.

Quartz Crystal Microbalance with Dissipation Monitoring (QCM-D). QCM-D measurements were performed with the Q-SENSE D300 system equipped with an Axial Flow Chamber (QAFC 301) (Q-SENSE AB, Gothenburg, Sweden).[42] Briefly, upon interaction of (soft) matter with the surface of a sensor crystal, changes in the resonance frequency, f, related to attached mass (including coupled water), and in the dissipation, D, related to frictional (viscous) losses in the adlayer are measured with a time resolution of better than 1 s.

Measurements in liquid environment were performed at a working temperature of 24 °C in exchange mode.[12] Resonance frequency and dissipation were measured at several harmonics (15, 25, 35 MHz) simultaneously. For every experiment, f and D were recorded prior to mica deposition (in air) and after mica deposition (in air and with added liquid). If not stated otherwise, (i) changes in dissipation and normalized frequency ($\Delta f_{norm} = \Delta f_n/n$, with n being the overtone number) are presented and (ii) adsorbed masses, Δm, are calculated according to the Sauerbrey equation,[43] $\Delta m = -C \cdot \Delta f_{norm}$, with $C = 17.7$ ng·cm^{-2}·Hz^{-1}.

For transferring the QCM-D sensors with adsorbed material from the QCM-D chamber to the AFM, sensors were unmounted with the aid of a suction holder (Meni CUP, Menicon Pharma, Illkirch Graffenstaden, France), ensuring that the sample remained permanently covered with liquid.

Atomic Force Microscopy (AFM). AFM measurements were performed in liquid using a Nanoscope VI-Multimode (VEECO, Dourdan, France), equipped with a J-scanner (120 μm). Before use, the contact mode fluid cell was washed by sonication in successive baths of ethanol and ultrapure water, followed by extensive rinsing in ethanol and blow-drying in a stream of nitrogen. Oxide-sharpened silicon nitride cantilevers with a nominal spring constant of 0.06 N/m (Digital Instruments, CA)

(36) Shao, Z.; Mou, J.; Czajkowsky, D. M.; Yang, J.; Yuan, J.-Y. *Adv. Phys.* **1996**, *45*, 1−86.
(37) Müller, D. J.; Schoenenberger, C.-A.; Schabert, F.; Engel, A. *J. Struct. Biol.* **1997**, *119*, 149−157.
(38) Berg, S.; Ruths, M.; Johannsmann, D. *Phys. Rev. E* **2002**, *65*, 026119.
(39) Berg, S.; Johannsmann, D.; Ruths, M. *J. Appl. Phys.* **2002**, *92*, 6905−6910.
(40) Berg, S.; Ruths, M.; Johannsmann, D. *Rev. Sci. Instrum.* **2003**, *74*, 3845−3852.
(41) Xu, B.; Wang, H.; Wang, Y.; Zhu, G.; Li, Z.; Wang, E. *Anal. Sci.* **2000**, *16*, 1061−1063.
(42) Rodahl, M.; Höök, F.; Krozer, A.; Brzezinski, P.; Kasemo, B. *Rev. Sci. Instrum.* **1995**, *66*, 3924−3930.
(43) Sauerbrey, G. *Z. Phys.* **1959**, *155*, 206−222.

Table 1. Parameters Investigated to Evaluate the Reliability of a QCM-D Measurement on Mica

	air−mica transition		mica−buffer transition		stability		mica
	$\Delta f^{\text{air-mica}}$ (−kHz)	$\Delta D^{\text{air-mica}}$ (10^{-6})	$\Delta f_n^{\text{mica-buffer}}$ (−Hz/$\sqrt{n}$)	$\Delta D_n^{\text{mica-buffer}}$ ($10^{-6}\cdot\sqrt{n}$)	$\lvert\Delta f/t\rvert$ (Hz/ h)	$\lvert\Delta D/t\rvert$ (10^{-6}/h)	cleavage plane
ideal[a]	10	0	675 ± 10[c]	268 ± 10[c]	<1	<0.1	no steps
acceptable[b]	5−50	0−50	100−125%	100−115%	<5	<1	few small steps

[a] Assuming the glue−mica compound as a rigid mass. [b] Resulting in reliable measurements. [c] Calculated from ref 46.

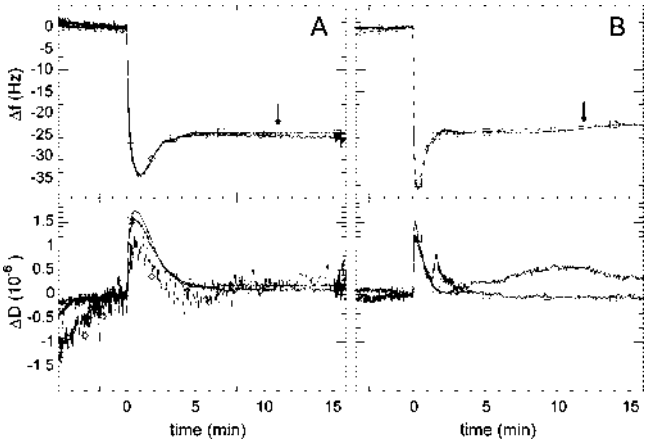

Figure 2. QCM-D response for the deposition of SUVs made of DOPC/DOPS (molar ratio 2:1) (A) and DOPC/DOPS (1:2) (B) onto a mica-coated QCM-D sensor in the presence of 2 mM calcium. Upper (lower) panel: changes in frequency (dissipation) at 15 MHz (−○−), 25 MHz (−□−), and 35 MHz (····). Arrows indicate rinses with buffer.

were exposed to UV/ozone (BHK, CA) for 10 min and rinsed with buffer prior to mounting in the AFM cell.

The mica-coated QCM-D sensors, covered with the sample, were attached to Teflon-coated (BYTAC, NORTON, OH) metal disks using double-sided tape (TESA, Hamburg, Germany) and installed on the AFM scanner. The AFM was equilibrated for 5−15 min prior to imaging.

Images were recorded in constant force contact mode at scanning rates of 4−8 Hz and a scan angle of 90°. Images were first-order plane-fitted and subsequently zero-order flattened.

Results and Discussion

Formation of Supported Lipid Bilayers (SLBs) on Mica-Coated QCM-D Sensors. To investigate the feasibility of quantitative QCM-D on mica-coated sensors, we selected as model system the formation of SLBs from SUVs made of DOPC and DOPS, a system that has been well characterized by AFM on mica[6] and by QCM-D on silica.[12]

Figure 2 demonstrates that the process of SLB formation on mica can be followed by QCM-D at several overtones (15, 25, and 35 MHz). Frequency and dissipation reveal a two-phase behavior, reflecting the initial adsorption of intact vesicles followed by the formation of an SLB. The final frequency shift, $\Delta f = -25 \pm 1$ Hz, was similar for all lipid mixtures investigated and matches values previously obtained on silica for lipid mixtures containing less than 50% DOPS.[12] Low final dissipation shifts ($\Delta D < 0.2\cdot10^{-6}$) witness a good quality of the bilayer.[16]

A bilayer could easily be formed with SUVs containing an amount of DOPS as high as 67% (Figure 2B) or 80% (data not shown). SLB formation on silica at such high vesicle charge was not achieved, hampered by phenomena of restructuration.[12] A detailed investigation of the influence of the support on the SLB formation is beyond the scope of this paper and will be reported elsewhere.

Stability, Sensitivity, and Reliability of QCM-D Measurements on Mica-Coated Sensors. Previous attempts to develop mica-coated sensors for QCM, when applied in liquid, resulted in limited stability and did not allow reliable quantitative investigations.[41] In addition, well-resolved responses could only be obtained at one frequency.[38−40]

The experimental data shown in Figure 2 are exemplary for the stability, sensitivity, and reliability that can be obtained with the applied procedure of mica deposition: after about 5 min of equilibration, a stability of better than 1 Hz/hour ($0.3\cdot10^{-6}$/hour) in frequency (dissipation) is reached; noise levels are around 0.2 Hz ($0.05\cdot10^{-6}$), which is similar to noise levels recorded for silica-coated sensors; final frequency and dissipation shifts are as expected for an SLB.[12,16]

In our initial attempts, however, we observed deviations from the expected QCM-D responses, such as variations in the frequency and dissipation shifts for the formation of an SLB. Indications of limited stability and sensitivity can still be seen for the 7th (3rd) overtone in Figure 2A (2B). This demonstrates that the very high load of the mica−glue compound (several micrometers thick) or its heterogeneous structure may perturb the QCM-D signal. The mica preparation procedure, in particular the steps involving mica cleavage (cf. Figure 1), turned out to be critical to obtain measurements of high quality and reliability.

Criteria of Reliability of a QCM-D Measurement on Mica. To establish an objective assessment of the reliability of a measurement, we evaluated how several parameters accessible by QCM-D were influenced by subtle variations in the deposition of the glue−mica compound (Table 1). These parameters were assessed by measuring changes in the QCM-D response upon application of the mica coating and upon application of the buffer solution.

(1) Application of the Glue−Mica Compound. The changes in frequency, $\Delta f^{\text{air-mica}}$, and dissipation, $\Delta D^{\text{air-mica}}$, associated with the application of the mica sheet were recorded. Reliable measurements showed frequency changes of $\Delta f^{\text{air-mica}}$ in the range of 5−50 kHz, which gives an estimate[44] for the maximum thickness of the mica layer of around 3 μm. $\Delta D^{\text{air-mica}}$ ranged from $5-50\cdot10^{-6}$. This is low with respect to the elevated change in frequency,[28] indicating that the glue−mica compound behaves as a rigid mass. Direct observation of characteristic color changes of the mica sheets[45] provided an independent evaluation of the thickness and confirmed the value of several micrometers obtained by QCM-D. In addition, this optical effect also allowed detection of steps in the mica cleavage plane as well as areas devoid of mica. Reliable measurements showed either no step or only few small steps. In contrast, thicker mica layers and layers showing

(44) The use of the Sauerbrey relation[43] is justified given the low dissipation changes. A frequency change of 50 kHz corresponds to an adsorbed mass of 885 μg cm^{-2}. Assuming the density of mica of 2.8 g cm^{-3}, this gives a thickness of around 3 μm. The glue layer contributed to less than 5 kHz to the frequency response, as measured after removing all mica from the QCM-D sensor. This corresponds to a thickness of less than 1 μm assuming a density of the glue of 1 g cm^{-3}.

(45) Israelachvili, J. N. *J. Coll. Int. Sc.* **1973**, *44*, 259−272.

large steps in the mica surface usually produced measurements of limited quality.

(2) Application of the Buffer Solution. The changes in frequency, $\Delta f^{\text{mica-buffer}}$, and dissipation, $\Delta D^{\text{mica-buffer}}$, resulting from the application of the buffer solution on the mica-coated sensors were analyzed. Reliable measurements showed variations in $\Delta f_n^{\text{mica-buffer}}/\sqrt{n}$ from −670 to −830 Hz and in $\Delta D_n^{\text{mica-buffer}}\sqrt{n}$ from 270 to $310 \cdot 10^{-6}$. These values are close to theoretical values[47] of $\Delta f_n^{\text{mica-buffer}}/\sqrt{n} = -675 \pm 10$ Hz and $\Delta D_n^{\text{mica-buffer}} \cdot \sqrt{n} = 268 \pm 10 \cdot 10^{-6}$, expected for the viscous response induced when a rigid support is exposed to buffer.[46,48] The error margins are though rather high, with negative (positive) deviations of up to 25% (15%) for f (D). The origin of these deviations is at present not clear. With the data currently available, no direct correlation between $\Delta f^{\text{air-mica}}$, $\Delta D^{\text{air-mica}}$, $\Delta f^{\text{mica-buffer}}$, and $\Delta D^{\text{mica-buffer}}$ could be established. This indicates that the variations are not due to a systematic influence of the thickness of the mica−glue compound on the responses in $\Delta f^{\text{mica-buffer}}$ and $\Delta D^{\text{mica-buffer}}$. Instead, we speculate that minor stresses in the glue−mica compound may be released upon application of the solution thus changing the "baseline".

The long-term stability of the signal was in best cases within instrumental error (<1 Hz/hour), indicating that the glue−mica compound was stable against water uptake or dissolution. Drifts observed in particular cases are thus likely to be attributed to stress-release or the formation of cleavage planes in the glue−mica compound.

Taken together, 9 out of 25 measurements showed to be reliable, that is, (i) the mica sheet completely covered the central part of the sensor (6-mm diameter), (ii) at least two overtones showed sufficient stability ($|\Delta f/t| < 5$ Hz/h, $|\Delta D/t| < 1 \cdot 10^{-6}$/h), and (iii) they exhibited the expected final shifts in frequency ($\Delta f = -25 \pm 1$ Hz) and dissipation ($\Delta D < 0.3 \cdot 10^{-6}$) for the formation of an SLB. All nine reliable measurements showed the acceptable characteristics given in Table 1 for at least two overtones and only one false positive was observed, demonstrating the validity of the criteria. Out of the last 10 measurements, 8 were reliable demonstrating the success of the mica deposition method. We emphasize that the possibility to record frequency and dissipation at several overtones is of high value to assess the reliability of the measurements.

The changes in f and D observed upon application of the mica and the buffer solution suggest that a properly prepared mica−glue compound, despite its thickness of several micrometers, does not perturb the QCM-D response to interfacial processes, that is, it behaves like a rigid mass. In consequence, this indicates that measured changes in f and D on mica supports can be interpreted in the same way as on silica or other commonly used surfaces.

Combining QCM-D and AFM on the Same Sample. To demonstrate the potential of combined measurements by QCM-D and AFM on mica, we studied the adsorption of the protein annexin A5 to SLBs made of DOPC/DOPS. Annexin has the potential to crystallize in two dimensions and the conditions for crystallization have been characterized before.[3,7]

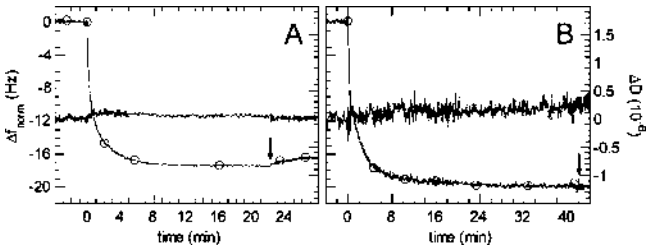

Figure 3. QCM-D response for the adsorption of annexin A5 on SLBs of different lipid composition: (A) DOPC/DOPS (1:1) in 200 μM calcium. (B) DOPC/DOPS (1:4) in 2 mM calcium. Changes in frequency (−○−) and dissipation (---) are shown at 25 MHz. Arrows indicate rinses with buffer.

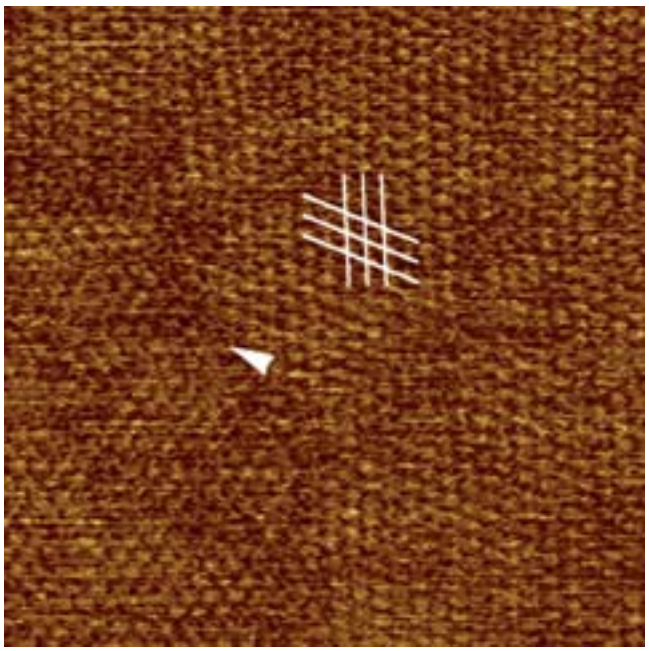

Figure 4. AFM image on a central area of the mica-coated QCM-D sensor after adsorption of annexin A5 (same experiment as in Figure 3B). Image size (z-limit): 250 nm (1 nm). A layer of p3-crystals covers entirely the surface. Grain boundaries (arrowhead) and the lattice (white lines) can be discerned.

The adsorption curves for annexin A5 on SLBs containing different amounts of DOPS (50% and 80%) (Figure 3) show monotonic kinetics (in frequency). The proteins remain stably bound after removing excess proteins from solution. The dissipation remains almost unchanged ($\Delta D < 0.1 \cdot 10^{-6}$) throughout the entire adsorption process, suggesting a tight association of the protein with the SLB.

Observation of the protein films by AFM immediately after adsorption in the QCM-D chamber—Figure 4 shows a representative image of the central area on the QCM-D sensor—allows a direct correlation with the QCM-D response. DOPC/DOPS−SLBs were completely covered by 2D crystalline assemblies. The assemblies could be identified as the p3 (Figure 4) or the p6 (not shown) crystal forms of annexin A5.[7,8] The AFM-images demonstrate thus that the final frequency shifts measured by QCM-D can be attributed to a complete layer of crystallized proteins.

Since the packing of the proteins in the crystals[49,50] and the protein molecular weight are known, the system allows

(46) Rodahl, M.; Kasemo, B. *Sens. Actuators, A* **1996**, *54*, 448−456.

(47) The changes in frequency and dissipation are given by $\Delta f = -c\sqrt{n{f_0}^3\rho_l\eta_l}$ and $\Delta D = 2c\sqrt{f_0\rho_1\eta_1/n}$ ($c = 0.64 \cdot 10^{-7}$ m^2 s kg^{-1} is a material constant, n the overtone number, $f_0 = 5$ MHz the fundamental frequency).[46] The given values were obtained by assuming a density and a viscosity of the liquid of $\rho_l = 1.0$ g cm^{-3} and $\eta_l = 8.9 \cdot 10^{-3}$ N s m^{-2}, respectively.

(48) Kanazawa, K. K.; Gordon, J. G., III. *Anal. Chem.* **1985**, *57*, 1770−1771.

(49) Oling, F.; Sopkova-De Oliveira Santos, J.; Govorukhina, N.; Mazères-Dubut, C.; Bergsma-Schutter, W.; Oostergetel, G.; Keegstra, W.; Lambert, O.; Lewit-Bentley, A.; Brisson, A. *J. Mol. Biol.* **2000**, *304*, 561−573.

(50) Oling, F.; Bergsma-Schutter, W.; Brisson, A. *J. Struct. Biol.* **2001**, *133*, 55−63.

Table 2. Dry and Wet Mass of 2D Crystalline Layers of Annexin A5

plane group symmetry	p6	p3	
Δf^b	-17.8 ± 1	-19.0 ± 1	Hz
ΔD^b	0.1 ± 0.1	0.1 ± 0.1	10^{-6}
$m_{QCM-D}{}^a$	315 ± 18	336 ± 18	ng·cm^{-2}
unit cell dimensions			
$A = b$	17.7[c]	9.4 ± 0.04[d]	nm
γ	120[c]	120[d]	deg
proteins per unit cell	9[c]	3[d]	
M_w		35.6	kDa
$m_{protein}$	196 ± 3	232 ± 4	ng·cm^{-2}
m_{H_2O}	119 ± 21	104 ± 22	ng·cm^{-2}
m_{H_2O}/m_{QCM-D}	38 ± 5	31 ± 5	%
d[e]	2.5 ± 0.3	2.8 ± 0.3	nm

[a] Calculated from ref 43. [b] Averaged over 2−3 measurements. [c] From ref 50. [d] From ref 49. [e] The density of proteins and buffer solution were 1.35 g cm^{-3} and 1.00 g cm^{-3}, respectively.

a direct determination of the water content and its contribution to the QCM-D signal (Table 2). A comparison of the dry mass per area, $m_{Protein}$, with the wet masses obtained by QCM-D, m_{QCM-D}, gives a solvent content (an effective thickness) of $38 \pm 5\%$ and $31 \pm 5\%$ ($d = 2.5 \pm 0.3$ nm and $d = 2.8 \pm 0.3$ nm) for the p6 and p3 lattices of annexin A5, respectively.

Remarkably, the solvent content is at the lower limit of previously reported estimates for globular proteins. For comparison, albumin and ferritin both adsorbing at submonolayer coverage on a solid support showed ∼43%[51] and ∼56%[52] of solvent content, respectively. For streptavidin, coupled to an SLB containing lipids with a CAP-biotin linker, a solvent content of ∼55%[32] was reported. We thus tentatively attribute the low solvent content observed for the annexin A5 layers to its dense 2D crystalline packings together with the tight association of annexin A5 to the membrane. The mass fraction of the solvent of a 3D crystal[53] of annexin A5 (∼43%[54]) is larger than the solvent content for the equivalent p3-crystal obtained by QCM-D ($31 \pm 5\%$). However, as the proteins in the 3D crystal form parallel sheets that are separated by a solvent layer of approximately 0.8 nm (as estimated from the 3D structure), the effective solvent content of the protein sheets is ∼31%, in agreement with the QCM-D results.

Conclusion and Perspectives

We show here that thin mica sheets can be deposited (glued) on QCM-D sensors, allowing measurements with high stability and sensitivity giving reliable quantitative information. On the basis of frequency and dissipation measurements at multiple overtones, criteria are identified which allow to characterize the quality of the mica−glue compound and to predict the reliability of a particular measurement.

With this development, the analysis of adsorption processes via the combined use of QCM-D and AFM, on identical surfaces, becomes feasible. Enabling more quantitative approaches in the study of processes of adsorption and self-assembly, such as SLB-formation and protein 2D crystallization, this is expected to give valuable new insight in their kinetics and their driving forces. An example is presented here with the monitoring of the 2D crystallization of proteins.

Improvement in the deposition of mica (in particular a better control of the mica cleavage) is expected to further increase the throughput and the reliability of QCM-D experiments on mica surfaces. Similar approaches may be pursued for other materials that can be applied (glued) as thin layers.[55,56]

Acknowledgment. Discussions with Johan Stålgren (Stanford), Kaoru Tamada (Riken, Japan), and Bernard Gauthier-Manuel (Besancon, France) on the mica deposition, with Michael Rodahl (Q-Sense, Sweden) on aspects of data interpretation as well as with Bernard Gallois and Thierry Granier (University Bordeaux I) on annexin A5 crystal structure are acknowledged. Ralf Richter is the recipient of a Ph.D. fellowship of the Conseil Régional d'Aquitaine, France. This research was supported by the Conseil Régional d'Aquitaine, the Fonds Européen de Développement Régional, and EC grants QLK2-CT2001-01339 and QLG3-CT2001-00902.

LA049827N

(51) Höök, F.; Vörös, J.; Rodahl, M.; Kurrat, R.; Böni, P.; Ramsden, J. J.; Textor, M.; Spencer, N. D.; Tengvall, P.; Gold, J.; Kasemo, B. *Colloids Surf., B: Biointerfaces* **2002**, *24*, 155−170.

(52) Caruso, F.; Furlong, D. N.; Kingshott, P. *J. Colloid Interface Sci.* **1997**, *186*, 129−140.

(53) Swairjo, M. A.; Concha, N. O.; Kaetzel, M. A.; Dedman, J. R.; Seaton, B. A. *Nat. Struct. Biol.* **1995**, *2*, 968−974.

(54) The reported Matthew coefficient, $M_V = 2.5$ Å^3·Da^{-1} (PDB number 1A8A), gives a volume fraction of the solvent of 51%. Assuming a solvent density of 1.0 g·cm^{-3} and a protein density of 1.35 g·cm^{-3}, this corresponds to a mass fraction of 43%.

(55) Ehahoun, H.; Gabrielli, C.; Keddam, M.; Perrot, H.; Cetre, Y.; Diguet, L. *J. Electrochem. Soc.* **2001**, *148*, B333−B336.

(56) Bucur, R. V.; Carlsson, J.-O.; Mecea, V. M. *Sens. Actuators, B* **1996**, *37*, 91−95.

III. The formation of solid-supported lipid bilayers

The formation of supported lipid bilayers (SLBs) by spreading of (small) vesicles from solution has been pioneered about 20 years ago by the group of McConnell[51]. Recent years have seen considerable advances in the understanding of this self-organization process which will be outlined here.

III.1. The mechanism of SLB-formation

In order to satisfactorily describe the mechanism of SLB-formation, two critical steps in the formation of supported lipid bilayers need to be understood: (i) the adhesion and rupture of vesicles on the support and (ii) the evolution of the supported bilayer patches thus formed into a complete SLB. Some theoretical and experimental contributions reported to date, including our work, will be briefly discussed here. Scheme III.1 provides an overview of mechanisms of vesicle rupture that have been reported or suggested in literature.

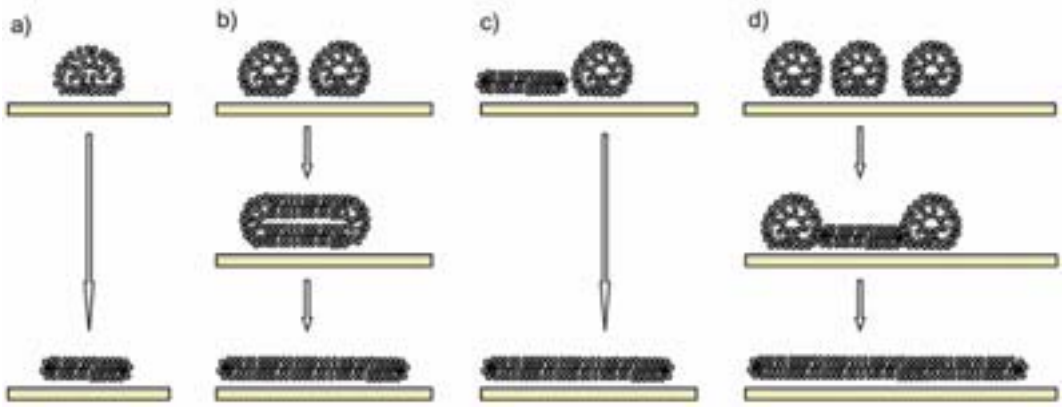

Scheme III.1 Mechanisms of vesicle rupture: (a) an isolated adsorbed vesicle ruptures spontaneously, driven by its support-induced deformation; (b) neighboring adsorbed vesicles fuse and eventually rupture; (c) the active edge of a supported bilayer patch induces the rupture of a neighboring vesicle; (d) the cooperative action of several neighboring vesicles leads to the rupture of a first vesicle (at the critical vesicular coverage). The active edge thereby exposed catalyzes the rupture of adjacent vesicles.

III.1.1. Adhesion and rupture of isolated vesicles

During the 90's Seifert and Lipowsky[44,47,303,304] developed a theory that considers the lipid bilayer as a thin (with respect to the bending radii) and flexible two-dimensional continuum embedded in three-dimensional space. Besides

considerable success in describing various shape changes of giant vesicles in solution, the theory also treated the adhesion and shape changes of isolated vesicles that encounter a surface[305]. Briefly, adhesion and deformation of the vesicle are determined by the balance between the gain in adhesion energy (as given by the adhesion area) and the cost in curvature energy (as given by the bilayer's bending rigidity). According to this model the adsorption behavior of vesicles should vary as a function of their size. In particular, adsorbed vesicles above a certain threshold size were predicted to rupture spontaneously (Scheme III.1a). In addition, neighboring vesicles that are too small to rupture individually may fuse into a larger vesicle which eventually ruptures (Scheme III.1b).

An AFM-study by Reviakine and Brisson[152], performed with egg-PC-vesicles on mica, indeed reported a clear size-dependence of the rupture propensity in calcium-free solution. The study also found indications for fusion events and thus provided support to the applicability of the model for small vesicles. It presents one of the rare examples of a quantitative treatment of the surface-induced rupture of small vesicles reported to date.

The predictions by Seifert and Lipowsky are, however, based solely on the comparison of the energies associated with the initial and final shapes. As considerable barriers may be associated to events like rupture and fusion, it is not straightforward to postulate that the shape-transitions towards the thermodynamically favorable shape will indeed take place within experimental time scales. It should furthermore be kept in mind that for small vesicles the bilayer thickness becomes comparable to its bending radius, limiting the applicability of the outlined continuum approach.

Indeed, the theory still lacks satisfactory application on other supports than mica. From the experimental data reported so far on titanium oxide[216], platinum[218] and silica[216] (see also Paper III) no clear evidence for fusion or for a size dependence of the deformation of vesicles[i] and their propensity to rupture could be found. While the experimental data available appear insufficient for a rigorous comparison with theory[ii], the results provide a first illustration of the important role of the solid support in the stability of adsorbed vesicles.

It should also be mentioned that a model has more recently been proposed by Zhdanov and Kasemo that treats the dynamics of vesicle rupture in terms of stress-induced fracture[306]. While its direct applicability to experimental data is limited, the model provides a rationale to include the influence of neighboring vesicles in the phenomenon of vesicle rupture. On the experimental side, evidence was found that the vesicle rupture is a thermally activated process[217,218].

---

[i] Reimhult et al.[216] actually found that the inner height (i.e., the total height decreased by the thickness of the incorporated lipid bilayers) of titanium-bound vesicles was proportional to the inner diameter of the corresponding free vesicle, suggesting that the surface-induced flattening is not dependent on vesicle size.

[ii] Paper III, the supplementary information of Paper IV and references [216,217,220] indicate promising model systems and experimental approaches to further investigate this question.

III.1.2. The critical vesicular coverage

An intriguing effect of the cooperative action of surface bound vesicles, which proved relevant for the conditions commonly employed to form SLBs, was reported by Keller and coworkers. Using a combination of QCM-D and SPR[215] together with computer simulations[307], the group could show (i) that isolated vesicles of egg-PC remain intact when bound to a silica support and (ii) that a certain surface density of vesicles was required in order to initiate the decomposition of surface-bound vesicles into bilayer patches. We will henceforward denote this density (and the effect) as the critical vesicular coverage. As QCM-D and SPR give average information about the adsorbed material, a small fraction of prematurely ruptured vesicles may potentially go undetected[216]. Our AFM-images in Paper III, however, provide direct evidence that silica wafers can indeed be covered with vesicles that remain stable for more than several hours, being devoid of bilayer patches over areas of several square micrometers.

If surface-bound vesicles do not move laterally - as seems the case on silica under some relevant conditions (discussed below and Paper III) - the interaction of the vesicles over long distances (i.e., more than several vesicle diameters) is considered unlikely. Consequently, the critical coverage is thought to originate from a *local* effect that involves a limited number of neighboring vesicles. Due to the statistic distribution of vesicles over the surface, this local effect, however, translates into an apparent critical coverage of the ensemble. The effect may be less localized under conditions that allow for the lateral rearrangement of surface-bound lipid material.

What is the nature of the effect that makes coverage a trigger for vesicle rupture? In the framework of the above-described interactions, we propose that the support-induced stress (or deformation) of an adsorbed vesicle is further enhanced by the adsorption of vesicles in its vicinity. When a certain local confinement of neighboring vesicles - corresponding to the critical coverage - is reached, the stress on the vesicle becomes sufficient to induce its rupture (Scheme III.1d). A similar mechanism was proposed earlier by Zhdanov and Kasemo[306]. They concluded that, for laterally mobile vesicles, an elevated coverage would be needed for such a mechanism to take effect (Scheme III.2b). Note that a high vesicular coverage may actually not be required, provided that the shape relaxation of two or more neighboring vesicles is constrained by their lateral immobilization (Scheme III.2a). Once one vesicle has ruptured, the rupture of neighboring vesicles is catalyzed by the active edge of the formed bilayer patch (see below). Our experimental findings related to the phenomenon of critical vesicular coverage are presented and further discussed in Papers III and IV.

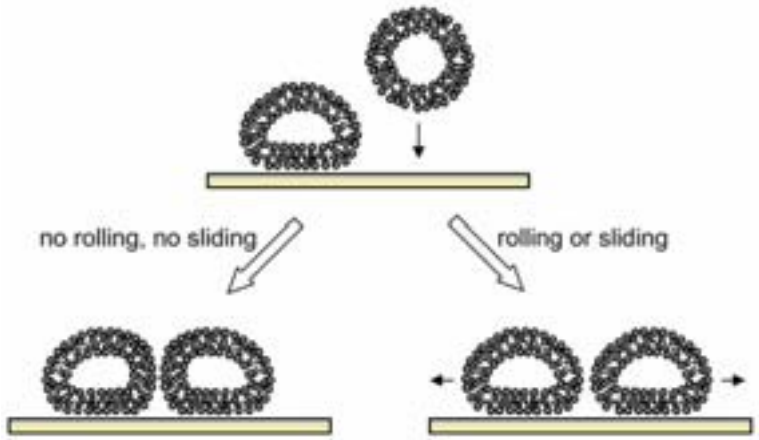

SCHEME III.2 Possible scenarios of the mutual interaction of neighboring vesicles. The surface-induced flattening of a newly adsorbing vesicle induces the deformation of a neighboring one. If sliding and rolling are inhibited (a), the deformation represents a persisting stress for the vesicles, and facilitates their rupture. Sliding or rolling along the surface can release the stress (b). Thus, if sliding or rolling is enabled, neighboring vesicles can only induce added stress (and thereby rupture) when a high overall packing of vesicles on the surface is attained.

III.1.3. Growth and coalescence of supported bilayers

Once a vesicle has ruptured, the resulting bilayer patch exposes an edge[308,309]. These edges are energetically unfavorable and, at least from a thermodynamic perspective, expected to promote the interaction with adjacent lipid material, such as the rupture of surface-bound vesicles (Scheme III.1c) or vesicles from solution. Provided the density of neighboring vesicles is sufficiently high, such a process can propagate in a cascade of rupture events across several neighboring vesicles leading to the formation of extended bilayer patches[307] (Paper III). On the same lines, adjacent bilayer patches are usually expected to coalesce in order to minimize the edge length[152] (Papers III and IV). Taken together, these effects increase the size of individual bilayer patches and the overall bilayer-coverage of the surface and will - in the ideal case - lead to a complete defect-free SLB.

The efficiency of the edge-induced processes relies strongly on the spatial arrangement of the bilayer patches and the vesicles. Paper IV illustrates that dynamic changes of the patch shape, enabled by the lateral mobility of lipid material on mica, can considerably influence the bilayer growth. As a detailed understanding of the (molecular) dynamics of edge-promoted processes is yet lacking, it appears difficult to set a limit on the maximum distance at which such effects can take place. In Paper III we show, however, that a vesicle can be situated as close as a few nanometers to the edge without getting ruptured, suggesting that the edge almost needs to contact a vesicle to induce its rupture.

In some cases the spatial arrangement of surface bound vesicles and bilayer patches may actually inhibit further propagation of the vesicle growth. For example, a vesicle that is located sufficiently distant from an edge to remain undisturbed may still prevent the encounter of other vesicles from solution with the edge (Scheme III.3). Such a vesicle, trapped in a bilayer hole, will thus stop the further propagation of bilayer growth. From simple geometrical considerations such an effect would be expected to be more pronounced for larger vesicles.

Indeed, a considerable amount (~1% of surface coverage) of residual vesicles has been reported in the case of larger egg-PC-vesicles on silica[216], while close to ideal bilayers can be formed with SUVs (paper III).

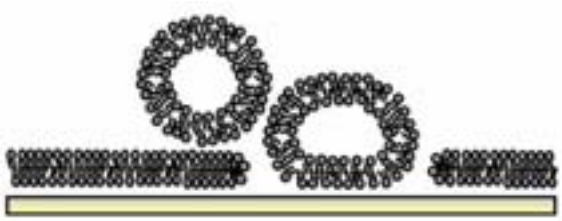

Scheme III.3 A "trapped" vesicle. The surface-bound vesicle is located sufficiently far away to remain unaffected by the bilayer edges though close enough to prevent the edge-induced rupture of other vesicles from solution. We propose such an arrangement to inhibit the further propagation of bilayer growth, leaving trapped vesicles as defects.

III.1.4. Lateral mobility of vesicles and bilayer patches

The lateral mobility and shape changes of surface-bound bilayers and vesicles (not to be confounded with the lateral diffusion of the lipid molecules) is of potential importance for several steps involved in the formation of SLBs. Effects can be expected for the phenomenon of critical vesicular coverage or for the fusion of surface-bound vesicles, as partly discussed above. Paper IV reports on the enhanced coalescence of bilayer patches induced by dynamic shape changes of the supported bilayer.

Using reflection interference contrast microscopy (RICM), Rädler et al.[52,310,311] observed that lipid bilayers, continuously formed from a deposited blob of concentrated DOPC in water, easily slide over surfaces of both mica and silica, while other hydrophilic surfaces (MgF_2) completely inhibited sliding. The kinetics of the sliding motion on mica could be described quantitatively by the shear flow of the thin water film that is sandwiched between the solid support and the bilayer[255,256] and a spreading coefficient of ~40 $\mu m^2/s$ was obtained[311].

The work by Rädler and coworkers demonstrates that the 2D mobility of surface-confined lipid assemblies can be high[312]. In strong contrast, we observed small vesicles and bilayer patches - formed from a mixture of DOPC and DOPS (molar ratio 4:1) in calcium-containing solution - to be entirely immobile on silica. Some mobility was retained on mica under otherwise identical conditions (c.f. Paper IV) or with egg-PC in magnesium-containing solution[147]. The kinetics of bilayer shape changes was, however, much slower than postulated from the action of a lubricating water film[147]. These discrepancies may in part be explained by the differences in the composition of the employed aqueous solutions, in particular, the pH (pure water usually has a pH around 6 while we used pH 7.4) and the presence of divalent ions. Indeed, Cremer and Boxer[313] reported a strong pH-dependence of bilayer spreading and found that spreading of PS-containing bilayers was facilitated (in the absence of divalent ions) as compared to PC-bilayers. The seemingly surprising range of variations in mobility illustrates the current lack in understanding of the coupling between the bilayer and the solid support.

The investigations by Rädler et al. gave rise to the idea that sliding-promoting (or "self-healing") surfaces should be ideal for the formation of defect–free SLBs[52,310]. In conjunction, it was found that surface-bound bilayer patches could increase in area by up to 6%[313] providing at least some material to cover defects[314]. Our results, however, indicate that close to perfect bilayers can also be obtained when bilayer patches and vesicles are virtually pinned to the surface (Paper III).

III.2. Pathways of vesicle deposition and SLB-formation

From the point of view of vesicle stability four main pathways of vesicle deposition can be identified (Scheme III.4). Adsorbed vesicles either (i) remain intact, giving rise to a supported vesicular layer (SVL) or rupture, (ii) spontaneously or (iii) after interaction with neighboring vesicles, in order to initiate the formation of an SLB. In a fourth scenario vesicles do not adsorb at all. Which pathway of vesicle deposition will be taken, is essentially determined by the interplay of bilayer-support, inter-bilayer and intra-bilayer interactions. In principle, the relative contribution of these interactions will be susceptible to the nature of the support (its surface charge, chemical composition, and roughness), the lipid vesicles (their composition, charge, size, and physical state), as well as the aqueous environment (the pH and ionic strength). In the following section the relative role of some of these parameters will be discussed.

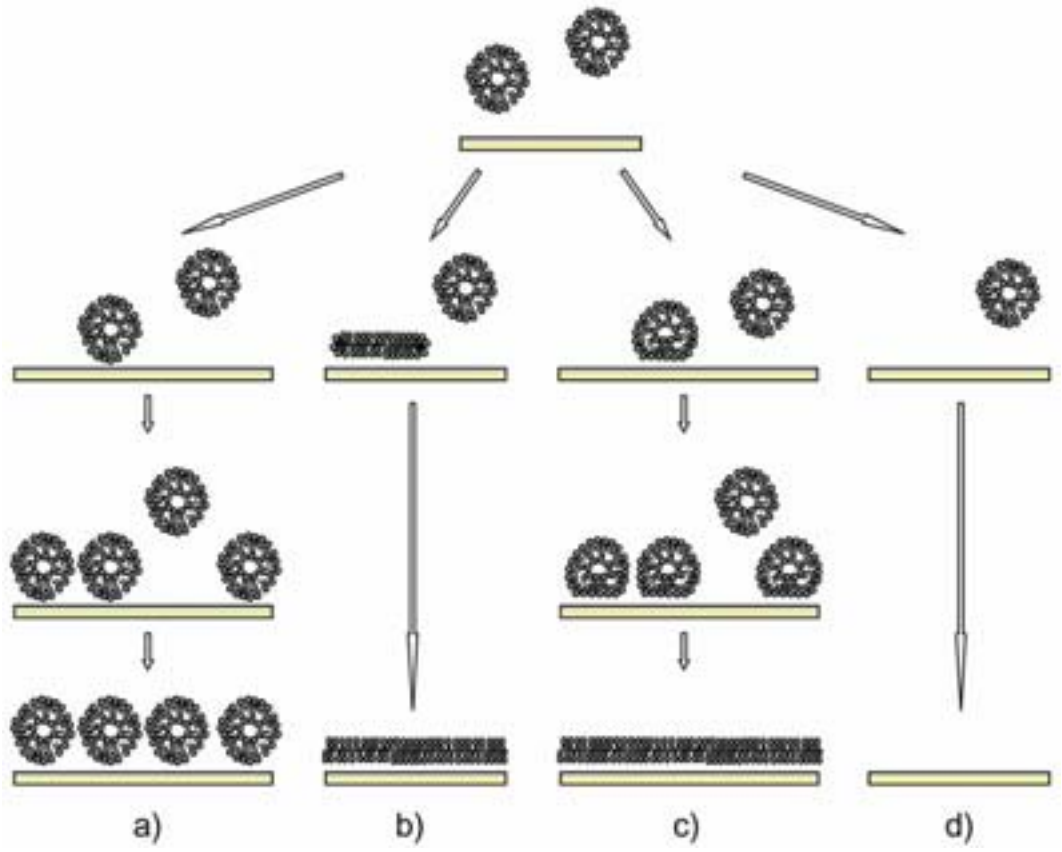

Scheme III.4 Pathways of vesicle deposition: (a) vesicles adsorb intact (SVL-formation); (b) adsorbed vesicles rupture spontaneously initiating SLB-formation; (c) vesicles rupture upon interaction with neighboring vesicles and trigger SLB-formation; (d) vesicles do not adsorb.

III.2.1. Electrostatic interactions

Several studies have pointed to the influence of the charge of support and lipids as well as the ionic strength of the solution on the adsorption of vesicles[91,310,313,315]. In particular, it was shown that the pH and the ionic strength of the solution[313] as

well as the vesicle charge[315] can be used to switch from the regime of SVL-formation to SLB-formation on glass. In systematic studies on silica and mica, reported in Papers III and IV, respectively, we provide evidence that all four pathways of vesicle deposition outlined in scheme III.4 can actually be generated by varying one experimental parameter only: the vesicle charge. These studies, yet mainly based on qualitative considerations, suggest that provided charges are present, the SLB-formation process will be strongly influenced by electrostatic interactions. Consequently, adjustments in the pH or the ionic strength are expected to constitute relatively simple means to optimize the formation of SLBs for a given surface and a given lipid composition.

It should be noted that the electrostatic interaction, usually considered long-range, becomes confined to only a few nanometers for the electrolyte concentrations (150 mM NaCl) used in our studies[iii]. Therefore, even the initial interactions between the support and the lipid vesicles or between two vesicles are likely to be influenced not only by mean electrostatic interactions and van der Waals forces (as described by the DLVO-theory[7]) but also by other short-range forces (such as steric interactions) and the discreteness of surface groups. This renders the microscopic picture of interactions involved in the adsorption process as well as a quantitative treatment of our data rather complex[iv].

III.2.2. The solid support

Probably being the most complex and most enigmatic parameter, the role of the solid support in the process of SLB-formation can not be underestimated.

Work on different supports has pointed out that hydrophilicity is a necessary but not a sufficient condition to promote the rupture of vesicles and subsequent SLB-formation. A number of reports has actually revealed difficulties to form SLBs on surfaces such as gold[69], TiO_2 or $SrTiO_2$[70,216] or platinum[218], leaving silicon-based materials, such as glass, Si_3N_4 or silica and mica as the most common surfaces used for the preparation of SLBs.

While surface roughness in general was shown to have considerable effects on the spreading of bilayers over solid supports[310,313], SLB-formation appears to be only little affected by roughness in the nanometer range, such as it is exhibited by the silica-coated QCM-D crystal (see Figure II.3, papers I and III)[v]. Also, no clear evidence has yet been found for a critical role of surface defects ("hot spots")[317] in the SLB-formation process. Although relatively little acknowledged in literature,

---

[iii] The Debye length, characteristic for the range of electrostatic interactions, is 0.8 nm for 150 mM NaCl[7].

[iv] Complementary measurements at lower ionic strength (and varied pH) may provide an attractive mean to investigate the role of electrostatic interactions quantitatively, as the electrostatic interactions become longer-ranged.

[v] It is remarkable that SLBs can even be formed on silica films exhibiting extreme roughness and porosity at the nanoscale, such as aerogels or xerogels, as recently shown[316]. Under such extreme conditions, however, the kinetics of SLB-formation and the quality of the final bilayer seem substantially affected.

the surface preparation may considerably influence the kinetics of lipid deposition and the nature of the lipid assembly that is ultimately formed (paper III). The hydroxylation state of silica surfaces, for example, can vary considerably, as a function of the manufacturing procedure, exposure to high temperature or to basic solutions[269]. As the hydroxylation influences the charge[318] and other physico-chemical properties of silica surfaces, it may affect the lipid deposition process.

The solid support has the appeal that it constitutes one of very few experimentally accessible parameters that affects only one variable in the interplay of bilayer-support, inter-bilayer and intra-bilayer interactions. Comparative approaches employing different surfaces under identical conditions can therefore be used to pin down the genuine influence of the solid support, both qualitatively and quantitatively, in the SLB-formation process[69,70,216,218]. In a pioneering study using QCM-D to monitor vesicle deposition, Keller et al.[69] demonstrated that SUVs of egg-PC remain intact on gold while they form SLBs on silica. Later, the same technique was used to correlate the tendency of rupture with the flattening of vesicles on various supports[216,218].

A systematic and comparative study of the SLB-formation on silica and mica, reported in Papers III and IV, enabled us to directly compare the influence of electrostatic interactions as well as the role of calcium in the bilayer-support interactions. The study illustrated that the role of the support can be rather complex, pointing out that appropriate future investigations will demand a better general understanding of processes at the solid-liquid interface down to the level of molecular interactions. In this context I will briefly compare the physico-chemical properties of mica and silica when immersed in aqueous solution. In particular, the charge of the employed surfaces is reviewed in more detail, giving credit to the recognized importance of electrostatic interactions.

III.2.3. Mica and silica in aqueous solution – a comparison

The combination of electrostatic interaction and van der Waals forces, as described by the DLVO-theory[7], is commonly considered to give a satisfactory description of the interactions between hydrophilic surfaces, such as mica and silica, at distances of more than a few nanometers[7]. A wealth of studies has though provided strong indications for substantial differences in how water and electrolytes interact with surfaces of mica[262,263,319] and silica[274,320,321]. While the nature of these interactions is still object of intense discussion (see references [274,321] and [4,322] for some different views) this has implications for the surface charge (and thus the magnitude of electrostatic interactions) as well as for short-range interactions (such as steric interactions) that are not covered by the DLVO-theory[7].

III.2.3.1. DLVO-forces

The high negative lattice charge (2.1 per nm^2) of mica is balanced by the interlayer potassium. Upon immersion in aqueous solution, the potassium ions dissociate and the surface charge becomes determined by the binding of other cations (H^+ or metal ions) from solution. Using SFA, Pashley and

Israelachvili[262,263,319] investigated the surface charge density, σ_0, and the surface potential, ψ_0, of mica as a function of the type of electrolyte. Ion adsorption could be described by a mass action model in which (hydrated) cations adsorb competitively to mica. These studies, experimentally limited to electrolyte concentrations of 10 mM and lower, revealed a detailed picture of the influence of the ionic strength, the valence of the cations and the pH on the surface charge. Values of σ_0 between -0.015 and -0.25 charges per nm^2 and of ψ_0 between 30 and 150 mV were obtained. Further electrophoretic measurements provided ζ-potentials in a similar range[149,323] (see the Appendix for a more detailed overview).

On silica, the surface charge originates from the deprotonation of the silanol groups. The point of zero charge of silica is around pH 2 [269]. The magnitude of the negative surface charge increases with increasing pH and with increasing concentration of (monovalent) electrolytes (see references [272-275] and the Appendix for a more detailed overview; surprisingly no (recent) data on the influence of multivalent ions on the silica charge was found). For illustration, close to physiological conditions (pH 7, 100 mM monovalent salt) a surface charge density of around -0.2 per nm^2 has been reported[272,275], corresponding to 5 % of ionized silanol groups. Note that even at high pH and ionic strength ionization is far from complete. Moreover, hydroxyl groups in partly dehydroxylated surfaces were found to be more acidic, giving rise to comparable or even higher surface charges despite the restricted number of ionization sites[269].

The surface charges reported for mica and silica are in the same range, suggesting that the experimental conditions (pH, electrolyte, surface preparation) may determine which of the surfaces is more charged. While a direct comparison by Toikka et al.[318] revealed a somewhat higher potential for silica at 0.2 mM NaCl and pH 5.8, they also noted substantial differences between different silica preparations. Furthermore, a few seconds of exposure of mica to air between cleavage and immersion in solution were found to substantially decrease the surface charge.

The van der Waals attraction on mica is larger than on silica. Non-retarded Hamaker constants of $A = 2 \cdot 10^{-20}$ J ($0.8 \cdot 10^{-20}$ J) have been reported for two surfaces of mica (silica) interacting in water[7].

III.2.3.2. Short-range interactions

In pure water, the DLVO-theory describes the interaction between two mica surfaces well down to zero separation[319]. The addition of electrolyte though leads to additional cation-type dependent repulsive forces at short range (nm)[262,263] which were interpreted as due to the adsorption of (hydrated) ions. These repulsive interactions become pronounced at NaCl-concentrations as low as 10 mM, while concentrations of $CaCl_2$ in the range of 1 M are needed to produce a similar effect. Also, divalent cations have been observed to resist rinsing when incubated at ≥ 100 mM [323,324].

For silica, repulsive non-DLVO forces at nm-separation have been observed even in pure water. While some experimental work indicates that the interfacial water adopts some degree of order[257,269,325] the forces were observed to decrease in the presence of monovalent ions[274], giving support to the (albeit controversial[4]) idea of hydration forces. For the interaction of small monovalent ions (such as Na^+, K^+) with silica, ion exchange seems to be prevalent as described by the classical theory of the electrostatic double layer[7,269]. Consequently, the adsorption of alkali metal ions varies little between species. Out of the divalent metal ions, calcium shows particular affinity to silica and coordinative binding to the silanol group has been invoked[269].

III.2.4. Other parameters

Without aiming for completeness, a number of additional parameters are listed below which have been shown to influence vesicle deposition and SLB-formation on solid supports.

Calcium ions: Divalent ions in general and calcium in particular appear notoriously surprising. The ions do not only participate in the screening of charges, thereby modifying the electrostatic interactions. They also directly interact, in often subtle ways, with surfaces and lipids[74,326]. As a general trend, calcium has been found to promote the adsorption and rupture of vesicles and SLB-formation[152,315,327]. Often minor concentrations (mM and below) of the ion are sufficient to generate significant effects. Illustrating examples of the role of calcium are presented and discussed in Papers III, IV and V.

Vesicle composition: Inhomogeneous lipid distributions and its effects on the process of SLB-formation have so far been little addressed. Papers IV and V demonstrate that, induced by the mica support and in conjunction with calcium, DOPS can be distributed asymmetrically between the two leaflets of an SLB that was formed from vesicles containing a mixture of DOPC and DOPS. Effects of the support on the charge distribution within the outer lipid leaflet of surface-bound giant vesicles (GUVs) have been reported earlier[305]. These findings suggest that the heterogeneous distribution of lipid species in SLBs may actually be more prominent than commonly appreciated.

Physical state of the vesicle: While most studies of bilayer formation were performed with fluid bilayers, the effect of cooling vesicles below the phase transition temperature has been investigated recently[220].

III.3. Persisting questions and perspectives

The above-given overview demonstrates that considerable advances have been made during the last decade in understanding the process of SLB-formation. In particular, a multitude of phenomena that are involved in the SLB-formation process have been uncovered and led to a qualitative understanding of the involved mechanisms. A number of issues, however, remain unsolved, some of which are outlined below:

- A better understanding of the interaction of vesicles with the solid support appears as one important objective for future work. The interest is fundamentally scientific on one hand, as described above. On the other hand, the improved understanding of surface-induced vesicle rupture may lead to improved protocols to form SLBs on supports other than mica, silica or glass, both of inorganic and organic nature, including approaches such as tethered[89], polymer-cushioned[64,72,90] or pore-spanning lipid bilayers[91,92].
- The differences in mobility of lipid assemblies on mica and on silica, reported in Papers III and IV, cannot be satisfactorily explained by the difference in roughness of these two supports. They illustrate the importance of understanding the nature of the thin solution layer that is sandwiched between the solid support and the lipid bilayer. Experimental approaches are desirable that allow for a quantitative comparison of the thickness and structural aspects of this layer. Elucidating the nature of the solution layer may also be the key to understand other subtle events, such as the 2D mobility of lipid molecules in the support facing monolayer or the asymmetric inter-leaflet distribution of lipids in mixed lipid systems (c.f. Paper V).
- Fusion of surface-bound vesicles, predicted by theory[44], has been suggested from experimental data on mica[152], but no clear evidence has so far been found on silica. It remains to be settled, under which conditions fusion can occur.
- A rigorous comparison between theory and experiment requires quantitative data. The studies outlined in Papers II, III and IV provide a multitude of experimental model systems together with the technical know-how to approach the questions of SLB-formation in a more quantitative manner. For example, a combination of QCM-D and AFM (and optical techniques) can provide reliable measurements of the quantifications of the critical vesicular coverage. Furthermore, the size and to some extent the shape of small surface bound vesicles can be determined from AFM data, allowing the flattening of single vesicles to be quantified. Transmission electron cryo-microscopy (Cryo-TEM) on nanoparticles may provide a complementary approach to address this question.
- Currently, little is known about the molecular mechanisms underlying the rupture of vesicles. This is illustrated by the fact that debate persists about the orientation (or sidedness) of the leaflets of a surface-bound bilayer patch as compared to their orientation in the original vesicle[153,328,329]. Settling this question may allow further conclusions about rupture mechanisms to be

drawn. It should be noted that the sidedness may vary depending on the type of rupture mechanism involved.

- A question that has as yet received little attention concerns the role of lipid transfer from the bulk to the surface and vice versa[236,252] in the final phase of SLB-formation. Two scenarios may rationalize the relevance of this issue. (i) The critical vesicular coverage for SLB-formation can be high, corresponding to a rather dense packing of vesicles. In comparison, rather simple geometrical considerations and recent experimental results[252] suggest that the lipid mass contained in a densely packed layer of vesicles may exceed what is needed to form an SLB. Thus, given appropriate conditions, lipid material would need to leave the surface in the final phase of SLB-formation. (ii) On the other hand, under the conditions reported so far for silica (c.f. paper III and ref. [215]), the SLB-formation does not go to completion, when removing the vesicles from solution after the critical vesicular coverage is reached. This indicates that the critical vesicular coverage alone is not sufficient to accomplish the formation of an SLB, but that the presence of lipid material in solution is also required.

Paper III

Ralf Richter, Anneke Mukhopadhyay and Alain Brisson

Pathways of lipid vesicle deposition on solid surfaces: a combined QCM-D and AFM study.

Biophysical Journal, **85** (2003), p. 3035-3047

Pathways of Lipid Vesicle Deposition on Solid Surfaces: A Combined QCM-D and AFM Study

Ralf Richter,* Anneke Mukhopadhyay,† and Alain Brisson*

*Laboratoire d'Imagerie Moléculaire et Nano-Bio-Technologie, Institut Europeen de Chimie et Biologie, Université Bordeaux 1, 33607 Pessac Cedex, France; and †Department of Biophysical Chemistry, Groningen Biomolecular Sciences and Biotechnology Institute, University of Groningen, Nijenborgh 4, 9747 AG Groningen, The Netherlands

ABSTRACT Supported lipid bilayers (SLBs) are popular models of cell membranes with potential biotechnological applications, yet the mechanism of SLB formation is only partially understood. In this study, the adsorption and subsequent conformational changes of sonicated unilamellar vesicles on silica supports were investigated by quartz crystal microbalance with dissipation monitoring and atomic force microscopy, using mixtures of zwitterionic, negatively charged, and positively charged lipids, both in the presence and in the absence of Ca^{2+} ions. Four different pathways of vesicle deposition could be distinguished. Depending on their charge, vesicles i), did not adsorb; ii), formed a stable vesicular layer; or iii), decomposed into an SLB after adsorption at high critical coverage or iv), at low coverage. Calcium was shown to enhance the tendency of SLB formation for negatively charged and zwitterionic vesicles. The role of vesicle-support, interbilayer, and intrabilayer interactions in the formation of SLBs is discussed.

INTRODUCTION

Supported lipid bilayers (SLBs[1]) are popular as model systems for cell membranes (Watts et al., 1984, 1986; Sackmann, 1996; Salafsky et al., 1996) and are promising for future applications in diagnostic devices and biomimetics (Cornell et al., 1997; Reviakine et al., 1998; Bieri et al., 1999; Kung et al., 2000). The creation of SLBs by the spreading of lipid vesicles on hydrophilic supports, pioneered by McConnell's group (Watts et al., 1984; McConnell et al., 1986), is attractive because of its simplicity and reproducibility. Considerable work, both experimental (Nollert et al., 1995; Rädler et al., 1995; Keller and Kasemo, 1998; Cremer and Boxer, 1999; Jass et al., 2000; Keller et al., 2000; Reviakine and Brisson, 2000; Johnson et al., 2002; Reimhult et al., 2002a,b) and theoretical (Lipowsky and Seifert, 1991; Seifert, 1997; Zhdanov et al., 2000; Zhdanov and Kasemo, 2001), has been devoted to understanding the driving forces involved in the adsorption of vesicles from solution and in the mechanisms of SLB formation.

Using techniques such as fluorescence microscopy (Nollert et al., 1995; Cremer and Boxer, 1999; Johnson et al., 2002), quartz crystal microbalance with dissipation monitoring (QCM-D) (Keller and Kasemo, 1998; Reimhult et al., 2002b), and atomic force microscopy (AFM) (Reviakine and Brisson, 2000), it has been established that vesicles made of PC lipids in the fluid phase form SLBs on silica, glass, or mica, whereas they do not rupture, forming stable supported vesicular layers (SVLs) on other surfaces such as titanium oxide or gold. Several studies have pointed to the influence of electrostatic interactions in general and the vesicle charge in particular on SLB formation (Nollert et al., 1995; Rädler et al., 1995; Cremer and Boxer, 1999). It is also well established that calcium can induce aggregation of negatively charged vesicles in solution (Wilschut et al., 1981; Marcelja, 1992) and influence the SLB formation of charged and neutral lipids (McLaughlin et al., 1978; Nollert et al., 1995; Reviakine and Brisson, 2000; Ekeroth et al., 2002) or the lipid domain distribution in SLBs (Reviakine et al., 2000). Although a clearer picture of the intermediates involved in SLB formation is emerging from recent studies, a detailed description of the respective contribution of the vesicle-support, intervesicle, and intravesicle interactions is still lacking.

We report here on a systematic study of the influence of vesicle charge and calcium-EDTA balance on the process of vesicle adsorption and SLB formation on silica. In this study, we combined a surface-sensitive method with high time resolution, QCM-D, and an imaging method with high spatial resolution, AFM, to investigate the behavior of vesicles with varying net charges, from positively charged pure dioleoyltrimethylammonium-propane (DOTAP) to mixtures of neutral dioleoylphosphatidylcholine (DOPC) and negatively charged dioleoylphospatidylserine (DOPS).

QCM-D, providing information about the mass and the conformational changes of adsorbed material, has been shown to be a useful tool to study the formation of SLBs (Keller and Kasemo, 1998; Keller et al., 2000; Reimhult et al., 2002a,b). In particular, the concept of an elevated critical vesicular coverage required to induce the decomposition of adsorbed vesicles into bilayer patches originated from QCM-D studies (Keller et al., 2000; Zhdanov et al., 2000).

AFM allows investigating the morphology of single vesicles and isolated bilayer patches (Jass et al., 2000;

Submitted February 12, 2003, and accepted for publication May 21, 2003.

Address reprint requests to Alain Brisson, E-mail: a.brisson@iecb-polytechnique.u-bordeaux.fr.

[1]The term SLB is used in this work, in contrast with the terms supported phospholipid bilayer (SPB) (Reviakine and Brisson, 2000) and supported planar bilayer (SPB) (Liebau et al., 2001), because it is a generalization valid for all types of lipids and surfaces of various roughness.

0006-3495/03/11/3035/13 $2.00

Pignataro et al., 2000; Reviakine and Brisson, 2000; Muresan and Lee, 2001) and following the formation of SLBs (Reviakine and Brisson, 2000), providing structural details of the SLB formation process.

Using this combined approach of QCM-D and AFM, several qualitatively different pathways of vesicle adsorption and SLB formation have been identified and characterized, and are reported here.

MATERIALS AND METHODS

Materials

DOPC, DOPS, and DOTAP were purchased from Avanti Polar Lipids (Alabaster, AL). Lyophilized cholera toxin B-subunit pentamer (B5), polyethylene glycol (PEG; average molecular weight 8 kDa), and other chemicals were purchased from Sigma (St. Louis, MO). Ultrapure water with a resistivity of 18.2 MΩ was used, prepared with a Maxima system (USF ELGA, Trappes, France). QCM-D sensor crystals (5 MHz), reactively sputter-coated with 50 nm silicon oxide, were purchased from Q-SENSE (Gothenburg, Sweden). Plates of (11 × 11) mm^2 of silicon wafer were provided by the Commissariat à l'Energie Atomique (Grenoble, France).

Buffer preparation

A buffer (buffer A) made of 150 mM NaCl, 2 mM NaN_3, and 10 mM HEPES, pH 7.4, was prepared in ultrapure water. EDTA or $CaCl_2$ was added to buffer A at 2 mM (final concentrations), respectively, as indicated in the text.

Vesicle preparation

Lipids were dissolved in chloroform, mixed in desired amounts, dried under a stream of nitrogen followed by drying in a vacuum desiccator overnight, resuspended at 1–2 mg/mL final concentration, and vortexed in EDTA buffer. Lipid mixtures were homogenized by five cycles of freeze-thawing and subsequent vortexing. Small unilamellar vesicles (SUVs) were obtained by sonication with a tip sonicator (Misonix, Farmingdale, NY) operated in a pulsed mode at 30% duty cycle for 30 min with refrigeration, followed by centrifugation in an Eppendorf centrifuge (10 min at 16,000 × g) to remove titanium particles. SUV suspensions were stored at 4°C under nitrogen and used within two weeks. Before use, vesicle suspensions were diluted to 0.1 mg/mL. Lipid concentrations were deduced from the mass of the lipids dissolved and, if applicable, by phosphorus content determination (Rouser et al., 1975) of the final lipid suspensions. Errors of <10% were obtained.

Protein preparation

B5 was resuspended in ultrapure water at 1 mg protein per mL. Before use, the solution was diluted to 10 μg/mL in the buffer used in the concerned measurement.

Substrate preparation

The QCM-D sensor crystals and silicon wafers were cleaned by two cycles of exposure to 2% sodium dodecyl sulfate solution for 15 min, rinsing with ultrapure water, blow-drying with nitrogen, and exposure to ultraviolet (UV)/ozone for 10 min. For UV/ozone treatment, the substrates were placed in the vicinity of a mercury grid lamp (BHK, Claremont, CA), mounted into a home-built chamber and driven by a suitable power source (BHK). Ozone is produced from the oxygen present in ambient air by the emitted UV light of wavelength 185 nm. By this treatment, the surface is cleaned from traces of organic contaminants (Vig, 1987) and rendered hydrophilic (Keller and Kasemo, 1998). In addition, the treatment enforces the formation of a thin layer of silica on the silicon wafer (Vig, 1987). The chemical nature of the surface of the silica wafers is thus expected to be similar to the silica coat on the QCM-D sensor crystals. Cleaned substrates were stored in air. Before use, they were re-exposed to UV/ozone for 10 min.

Quartz crystal microbalance with dissipation monitoring

QCM-D measurements were performed with the Q-SENSE D300 system equipped with a QAFC 301 axial flow chamber (Q-SENSE), as described in detail elsewhere (Rodahl et al., 1995). Upon interaction of (soft) matter with the surface of a sensor crystal, changes in the resonance frequency, f, related to attached mass (including coupled water), and in the dissipation, D, related to frictional (viscous) losses in the adlayer are measured with a time resolution of better than 1 s.

Measurements were performed in exchange mode, i.e., a volume of ~0.5 mL of temperature-stabilized and degassed sample liquid was delivered to the chamber containing the sensor crystal (internal volume, 50 μL) to ensure a complete exchange of the liquid. Signal distortion (peaks of $|\Delta f| < 5$ Hz and $|\Delta D| < 0.6 \cdot 10^{-6}$ are commonly observed) upon flushing is limited to a few seconds. In this way, processes of adsorption and surface adlayer changes can be followed in situ while subsequently exposing different solutions to the surface. Measurement data for f and D were acquired at several harmonics (15, 25, and 35 MHz) simultaneously. All measurements were performed at a temperature of 24–25°C, to within 0.05 K.

If not stated otherwise, changes in dissipation and normalized frequency ($\Delta f_{norm} = f_n/n$, with n being the overtone number) of the third overtone (n = 3, i.e., 15 MHz) are presented here. Adsorbed masses, Δm, are deduced according to the Sauerbrey equation, $\Delta f_{norm} = -\Delta m/C$, with C = 17.7 ng cm^{-2} Hz^{-1}, valid for thin, rigid films coupled without friction to the sensor surface. The equation has been demonstrated to be valid for lipid bilayers on surfaces (Keller and Kasemo, 1998) and to slightly underestimate the mass of adsorbed, nonruptured SUVs (error in the order of 5% (Reimhult et al., 2002b)).

Atomic force microscopy

AFM measurements were performed in liquid using a Nanoscope VI-MultiMode (Veeco, Dourdan, France), equipped with a J-scanner (120 μm). The tapping-mode fluid cell was washed by sonication in successive baths of ethanol and ultrapure water, followed by extensive rinsing in ethanol and blow-drying in a stream of nitrogen.

Oxide-sharpened silicon nitride cantilevers with a nominal spring constant of 0.06 N/m (Digital Instruments, Santa Barbara, CA) were exposed to UV/ozone for 10 min, immersed in a 3% PEG solution for 1 h and extensively rinsed with buffer before mounting in the AFM cell.

Silicon wafers were attached to Teflon-coated metal disks (BYTAC, Norton, OH), using double-sided tape (TESA, Hamburg, Germany) and covered with buffer. Vesicle solutions were added in desired concentrations, incubated for desired times, extensively rinsed with buffer, and installed on the AFM scanner. The AFM was equilibrated for 30 min before imaging. For further incubation of vesicles, the AFM head was unmounted and subsequently remounted without disrupting the liquid film present on the wafer.

Images were acquired in tapping mode at a scanning rate of 1 Hz and a scan angle of 90°. A resonance frequency ~7 kHz was chosen with low free amplitude (0.3–0.4 V) and low load upon scanning. Images were flattened and plane-fitted except when otherwise stated.

Lipid structures such as surface-bound vesicles are known to be easily modified by interactions with the AFM tip (Jass et al., 2000; Reviakine and Brisson, 2000; Richter and Brisson, 2003). Images were recorded in tapping mode with PEG-modified tips as this setup was observed to show the smallest tip-sample interactions. The substrate of choice for the AFM studies

was the silica wafer because its flatness allows easy detection of objects in contrast to the rough QCM-D crystal surface (Richter and Brisson, 2003).

RESULTS

Pathways of vesicle deposition by QCM-D

Three basic types of QCM-D responses were obtained, depending on the lipid mixture used and the calcium-EDTA balance (Fig. 1).

Formation of a supported vesicular layer

Upon adsorption of SUVs made of DOPC and DOPS (molar ratio 1:1) in the presence of EDTA, the frequency decreases monotonically and equilibrates slowly at a level of $\Delta f_{fin} = -54 \pm 4$ Hz (Fig. 1 *A*). The dissipation increases and equilibrates at an elevated level of $\Delta D_{fin} = 2.9 \pm 0.3 \cdot 10^{-6}$. These Δf_{fin} and ΔD_{fin} values are representative of the formation of a flexible layer of vesicles, as reported previously by Keller and Kasemo (1998) for egg yolk phosphatidylcholine (egg-PC) on gold. f and D remain stable upon rinsing with buffer, indicating that the vesicles are adsorbed in a stable manner at timescales investigated here.

Formation of a continuous SLB: case 1

The QCM-D response observed when adsorbing SUVs made of DOPC/DOPS (molar ratio 4:1) in the presence of EDTA shows a two-phase process (Fig. 1 *B*). The initial phase is similar to the case described above. However, after reaching extremes, $\Delta f_{min} = -58$ Hz and $\Delta D_{max} = 2.4 \cdot 10^{-6}$, a second phase is observed, which is characterized by an increase of the frequency and a decrease of the dissipation, equilibrating at levels of $\Delta f_{fin} = -24.5$ Hz and $\Delta D_{fin} = 0.1 \cdot 10^{-6}$, respectively. This behavior is similar to a response previously reported for egg-PC on silica (Keller and Kasemo, 1998; Keller et al., 2000), which was interpreted as follows: the first phase reflects the adsorption of a vesicular layer of elevated coverage, Δf_{min} being a measure for the vesicular coverage; the second phase corresponds to the formation of a continuous SLB. The value of $\Delta f_{fin} = -24.5$ Hz corresponds to an adsorbed mass of 434 ng/cm^2. Taking into account the average molecular lipid weight and the lipid molecular area, this value supports the view of a continuous hydrated SLB (Keller and Kasemo, 1998).

If rinsing with buffer is performed before the expected minimum frequency, the Δf and ΔD signals remain constant (data not shown). In contrast, rinsing after the minimum frequency results in further increase of f and decrease of D, indicating ongoing vesicle decomposition (Keller et al., 2000) (data not shown).

To verify whether lipids covered the entire silica surface, the B5 protein was used as a reporter of accessible silica surface. Control experiments showed indeed that B5 is adsorbing onto silica at high coverage ($\Delta f = -15$ Hz, data not shown) as well as to mica but not to DOPC/DOPS SLBs (Reviakine and Brisson, 2000). No binding of B5 was detectable after formation of a DOPC/DOPS SLB (data not shown), indicating that the SLB was continuous.

Formation of a continuous SLB: case 2

Fig. 1 *C* shows the adsorption behavior of pure DOTAP SUVs in EDTA. Upon adsorption, the frequency decreases monotonically, reaching an equilibrium level of $\Delta f_{fin} = -20.5$ Hz. The dissipation shows a peak ($\Delta D_{max} = 0.6 \cdot 10^{-6}$) soon after the onset of adsorption (at $\Delta f = -12$ Hz) before equilibrating at a level of $\Delta D_{fin} = 0.2 \cdot 10^{-6}$. Further addition of B5 resulted in low amounts of adsorption ($|\Delta f| \leq 0.5$ Hz, data not shown), indicating that an SLB covered most of the surface, but local defects estimated to represent <5% of the surface subsisted.

For this response, not reported in the literature before, we propose the following interpretation: i), an SLB is formed, covering most of the surface, and ii), the onset of bilayer formation occurs at low surface coverage, in opposition to case 1, indicating that either adsorbed SUVs rupture spontaneously, or that only a few contacts between adsorbed

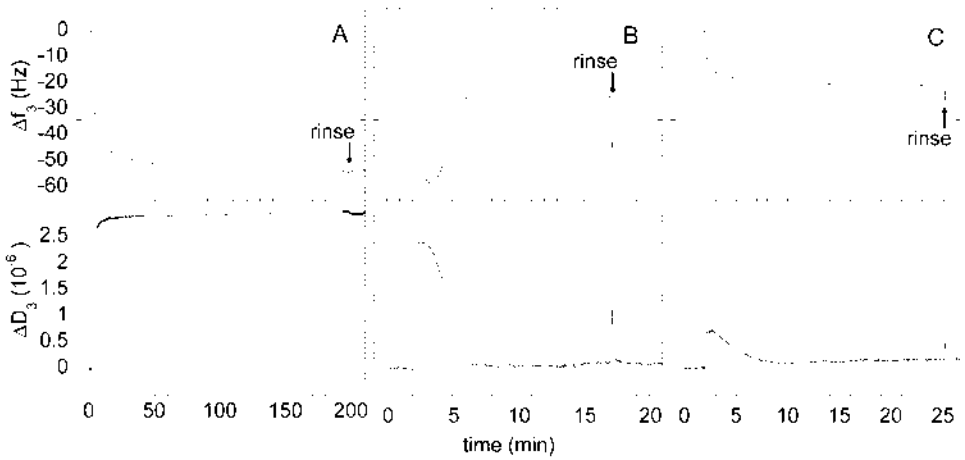

FIGURE 1 QCM-D responses for the deposition of different lipid mixtures on SiO_2 in the presence of 2 mM EDTA. Changes in frequency and dissipation at 15 MHz (*upper* and *lower panels*, respectively). (*A*) DOPC/DOPS (molar ratio increase 1:1), example of formation of an SVL. (*B*) DOPC/DOPS (4:1), example of SLB formation (case 1) triggered at an elevated critical vesicular coverage. (*C*) DOTAP, example of SLB formation (case 2) triggered at low vesicular coverage. Lipid exposure starts at 2 min; rinses with EDTA-containing buffer (*arrows*).

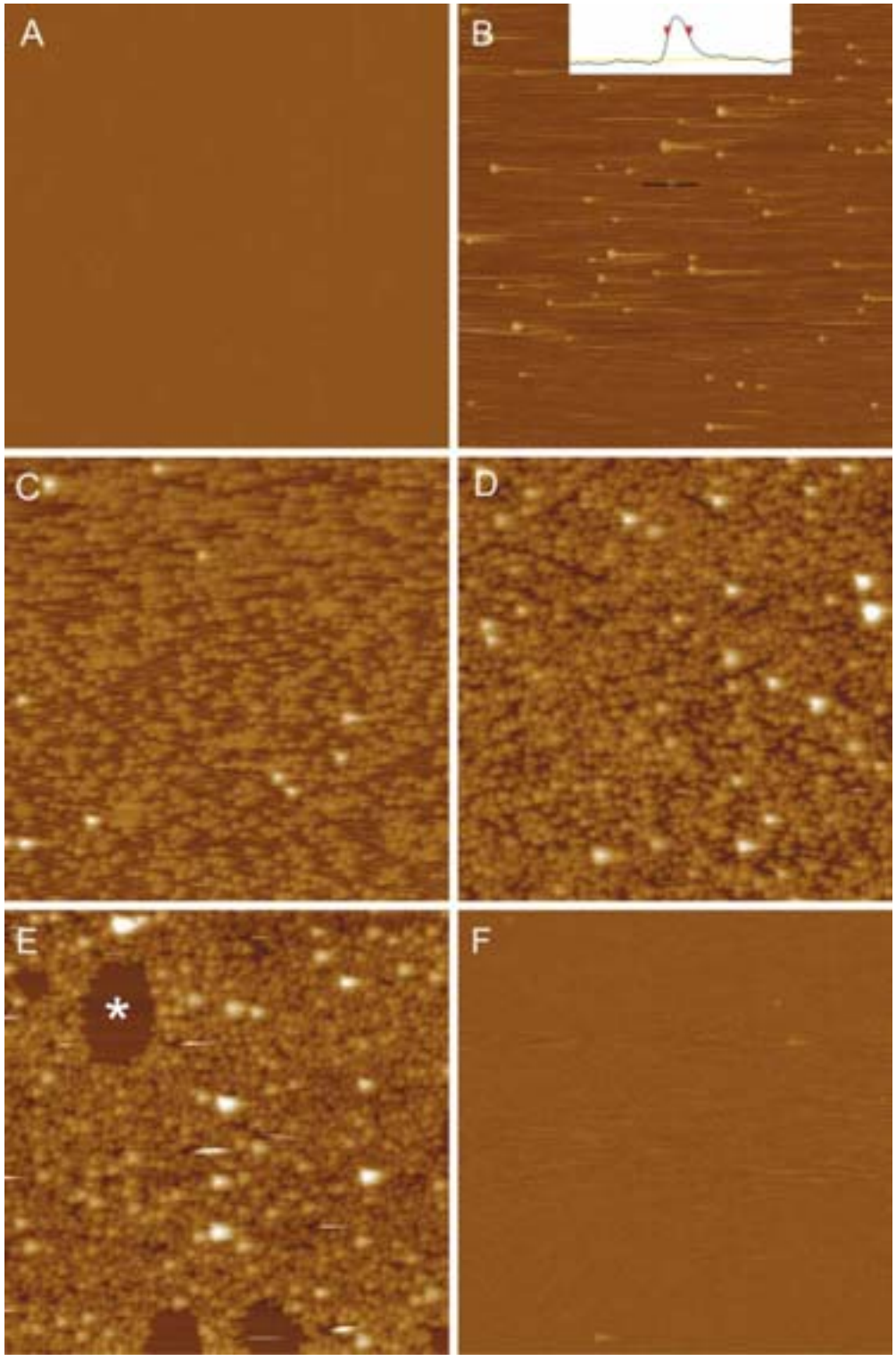

FIGURE 2 ''Snapshots'' of the SLB-formation process for DOPC/DOPS (4:1) on a silica wafer by AFM. The support was subsequently exposed to lipid concentrations (exposure time) of (*A*) 0 μg/mL (0 min), (*B*) 1 μg/mL (5 min), (*C*) 5 μg/mL (3 min) + 8 μg/mL (8 min), (*D*) 7 μg/mL (10 min) + 10 μg/mL (15 min), (*E*) 16 μg/mL (10 min), and (*F*) 25 μg/mL (10 min) before rinsing with buffer and imaging. To minimize the effect of tip artifacts, a new spot on the wafer was used for each AFM image. Image size (*z*-scale), 2 μm (50 nm). (*B*, *inset*) Cross section showing a circular object of 12-nm height and 25-nm width identified as an adsorbed vesicle. Tails along the scan direction are believed to be due to a combination of weak tip-sample interaction and low gains chosen for image acquisition. (*B–E*) Vesicular coverage increases. (*E*) At high coverage, bilayer patches (*asterisk*) are observed.

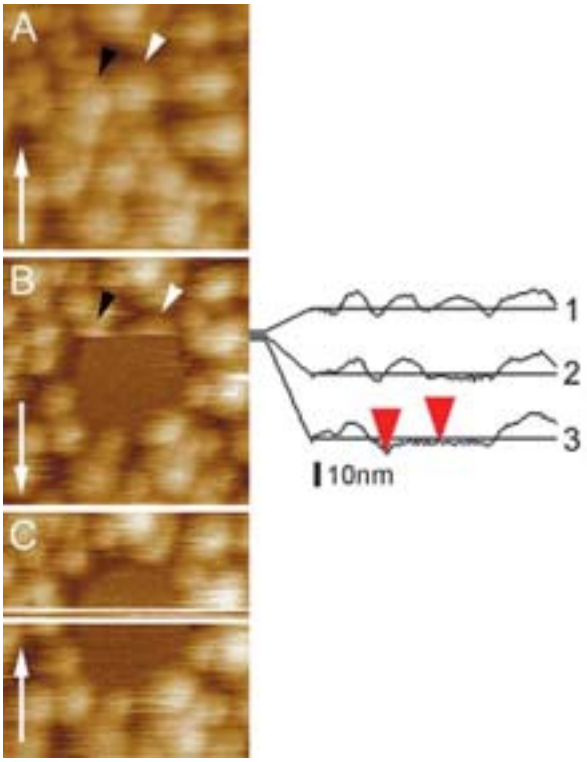

FIGURE 3 AFM images of an event of vesicle rupture and bilayer patch formation. The images were subsequently recorded on the same spot at a stage of bilayer formation of DOPC/DOPS (4:1) corresponding to Fig. 2 *D*. The slow scan direction is indicated (*arrows*). Fast scan direction from right to left. Image size (*z*-scale), 250 nm (40 nm). (*A*) First image, all vesicles are intact. (*B*) Second image, two vesicle segments are resolved (*arrowheads*) followed by a bilayer domain, indicating the rupture of vesicles. Cross sections of subsequent scan lines (*right*), the right vesicle (*white arrowhead*) is transformed into a bilayer patch induced by the AFM tip. The left vesicle next to it (*black arrowhead*) remains intact at scan line 2. At scan line 3, the left vesicle is ruptured, likely induced by the ''active edge'' of the bilayer patch originating from the vesicle ruptured first. The height between the red markers, 4.1 nm, corresponds to the thickness of a bilayer. (*C*) Third image, the rupture of single vesicles induced the transformation of adjacent vesicles into a stable bilayer patch. A small gap (a few nanometers) separates the patch edges from neighboring intact vesicles. A part of the image is distorted because the tip was accidentally retracted from the surface.

vesicles are necessary to induce the formation of bilayer patches.

Vesicle deposition and bilayer formation by AFM

Whereas QCM-D allows a global characterization of the vesicle deposition process with high temporal resolution, AFM was employed to provide information on the local organization of surface-bound lipid material. We focused on the two pathways that lead to SLB formation. ''Snapshots'' of the process of vesicle adsorption and SLB formation were recorded after adding SUV solutions of increasing concentration in a stepwise fashion. For practical reasons, calcium-containing buffer was used for these experiments.

Formation of a continuous SLB: case 1

A series of images obtained for vesicles of DOPC/DOPS (4:1) is shown in Fig. 2. Adsorbed SUVs are resolved as round objects with a minimum diameter of 20–25 nm and a minimum height of 12 nm, as previously described (Reviakine and Brisson, 2000). The vesicular coverage increased (Fig. 2, *B–D*) with increasing vesicle exposure. At an elevated coverage, flat patches appeared (*asterisk* in Fig. 2 *E*) and were determined to be supported bilayers (see below) that eventually formed a continuous defect-free bilayer (Fig. 2 *F*). The imaged lipid structures were stable and no lateral diffusion could be detected over the timescale of 1 h. Bilayer patches show predominantly convex but noncircular shapes. The size distribution of surface-bound vesicles did not change with increasing surface coverage, as evaluated by the eye.

Occasionally, the AFM tip was observed to induce the rupture of a vesicle (Fig. 3), which allowed us to access details of the process of SLB formation. As the vesicle decomposition is fast compared to the scan speed of the AFM, only a segment of the originally intact vesicle (*white arrowhead* in Fig. 3, *A* and *B*) was observed, whereas the rest was transformed into a bilayer (Jass et al., 2000). The rupture of a single vesicle induced the transformation of neighboring adsorbed vesicles into a bilayer patch (Fig. 3 *B*). The bilayer nature of the resulting patches is deduced from their homogeneous flatness and their height of ~4 nm. Bilayer patches corresponded in size to the merging of 5–50 immobilized vesicles, as determined by counting of the vesicles present before and after patch formation. Note that a small gap (a few nanometers) separates the patch edges from neighboring unruptured vesicles. A detailed analysis of the tip-induced vesicle decomposition event shown in Fig. 3 *B* provides further information on the process of rupture propagation. Considering that one vesicle (*white arrowhead*) is ruptured at the scan line shown in cross section 2, a second vesicle next to it (*black arrowhead*) remains intact at this scan line, whereas it is ruptured at the subsequent scan line (cross section 3). Similar images were found repeatedly, and, because tip-induced rupture events are extremely rare, we must conclude that the rupture of the second vesicle (*black arrowhead*) was induced by the rupture of the first vesicle (*white arrowhead*) within ~1 s, most likely due to the ''active edge'' effect. The fact that no larger vesicle could be detected by AFM in the vicinity of ruptured vesicles suggests that fusion between vesicles does not take place in this system.

Formation of a continuous SLB: case 2

A similar series of AFM images was recorded to follow the process of SLB formation with SUVs of DOTAP (Fig. 4). At low lipid coverage, flat patches with a height of ~4 nm are observed, as expected for bilayer patches. The smallest

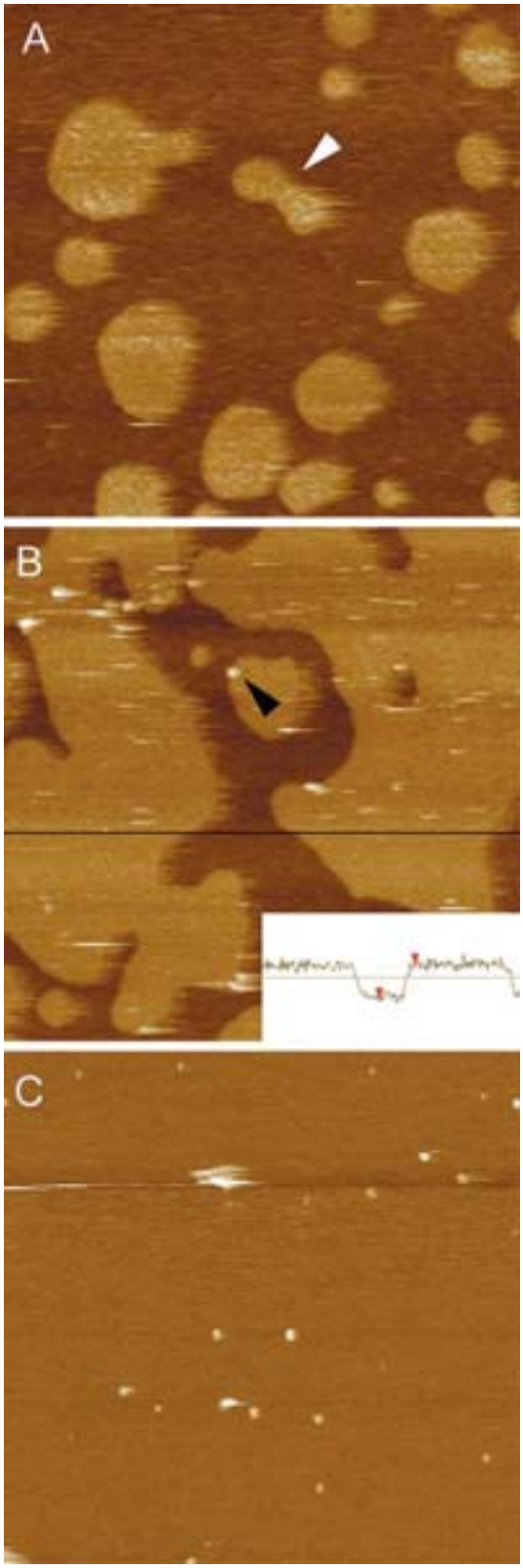

FIGURE 4 ''Snapshots'' of the SLB-formation process for DOTAP on a silica wafer. The support was subsequently exposed to lipid concentrations (exposure time) of (*A*) 1 μg/mL (4 min) + 2 μg/mL (20 min), (*B*) 5 μg/mL (6 min) + 8 μg/mL (20 min) + 25 μg/mL (20 min), and (*C*) 130 μg/mL (30 min) before rinsing with buffer and imaging. To minimize the effect of tip artifacts, a new spot on the wafer was used for each AFM image. Image size (*z*-scale), 1 μm (20 nm). (*B*) Flat domains with a height of ~4 nm (*inset*, height between red markers, 4.1 nm) identified as bilayer patches. (*A*) The dumbbell-like shape of a patch (*white arrowhead*) appears to be the result of two decomposed vesicles. With increasing coverage, domains merge (*A* and *B*) and eventually form a continuous bilayer (*C*). Elevated objects of ~20 nm diameter, initially observed predominantly at (*B*) the edges of growing patches (*black arrowhead*), remain upon completion of the SLB formation and are suggested to result from contaminations in the DOTAP solution.

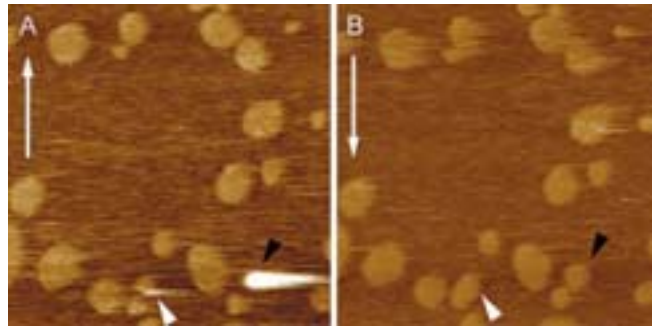

FIGURE 5 AFM images subsequently recorded on the same spot at an early stage of bilayer formation of DOTAP. The slow scan direction is indicated (*arrows*). Fast scan direction from left to right. Image size (*z*-scale), 1 μm (20 nm). (*A*) First image, vesicle segments (*white arrowhead*) indicate rupture induced by the AFM tip. Rarely, entire vesicles (*black arrowhead*) can be observed. (*B*) Second image, all vesicles have transformed into bilayer patches (*arrowheads*).

patches have a diameter of 40 nm, as expected for single ruptured SUVs. The diameter of the patches ranges from 40 nm to 250 nm, corresponding to approximate vesicle sizes of 25–125 nm. The size distribution is thus considerably larger as compared with DOPC/DOPS (4:1). Note the dumbbell-like shape of some bilayer patches (*arrowhead* in Fig. 4 *A*), which appears to be the result of two or more decomposed vesicles. The patch morphology was stable upon repeated imaging.

Bilayer patches coalesce with increasing vesicle exposure (Fig. 4, *A* and *B*) and finally form a film that entirely covers the surface (Fig. 4 *C*). A number of elevated objects of ~20 nm diameter, observed initially predominantly at the edges of growing patches (*arrowhead* in Fig. 4 *C*), remain when the SLB formation is complete. They do not diffuse and are stable upon enhanced forces exerted by the AFM tip. The fact that they are immobilized together with the lipids suggests that these defects result from contaminations in the DOTAP solution.

Occasionally, the presence of immobilized unruptured vesicles was detected at low lipid coverage (Fig. 5). Most of these vesicles could be visualized only in part (*white arrowheads* in Fig. 5 *A*)—despite exceptions (*black arrowhead* in Fig. 5 *A*)—and were transformed into a bilayer patch during the first scan, indicating a high susceptibility to interactions with the AFM tip. The fact that the AFM signal

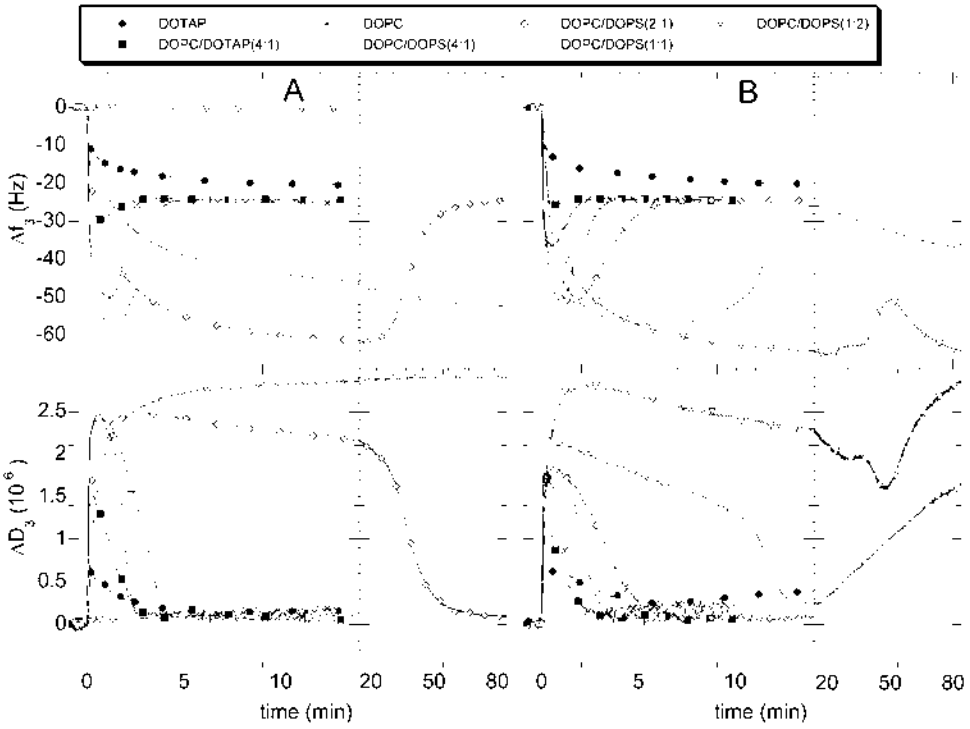

FIGURE 6 QCM-D response for the deposition of various lipid mixtures, indicated in the upper inset, on SiO_2 in the presence of 2 mM EDTA (*A*) and 2 mM $CaCl_2$ (*B*). Changes in frequency (*upper panel*) and dissipation (*lower panel*) are given for the third overtone (15 MHz). The timescale is split into two parts to allow representation of the complete deposition process for DOPC/DOPS (molar ratio 2:1 (*A*), 1:1 (*A* and *B*), and 1:2 (*B*)).

is highly sensitive to the presence of vesicle remnants and that most bilayer patches are devoid of any associated remnants indicates that the DOTAP vesicles rupture spontaneously before interaction with the tip.

Charge dependence of vesicle adsorption and SLB formation

The three pathways of vesicle deposition presented above reveal the influence of the charge of SUVs on the process of vesicle deposition and SLB formation. The effects of lipid composition and calcium-EDTA balance were then investigated in a systematic manner by QCM-D. The deposition of SUVs made of the lipid mixtures DOTAP, DOPC/DOTAP (molar ratio, 4:1), DOPC, and DOPC/DOPS (4:1, 2:1, 1:1, and 1:2) was followed both in the presence of the calcium chelator EDTA (Fig. 6 *A*) and in the presence of Ca^{2+} ions (Fig. 6 *B*). The results are summarized in Table 1.

In the presence of EDTA, SLB formation of case 1 was observed for pure DOPC and at low positive (DOPC/DOTAP (4:1)) and negative (DOPC/DOPS (4:1, 2:1)) vesicle charges. At high negative charge (DOPC/DOPS (1:2)), no adsorption was measurable over the time range of 2 h ($|\Delta f| < 1$ Hz, data not shown). This situation is herewith referred to as the fourth pathway.

In the presence of Ca^{2+} ions, bilayer formation was initiated for all lipid mixtures investigated (Fig. 6 *B*). Pure DOTAP showed SLB formation of case 2. For pure DOPC and mixtures with low content of charged lipids (DOPC/DOTAP (4:1)) and DOPC/DOPS (4:1, 2:1), the SLB was complete (case 1) and stable. At intermediate (DOPC/DOPS (1:1)) and high (DOPC/DOPS (1:2)) negative lipid charge, an additional process set in during SLB formation that we refer to as restructuration and describe hereafter.

In the case of bilayer formation of case 1, $|\Delta f_{min}|$ showed pronounced charge dependence (Fig. 7 *A*). $|\Delta f_{min}|$ increased when scanning from positive charge to negative charge, both with Ca^{2+} ions and with EDTA. At a given charge content, $|\Delta f_{min}|$ was smaller in the presence of Ca^{2+} ions. A final frequency shift of $\Delta f_{fin} = -24.5 \pm 0.5$ Hz ($n = 13$) was measured for all lipid mixtures studied, except for DOTAP and for conditions leading to restructuration (see below). The low value obtained with DOTAP ($\Delta f_{fin} = -20.5 \pm 0.5$ Hz, $n = 4$) could in part be attributed to an incomplete coverage of the silica surface, as described above. In addition, differences in molecular weight, surface area occupied per lipid molecule, or hydration of the lipid headgroup between DOTAP and either DOPC or DOPS are likely to explain remaining deviations.

Kinetics of initial vesicle adsorption and SLB formation

In terms of kinetics, two phases need to be distinguished: i), the initial adsorption of vesicles, and ii), vesicle adsorption and conformational changes at elevated surface coverage.

Kinetics of the initial adsorption of vesicles

In the presence of EDTA, lipid mixtures with positive (DOTAP, DOPC/DOTAP (4:1)), neutral (DOPC), and low

TABLE 1 Parameters measured by QCM-D for the deposition of vesicles with varying lipid composition

Lipid ratio			[Ca]	Δf_{min}	m_{max}	ΔD_{max}	Δf_{fin}	m_{fin}	ΔD_{fin}	t_{SLB}	Vesicle deposition
DOTAP	DOPC	DOPS	(mM)	(Hz)	(ng/cm^2)	(10^{-6})	(Hz)	(ng/cm^2)	(10^{-6})	(min)	pathway
1	-	-	0	-	-	0.8	−20.5	363	0.2	10	SLB (I)
1	4	-	0	−32	566	1.5	−24.5	434	0.1	3	SLB (II)
-	1	-	0	−52	920	2.4	−25	443	0.15	3	SLB (II)
-	4	1	0	−60	1062	2.4	−24.5	434	0.1	4.5	SLB (II)
-	2	1	0	−62	1097	2.5	−24.5	434	0.1	80	SLB (II)
-	1	1	0	−54	956	2.9	-	-	-	-	SVL
-	1	2	0	0	0	0	-	-	-	-	No adsorption
1	-	-	2	-	-	0.75	−20.5	363	0.35	11	SLB (I)
1	4	-	2	−26	460	1.4	−24.5	434	0.1	2	SLB (II)
-	1	-	2	−35	620	1.8	−24.5	434	0.2	2.6	SLB (II)
-	4	1	2	−51	903	2.3	−24.5	434	0.1	3.3	SLB (II)
-	2	1	2	−53	938	1.8	−24.5	434	0.1	8	SLB (II)
-	1	1	2	−59	1044	2.1	-	-	-	17*	SLB (II), restructuration
-	1	2	2	−65	1151	2.8	-	-	-	57*	SLB (II), restructuration

*Extrapolated estimates.

negative (DOPC/DOPS (4:1)) charge show similar initial adsorption rates. Kinetics slow down with increasing negative charge (DOPC/DOPS (2:1, 1:1)), and no adsorption is detected with DOPC/DOPS (1:2). A similar trend is observed in the presence of calcium, though the slowdown of kinetics is shifted toward higher negative-charge content. Considering the experimental setup chosen (essentially standing liquid), it is likely that adsorption is transport-controlled (Adamczyk et al., 1994) at net-positive, net-neutral, or low net-negative vesicle charge. The decreased rate of initial adsorption observed at high negative vesicle charge indicates that the adsorption becomes limited by an energy barrier. The barrier increases with increasing negative lipid charge and decreases in the presence of calcium.

Kinetics of SLB formation

Both in the presence of EDTA and in the presence of calcium, the time, t_{SLB}, needed to form an SLB is smallest for DOPC and DOPC/DOTAP(1:4) and increases with increasing negative vesicle charge (Fig. 7 *B*). For DOPC- or DOPS-containing mixtures, bilayer formation is faster in calcium than in EDTA. For high positive lipid charge (pure DOTAP), note the extended time with slow adsorption rate before equilibration (Fig. 6).

Reproducibility

In the initial stage of investigations related to this study, it turned out that the preparation of both surface and SUVs could critically influence the process of vesicle deposition. In particular, the tendency to form SLBs and the quality of formed bilayers as well as the onset and extent of restructuration (see below) varied considerably. Rigorously following the above-indicated preparation protocol, however, enabled us to obtain reproducible results. Variations indicated as error bars above are derived from two to three measurements performed with the same SUV solutions of varied age (some hours to two weeks).

Restructuration

An additional response, not reported in the literature before, was observed for SUVs with intermediate and high negative lipid charge (DOPC/DOPS (1:1, 1:2)) in the presence of Ca^{2+} ions. During SLB formation, the increase in frequency and the decrease in dissipation were followed by a slow decrease/increase in f and D, respectively. For DOPC/DOPS (1:2), this process sets in early, whereas for DOPC/DOPS (1:1) (Fig. 8, referred to hereafter) the onset is near the end of SLB formation. The dissipation change, corresponding with $\Delta D = 1.3 \cdot 10^{-6}$ per hour of this ongoing process, is high with respect to the frequency change, $\Delta f = -10$ Hz per hour, indicating the presence of lipid material deposited in a flexible state. The surface adlayer remained essentially stable upon rinsing with a calcium-containing buffer (see *arrow 1* in Fig. 8), though the dissipation continued to increase. In contrast, rinsing with EDTA (*arrow 2* in Fig. 8) had a striking effect. An instantaneous increase in dissipation by more than $1 \cdot 10^{-6}$ was followed by a quick increase/decrease in f and D, respectively. Further rinsing with calcium-containing buffer (*arrow 3* in Fig. 8) resulted in final values for frequency, $\Delta f_{fin} = -24$ Hz, and dissipation, $\Delta D_{fin} = 0.2 \cdot 10^{-6}$, which are characteristic of a complete SLB. The formed bilayer was stable upon re-exposure to calcium-containing buffer or lipids (data not shown).

To better understand this process, lipids present in solution were washed away shortly after the maximum/minimum dissipation and frequency, respectively (*dashed curves* in Fig. 8). An initial increase in f and decrease in D were observed, which is believed to reflect ongoing vesicle

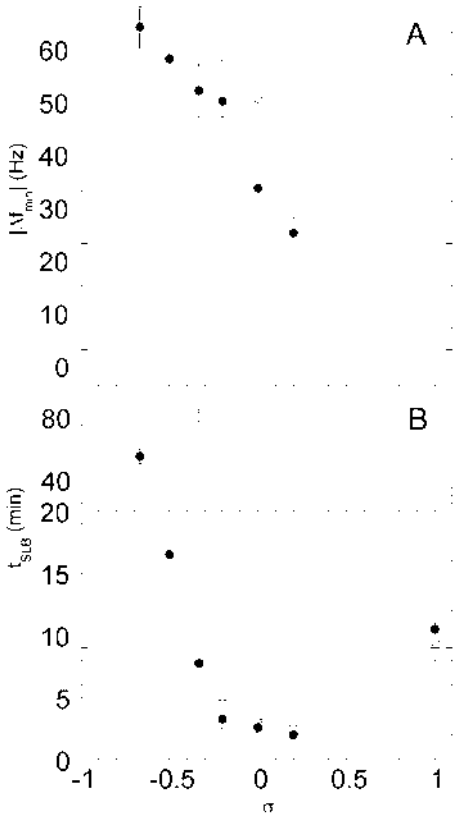

FIGURE 7 (*A*) Relationship between the local minimum frequency, $|\Delta f_{min}|$, and the fractional lipid charge, σ (identical with average number of charges per lipid molecule). Data are derived from lipid mixtures showing bilayer formation of case 1 as presented in Fig. 6 in the presence of EDTA (*open circles*) and calcium (*filled circles*), respectively. (*B*) Graph showing the time needed for bilayer formation, t_{SLB}, versus σ. Data are derived from lipid mixtures showing bilayer formation as presented in Fig. 6 in the presence of EDTA (*open circles*) and calcium (*filled circles*), respectively. t_{SLB} is determined from the onset of adsorption to equilibration of the signals in f and D. For DOPC/DOPS (molar ratio 1:1 and 1:2), extrapolated estimates are given.

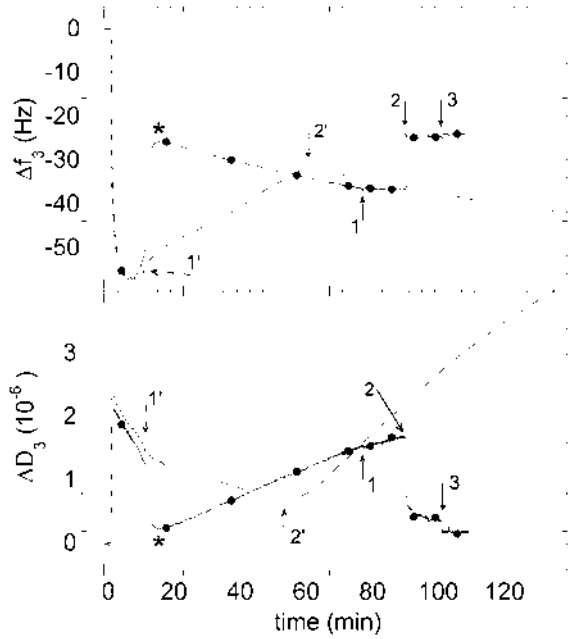

FIGURE 8 Restructuration of the adsorbed material into a more flexible conformational state after the onset of bilayer formation. QCM-D response for the adsorption of DOPC/DOPS (molar ratio 1:1) to SiO_2 in the presence of 2 mM $CaCl_2$. Changes in frequency (*upper panel*) and dissipation (*lower panel*) are given for two experiments, i), continuous line with closed circles, and ii), dashed line. In i), lipids present in solution were washed away ~65 min after the onset of restructuration (*asterisk*) by rinsing with calcium-containing buffer (*arrow 1*). A subsequent rinse with EDTA (*arrow 2*) resulted in a collapse of the flexible adlayer. The final values of Δf and ΔD after re-exposure to calcium (*arrow 3*) confirmed the formation of a complete SLB. In ii), removal of lipids present in solution was performed before the onset of restructuration by rinsing with calcium-containing buffer (*arrow 1′*). A decrease in f and an increase in D (*arrow 2′*) confirmed restructuration of surface-bound material in the absence of vesicles in solution.

decomposition (cf. Fig. 1 *B*). However, f subsequently decreased and D increased slowly (*arrow 2′* in Fig. 8). Since no extra lipid material was present in solution, these changes must correspond to a change of conformation or restructuration of the material adsorbed on the silica surface. The changes observed in f and D indicate that the restructured material was highly flexible and that additional water was associated with it.

DISCUSSION

In this study, we combined QCM-D and AFM methods to investigate the deposition of lipid vesicles of different net composition on silica surfaces. The main results are schematically described in Fig. 9. Three different pathways of vesicle deposition are distinguished: i), formation of a vesicular layer (scheme *C*), ii), formation of an SLB where vesicle decomposition occurs either at a high surface coverage (scheme *B*), and iii), at low surface coverage (scheme *A*). A fourth scenario corresponds with the absence of vesicle adsorption (scheme *D*).

Our results show that, for the lipid systems presented here, the net charge of the vesicles is the determining parameter for the type of pathway of vesicle decomposition.

Influence of the lipid charge on the vesicle deposition pathway

The processes of lipid vesicle deposition and SLB formation are governed by many types of interactions, as already extensively investigated experimentally and theoretically (Lipowsky and Seifert, 1991; Israelachvili, 1992; Seifert, 1997; Cremer and Boxer, 1999; Reviakine and Brisson, 2000; Zhdanov et al., 2000; Zhdanov and Kasemo, 2001; Reimhult et al., 2002a): i), the interaction between lipid vesicles and the support, ii), the interaction between adsorbed vesicles, and iii), the molecular interactions within adsorbed

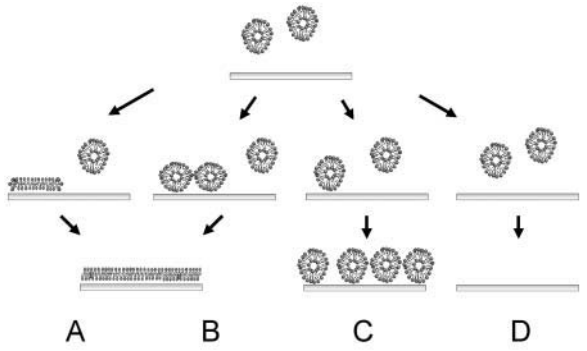

FIGURE 9 Schematic presentation of the pathways of vesicle deposition and SLB formation described in the text. (*A*) Formation of an SLB triggered at low vesicular coverage. (*B*) Formation of an SLB triggered at high vesicular coverage. (*C*) Formation of an SVL. (*D*) Inhibited adsorption.

vesicles, characterized by the bending modulus. It is logical to consider that electrostatic forces contribute to these three interactions, although a detailed description of their role as compared with other interactions such as that of van der Waals and steric interactions (Israelachvili, 1992) remains to be elucidated. Phenomenologically, a vesicle will rupture if the deformation that results from the three types of interactions exceeds a given threshold value. We will consider briefly our results according to this basic framework.

The fact that DOTAP SUVs, which are positively charged, rupture individually on negatively charged silica supports (Ducker et al., 1992; Arai et al., 1996) must reflect a strong vesicle-support electrostatic interaction, and possibly a reduced stability of isolated vesicles. On the other hand, the slow late stage of bilayer formation could result from an electrostatic repulsion between adsorbed DOTAP patches and SUVs in solution.

Vesicles with low positive (DOPC/DOTAP (4:1)), neutral (DOPC), or negative charge (DOPC/DOPS (4:1, 2:1)) adsorb but are not sufficiently deformed to auto-decompose. To induce decomposition, additional stress has to be provided by cooperative action of neighboring vesicles, i.e., a critical vesicular coverage is needed for bilayer formation (Keller et al., 2000; Reviakine and Brisson, 2000; Zhdanov et al., 2000). The fact that vesicle decomposition does not occur upon rinsing before the minimum frequency indicates that decomposition starts at or $\sim\Delta f_{min}$ and justifies using $|\Delta f_{min}|$ as a measure for the critical coverage. The increase of the critical coverage with decreasing vesicle charge (Fig. 7 *A*) is likely to reflect the fact that the interaction between vesicle and support is becoming less attractive as its electrostatic component diminishes, vanishes, or becomes repulsive for low positive, neutral, or negative vesicle charge, respectively. Interestingly, the dependence between $|\Delta f_{min}|$ and the fractional lipid charge, σ, is linear (Fig. 7 *A*), which deserves further investigation.

For vesicles with high net negative charge (DOPC/DOPS (1:1)), a stable SVL is obtained, indicating that, due to the combination of decreased vesicle-support interaction and increased intervesicle repulsion, vesicle decomposition cannot be initiated even at the highest attainable coverage. This adsorption barrier is responsible for the decreased initial adsorption rates observed for vesicles with a high net negative charge (DOPC/DOPS (2:1, 1:1)) and, eventually, the inhibition of adsorption for the highest negative charge employed (DOPC/DOPS (1:2)).

Effect of calcium

Calcium has already been reported to play an essential role in the process of bilayer formation, even at millimolar concentrations (McLaughlin et al., 1978; Gregory and Ginsberg, 1984; Feigenson, 1989; Leckband et al., 1993; Nollert et al., 1995; Reviakine et al., 2000). Our results confirm that calcium shifts the ability of bilayer formation toward higher negative vesicle charge. It is likely that this is due to the ability of the bivalent ion to ''bridge'' negatively charged entities such as the carboxylate groups in DOPS, the phosphate groups in DOPC and DOPS, or negative charges on the silica surface. In particular, the increase of the initial adsorption rates in the presence of calcium for DOPC/DOPS mixtures of composition ratio 2:1 and lower indicates the increased interaction between lipids and support.

Lateral organization

AFM provides local structural information on the formation of SLBs and further supports the interpretation of the QCM-D signal. The visualization of single vesicles, as well as patches of supported bilayers, gives insight into the structural changes of the surface-bound lipid material.

The case of DOPC/DOPS (4:1) is a typical example of bilayer formation induced at an elevated critical vesicular coverage. The use of the AFM tip as nanotweezers to induce the rupture of single vesicles allowed following the decomposition of neighboring vesicles into a bilayer patch. The obtained images suggest that supported bilayer domains grow by interaction of their active edges with adjacent vesicles. The visualization, in subsequent scan lines, of intermediate states of the bilayer domain growth (Fig. 3) allows estimating the propagation time to be in the order of 1 s. Domain growth stops as soon as a gap between the bilayer patch and neighboring vesicles is present. As supported vesicles and bilayer patches do not diffuse (at the timescale of minutes), the growth of SLBs in the absence of vesicles in solution is slow or eventually halts. The contribution of additional vesicles from solution is required to initiate new cascades of vesicle rupture events. This process, combined with formation of new bilayer patches, continues until eventually the whole surface is covered (Reviakine and Brisson, 2000; Zhdanov et al., 2000).

In the case of the DOPC/DOPS (4:1) mixture, our results indicate that bilayer formation does not involve fusion of surface-bound vesicles because i), the size distribution of surface-bound vesicles did not change dramatically with increasing surface coverage, and ii), no indications of fusion intermediates could be found when inducing the formation of bilayer patches by the AFM tip (Fig. 3).

For both SLB-formation pathways, stable bilayer patches of noncircular shape have been observed. This indicates support-induced constraints on the lipid mobility, as a non-constrained patch would adopt the thermodynamically favorable circular shape (Muresan and Lee, 2001). It is unclear, though, whether the mobility constraints are prevalent in the entire support-facing monolayer or only on its edges.

We suggest that the large size distribution of bilayer patches, observed for DOTAP at low coverage, originates from a large size distribution of vesicles present in solution. The formation of DOTAP-SUVs by sonication might be more difficult due to the elevated charge density, as compared with DOPC. It is considered less likely that the bilayer patches are the result of the fusion of several small vesicles on the surface since this should result in more homogeneous surface coverage than observed.

Even though the overall results obtained by AFM and QCM-D confirmed each other, it should be underlined that the supports used for AFM and QCM-D were not identical. Notably, the fact that SLB formation with DOTAP was found to be complete on silica wafers by AFM, whereas some uncovered support was detected by QCM-D, could be due to varying surface roughness or slightly different chemical properties of the support. Also, a detailed analysis of adsorbed lipid material in terms of surface coverage was not attempted here because of difficulties to independently extract accurate values from AFM and QCM-D data.

Restructuration

For a number of lipid compositions, a restructuration of surface-bound lipid material into a more flexible state upon association of water was observed to set in before the SLB formation was finished. This underlines that SLB formation is largely dependent on the lipid composition, and that the exposure of vesicles to a solid support can lead to more diverse structures than SVLs and SLBs.

Restructuration was characterized by kinetics significantly slower than the bilayer formation. Calcium plays an important role in this process, as it was never observed in EDTA and as the flexible structure collapses within seconds after exposure to EDTA. It remains to be elucidated which parts of the surface-bound lipid material—vesicles or bilayer patches—participate in the restructuration, and what is the mesoscopic structure of the flexible adlayer. However, since restructuration is not reinduced by adding Ca^{2+} ions or vesicles on a continuous bilayer formed by collapse with EDTA (Fig. 8), we tentatively propose that restructuration is triggered by active bilayer edges.

The influence of electrostatic interaction in general and the lipid charge in particular on vesicle deposition and SLB formation has frequently been reported (Nollert et al., 1995; Cremer and Boxer, 1999; Egawa and Furusawa, 1999). We could demonstrate that the variation of the lipid charge only can lead to several different vesicle deposition pathways. Notably, the pathway of bilayer formation induced at low vesicular coverage could be observed for the first time by QCM-D, which allowed a direct comparison of the two pathways of bilayer formation reported. The charge changes the balance between vesicle-support, intervesicle, and intra-bilayer interactions and is thus a determinant of the vesicle deposition pathway.

It is understood that the two pathways of SLB formation established here are not exclusive. Other pathways are possible, including an intermediate step of fusion of surface-bound vesicles, as observed for small vesicles of egg-PC on mica (Reviakine and Brisson, 2000). The three types of interactions (bilayer-support, interbilayer, and intrabilayer) might also influence the molecular interaction of lipids in a bilayer, e.g., leading to segregation (Reviakine et al., 2000) or changes in the bilayer fluidity, and thus indirectly change the stability of adsorbed vesicles and the vesicle decomposition pathway.

The results obtained by AFM confirm the interpretation of QCM-D data on SLB formation presented here as well as by Kasemo and co-workers (Keller and Kasemo, 1998; Keller et al., 2000; Reimhult et al., 2003). The study emphasizes the complementarity between QCM-D, which is a quick and straightforward method and enables screening for relevant experimental conditions, and AFM, which allows detailed structural investigation, yet is more laborious for soft samples.

It can be anticipated that the combination of these techniques as well as other techniques such as fluorescence microscopy (Boxer, 2000; Johnson et al., 2002; Kiessling and Tamm, 2003) or spectroscopy (Watts et al., 1986), surface plasmon resonance (Keller et al., 2000), and ellipsometry (Benes et al., 2002) will help to improve the description of the SLB-formation pathways. Important questions to be answered are the exact role of vesicles in solution in the late stage of the SLB-formation process, the influence of lateral diffusion of adsorbed vesicles/bilayer patches, the role of fusion intermediates, the orientation of the lipid layers after vesicle rupture, the critical vesicular coverage preceding SLB formation, and the possible loss of surface-bound lipid material.

CONCLUSION

This report demonstrates that the variation of the charge of lipid vesicles allowed tuning the pathway of bilayer formation. It was established that several pathways of vesicle deposition and bilayer formation are possible. The

lipid charge changes the balance between vesicle-support, intervesicle, and intrabilayer interactions, thus becoming a determinant of the vesicle-deposition pathway. Calcium was shown to enhance the tendency of bilayer formation.

The basic techniques employed, AFM and QCM-D, were shown to be highly complementary for this study, providing an effective characterization of both the overall dynamics and a spatially resolved picture of the lipid deposition process. The ability to predict and control the formation of SLBs is a potentially important step toward designing biofunctional surfaces.

Discussions with Fredrik Höök (Q-Sense), Erik Reimhult (Chalmers, Gothenburg, Sweden), and Olivier Lambert (Institut Europen de Chimie et Biologie) are acknowledged. We thank Patrice Caillat and Claude Vauchier (Commissariat à l'Energie Atomique-Laboratoire d'Electronique de Technologie de l'Information, Grenoble, France) for the gift of silicon wafers.

R.R. is the recipient of a PhD fellowship from the Conseil Régional d'Aquitaine, France. This research was supported by the Conseil Régional d'Aquitaine, the Fonds Européen de Développement Régional, and European Commission grants QLK2-CT2001-01339 and QLG3-CT2001-00902.

REFERENCES

Adamczyk, Z., B. Siwek, M. Zembala, and P. Belouschek. 1994. Kinetics of localized adsorption of colloid particles. *Adv. Colloid Int. Sci.* 48:151–280.

Arai, T., D. Aoki, Y. Okabe, and M. Fujihira. 1996. Analysis of surface forces on oxides in aqueous solutions using AFM. *Thin Solid Films.* 273:322–326.

Benes, M., D. Billy, W. T. Hermens, and M. Hof. 2002. Muscovite (mica) allows the characterisation of supported bilayers by ellipsometry and confocal fluorescence correlation spectroscopy. *Biol. Chem.* 383:337–341.

Bieri, C., O. P. Ernst, S. Heyse, K. P. Hofmann, and H. Vogel. 1999. Micropatterned immobilization of a G protein-coupled receptor and direct detection of G protein activation. *Nat. Biotechnol.* 17:1105–1108.

Boxer, S. G. 2000. Molecular transport and organization in supported lipid membranes. *Curr. Opin. Chem. Biol.* 4:704–709.

Cornell, B. A., V. L. Braach-Maksvytis, L. G. King, P. D. Osman, B. Raguse, L. Wieczorek, and R. J. Pace. 1997. A biosensor that uses ion-channel switches. *Nature.* 387:580–583.

Cremer, P. S., and S. G. Boxer. 1999. Formation and spreading of lipid bilayers on planar glass supports. *J. Phys. Chem. B.* 103:2554–2559.

Ducker, W. A., T. J. Senden, and R. M. Pashley. 1992. Measurement of forces in liquids using a force microscope. *Langmuir.* 8:1831–1836.

Egawa, H., and K. Furusawa. 1999. Liposome adhesion on mica surface studied by atomic force microscopy. *Langmuir.* 15:1660–1666.

Ekeroth, J., P. Konradsson, and F. Höök. 2002. Bivalent-ion-mediated vesicle adsorption and controlled supported phospholipid bilayer formation on molecular phosphate and sulfate layers on gold. *Langmuir.* 18:7923–7929.

Feigenson, G. W. 1989. Calcium ion binding between lipid bilayers: the four-component system of phosphatidylserine, phosphatidylcholine, calcium chloride, and water. *Biochemistry.* 28:1270–1278.

Gregory, D. P., and L. Ginsberg. 1984. Calcium association with phosphatidylserine: modification by cholesterol and phosphatidylcholine in monolayers and bilayers. *Biochim. Biophs. Acta.* 769:238–244.

Israelachvili, J. N. 1992. Intermolecular and Surface Forces. Academic Press, London.

Jass, J., T. Tjärnhage, and G. Puu. 2000. From liposomes to supported, planar bilayer structures on hydrophilic and hydrophobic surfaces: an atomic force microscopy study. *Biophys. J.* 79:3153–3163.

Johnson, J. M., H. Taekijp, S. Chu, and S. G. Boxer. 2002. Early steps of supported bilayer formation probed by single vesicle fluorescence assays. *Biophys. J.* 83:3371–3379.

Keller, C. A., K. Glasmästar, V. P. Zhdanov, and B. Kasemo. 2000. Formation of supported membranes from vesicles. *Phys. Rev. Lett.* 84:5443–5446.

Keller, C. A., and B. Kasemo. 1998. Surface specific kinetics of lipid vesicle adsorption measured with a quartz crystal microbalance. *Biophys. J.* 75:1397–1402.

Kiessling, V., and L. K. Tamm. 2003. Measuring distances in supported bilayers by fluorescence interference-contrast microscopy: polymer supports and SNARE proteins. *Biophys. J.* 84:408–418.

Kung, L. A., L. Kam, J. S. Hovis, and S. G. Boxer. 2000. Patterning hybrid surfaces of proteins and supported lipid bilayers. *Langmuir.* 16:6773–6776.

Leckband, D. E., C. A. Helm, and J. Israelachvili. 1993. Role of calcium in the adhesion and fusion of bilayers. *Biochemistry.* 32:1127–1140.

Liebau, M., A. Hildebrand, and R. H. Neubert. 2001. Bioadhesion of supramolecular structures at supported planar bilayers as studied by the quartz crystal microbalance. *Eur. Biophys. J.* 30:42–52.

Lipowsky, R., and U. Seifert. 1991. Adhesion of vesicles and membranes. *Mol. Crys. Liq. Cryst.* 202:17–25.

Marcelja, S. 1992. Electrostatics of membrane adhesion. *Biophys. J.* 61:1117–1121.

McConnell, H. M., T. H. Watts, R. M. Weis, and A. A. Brian. 1986. Supported planar membranes in studies of cell-cell recognition in the immune system. *Biochim. Biophys. Acta.* 864:95–106.

McLaughlin, A., C. Grathwohl, and S. McLaughlin. 1978. The adsorption of divalent cations to phosphatidylcholine bilayer membranes. *Biochim. Biophys. Acta.* 513:338–357.

Muresan, A. S., and K. Y. C. Lee. 2001. Shape evolution of lipid bilayer patches adsorbed on mica: an atomic force microscopy study. *J. Phys. Chem. B.* 105:852–855.

Nollert, P., H. Kiefer, and F. Jähnig. 1995. Lipid vesicle adsorption versus formation of planar bilayers on solid surfaces. *Biophys. J.* 69:1447–1455.

Pignataro, B., C. Steinem, H.-J. Galla, H. Fuchs, and A. Janshoff. 2000. Specific adhesion of vesicles monitored by scanning force microscopy and quartz crystal microbalance. *Biophys. J.* 78:487–498.

Reimhult, E., F. Höök, and B. Kasemo. 2002a. Temperature dependence of formation of a supported phospholipid bilayer from vesicles on SiO_2. *Phys. Rev. E.* 66:051905.

Reimhult, E., F. Höök, and B. Kasemo. 2002b. Vesicle adsorption on SiO_2 and TiO_2: dependence on vesicle size. *J. Chem. Phys.* 117:7401–7404.

Reimhult, E., F. Höök, and B. Kasemo. 2003. Intact vesicle adsorption and supported biomembrane formation from vesicles in solution: influence of surface chemistry, vesicle size, temperature and osmotic pressure. *Langmuir.* In press.

Reviakine, I., W. Bergsma-Schutter, and A. Brisson. 1998. Growth of protein 2-D crystals on supported planar lipid bilayers imaged in situ by AFM. *J. Struct. Biol.* 121:356–361.

Reviakine, I., and A. Brisson. 2000. Formation of supported phospholipid bilayers from unilamellar vesicles investigated by atomic force microscopy. *Langmuir.* 16:1806–1815.

Reviakine, I., A. Simon, and A. Brisson. 2000. Effect of Ca^{2+} on the morphology of mixed DPPC-DOPS supported phospholipid bilayers. *Langmuir.* 16:1473–1477.

Richter, R., and A. Brisson. 2003. Characterization of lipid bilayers and protein assemblies supported on rough surfaces by atomic force microscopy. *Langmuir.* In press.

Rodahl, M., F. Höök, A. Krozer, P. Brzezinski, and B. Kasemo. 1995. Quartz crystal microbalance setup for frequency and Q-factor measurements in gaseous and liquid environments. *Rev. Sci. Instrum.* 66:3924–3930.

Rouser, G., S. Fleisher, and A. Yamamoto. 1975. Two-dimensional thin layer chromatographic separation of polar lipids and determination of phospholipids by phosphorus analysis of spots. *Lipids*. 5:494–496.

Rädler, J., H. Strey, and E. Sackmann. 1995. Phenomenology and kinetics of lipid bilayer spreading on hydrophilic surfaces. *Langmuir*. 11:4539–4548.

Sackmann, E. 1996. Supported membranes: scientific and practical applications. *Science*. 271:43–48.

Salafsky, J., J. T. Groves, and S. G. Boxer. 1996. Architecture and function of membrane proteins in planar supported bilayers: a study with photosynthetic reaction centers. *Biochemistry*. 35:14773–14781.

Seifert, U. 1997. Configuration of fluid membranes and vesicles. *Adv. Phys*. 46:13–137.

Watts, T. H., A. A. Brian, J. W. Kappler, P. Marrack, and H. M. McConnell. 1984. Antigen presentation by supported planar membranes containing affinity-purified I-Ad. *Proc. Natl. Acad. Sci. USA*. 81:7564–7568.

Watts, T. H., H. E. Gaub, and H. M. McConnell. 1986. T-cell-mediated association of peptide antigen and major histocompatibility complex protein detected by energy transfer in an evanescent wave-field. *Nature*. 320:179–181.

Vig, J. R. 1987. UV/ozone cleaning of surfaces. *In* Treatise on Clean Surface Technology. K. L. Mittal, editor. Plenum Press, New York. 1–26.

Wilschut, J., N. Düzgünes, and D. Papahadjopoulos. 1981. Calcium/magnesium specificity in membrane fusion: kinetics of aggregation and fusion of phophatidylserine vesicles and the role of bilayer curvature. *Biochemistry*. 20:3126–3133.

Zhdanov, V. P., and B. Kasemo. 2001. Comments on rupture of adsorbed vesicles. *Langmuir*. 17:3518–3521.

Zhdanov, V. P., C. A. Keller, K. Glasmästar, and B. Kasemo. 2000. Simulation of adsorption kinetics of lipid vesicles. *J. Chem. Phys*. 112:900–909.

Paper IV

Ralf P. Richter and Alain R. Brisson

Following the formation of supported lipid bilayers on mica – a study combining AFM, QCM-D and ellipsometry.

Submitted to the Biophysical Journal

Following the formation of supported lipid bilayers on mica – a study combining AFM, QCM-D and ellipsometry

RUNNING TITLE: SLB-formation on mica

Ralf P. Richter and Alain R. Brisson*

Laboratoire d'Imagerie Moléculaire et Nano-Bio-Technologie, IECB, UMR-CNRS 5471, Université Bordeaux I, 2 Rue Robert Escarpit, 33607 Pessac Cedex, France

*Corresponding author. E-mail: a.brisson@iecb.u-bordeaux.fr

KEYWORDS: mica; silica; quartz crystal microbalance with dissipation monitoring (QCM-D); atomic force microscopy (AFM); ellipsometry; supported lipid bilayer (SLB); supported vesicular layer (SVL); dioleoylphospatidylserine (DOPS); dioleoylphosphatidylcholine (DOPC); dioleoyltrimethylammonium-propane (DOTAP); poly(L-lysine)-*g*-poly(ethylene glycol) (PLL-*g*-PEG)

ABSTRACT

Supported lipid bilayers (SLBs) are popular models of cell membranes with potential biotechnological applications and an understanding of the mechanisms of SLB-formation is now emerging. Here we characterize, by combining atomic force microscopy (AFM), quartz crystal microbalance with dissipation monitoring (QCM-D) and ellipsometry, the formation of SLBs on mica from sonicated unilamellar vesicles using mixtures of zwitterionic, negatively and positively charged lipids. The results are compared with those we reported previously on silica (Richter et al., *Biophys. J.* **2003**, *85*, 3035-3047). As on silica, electrostatic interactions were found to determine the pathway of

lipid deposition. However, fundamental differences in the stability of surface-bound vesicles and the mobility of SLB-patches were observed, and point out the determining role of the solid support in the SLB-formation process. The presence of calcium was found to have a much more pronounced influence on the lipid deposition process on mica than on silica, suggesting a specific interaction between (negatively charged) lipids, calcium and mica. In addition, we show that the use of PLL-*g*-PEG modified tips considerably improves the AFM-imaging of surface-bound vesicles and bilayer patches and evaluate the effects of the AFM-tip on the apparent size and shape of these soft structures.

INTRODUCTION

Supported lipid bilayers (SLBs), formed by the spreading of vesicles from solution (Watts et al., 1984; McConnell et al., 1986), have already found widespread use as mimics of cell membranes (Watts et al., 1984; Sackmann, 1996; Salafsky et al., 1996; Reviakine et al., 1998; Milhiet et al., 2002; Yip et al., 2002) and are attractive as building blocks for biotechnological applications (Sackmann, 1996; Boxer, 2000; Reviakine and Brisson, 2001; Kam and Boxer, 2003; Larsson et al., 2003). It is only in the recent years that a detailed image of the structural intermediates of the formation of SLBs is emerging from both experimental (Rädler et al., 1995; Keller and Kasemo, 1998; Jass et al., 2000; Keller et al., 2000; Reviakine and Brisson, 2000; Johnson et al., 2002; Reimhult et al., 2003; Richter et al., 2003) and theoretical studies (Seifert and Lipowsky, 1990; Seifert, 1997; Zhdanov et al., 2000), though many issues about the formation of SLBs remain to be explored. We do not have, at present, a comprehensive understanding of the driving forces of the SLB-formation process (Nollert et al., 1995; Reviakine and Brisson, 2000; Zhdanov and Kasemo, 2001; Reimhult et al., 2002b; Richter et al., 2003). In particular, the role of the solid support in the rupture of vesicles and the promotion of SLB-formation (Keller and Kasemo, 1998; Starr and Thompson, 2000; Reimhult et al., 2003; Richter and Brisson, 2004) remains poorly understood.

Silica-based surfaces and mica are the prototypes of solid supports that are currently used to form solid-supported lipid bilayers. Notably, previous studies have provided indications for some differences in the SLB-formation process on these supports, such as the role of calcium (Reviakine and Brisson, 2000; Richter et al., 2003) and the influence of the vesicle size on rupture (Reviakine and Brisson, 2000; Reimhult et al., 2002b). A detailed comparison of the SLB-formation process between these surfaces is though still lacking.

A multitude of techniques, such as fluorescence microscopy (Nollert et al., 1995; Johnson et al., 2002), quartz-crystal microbalance with dissipation monitoring (QCM-D) (Keller and Kasemo, 1998; Keller et al., 2000; Reimhult et al., 2002a; Reimhult et al., 2002b; Reimhult et al., 2003; Richter et al.,

2003; Seantier et al., 2004), atomic force microscopy (AFM) (Jass et al., 2000; Reviakine and Brisson, 2000; Richter et al., 2003; Tokumasu et al., 2003; Seantier et al., 2004), surface plasmon resonance (SPR) (Keller et al., 2000) and ellipsometry (W. T. Hermens, personal communication) has been used to investigate the SLB-formation process. We have recently illustrated the complementary nature of AFM and QCM-D for the analysis of vesicle adsorption and SLB-formation on silica (Richter et al., 2003). Giving access to spatially resolved structural information on the nanometer scale and overall adsorption and reorganization dynamics, respectively, the combination of both techniques has enabled the identification and characterization of several different SLB-formation pathways stressing the importance of electrostatic interactions in the SLB-formation process. Others have pointed out the complementary aspects between QCM-D and optical surface-sensitive methods, such as SPR (Keller et al., 2000) or ellipsometry: while optical methods allow measuring the dry mass of the adsorbed lipids, QCM-D provides not only the hydrated mass, but also a direct mean (the dissipation) to distinguish between different phases of the adsorbate - surface-bound vesicles or bilayer patches (Keller et al., 2000). As such, the combination of QCM-D and SPR has allowed establishing the concept of local critical vesicular coverage (Keller et al., 2000). Recent work has also demonstrated that *in-situ* measurements on mica can be performed both with ellipsometry (Benes et al., 2002) and with QCM-D (Richter and Brisson, 2004) in a reproducible manner, opening up for the joint use of QCM-D, ellipsometry and AFM on this support.

In this study, we combine sequential measurements by QCM-D and AFM on identical supports, complemented by ellipsometry, to characterize the vesicle adsorption and the SLB-formation on mica. As in a previous study on silica (Richter et al., 2003), we employ vesicles with varying net charges, from positively charged dioleoyltriammonium-propane (DOTAP) to mixtures of zwitterionic dioleoylphosphatidylcholine (DOPC) and negatively charged dioleoylphophatidylserine (DOPS). This allows for a quantitative comparison between the lipid deposition on mica and on silica and gives new

insight in the role of the solid support, the lipid mixture and the calcium-EDTA balance in the SLB-formation process.

MATERIALS AND METHODS

Materials:

Dioleoylphosphatidylcholine (DOPC), dioleoylphospatidylserine (DOPS) and dioleoyltrimethylammonium-propane (DOTAP) were purchased from Avanti Polar-Lipids (AL, USA). Lyophilized poly(L-lysine)-*g*-poly(ethylene glycol) (PLL-*g*-PEG) with a 20 kDa poly(L-lysine)-backbone, side chains of 2 kDa poly(ethylene glycol) and a grafting ratio of $g = 3.4$ (Huang et al., 2002) was synthesized and kindly provided by the group of M. Textor (ETH, Zurich, Switzerland). Other chemicals were purchased from Sigma. Ultrapure water with a resistivity of 18.2 MΩ was used (Maxima, USF ELGA, France).

Muscovite mica disks of 12 mm diameter were purchased from Metafix (Montdidier, France). QCM-D sensor crystals (5 MHz), reactively sputter-coated with 50 nm silicon oxide, were purchased from Q-SENSE (Gothenburg, Sweden). Low viscosity epoxy glue (EPOTEK 377) for the mica-gluing was purchased from Gentec Benelux (Waterloo, Belgium).

A buffer solution made of 150 mM NaCl, 3 mM NaN_3 and 10 mM HEPES, pH 7.4, was prepared in ultrapure water, and either 2 mM EDTA or 2 mM $CaCl_2$ were added as indicated in the text. Small unilamellar vesicles (SUVs) of desired lipid mixture were prepared by sonication as described earlier (Richter et al., 2003). Before use vesicle suspensions were diluted at 0.1 mg/mL if not otherwise stated.

Quartz Crystal Microbalance with Dissipation Monitoring (QCM-D):

QCM-D measurements (Rodahl et al., 1995) were performed with the Q-SENSE D300 system equipped with an Axial Flow Chamber (QAFC 302) (Q-SENSE AB, Gothenburg, Sweden). Briefly, upon interaction of (soft) matter with the surface of a sensor crystal, changes in the resonance frequency, f, related to attached mass (including coupled water), and in the dissipation, D, related to frictional (viscous) losses in the adlayer are measured with a time resolution of better than 1 s.

The QCM-D sensor crystals were coated with mica and verified to operate stably and reliably according to a previously described protocol (Richter and Brisson, 2004).

Measurements were performed in exchange mode (described in detail elsewhere (Richter et al., 2003)), if not otherwise stated. This mode allows following processes of adsorption and surface adlayer changes *in situ* while sequentially exposing different solutions to the surfaces. Resonance frequency and dissipation were measured at several harmonics (15, 25, 35 MHz) simultaneously. The working temperature was 24°C. Occasionally, flow mode was employed, i.e., the sample was continuously delivered to the measurement chamber (flow speed 80 μL/min) by the aid of a peristaltic pump (ISM832A, Ismatec, Zürich, Switzerland).

If not stated otherwise, changes in dissipation and in normalized frequency ($\Delta f_{norm} = \Delta f_n/n$, with n being the overtone number) of the third overtone (n = 3, i.e., 15 MHz) are presented. Adsorbed masses, Δm, are calculated according to the Sauerbrey equation (Sauerbrey, 1959), $\Delta m = -C \cdot \Delta f_{norm}$, with $C = 17.7$ ng·cm^{-2}·Hz^{-1}. The equation has been demonstrated to be valid (within 5% error) for lipid bilayers or adsorbed non-ruptured SUVs on rigid sensor coatings with a thickness ranging from several nanometers (such as evaporated gold or sputtered silica (Keller and Kasemo, 1998; Reimhult et al., 2002b)) to several micrometers (such as glued mica-sheets (Richter and Brisson, 2004)).

For transfer of QCM-D sensors with adsorbed material from the QCM-D chamber to the AFM, the sensors were unmounted with the aid of a suction holder (Meni CUP, Menicon Pharma, Illkirch Graffenstaden, France), ensuring that the sample remained permanently covered with liquid.

Ellipsometry:

Ellipsometry is an optical technique based on the measurement of changes in the ellipsometric angles, Δ and Ψ (Cuypers et al., 1983; Tompkins, 1993), of elliptically polarized light upon reflection at a planar surface. These changes are sensitive to the presence of thin deposited films and, consequently, the method allows monitoring adsorption phenomena *in situ*, at the solid-liquid interface, with a mass resolution in the range of 5 to 10 ng·cm^{-2}. The employed null-ellipsometer setup has a time resolution of 10 to 15 s and is described in detail elsewhere (Cuypers et al., 1983; Corsel et al., 1986).

In the present study we consider the change in the angle Δ only, which is roughly proportional to the (dry) lipid mass adsorbed to mica (Benes et al., 2002).

Measurements were performed in an open cuvette system (Corsel et al., 1986), at room temperature. Mica disks were glued on an aluminum slide over a hole (8 mm diameter) using melted wax (Benes et al., 2002). The backside of the mica discs was rendered opaque with emery paper prior to gluing onto the aluminum slide. Uniform mica-surfaces were obtained by cleavage of the front side with adhesive tape and immediately mounted in the buffer-filled cuvette. The buffer (~3 mL) was stirred with a magnetic stirrer (~1000 rpm). Samples were pipetted at appropriate concentrations into the buffer. Rinses were realized by injecting ~30 mL of buffer (injection rate ~1 mL/s) while simultaneously withdrawing excess liquid.

Preparation of PLL-*g*-PEG-coated AFM tips:

Oxide-sharpened silicon nitride cantilevers with a nominal spring constant of 0.06 N/m (Digital Instruments, CA, USA) were rinsed in water and ethanol, blow-dried with nitrogen, and exposed to UV/ozone (BHK, CA, USA) for 10 min (Richter et al., 2003). The cleaned tips were transferred immediately into a solution of 1 mg/mL PLL-*g*-PEG in 10 mM HEPES, pH 7.4. After 30 min of immersion, the tips were withdrawn, rinsed with ultrapure water and blow-dried with nitrogen. PLL-*g*-PEG-modified tips were stored on Gel-Pak (Scotch, CA, USA) under nitrogen and used within four weeks.

Atomic Force Microscopy (AFM):

AFM measurements were performed in liquid using a Nanoscope IV-Multimode (VEECO, Dourdan, France), equipped with a J-scanner (120 μm). Before use, the tapping mode fluid cell was washed in successive baths of ethanol and ultrapure water, followed by extensive rinsing in ethanol and blow-drying in a stream of nitrogen. Tubings and O-ring were sonicated in ethanol and water, rinsed with ethanol and blow-dried in nitrogen.

For AFM-investigations subsequent to QCM-D measurements, mica-coated QCM-D sensors, covered with the sample, were attached to Teflon-coated (BYTAC, NORTON, OH, USA) metal disks using double-sided tape (TESA, Hamburg, Germany) and installed on the AFM scanner. In all other cases, mica disks were glued to Teflon-coated metal disks using the epoxy glue. Uniform surfaces were obtained by cleavage with adhesive tape and immediately covered with buffer solution. The AFM was equilibrated for 5 to 30 minutes prior to imaging.

Images were recorded in contact mode or tapping mode as indicated. Contact mode images were acquired at scanning rates of 4-8 Hz while manually adjusting the force to a minimum (< 200 pN). Tapping mode images were acquired at scanning rates of 1-2 Hz. A resonance frequency ~7 kHz was chosen with low free amplitude (0.4-0.6 V) and minimum load upon scanning. Images were first-order plane-fitted and subsequently zero-order flattened except otherwise stated.

RESULTS

The formation of SLBs from SUVs made of DOPC and DOPS (molar ratio 4:1) in 2 mM $CaCl_2$ has already been well characterized by QCM-D on silica (Richter et al., 2003) and to some extent by AFM on mica (Reviakine and Brisson, 2000) and was chosen as a reference system in our study. The overall kinetics of the SLB-formation process on mica by QCM-D (figure 1) reveals a two-phase behavior. In the first phase the frequency decreases beyond -25 Hz (Δf_{min} = -39 Hz) while the dissipation increases ($\Delta D_{max} = 1.6 \cdot 10^{-6}$), evidencing the adsorption of a substantial amount of non-ruptured vesicles. Final shifts in frequency (Δf_{fin} = -25 Hz) and dissipation ($\Delta D_{fin} < 0.2 \cdot 10^{-6}$) after the second phase match values previously obtained on silica (Keller and Kasemo, 1998; Richter et al., 2003) and indicate the presence of an SLB. AFM-imaging of the final state of the surface adlayer revealed a flat surface devoid of defects on areas of 25 μm^2 and more and confirmed the presence of a confluent (ideal) bilayer (figure 6B).

The early phase of SLB-formation

In some measurements, the SLB-formation process was interrupted by rinsing with buffer at an early stage, i.e., long before the maximum in dissipation and minimum in frequency were reached (figure 2A). As the surface coverage is low, interactions between vesicles are expected to be negligible and hence the stability of *isolated* vesicles can be investigated. After rinsing, the frequency (dissipation) slowly increased (decreased), indicating that vesicles are not stable. AFM-images of the surface one hour after rinsing (figure 2B and C) revealed the presence of two types of objects, identified as immobilized vesicles and bilayer patches, respectively, from their apparent shapes and heights (Reviakine and Brisson, 2000; Richter et al., 2003). We believe that the distribution of vesicles and bilayer patches revealed in the image closely resembles the true distribution and is not significantly altered by the imaging process (see also below).

The smallest vesicles and bilayer patches had an apparent diameter of ~25 nm and ~28 nm (for details of the size determination see the Supplementary Information), respectively, close to the size

expected from SUVs. Notably, the size of both vesicles and SLB-patches was heterogeneous, i.e. both small and large patches (vesicles) were present, indicating a rather weak dependence of the rupture tendency on the vesicle size over the size distribution observed here. (Almost) all lipid patches exhibited a circular shape.

Both vesicles and bilayer patches were found not to move laterally over the time range of 10 minutes and more (except at relatively high imaging forces). AFM images acquired at low lipid coverage (c.f. figure 2B) did only exceptionally (presumably due to tip artifacts) reveal vesicles or bilayer patches that disappeared upon imaging.

In order to verify whether lipid material desorbs from the mica-surface, we monitored the SLB-formation process by ellipsometry. As this optical technique senses the dry mass, net-desorption of material would be directly detected as an increase in the ellipsometric angle Δ. After interrupting the SLB-formation process at a lipid coverage corresponding to about 30% of a complete SLB (figure 2D), Δ remained stable, confirming that lipid material did not desorb. Therefore, we interpret the QCM-D response after the rinsing step as shown in figure 2A as due to the decomposition of surface-bound vesicles into bilayer patches, the increase (decrease) in frequency (dissipation) being caused by the loss of water associated to and the changes in the rigidity of the lipid structures. Consequently, the QCM-D data indicate that the typical time for the spontaneous transition of isolated mica-bound vesicles into bilayer patches is in the range of minutes to hours. This is a remarkable difference compared to isolated vesicles on silica which remained stable over days under identical conditions (Richter et al., 2003).

Stability and mobility of small SLB-patches

In order to investigate the stability of bilayer patches, a certain area was imaged repetitively with varying forces (figures 3). While almost all SLB-patches remained immobile and kept their initial shape, connections between a few distant patches (asterisks in figure 3B) were established, likely induced by the AFM-tip that was temporarily operated at an elevated force. The resulting patches clearly reshaped into circular objects (figure 3C), the area of which corresponded roughly (for details

see the Supplementary Information) to the sum of the areas of the initial patches, confirming that coalescence events were tracked. The centre of mass of the merging patches remained approximately fixed during the merger event. Given the image acquisition time of around 2 minutes and the fact that connections are visible over several scan lines (corresponding to around 0.2 s each), the time needed for coalescence and reshaping can be estimated to be in the range of a few seconds to a few minutes. We note that, in contrast to our observation on mica, small SLB-patches of stable non-circular shape were observed on silica (Richter et al., 2003).

The lateral movement of lipid material associated with the coalescence of two patches (figure 4A) can trigger (a cascade of) subsequent events of coalescence with other neighboring patches (figures 4B-D), leading to substantial modifications in the organization of the surface-bound lipid material. It is easily conceivable that also intact adsorbed vesicles can be ruptured by contact with the approaching (active) edge of a neighboring bilayer patch. Shape changes due to coalescence can thus play a significant role in the organization of lipid material during the SLB-formation process.

The late phase of SLB-formation

Figure 5A demonstrates that after rinsing at a later stage, i.e., shortly after the minimum (maximum) in frequency (dissipation) is reached, a considerable rearrangement of the surface-bound lipid material takes place within minutes. In the absence of vesicles in solution, Δf increased above -25 Hz (to -16 Hz) and ΔD decreased to $0.4 \cdot 10^{-6}$, indicating that the major part of adsorbed vesicular material was transformed into bilayers patches. Corresponding AFM-images showed indeed extended domains of lipid bilayers coexisting with a small number of vesicles (figure 5B) and ellipsometry experiments indicated that no significant desorption occurred in similar conditions (figure 5C).

Interestingly, non-circularities persisted on large patches (i.e. with a radius larger than ~200 nm) over times of one hour and more. Surprisingly, patch boundaries with local radii of curvature smaller than 150 nm (arrowheads in figure 5B) could be found, indicating the presence of forces/obstacles that

counteract the shape equilibration that would be expected from minimization of the line tension (Rädler et al., 1995; Muresan and Lee, 2001).

AFM-images acquired after interrupting the SLB-formation at an even later stage, showed an apparently confluent bilayer in which local defects persisted (figure 6A). Elongated defects of several micrometers in length and down to a few nanometers in width could be observed, which were particularly frequent after incubation with SUV solutions at low concentration (10 μg/mL). Notably, the apparent local radius of curvature of the bilayer boundary at the ends of some of these defects (arrowheads in figure 6A) was in the range of 10 nm. Given our experimental conditions, we estimate that such small radii are at the limit of resolution. It is therefore not clear, whether the apparent topography reflects a truly continuous bilayer boundary or whether, instead, it marks the endpoint of a zone (dotted line in figure 6A) at which two patch boundaries appose with each other without coalescing, the gap between them being small enough to remain unresolved by AFM. Whatever the true topography, some of these defects remained stable over hours, again indicating the presence of forces that inhibit shape equilibration (Benvegnu and McConnell, 1992).

Subsequent re-incubation as well as incubation without interruption led to bilayers that were close to defect-free, as seen from the AFM-images (figure 6B). In order to verify whether defects persisted that were invisible to AFM, some DOPS-containing bilayers were incubated with the protein annexin A5 and the growth of two-dimensional crystals was followed as described elsewhere (Reviakine et al., 1998). Round-shaped crystals were observed as expected for undisturbed crystal growth (Reviakine et al., 1998) (not shown), while elongated discontinuities in the supporting bilayer are expected to locally prevent crystal growth thereby distorting the crystal's shape.

Influence of the vesicle charge and the presence of calcium on the SLB-formation on mica

The vesicle charge and the presence of calcium were previously shown to have a pronounced influence on the lipid deposition pathways on silica (Richter et al., 2003). For comparison, we followed the global kinetics of lipid deposition on mica for vesicles of varying charge in the presence of the

calcium chelator EDTA and in the presence of 2 mM calcium ions, respectively, by QCM-D. The vesicle charge was varied by mixing appropriate amounts of positively charged (DOTAP), zwitterionic (DOPC) and negatively charged (DOPS) lipids. For a quantitative comparison of the lipid deposition process, the minimum in frequency, Δf_{min}, and the maximum in dissipation, ΔD_{max}, were determined. SLB-formation, if occurring, was additionally characterized by the time, t_{SLB}, required to attain stable values in frequency, Δf_{fin}, and dissipation, ΔD_{fin}. Furthermore, the stability of adsorbed isolated vesicles was checked by interrupting the SLB-formation at low coverage. Table 1 and figures 7 and 8 summarize the obtained results.

In the absence of calcium, SUVs made from DOPC adsorbed to mica (figure 7B) but did not rupture at moderate lipid concentrations (100 μg/mL), in agreement with previous studies (Reviakine and Brisson, 2000). In contrast, SLB-formation was observed on silica (Richter et al., 2003). Rather small amounts of negative charges (20% DOPS) were sufficient to completely inhibit lipid adsorption. Similarly, vesicle adsorption was hampered on silica with increasing negative vesicle charge, although inhibition occurred only at considerably higher negative charge (50% DOPS) (Richter et al., 2003). These observations suggest that the (electrostatic) repulsion between negatively charged vesicles and the support is stronger with mica than with silica. In conjunction, we note that no SLBs could be formed on mica with DOPS-containing SUVs. For comparison, SLB-formation was inhibited on silica only at a DOPS-content of 33% and more (Richter et al., 2003).

QCM-D responses indicated the formation of SLBs for all types of positively charged SUVs investigated. These observations are qualitatively similar to silica. It is though notable, that the formation of mica-SLBs with pure DOTAP-SUVs (figure 7C) exhibited very low dissipation values ($\Delta D_{max} < 0.5 \cdot 10^{-6}$) throughout the whole SLB-formation process. Corresponding values on silica were slightly higher ($\Delta D_{max} = 0.8 \pm 0.1 \cdot 10^{-6}$) (Richter et al., 2003), indicating that the tendency towards immediate rupture of isolated DOTAP-vesicles is even more pronounced on mica.

The formation of a supported vesicular layer (SVL) with DOPC-SUVs (figure 7B) deserves some additional attention. The adsorption of these vesicles was partly reversible (Reviakine and Brisson, 2000), which is exceptional for the vesicle-surface interactions that we have so far investigated on silica and on mica. The frequency shift of $|\Delta f_{min}| = 103$ Hz, indicates a high surface coverage (Keller and Kasemo, 1998). Interestingly, the QCM-D responses after the addition of calcium (figure 7B) suggest that the SVL is converted into a *complete* supported lipid bilayer, even though no vesicles were present in solution. Furthermore, the maximum dissipation shift for the mica-supported vesicular layer, $\Delta D_{max} = 10 \cdot 10^{-6}$, is remarkably high, resulting in a ratio between dissipation and frequency of $\Delta D_{max}/|\Delta f_{min}| = 0.10 \cdot 10^{-6} \cdot Hz^{-1}$. This is significantly more than on silica ($0.06 \cdot 10^{-6} \cdot Hz^{-1}$) (Richter et al., 2003), and indicates that DOPC vesicles become less flattened on mica than on silica (Reimhult et al., 2002b)[1]

In the presence of calcium, SLBs were formed over the entire range of lipid mixtures investigated. Notably, SLBs could be formed from vesicles containing as much as 80% DOPS. A detailed examination revealed a tendency of t_{SLB} and $|\Delta f_{min}|$ to decrease towards higher negative charges (figure 8). This evidences that increasing DOPS-content facilitates SLB-formation on mica. Notably, the opposite was observed on silica. The influence of calcium on the SLB-formation process for DOTAP-containing vesicles was minor.

Isolated mica-bound vesicles that contained only DOPC or small amounts of DOTAP were found to be stable over minutes and hours (figure 7A), similar to the results obtained on pure silica (Keller et al.,

[1] For simplicity, we have compared the ratio of $\Delta D_{max}/|\Delta f_{min}|$. Note, however, that in addition to the flattening of the vesicle, the inter-vesicle interaction at high surface coverage can affect $\Delta D/\Delta f$. This potential artifact can be avoided by comparing the $\Delta D/|\Delta f|$-values at low vesicular coverage (Reimhult et al., 2002b). Corresponding values are $0.14 \cdot 10^{-6} \cdot Hz^{-1}$ and $0.08 \cdot 10^{-6} \cdot Hz^{-1}$ (at $n = 7$) on mica and silica, respectively, supporting our conclusions that DOPC vesicles become more flattened on silica.

2000). Isolated vesicles from all lipid mixtures containing 20% and more DOPS, however, slowly but measurably transformed into SLB-patches.

Influence of the AFM-tip on the imaging of lipid vesicles and SLB-patches

Lipid structures such as surface-bound vesicles or bilayer patches are known to be easily modified by interactions with the AFM-tip (Jass et al., 2000; Reviakine and Brisson, 2000; Richter and Brisson, 2003; Liang et al., 2004). During initial investigations with non-modified tips it became apparent that the lipid material can mediate strong tip-sample interactions (Richter and Brisson, 2003), which renders the imaging of heterogeneous lipid structures such as coexisting bilayer patches and vesicles unstable and prone to artifacts (in particular for low scan speeds and small image sizes). As demonstrated by the AFM-images shown here, the modification of the AFM-tip with PLL-*g*-PEG resulted in an improved control in imaging such lipid structures down to image sizes of 1 μm and less. When forces exerted by the AFM-tip were adjusted to a minimum, vesicles and bilayer patches could be imaged intact (c.f. figure 5B). Alternatively, increased forces could be employed to induce the rupture of vesicles (arrowheads in figures 2B and C), the coalescence of bilayer patches (c.f. figures 3 and 4) or the displacement of lipid structures (not shown).

Imaging in tapping mode provided least disturbance of the lipid material, though also images in contact mode could be obtained with only minor artifacts, such as occasional tip-induced vesicle rupture. In particular, small bilayer patches appeared (almost) circular and immobile both in tapping and contact mode, indicating that small lateral forces did not significantly alter the location or overall shape of the patches.

Effects of the AFM-tip on the apparent size of the bilayer patches

We did, however, observe small but significant variations in the apparent sizes of the patches, depending on the applied force (see Supplementary Information). The apparent radius (height) of the bilayer patches was observed to decrease by around 5 nm (0.2 nm) when increasing the normal force by around 200 pN from the minimum force required for proper tracking of the surface. Similarly, the

height of surface-bound vesicles was observed to vary by a few nanometers. This indicates that the forces exerted by the tip can induce lateral or normal compression of the lipid assemblies (as well as the tip-coating). Next to tip-convolution effects, the sample deformation thus renders the determination of the correct size of adsorbed vesicles and bilayer patches a complex task, as discussed in the Supplementary Information.

DISCUSSION

In this study, we combine QCM-D, ellipsometry and AFM to provide a detailed picture of the pathways of deposition of lipid vesicles on mica. Previous experimental (Keller et al., 2000; Reviakine and Brisson, 2000; Johnson et al., 2002; Richter et al., 2003) and theoretical (Seifert and Lipowsky, 1990; Seifert, 1997; Zhdanov et al., 2000) studies have shown that adsorbed lipid vesicles can transform into bilayer patches via (at least) three different mechanisms: (i) spontaneous rupture of isolated vesicles, (ii) rupture of vesicles induced by high vesicle density (critical vesicular coverage) and (iii) rupture of vesicles induced by the (active) edge of a bilayer patch. We show here that, by varying the vesicle composition and the calcium-EDTA balance, all above-described mechanisms can be reproduced on mica, and that significant differences exist between mica and silica.

Rupture of isolated vesicles

The time from adsorption to rupture of isolated vesicles, i.e. surface-bound vesicles at sufficiently low coverage, can vary widely. Whereas we found DOTAP to rupture faster than what can be resolved (~1 s) by the employed techniques, DOPC-vesicles were stable (figure 7A) in 2 mM $CaCl_2$ over experimental time scales (~1 h). Both extremes can be understood from a thermodynamic perspective of the interaction between vesicle and support and have been described before (Lipowsky and Seifert, 1991; Seifert, 1997; Reviakine and Brisson, 2000).

We report here on an intermediate time range (minutes to hours) that is needed for DOPS-containing vesicles to rupture in the presence of calcium, which highlights the importance of the kinetic perspective (Zhdanov and Kasemo, 2001). The parameters that govern the rupture dynamics remain to be elucidated and will be discussed further below.

Rupture induced by critical vesicular coverage

The pathway of vesicle rupture induced by the cooperative action of neighboring adsorbed vesicles has been described and characterized in detail on silica (Keller et al., 2000; Reimhult et al., 2002a; Reimhult et al., 2002b; Richter et al., 2003). Similar to silica (Keller et al., 2000), isolated vesicles

containing pure DOPC or DOPC/DOTAP (4:1) were observed to be stable when adsorbed on mica in the presence of calcium (c.f. figure 7A). The formation of SLBs at higher surface coverage evidences that the influence of neighboring vesicles is necessary to induce the rupture of the first vesicles, indicating that the phenomenon of critical vesicular coverage is also present on mica (Reviakine and Brisson, 2000).

Coexistence of several vesicle rupture mechanisms

Once a few vesicles have ruptured by one of the two above-described mechanisms, further vesicle rupture can also be induced by the (active) edge of bilayer patches, enhancing the growth of bilayer patches and, eventually, leading to the formation of an SLB.

As mentioned above it takes minutes to hours for isolated DOPS-containing vesicles to rupture (c.f. figure 2). On the other hand, the time needed to form an SLB is in the range of a few minutes with the employed lipid concentration (~100 μg/mL). This raises the question whether the combination of rupture of isolated vesicles and edge-induced rupture is sufficient to explain the SLB-formation at such short time scales. If vesicle adsorption is much faster than the rupture of isolated vesicles, the surface density of intact vesicles may locally become elevated. This suggests in alternative that rupture induced via the critical vesicular coverage coexists with the rupture of isolated vesicles. Future theoretical treatments, similar to the ones described earlier by Zhdanov et al. (2000) may allow distinguishing between these two scenarios. Also, as the time needed to establish the critical vesicular coverage is dependent on the bulk lipid concentration, this experimental parameter provides the means for controlling the balance between the rupture of isolated vesicles and rupture induced by the critical vesicular coverage.

We note that the presence of a local minimum in frequency and a local maximum in dissipation, as commonly observed by QCM-D, is a necessary but not a sufficient condition to identify the critical vesicular coverage as the unique mechanism for the formation of the first bilayer patches. Additional AFM-imaging - allowing for the examinations on the level of a single vesicle - or interrupted QCM-D

measurements – allowing for the investigation of the overall stability of the adsorbed lipid material - are required to ascertain that the critical vesicular coverage is the only rupture-initiating mechanism present.

The role of shape changes in bilayer patches

AFM data indicate that the interactions between lipids and the mica support are sufficiently strong in order for SLB-patches and bound vesicles to be stably located in the presence of small and transient forces. On the other hand, the interactions are sufficiently weak to allow for movements and/or reshaping in the presence of permanent forces, such as the line tension of small non-circular patches (c.f. figure 3) (Muresan and Lee, 2001). This sliding motion has important consequences, as reshaping patches can catalyze mergers with neighboring patches (c.f. figure 4) or vesicles and thereby enhance vesicle rupture via active bilayer edges.

It may be tempting to postulate that such an effect can be of considerable value to fill up defects in the bilayer during the final stage of SLB-formation. In the light of our observation that the propensity for shape changes is decreased (at least locally) at higher coverage (figure 6A) such a conclusion appears premature. However, as demonstrated earlier for silica (Richter et al., 2003), close to defect-free SLBs can be formed without reshaping being present. A potential origin for the decreased speed of shape relaxation may be the presence of contaminations in the bilayer or on the solid support.

Taken together, our results demonstrate that the time scales associated with the different mechanisms of vesicle rupture can vary. As the mechanisms of vesicle rupture can coexist and exhibit some degree of interdependence, a multitude of SLB-formation pathways can occur.

Comparing silica and mica – the role of calcium

Several pronounced differences in the deposition of lipid vesicles and in the SLB-formation on mica and silica supports can be deduced. For simplicity, we distinguish two situations, namely the absence and the presence of calcium.

In the absence of calcium, repulsive (attractive) interactions between negatively (positively) charged vesicles and the negatively charged support are stronger on mica than on silica. This underlines the important role of electrostatic interactions and suggests that mica may be more strongly negatively charged than silica[2].

We found that vesicles made of DOPC become less flattened on mica than on silica. In opposition, the attractive van der Waals forces are expected to be higher on mica than on silica[3]. This may indicate that electrostatic double layer forces are sufficiently strong to outweigh the van der Waals forces, despite the small surface potential of DOPC under the employed conditions (Egawa and Furusawa, 1999). Alternatively, additional short-ranged forces may substantially influence the vesicle-support interaction[4]. While it remains difficult to identify the exact nature of the interaction forces, this example is illustrative for the subtleties of the vesicle-support interactions.

The presence of calcium has a remarkable effect on the lipid deposition on mica as evidenced by the fact that SLBs can be formed at a DOPS-content of 80% and more (Reviakine et al., 2001; Richter and Brisson, 2004). Recent results (Richter et al.) indicate that, during SLB-formation, DOPS-molecules become distributed asymmetrically between the two SLB-leaflets. Calcium's exceptional capacity to promote SLB-formation correlates thus with our finding that DOPS molecules become enriched in the SLB's mica-facing side, suggesting the presence of a particular calcium-mediated interaction between mica and DOPS. It is tempting to identify the (re)distribution of DOPS within and in-between (flip-flop) the leaflets of adsorbed vesicles as the determinant parameter for the slow rupture kinetics that we

---

[2] Surface charges around 0.1 electron per nm^{-2} have been reported for both mica (Pashley, 1981a; Pashley, 1981b) and silica (Bolt, 1957; Considine and Drummond, 2001), with significant variations as a function of electrolyte concentration, pH and surface preparation (Toikka and Hayes, 1997; Morigaki et al., 2002; Penfold et al., 2002).

[3] Non-retarded Hamaker constants of $A = 2 \cdot 10^{-20}$ J ($0.8 \cdot 10^{-20}$ J) have been reported for two surfaces of mica (silica) interacting in water (Israelachvili, 1992).

[4] Silica and mica are known to exhibit remarkable differences in their short-range interactions (Chapel, 1994; Israelachvili and Wennerström, 1996).

observed for isolated DOPS-containing vesicles. Interestingly, Yaroslavov et al. (1994; 1998) have reported that a membrane-binding polycationic polymer can induce the redistribution of negatively charged lipids towards the outer leaflet of SUVs, although the mechanism of this polycation-induced flip-flop remains little understood. It appears conceivable that the calcium-mediated interaction between mica and DOPS, in conjunction with the stress that other vesicle-support interactions exert on the vesicle, may enhance lipid flip-flop in mica-bound vesicles, thereby promoting their rupture.

We note that the SLB-promoting effect of calcium is not restricted to DOPS but extends also to DOPC. While calcium was observed to facilitate adsorption and SLB-formation on silica, too, the effect was considerably less pronounced.

Mica-bound lipid material retained some degree of mobility, whereas bilayer patches were found to be immobile on silica. Could a difference in the roughness of the two supports explain this effect (Rädler et al., 1995)? The roughness of silica wafers employed in the reference study (Richter et al., 2003), was in the range of 0.1 nm (Richter and Brisson, 2003), i.e., well below what is generally considered the thickness of the water layer between the lipids and the solid support (Bayerl and Bloom, 1990; Johnson et al., 1991). We therefore refrain from attributing the observed differences entirely to roughness. Other effects may be induced by the nature of the interactions between the solid support and bilayer patches and/or their boundary.

The current study thus underlines the important role of the solid support in determining the lipid deposition pathway. Whereas the investigations undertaken in this work identified important parameters that determine the lipid deposition pathway, it is hoped that further detailed comparative studies on mica, silica and other surfaces (such as titanium oxide) at varying ionic strength and calcium content will provide access to information on the quantitative as well as molecular level. In particular, such investigations may help to separate the contribution of vesicle-support, inter-vesicle and intra-bilayer interactions, respectively, in the lipid deposition process and, in particular, to elucidate the molecular nature of the calcium-mediated interaction between DOPS and the support.

Combining QCM-D, AFM and Ellipsometry

We emphasize the importance of combining QCM-D, ellipsometry and AFM to obtain the results reported in this study. The application of all techniques on an identical support allowed obtaining kinetic information about the adsorption, desorption and rupture of vesicles with high time resolution as well as detailed information about local structural changes of the lipid assemblies. While the multi-technique approach gives an improved control over possible experimental artifacts, the combination on an identical support opens up for a detailed quantitative investigation of SLB-formation or other self-assembly processes.

Influences of the AFM-tip on the appearance of immobilized vesicles and SLB-patches

The modification of the AFM-tip with a lipid-repelling polymer proved essential in order to reproducibly obtain images of different coexisting lipid structures. Both SLB-patches and vesicles could be imaged stably and without lateral displacement. Furthermore, controlled tip-forces allowed investigating shape transitions such as patch movement and coalescence or vesicle rupture. Such events can potentially be exploited to quantify the influence of the tip on the apparent size of surface-bound vesicles and bilayer patches. In particular, the coalescence of patches can be exploited to determine the correct size of bilayer patches and the rupture of adsorbed, flattened vesicles can be used to estimate the diameter of the corresponding non-flattened vesicle as well as to evaluate the influence of the tip on the apparent width of a vesicle (see Supplementary Information).

CONCLUSION AND PERSPECTIVES

The combination of QCM-D, AFM and ellipsometry has allowed identifying and characterizing a multitude of processes that take place from the adsorption of vesicles to the formation of a complete SLB on mica. While most of these processes act locally, their interdependence and kinetics determine together the overall dynamics of the SLB-formation process.

Our study provides evidence for important differences in the interaction of lipids with silica and mica, stressing the importance of the solid support, the calcium-EDTA balance and electrostatic interactions in the SLB-formation process.

The improved imaging of surface-confined lipid structures demonstrated in this study together with the exploitation of the shape transitions (Supplementary Information) for size determinations open up for the reliable quantification of adsorbed lipid material and for the investigation, in detail, of the shape of surface-bound vesicles.

ACKNOWLEDGEMENTS

The group of Markus Textor (ETH, Zurich, Switzerland) is acknowledged for providing the PLL-*g*-PEG. We thank Wim Hermens (University of Maastricht, The Netherlands) for providing access to the ellipsometre as well as Aleš Benda and Martin Beneš (Heyrovský Institute, Prague, Czech Republic) for help with its setup. Sylvie Bordère (ICMCB, Bordeaux, France) and Ilya Reviakine (Technical University Clausthal, Clausthal-Zellerfeld, Germany) are acknowledged for discussions around the shape of confined bilayer patches and the SLB-formation process, respectively. Ralf Richter was partly supported by the CNRS, the Ministère délégué à la Recherche (France), the Conseil Régional d'Aquitaine (France) and by EC grant FP6-NMP4-CT2003-505868 "Nanocues". This research was supported by the Conseil Régional d'Aquitaine, the Fonds Européen de Développement Régional, and EC grant FP6-NMP4-CT2003-505868 "Nanocues".

REFERENCES

Bayerl, T.M., and M. Bloom. 1990. Physical properties of single phospholipid bilayers adsorbed to micro glass beads. A new vesicular model system studied by ^{2}H-nuclear magnetic resonance. *Biophys. J.* 58:357-362.

Benes, M., D. Billy, W.T. Hermens, and M. Hof. 2002. Muscovite (mica) allows the characterization of supported bilayers by ellipsometry and confocal fluorescence correlation spectroscopy. *Biol. Chem.* 383:337-341.

Benvegnu, D.J., and H.M. McConnell. 1992. Line Tension between Liquid Domains in Lipid Monolayers. *J. Phys. Chem.* 96:6820-6824.

Bolt, G.H. 1957. Determination of the Charge Density of Silica Sols. *J. Phys. Chem.* 61:1166-1169.

Boxer, S.G. 2000. Molecular transport and organization in supported lipid membranes. *Curr. Opin. Chem. Biol.* 4:704-709.

Chapel, J.-P. 1994. Electrolyte Species Dependent Hydration Forces between Silica Surfaces. *Langmuir* 10:4237-4243.

Considine, R.F., and C.J. Drummond. 2001. Surface Roughness and Surface Force Measurement: A Comparison of Electrostatic Potentials Derived from Atomic Force Microscopy and Electrophoretic Mobility Measurements. *Langmuir* 17:7777-7783.

Corsel, J.W., G.M. Willems, J.M.M. Kop, P.A. Cuypers, and W.T. Hermens. 1986. The Role of Intrinsic Binding Rate and Transport Rate in the Asorption of Prothrombin, Albumin and Fibrinogen to Phospholipid Bilayers. *J. Colloid Interface Sci.* 111:544-554.

Cuypers, P.A., J.W. Corsel, M.P. Janssen, J.M.M. Kop, W.T. Hermens, and H.C. Hemker. 1983. The Adsorption of Prothrombin to Phosphatidylserine Multilayers Quantitated by Ellipsometry. *J. Biol. Chem.* 258:2426-2430.

Egawa, H., and K. Furusawa. 1999. Liposome Adhesion on Mica Surface Studied by Atomic Force Microscopy. *Langmuir* 15:1660-1666.

Huang, N.-P., J. Vörös, S.M. De Paul, M. Textor, and N.D. Spencer. 2002. Biotin-Derivatized Poly(L-lysine)-*g*-poly(ethylene glycol): A Novel Polymeric Interface for Bioaffinity Sensing. *Langmuir* 18:220-230.

Israelachvili, J., and H. Wennerström. 1996. Role of hydration and water structures in biological and colloidal interactions. *Nature* 379:219-225.

Israelachvili, J.N. 1992. Intermolecular and Surface Forces. Academic Press Limited, London.

Jass, J., T. Tjärnhage, and G. Puu. 2000. From liposomes to supported, planar bilayer structures on hydrophilic and hydrophobic surfaces: an atomic force microscopy study. *Biophys. J.* 79:3153-3163.

Johnson, J.M., H. Taekijp, S. Chu, and S.G. Boxer. 2002. Early Steps of Supported Bilayer Formation Probed by Single Vesicle Fluorescence Assays. *Biophys. J.* 83:3371-3379.

Johnson, S.J., T.M. Bayerl, D.C. McDermott, W.A. Adam, A.R. Rennie, R.K. Thomas, and E. Sackmann. 1991. Structure of an adsorbed dimyristoylphosphatidylcholine bilayer measured with specular reflection of neutrons. *Biophys. J.* 59:289-294.

Kam, L., and S.G. Boxer. 2003. Spatially Selective Manipulation of Supported Lipid Bilayers by Laminar Flow: Steps Toward Biomembrane Microfluidics. *Langmuir* 19:1624-1631.

Keller, C.A., K. Glasmästar, V.P. Zhdanov, and B. Kasemo. 2000. Formation of supported membranes from vesicles. *Phys. Rev. Lett.* 84:5443-5446.

Keller, C.A., and B. Kasemo. 1998. Surface Specific Kinetics of Lipid Vesicle Adsorption Measured with a Quartz Crystal Microbalance. *Biophys. J.* 75:1397-1402.

Larsson, C., M. Rodahl, and F. Höök. 2003. Characterization of DNA Immobilization and Subsequent Hybridization on a 2D Arrangement of Streptavidin on a Biotin-Modified Lipid Bilayer Supported on SiO_2. *Anal. Chem.* 75:5080-5087.

Liang, X., G. Mao, and K.Y.S. Ng. 2004. Probing small unilamellar EggPC vesicles on mica surface by atomic force microscopy. *Colloids Surf. B* 34:41-51.

Lipowsky, R., and U. Seifert. 1991. Adhesion of Vesicles and Membranes. *Mol. Crys. Liq. Cryst.* 202:17-25.

McConnell, H.M., T.H. Watts, R.M. Weis, and A.A. Brian. 1986. Supported planar membranes in studies of cell-cell recognition in the immune system. *Biochim. Biophys. Acta* 864:95-106.

Milhiet, P.E., M.-C. Giocondi, O. Baghdadi, F. Ronzon, B. Roux, and C. le Grimellec. 2002. Spontaneous insertion and partitioning of alkaline phosphatase into model lipid rafts. *EMBO reports* 3:485-490.

Morigaki, K., T. Baumgart, U. Jonas, A. Offenhäuser, and W. Knoll. 2002. Photopolymerization of Diacetylene Lipid Bilayers and its Application to the Construction of Micropatterned Biomimetic Membranes. *Langmuir* 18:4082-4089.

Muresan, A.S., and K.Y.C. Lee. 2001. Shape Evolution of Lipid Bilayer Patches Adsorbed on Mica: an Atomic Force Microscopy Study. *J. Phys. Chem. B* 105:852-855.

Nollert, P., H. Kiefer, and F. Jähnig. 1995. Lipid Vesicle Adsorption versus Formation of Planar Bilayers on Solid Surfaces. *Biophys. J.* 69:1447-1455.

Pashley, R.M. 1981a. DLVO and Hydration Forces between Mica Surfaces in Li^+, Na^+, K^+ and Cs^+ Electrolyte Solutions: A Correlation of Double-Layer and Hydration Forces with Surface Cation Exchange Properties. *J. Colloid Interface Sci.* 83:531-546.

Pashley, R.M. 1981b. Hydration forces between mica surfaces in aqueous electrolyte solutions. *J. Colloid Interface Sci.* 80:153-162.

Penfold, J., E. Staples, and I. Tucker. 2002. On the Consequences of Surface Treatment on the Adsorption of Nonionic Surfactants at the Hydrophilic Silica-Solution Interface. *Langmuir* 18:2967-2970.

Reimhult, E., F. Höök, and B. Kasemo. 2002a. Temperature dependence of formation of a supported phospholipid bilayer from vesicles on SiO_2. *Phys. Rev. E* 66:051905-051901-051904.

Reimhult, E., F. Höök, and B. Kasemo. 2002b. Vesicle adsorption on SiO_2 and TiO_2: Dependence on vesicle size. *J. Chem. Phys.* 117:7401-7404.

Reimhult, E., F. Höök, and B. Kasemo. 2003. Intact vesicle adsorption and supported biomembrane formation from vesicles in solution: influence of surface chemistry, vesicle size, temperature and osmotic pressure. *Langmuir* 19:1681-1691.

Reviakine, I., A. Bergsma-Schutter, A.N. Morozov, and A. Brisson. 2001. Two-Dimensional Crystallization of Annexin A5 on Phospholipid Bilayers and Monolayers: A Solid-Solid Phase Transition Between Crystal Forms. *Langmuir* 17:1680-1686.

Reviakine, I., W. Bergsma-Schutter, and A. Brisson. 1998. Growth of Protein 2-D Crystals on Supported Planar Lipid Bilayers Imaged in Situ by AFM. *J. Struct. Biol.* 121:356-361.

Reviakine, I., and A. Brisson. 2000. Formation of Supported Phospholipid Bilayers from Unilamellar Vesicles Investigated by Atomic Force Microscopy. *Langmuir* 16:1806-1815.

Reviakine, I., and A. Brisson. 2001. Streptavidin 2D crystals on Supported Phospholipid Bilayers: Towards Constructing Anchored Phospholipid Bilayers. *Langmuir* 17:8293-8299.

Richter, R.P., and A. Brisson. 2003. Characterization of lipid bilayers and protein assemblies supported on rough surfaces by atomic force microscopy. *Langmuir* 19:1632-1640.

Richter, R.P., and A. Brisson. 2004. QCM-D on mica for parallel QCM-D - AFM studies. *Langmuir* 20:4609-4613.

Richter, R.P., N. Maury, and A. Brisson. submitted. On the effect of the solid support on the inter-leaflet distribution of lipids in supported lipid bilayers. *Langmuir*.

Richter, R.P., A. Mukhopadhay, and A. Brisson. 2003. Pathways of lipid vesicle deposition on solid surfaces: a combined QCM-D and AFM study. *Biophys. J.* 85:3035-3047.

Rodahl, M., F. Höök, A. Krozer, P. Brzezinski, and B. Kasemo. 1995. Quartz crystal microbalance setup for frequency and Q-factor measurements in gaseous and liquid environments. *Rev. Sci. Instrum.* 66:3924-3930.

Rädler, J., H. Strey, and E. Sackmann. 1995. Phenomenology and Kinetics of Lipid Bilayer Spreading on Hydrophilic Surfaces. *Langmuir* 11:4539-4548.

Sackmann, E. 1996. Supported Membranes: Scientific and Practical Applications. *Science* 271:43-48.

Salafsky, J., J.T. Groves, and S.G. Boxer. 1996. Architecture and Function of Membrane Proteins in Planar Supported Bilayers: A Study with Photosynthetic Reaction Centers. *Biochemistry* 35:14773-14781.

Sauerbrey, G. 1959. Verwendung von Schwingquartzen zur Wägung dünner Schichten und zur Mikrowägung. *Z. Phys.* 155:206-222.

Seantier, B., C. Breffa, O. Félix, and G. Decher. 2004. In Situ Investigations of the Formation of Mixed Supported Lipid Bilayers Close to the Phase Transition Temperature. *Nano Letters* 4:5-10.

Seifert, U. 1997. Configuration of fluid membranes and vesicles. *Adv. Phys.* 46:13-137.

Seifert, U., and R. Lipowsky. 1990. Adhesion of vesicles. *Phys. Rev. A* 42:4768-4771.

Starr, T.E., and N.L. Thompson. 2000. Formation and Characterization of Planar Phospholipid Bilayers Supported on TiO_2 and $SrTiO_3$ Single Crystals. *Langmuir* 16:10301-10308.

Toikka, G., and R.A. Hayes. 1997. Direct Measurement of Colloidal Forces between Mica and Silica in Aqueous Electrolyte. *J. Colloid Interface Sci.* 191:102-109.

Tokumasu, F., A.J. Jin, G.W. Feigenson, and J.A. Dvorak. 2003. Atomic force microscopy of nanometric liposome adsorption and nanoscopic membrane domain formation. *Ultramicroscopy* 97:217-227.

Tompkins, H.G. 1993. A User's Guide to Ellipsometry. Academic Press, Inc., London. 260 p.

Watts, T.H., A.A. Brian, J.W. Kappler, P. Marrack, and H.M. McConnell. 1984. Antigen presentation by supported planar membranes containing affinity-purified I-A^d. *Proc. Natl. Acad. Sci. USA* 81:7564-7568.

Yaroslavov, A.A., E.A. Kiseliova, O.Y. Udalykh, and V.A. Kabanov. 1998. Integrity of Mixed Liposomes Contacting a Polycation Depends on the Negatively Charged Lipid Content. *Langmuir* 14:5160-5163.

Yaroslavov, A.A., V.E. Kul'kov, A.S. Polinsky, B.A. Baibakov, and V.A. Kabanov. 1994. A polycation causes migration of negatively charged phopholipids from the inner to outer leaflet of the liposomal membrane. *FEBS Lett.* 340:121-123.

Yip, C.M., A.A. Darabie, and J. McLaurin. 2002. Aβ42-Peptide Assembly on Lipid Bilayers. *J. Mol. Biol.* 318:97-107.

Zhdanov, V.P., and B. Kasemo. 2001. Comments on Rupture of Adsorbed Vesicles. *Langmuir* 17:3518-3521.

Zhdanov, V.P., C.A. Keller, K. Glasmästar, and B. Kasemo. 2000. Simulation of adsorption kinetics of lipid vesicles. *J. Chem. Phys.* 112:900-909.

TABLES

TABLE 1

Parameters measured by QCM-D for the deposition of vesicles with varying lipid composition.

lipid ratio DOTAP	DOPC	DOPS	[Ca] (mM)	Δf_{min} (Hz)	ΔD_{max} (10^{-6})	Δf_{fin} (Hz)	ΔD_{fin} (10^{-6})	t_{SLB} (min)	vesicle deposition pathway	stability of vesicles at low coverage
1	-	-	0 [c]	-	0.5	-25	0.2	12	SLB	fast rupture[a]
1	4	-	0 [c]	-35	2.7	-27	0.8	3	SLB	no rupture, no desorption
-	1	-	0 [c]	-103	10.0	-	-	-	SVL	no rupture, slow desorption
	9	1	0 [c]	-13	2.0	-	-	-	SVL	-
-	4	1	0 [c]	0	0	-	-	-	no adsorption	-
1	-	-	2	-	0.3	-24	0.2	10	SLB	fast rupture[a]
1	4	-	2	-32	1.8	-26.5	0.5	3	SLB	no rupture, no desorption
-	1	-	2	-50	4.0	-25	0	5	SLB	no rupture, no desorption
-	9	1	2	-50	2.6	-25	0	3.3	SLB	-
-	4	1	2	-45	2.5	-26	0.2	3.3	SLB	slow rupture[b]
-	2	1	2	-34	1.7	-25.5	0.2	5	SLB	slow rupture[b]
-	1	1	2	-36	1.5	-25.5	0.2	1.3	SLB	slow rupture[b]
-	1	2	2	-34	1.5	-25.5	0.2	2	SLB	slow rupture[b]
-	1	4	2	-32	1.0	-26	0.2	1.3	SLB	slow rupture[b]

[a] rupture within seconds or less after adsorption; [b] rupture within minutes or hours after adsorption; [c] measured in the presence of 2 mM EDTA

FIGURE LEGENDS

FIGURE 1

QCM-D response, i.e., changes in frequency (-o-) and dissipation (---), for the deposition of SUVs composed of DOPC/DOPS (molar ratio 4:1) on mica in 2 mM $CaCl_2$. Lipid exposure starts at 0 min. The peak in dissipation and the minimum in frequency indicate the presence of intact vesicles bound at an intermediate state. The final frequency shift of -25 Hz and the low final dissipation shift indicate the presence of an SLB. A rinse with buffer (*arrow*) does not affect the SLB.

FIGURE 2

SLB-formation from SUVs made of DOPC/DOPS (4:1) interrupted at an early stage. (*A*) QCM-D response (frequency, Δf (-o-), and dissipation, ΔD (---), at 25 MHz): after the rinse (*arrow*), the adsorbed vesicles are not stable. (*B*-*C*) Two sequential images recorded after transfer of the mica-coated QCM-D sensor to the AFM: vesicles and bilayer patches, identified by their height and shape (cross-section in *inset*, green and red arrowheads, respectively) coexist. A few vesicles (*asterisks*) become ruptured by the influence of the AFM-tip. Image size (z-scale): 1 μm (20 nm); the slow scan direction (contact mode) is indicated (*arrows*). (*D*) Changes in the ellipsometric angle, $\Delta\Delta$: after the rinse (*solid line, arrow*) at $\Delta\Delta = -0.18°$, corresponding to 30% of a complete SLB, the signal remains stable confirming that lipid material is not desorbing. For comparison, the response for the formation of a complete SLB is shown (*dotted line*), resulting in $\Delta\Delta = -0.6°$. Lipid deposition for the ellipsometry measurements was performed at concentrations of ~5 μg/mL (*solid line*) and ~10 μg/mL (*dotted line*), respectively.

FIGURE 3

Sequential AFM-images (contact mode) before (*A*), during (*B*) and after (*C*) the merger of bilayer patches of DOPC/DOPS (4:1). Images *A* and *C* are scanned at lowest possible forces (~100 pN). In image *B* the force was slightly increased (~300 pN) inducing the merger (*arrowheads*) of several

patches (*asterisks*). Image size (z-scale): 1.25 μm (10 nm); the slow scan direction is indicated (*arrows*).

FIGURE 4

Sequential AFM-images (contact mode) of coalescence events of bilayer patches of DOPC/DOPS (4:1). After the tip-induced merger of patches 1-3 (*A*), the coalescence with patches 4 (*B*), 5-6 (*C*) and 7 (*D*) is induced by the movements of the reshaping patch. Image size (z-scale): 1.75 μm (10 nm); the slow scan direction is indicated (*arrows*).

FIGURE 5

SLB-formation from SUVs made of DOPC/DOPS (4:1) interrupted at a late stage. (*A*) QCM-D response (frequency, Δf (-o-), and dissipation, ΔD (---), at 25 MHz): after the rinse (*arrow*) close to the minimum in frequency, surface-bound lipid material undergoes quick structural changes. (*B*) AFM-image (tapping mode) taken after the transfer of the sample: extended patches coexist with a few vesicles (*asterisks*). The bilayer patches exhibit edges with small local radius of curvature (<150 nm, *arrowheads*). Image size (z-scale): 1.5 μm (20 nm). (*C*) Changes in the ellipsometric angle, $\Delta\Delta$: after rinsing (*solid line, arrow*) at $\Delta\Delta = -0.41°$, corresponding to 68% of a complete SLB, the signal remains stable confirming that lipid material is not desorbing. The response for the formation of a complete SLB is shown for comparison (*dotted line*). Lipid deposition for the ellipsometry measurements was performed at concentrations of ~20 μg/mL (*solid line*) and ~10 μg/mL (*dotted line*), respectively.

FIGURE 6

(A) AFM-image of an SLB formed from a solution of 10 μg/mL SUVs made of DOPC/DOPS (4:1) and interrupted at a very late stage (contact mode). Numerous elongated defects persist. The ends of some of these defects (*arrowheads*) appear sharp. It is not clear whether these ends indeed represent a true bilayer boundary with a small but finite radius of curvature (~15 nm). Alternatively, these points may mark the limits of an unresolved gap (*dotted line*) between two bilayer patches. (B) AFM-image of an

SLB formed from a solution of 100 μg/mL SUVs made of DOPC/DOPS (4:1) (tapping mode). The bilayer is ideal without visible defects, except for two protrusions (*arrowheads*), likely to be trapped vesicles. Image size (z-scale): 10 μm (10 nm).

FIGURE 7

QCM-D responses (frequency, Δf (-o-), and dissipation, ΔD (---)) for the deposition of 0.1 mg/mL SUVs composed of different lipids on mica. Lipid exposure starts at 0 min. (*A*) DOPC in 2 mM $CaCl_2$ (25 MHz, flow mode): after the rinse (*black arrow*) at an early stage of SLB-formation, Δf and ΔD remain stable, indicating that adsorbed vesicles are stably bound and do neither desorb nor rupture; re-incubation with SUVs (*white arrow*) leads to completion of the SLB-formation. (*B*) DOPC in 2 mM EDTA (35 MHz, flow mode): formation of an SVL exhibiting high dissipation; a rinse with EDTA-containing buffer (*black arrow*) leads to partial desorption of the vesicles; a rinse with calcium containing buffer (*black dotted arrow*) leads to the formation of an SLB, as characterized by a frequency shift of -26 Hz and a very low dissipation shift; subsequent addition of SUVs in 2 mM $CaCl_2$ (*white arrow*) does not further affect the SLB. (*C*) DOTAP in 2 mM EDTA (35 MHz, flow mode): formation of an SLB; vesicles rupture instantaneously upon adsorption.

FIGURE 8

The local minimum in frequency, $|\Delta f_{min}|$ (*A*, *C*), and SLB-formation time, t_{SLB} (*B*, *D*), as a function of the fractional lipid charge, σ, (≡ average number of charges per lipid molecule). Data for mica (*filled circles*) and silica (*open circles*, adapted from ref. (Richter et al., 2003)) are shown in the presence of 2 mM EDTA (*A*, *B*) and 2 mM calcium (*C*, *D*), respectively. Data are given for lipid mixtures and conditions that lead to SLB-formation; $|\Delta f_{min}|$ is indicated only if the SLB-formation exhibits a local minimum in frequency.

FIGURE 1

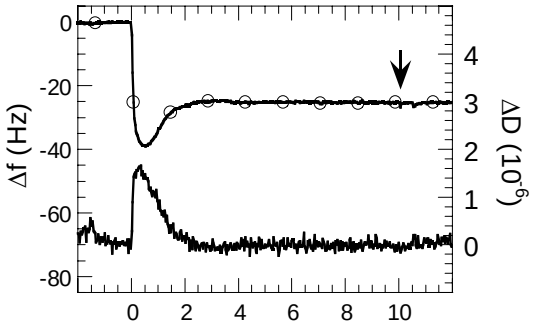

FIGURE 2

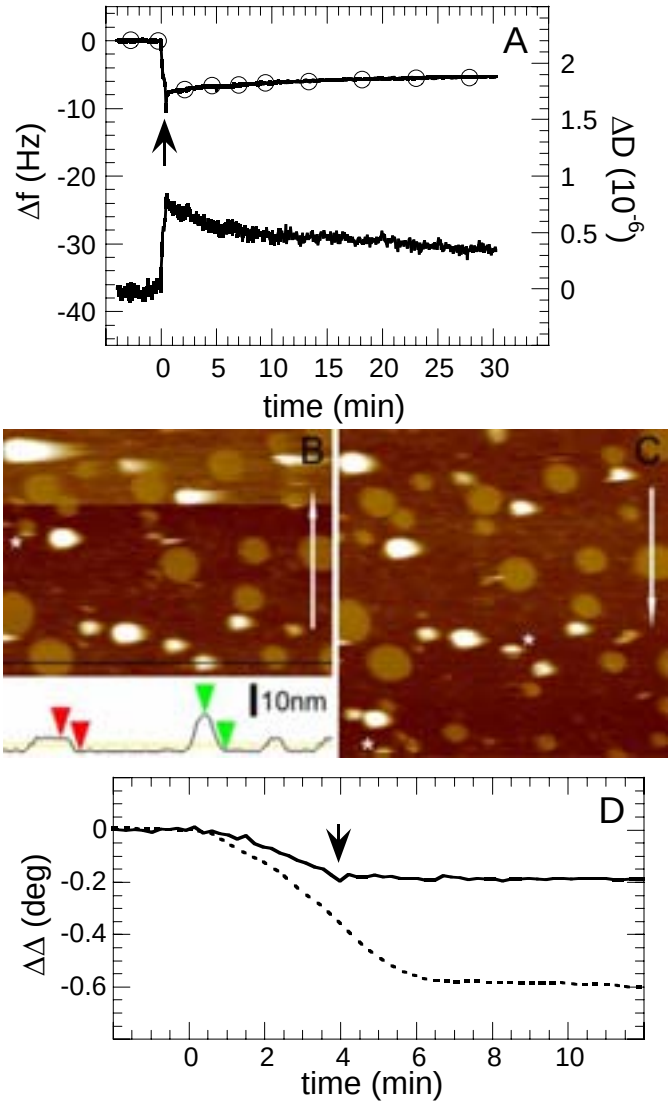

FIGURE 3

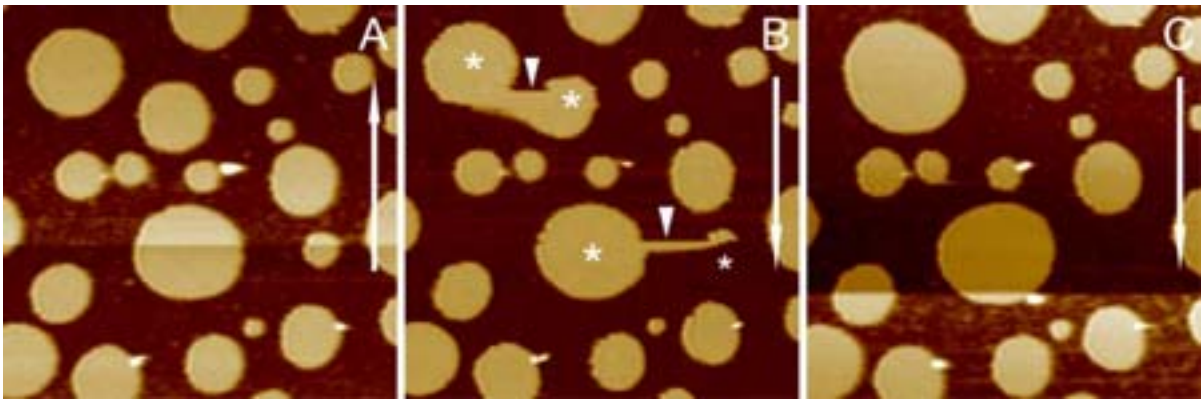

FIGURE 4

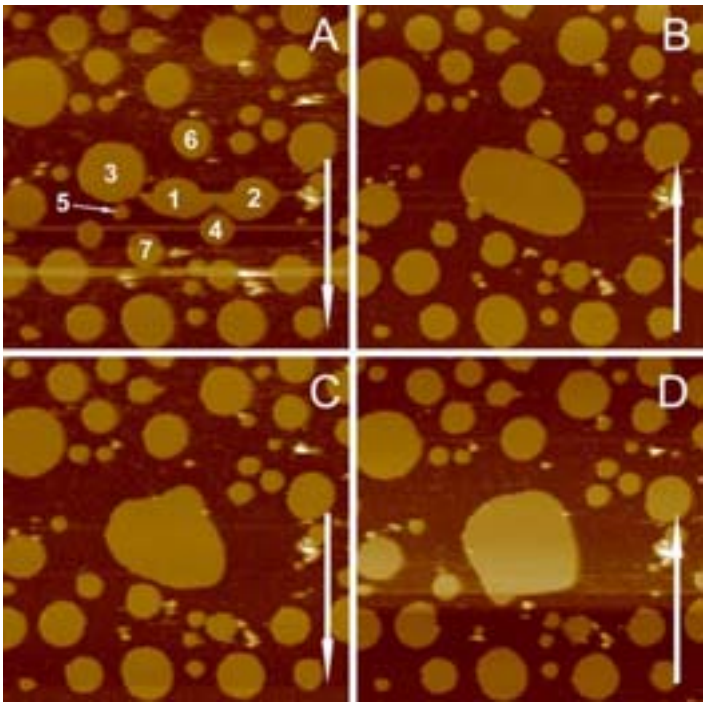

FIGURE 5

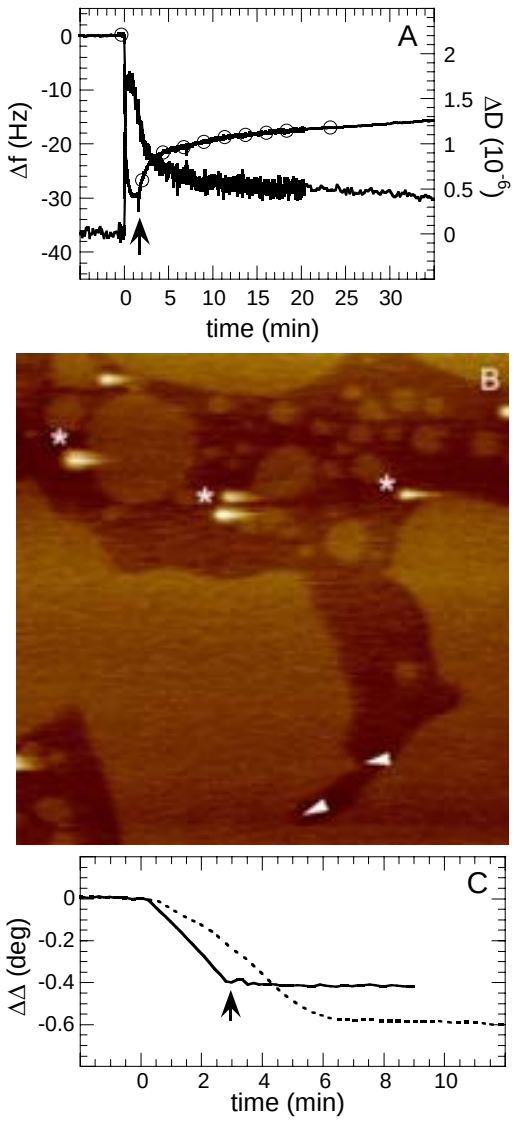

FIGURE 6

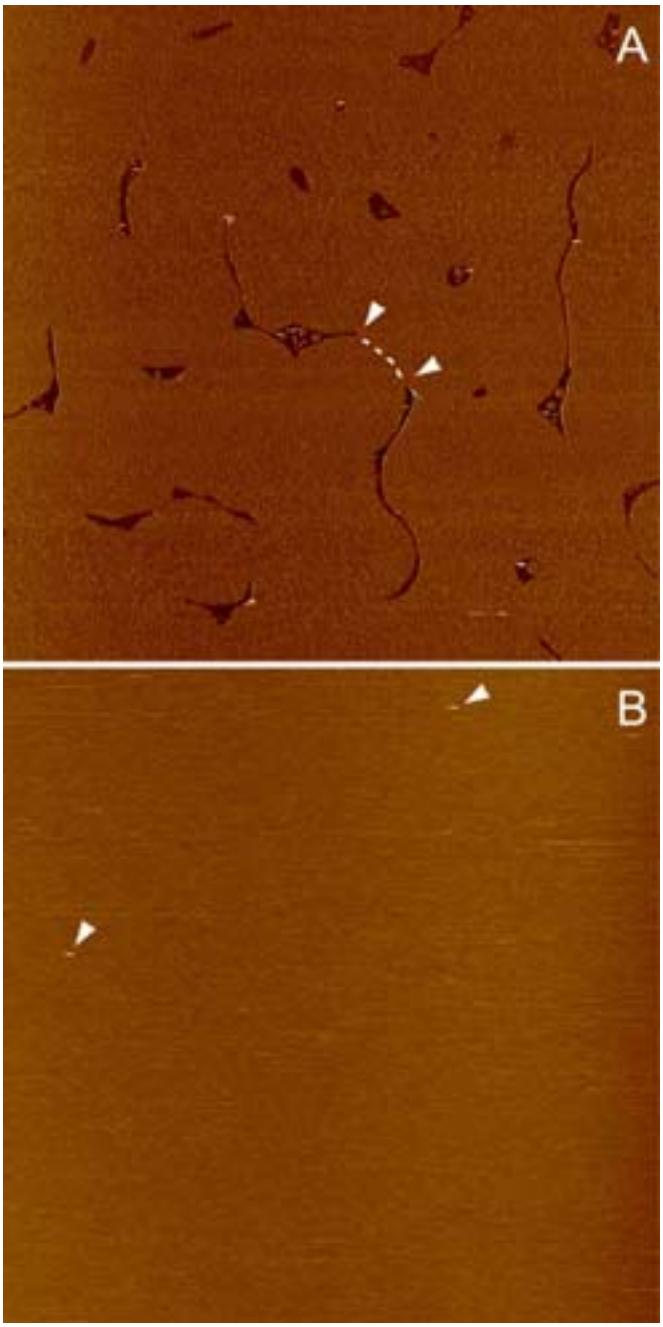

FIGURE 7

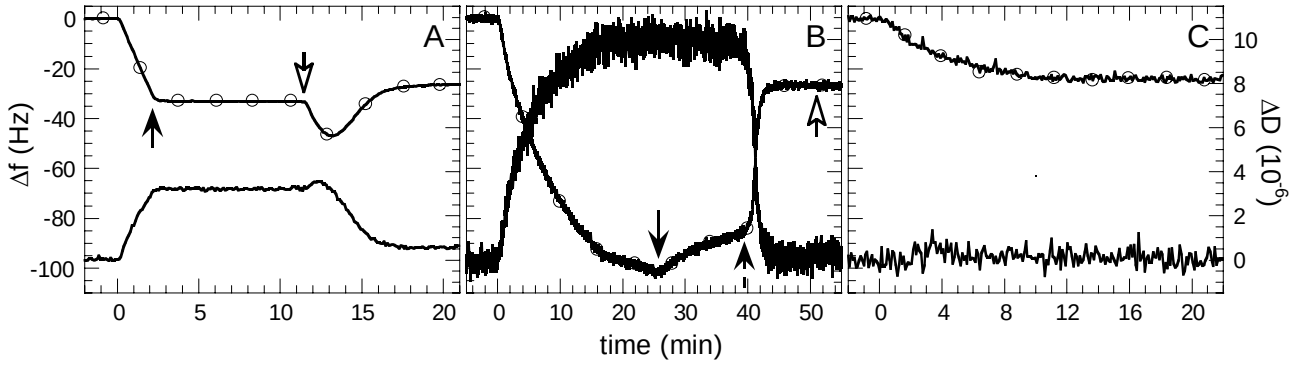
A
B
C
Δf (Hz)
ΔD (10⁻⁶)
time (min)
0
-20
-40
-60
-80
-100
0
5
10
15
20
0
10
20
30
40
50
0
4
8
12
16
20
10
8
6
4
2
0

FIGURE 8

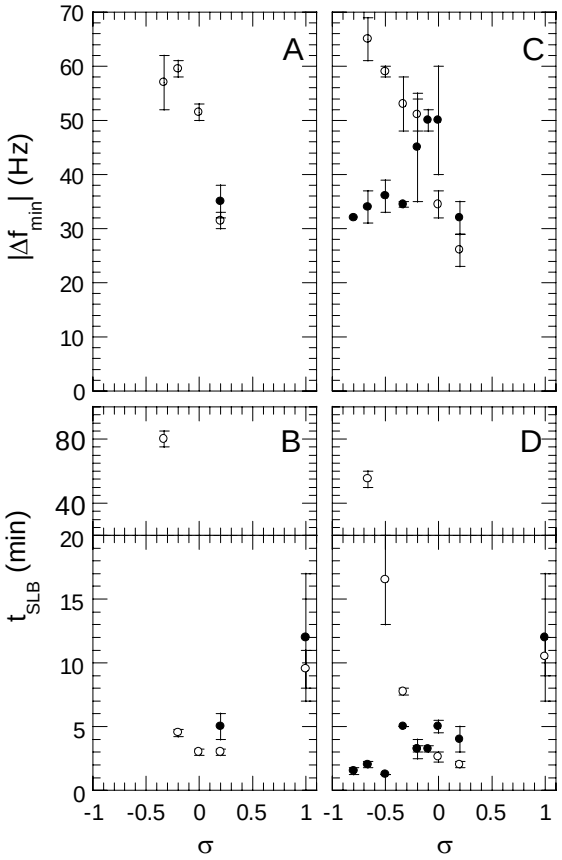

SUPPLEMENTARY INFORMATION

Manuscript title: Following the formation of supported lipid bilayers on mica – a study combining AFM, QCM-D and ellipsometry

Authors: Ralf P. Richter and Alain R. Brisson

Evaluating the effect of the AFM-tip on the apparent size of vesicles and bilayer patches

Both vesicles and bilayer patches are by nature soft and compressible objects. Therefore, the apparent size of these objects, as measured by AFM, is potentially affected not only by the tip-convolution (leading to size overestimation for lateral features) but also by the compression of the objects (leading to size underestimation). While the question of deformation of vesicles normal to the surface has been addressed recently (Liang et al., 2004), little experimental data is available about the lateral deformation of vesicles and bilayer patches. We demonstrate here how shape changes that were observed in our study, namely, the coalescence of pairs of bilayer patches into larger patches and the transformation of vesicles into bilayer patches, can be used to address this question.

1. Determining the true size of bilayer patches from their apparent size in AFM-images

The apparent radius of the bilayer patches was observed to decrease by around 5 nm when increasing the normal force by around 200 pN from the minimum force (50-100 pN) required for proper tracking of the surface. This indicates that increased forces can indeed lead to the lateral squeezing of soft material, though it is unclear whether the observed effects can be attributed to the compression of the lipid patch, to the soft coating of the AFM-tip (the radius of gyration of the PEG-chains is in the range of 2 nm (Kenausis et al., 2000)) or to both effects. In the frame of this work we assume that the interplay of compression effects and tip-convolution will determine the apparent patch radius (scheme SI.1). In the following we will show that, based on a simple model, the real size of bilayer patches can be determined from their apparent size by analyzing the merger of two neighboring patches into one larger patch.

We utilize the assumption that the area covered by the initial patches with real radii r_A and r_B is conserved upon merger into one patch with radius r_{AB}:

$$S_{AB} = \pi r_{AB}^2 = \pi r_A^2 + \pi r_B^2 = S_A + S_B . \quad (1)$$

Furthermore, we define the apparent radii as

$$r_i^{app} = r_i + \Delta r \text{ for } i = \text{A, B or AB} \quad (2)$$

and assume that the perturbations Δr are induced locally upon scanning of the patch-boundaries, i.e., Δr is not dependent on the patch size[i]. Note that Δr is a function of the height, h^*, over the mica surface at which the patch size is measured and depends on the normal force applied by the scanning tip, F_{tip} (c.f. scheme SI.1). It is convenient to define the ratio $k = r_B / r_A$ with $0 < k \leq 1$ as well as

$$c = \frac{r_A + r_B - r_{AB}}{r_{AB}} = \frac{1+k}{\sqrt{1+k^2}} - 1 \text{ with } 0 < c \leq \sqrt{2} - 1 \approx 0.41 . \quad (3)$$

The apparent areas occupied by the merged patch and the merging patches are then

$$S_{AB}^{app} = \pi\left(r_{AB}^{app}\right)^2 = \pi\left(r_{AB} + \Delta r\right)^2 \text{ and} \quad (4a)$$

$$S_A^{app} + S_B^{app} = \pi\left[\left(r_A^{app}\right)^2 + \left(r_B^{app}\right)^2\right] = \pi\left[\left(r_{AB} + \Delta r\right)^2 + 2c\Delta r r_{AB} + \Delta r^2\right], \quad (4b)$$

respectively, resulting in a change in apparent area upon merger of

$$\Delta S^{app} = S_A^{app} + S_B^{app} - S_{AB}^{app} = 2c\pi\Delta r r_{AB}^{app} + (1-2c)\pi\Delta r^2 = 2c\pi\Delta r r_{AB} + \pi\Delta r^2 . \quad (4c)$$

It follows that

$$\Delta S^{app} = 0 \text{ for } \Delta r = 0 , \quad (5a)$$

$$\Delta S^{app} > 0 \text{ for } \Delta r > 0 \text{ as well as} \quad (5b)$$

$$\Delta S^{app} < 0 \text{ for } \Delta r < 0 \text{ and } r_{AB} > \left|\Delta r / 2c\right| . \quad (5c)$$

[i] For simplicity we consider only the average radius and average perturbations and do not take into account asymmetric perturbation as, e.g., induced by the tip scanning in contact mode. Similar conclusions hold though for the asymmetric case.

The relations 5a-c imply that for sufficiently large patch sizes ($r_{AB} > |\Delta r / 2c|$), the underestimation (overestimation) of the patch size always leads to negative (positive) values of ΔS^{app}. ΔS^{app} becomes zero *only* if the apparent patch sizes equal the real sizes. Furthermore, the magnitude of the change in apparent area increases as a linear function of the (real and apparent) patch sizes. Consequently, measuring ΔS^{app} for some merger events such as those shown in figure 3 should enable to verify whether the apparent patch size corresponds to the real patch size.

In figure SI.1 ΔS^{app} is plotted as a function of r_{AB}^{app} (obtained at different heights, h^*) for a few merger events. Both negative and positive values of ΔS^{app} were observed, indicating that indeed both tip-induced compression and tip-convolution effects can influence the apparent patch size significantly. Smallest perturbations ($\Delta S^{app} \approx 0$) were in most cases obtained when the patch size was determined at a height between 1.5 and 0.3 nm below the top of the patch.

In order to get an estimate of the relative influence of squeezing and tip-convolution we plotted the apparent patch radius as a function of h^* (figure SI.2). At lowest forces ($F_{tip} \approx$ 50-100 pN), the apparent radius coincides with the true radius at heights close to the top of the patch ($h^* \approx 4.3$ nm) and tip-convolution effects lead to a considerable overestimation with decreasing heights (~15 nm over a height range of 3 nm). For slightly increased forces ($F_{tip} \approx 300$ pN), the true radius is obtained at a height between 2.9 and 3.9 nm, thus giving an underestimation of 2 to 6 nm at heights close to the top of the patch.

In conclusion, over a reasonable range of low forces (≤300 pN) within which the normal tip-forces can be maintained experimentally, the apparent radius of a bilayer patch, determined at a height close to the top of the patch, will be close (within ~5 nm) to its true radius. For the following investigations we thus use the patch size measured at minimum forces as a representation of the true patch size.

2. Relationship between the radii of a small vesicle and of its resulting bilayer patch

Having established a method to determine the true size of bilayer patches, we can now estimate the size of the corresponding vesicles. Geometric constraints on the packing of lipids lead to unequal repartition of lipid material in the inner and outer leaflet of small vesicles. The amount of lipid material that can occupy each leaflet is assumed to be determined by the radii of the inner and the outer leaflet, r_i and r_o, respectively (c.f. scheme SI.2). The difference of the radii, $r_{ml} = r_o - r_i$, corresponds to the thickness of a lipid monolayer (2.5±0.5 nm)[ii]. Furthermore it is reasonable to assume $S_p = (S_i + S_o)/2$ with S_i, S_o and S_p being the area of the inner and outer leaflet of the vesicle as well as the planar bilayer patch formed from the vesicle, respectively. The relationship between r_i and the radius of the bilayer patch, r_p, of

$$r_i = \tfrac{1}{2}\left(\sqrt{r_p^2 - r_{ml}^2} - r_{ml}\right) \qquad (6a)$$

is easily obtained. Equation 6a can be well approximated by the linear relationship[iii]

$$r_i = \tfrac{1}{2}\left(r_p - r_{ml}\right). \qquad (6b)$$

Furthermore the ratio of lipid repartition between the membrane leaflets is described by

$$\frac{S_o}{S_i} = 1 + \frac{2r_i r_{ml} + r_{ml}^2}{r_i^2}. \qquad (7)$$

For the smallest measured patch radius, $r_p = 14\pm2$ nm, we obtain an inner radius of the vesicle of $r_i = 5.8\pm1.3$ nm, and an outer vesicle radius of $r_v = r_i + 2r_{ml} = 10.8 \pm 1.8\text{nm}$, close to the expected size

[ii] The chosen assumptions imply that the packing of the lipid material is determined by the lipid headgroups in the inner leaflet and by the lipid tails in the outer leaflet (i.e., the shape of a lipid molecule is approximated as a cylinder). Alternatively, one may consider the lipid packing to be determined by the headgroups in both leaflets (i.e., approximate the lipid shape as a truncated cone with the lipid head being located on the cone's base). In this case r_o becomes r_v, $r_{ml} = 5\pm1$ nm (the thickness of a lipid bilayer), and $r_v = r_i + r_{ml}$. While the choice of the model strongly affects the lipid repartition ratio, S_o/S_i, the difference in the vesicle radius is small (1.3 nm).

[iii] The linear form overestimates r_i by less than 0.2 nm for $r_p \geq 10$ nm.

of SUVs. The lipid repartition ratio between the outer and the inner leaflet is around 2.0, in accordance with commonly given values of 1.5 to 3 (Yeagle, 1987).

Taken together the proposed model allows deducing the size of a spherical vesicle from the size of the corresponding bilayer patch with an error of a few nanometers.

3. The flattening of surface-bound vesicles

Upon encounter with the surface, adsorbing vesicles become flattened. We selected events of vesicle rupture into bilayer patches to compare the dimensions of the flattened vesicle, as measured by AFM, with the size of the corresponding spherical vesicles, as calculated according to equation 6b. In figure SI.3A the apparent height of the surface-bound vesicles is plotted as a function of the diameter of the corresponding spherical vesicle. It is immediately apparent that the heights are much smaller than the diameter of the initial vesicle, indicating substantial flattening. Interestingly, the height increases close to linearly with the vesicle size, though the linear fit does not go through the plot's origin. This can be rationalized by the fact that the vesicle's shell (the bilayer) does not contribute to the flattening. Therefore we will henceforward operate with vesicle dimensions, that are reduced by the thickness of the included bilayer(s), i.e., the inner height, $h_i^{app} = h^{app} - 4r_{ml} = h^{app} - 10\text{nm}$, and the inner diameter, $2r_i$ (c.f. figure SI.3A). Consequently, we find that the apparent inner height corresponds to only 20% of the vesicle's original inner diameter.

We performed some measurements at varying forces on some of the vesicles to investigate whether the flattening could, at least in part, be due to elastic deformations induced by the AFM-tip. Indeed, the height was observed to change, though only by a few nanometers over a force range of 100 to 300 pN. An example of the height variation is given by the three experimental points at $2r_i = 163$ nm in figure SI.3A, which all belong to the same vesicle. Similar experimental observations have been reported by Liang et al. (2004). In addition, an estimate of the normal indentation of the vesicles using the Hertz contact model (Laney et al., 1997; Liang et al., 2004) gave small but significant indentations

of 3-4 nm (6-8 nm) at forces of 100 pN (300 pN)[iv]. In conclusion, while the measured heights may slightly underestimate the true heights, they do not change our finding that surface-bound vesicles are considerably flattened.

Having evaluated both r_i and h_i, it becomes eventually possible to calculate the expected width of the surface-bound vesicle. We assume that the inside shape of the flattened vesicle can be modeled as a spherical cap[v]. As the surface area of the spherical unbound vesicle with radius r_i should correspond to the surface area of the spherical cap, characterized by its height, h_i, and width, $d_i = d - 4r_{ml} = d - 10\text{nm}$ (c.f. scheme SI.3), we obtain $4\pi r_i^2 = \pi\left(\frac{1}{2}d_i^2 + h_i^2\right)$ or

$$d_i = \sqrt{8r_i^2 - 2h_i^2}\ . \qquad (8)$$

In figure SI.3B both the apparent width, d_i^{app} - as measured by AFM at a height, $h^* \approx 5$ nm - and the calculated width, d_i - using equation 8 and h_i^{app} - are plotted against $2r_i$. Notably, the apparent width is significantly larger than the calculated width for small vesicle sizes with deviations of 20 nm and more. Based on the performed calculations and our results for the bilayer we suggest that this overestimation is due to tip-convolution effects. Almost surprisingly, apparent and calculated values correspond well for larger vesicle sizes, suggesting that the overall influence of the tip cancels out to give close to real values for the dimensions of the adsorbed vesicle. Additional measurements on a larger population of large vesicles appear though necessary to ensure the significance of this observation.

[iv] The numbers were obtained with a bending modulus, $\kappa = 0.25 \cdot 10^{-19}$ J (Seifert and Lipowsky, 1995), a Poisson ratio, $\nu = 0.5$ (Laney et al., 1997), and a thickness of 4.5 nm of the bilayer and a tip radius of 20 nm.

[v] For large vesicles ($r_v >> \Delta r$) the form of a spherical cap was indeed predicted for surface-bound vesicles with constant surface area and variable inner volume (Seifert and Lipowsky, 1990). Furthermore, calculations using the shape of a half-ellipsoid gave very similar results, indicating a relatively weak dependence of the calculated width on the shape model.

Summary and Outlook

The possibility to track events of vesicle rupture and patch coalescence allowed us to investigate the error associated to measuring the size of vesicles and bilayer patches by AFM. The size of bilayer patches and the height of immobilized vesicles can be measured with fairly good accuracy under appropriate conditions, the measured width of the vesicle, though, was considerably overestimated.

While the study demonstrated the feasibility of this approach to investigate the size and the shape of soft material, there is room for improvement. This includes the use of larger vesicles to increase the size range investigated. Another improvement would be approaches of image reconstruction (Villarrubia, 1994; Williams et al., 1996), which could be reliably achieved by co-incubation of vesicles with particles of similar size and shape.

APPENDIX

Determination of the apparent lateral dimensions of vesicles and bilayer patches

The apparent area occupied by a lipid bilayer patch, S^{app}, was determined with the particle analysis routine integrated in the Nanoscope software (VEECO, Dourdan, France). The average apparent radius, r^{app}, of a bilayer patch was calculated as $r^{app} = \sqrt{(S^{app}/\pi)}$. The average apparent radius of surface-bound vesicles was calculated as the geometric mean of the radii measured along the fast and the slow scan axis. The apparent radius along the slow scan axis was determined as half the measured vesicle diameter. The radius along the fast scan axis was measured only on the side on which the tip approaches the vesicle, in order to avoid errors due to improper sample tracking.

REFERENCES

Kenausis, G.L., J. Vörös, D.L. Elbert, N. Huang, R. Hofer, L. Ruiz-Taylor, M. Textor, J.A. Hubbell, and N.D. Spencer. 2000. Poly(L-lysine)-*g*-Poly(ethylene glycol) Layers on Metal Oxide Surfaces: Attachment Mechanism and Effects of Polymer Architecture on Resistance to Protein Adsorption. *J. Phys. Chem. B* 104:3298-3299.

Laney, D.E., R.A. Garcia, S.M. Parsons, and H.G. Hansma. 1997. *Biophys. J.* 72:806.

Liang, X., G. Mao, and K.Y.S. Ng. 2004. Probing small unilamellar EggPC vesicles on mica surface by atomic force microscopy. *Colloids Surf. B* 34:41-51.

Seifert, U., and R. Lipowsky. 1990. Adhesion of vesicles. *Phys. Rev. A* 42:4768-4771.

Seifert, U., and R. Lipowsky. 1995. Morphology of Vesicles. *In* Structure and Dynamics of Membranes. From Cells to Vesicles. Lipowsky R, Sackmann E, editors. Elsevier, Amsterdam. 403-464.

Villarrubia, J.S. 1994. Morphological estimation of tip geometry for scanned probe microscopy. *Surf. Sci.* 321:287-300.

Williams, P.M., K.M. Shakesheff, M.C. Davies, D.E. Jackson, C.J. Roberts, and S.J. Tendler. 1996. Blind reconstruction of scanning probe image data. *J. Vac. Sci. Technol. B* 14:1557-1562.

Yeagle, P. 1987. The Membranes of Cells. Academic Press, Inc., Orlando.

FIGURE LEGENDS

FIGURE SI.1

Change in the apparent area, ΔS^{app}, upon merger of two bilayer patches (c.f. figure 3) as a function of r_{AB}^{app}. Each set of symbols, connected by a line, represents the values that were determined from measurements of the patch sizes before and after the same merger event at different heights over the surface. The arrow indicates the evolution of the height. The height varies by 0.5 nm from symbol to symbol, spanning over a distance from 2.8 nm to 0.3 nm from the top of the patch (4.6±0.2 nm). The forces, F_{tip}, varied between 100 and 300 pN for different merger events. Changes in F_{tip} before and after the merger were though corrected for by taking into account the change in apparent radius of stable patches that were located in the proximity of the merging patches. r_{AB}^{app} is normalized by c (c.f. equation 4). Both negative and positive values of ΔS^{app} occur, indicating the presence of compression and tip-convolution effects, respectively. Close to zero area changes, i.e., the condition for the determination of the true patch size from the apparent patch size (c.f. equation 5), are usually obtained at heights within 1.5 nm from the top of the bilayer.

FIGURE SI.2

Apparent radius, r^{app}, of some bilayer patches measured as a function of the height, h^*, over the mica surface. The patches resulted from coalescence of two patches and were imaged at forces, F_{tip}, between 100 and 300 pN. Dotted lines mark the confidence-range of the true patch radius (c.f. figure 1). At lowest normal forces, the apparent radius coincides with the real radius for heights of 4.4 nm, i.e., close to the top of the bilayer (#8 and #23). For slightly increased forces, the real radius is found at heights of 2.9 to 3.9 nm (#2, #7 and #20). The apparent radius varies by around 15 nm over the investigated height range, likely due to the interplay of compression and tip-convolution.

FIGURE SI.3

Comparison of the apparent dimensions of the flattened vesicle with the calculated dimensions of the corresponding spherical vesicle. (A) Apparent height, h^{app}, versus the diameter, $2r_v$, of the

corresponding spherical vesicle. r_v was determined from the size of the corresponding bilayer patch (equation 6b). The close to linear relationship (dotted line) crosses the origin when the inner dimensions, $h_i^{app} = h^{app} - 10\text{nm}$ and $2r_i$, are employed instead, giving a proportionality of $h_i^{app}/2r_i = 0.2$. (B) Apparent widths, d^{app} and $d_i^{app} = d_f^{app} - 10\text{nm}$ (+), and calculated widths, d and $d_i = d - 10\text{nm}$ (×, calculated according to equation 8, using h_i^{app}), versus the diameters, $2r$ and $2r_i$. At small vesicle size, the apparent width overestimates the calculated width by 20 nm and more, indicating the effect of tip-convolution. Surprisingly, the error diminishes at larger vesicle size. The linear relationship (dotted line) of $d_i/2r_i = 1.38$ is close to the maximum attainable value of 1.41.

SCHEME SI.1

An AFM-tip imaging a bilayer patch. Tip convolution (black solid line) leads to an apparent patch size, r^{app}, that increases with decreasing height, h^*, at which it is measured. Depending on the tip-force, F_{tip}, the edges of the bilayer (or the tip coating) may become laterally compressed, leading to a decreased apparent patch size (yellow dotted line).

SCHEME SI.2

The model of a small spherical vesicle. The two lipid monolayers are confined between the radii, r_i and r_v.

SCHEME SI.3

A spherical cap as the model of a surface-bound, flattened vesicle.

FIGURE SI.1

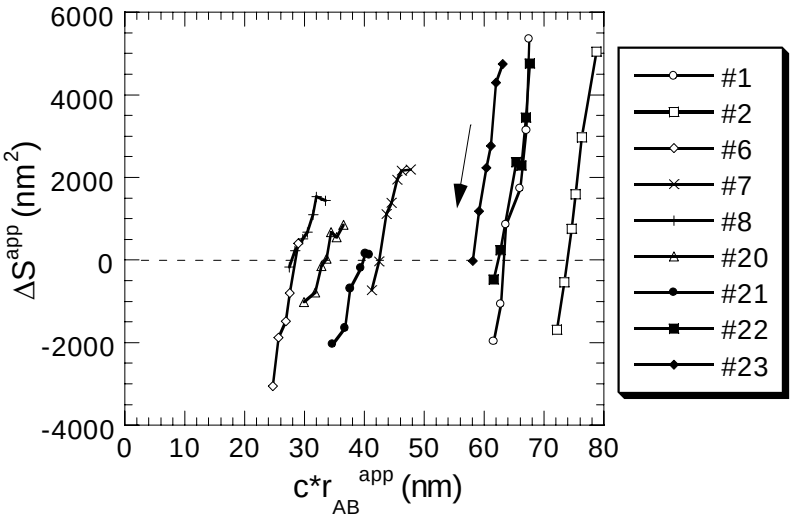

FIGURE SI.2

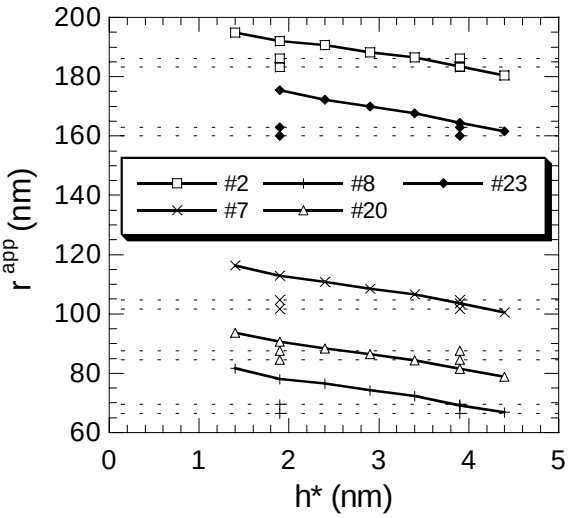

FIGURE SI.3

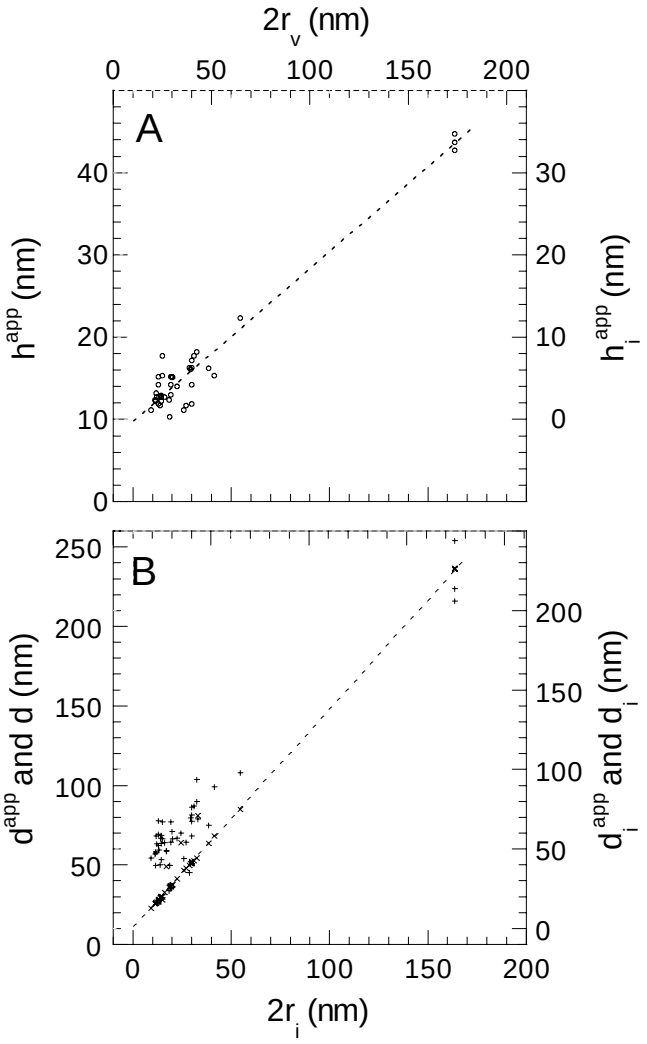
2r_v (nm)
0
50
100
150
200
A
40
30
20
10
0
h^app (nm)
30
20
10
0
h_i^app (nm)
B
250
200
150
100
50
0
d^app and d (nm)
200
150
100
50
0
d_i^app and d_i (nm)
0
50
100
150
200
2r_i (nm)

SCHEME SI.1

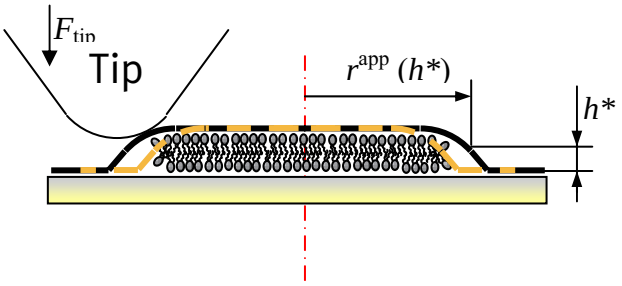

SCHEME SI.2

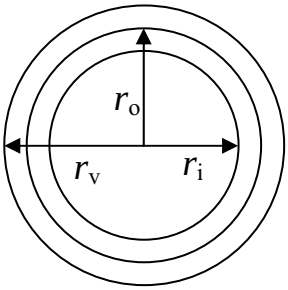

SCHEME SI.3

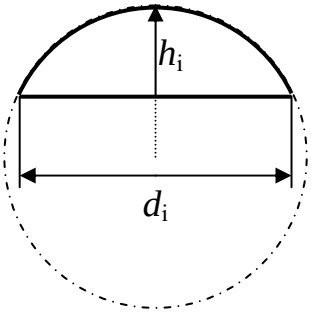

Paper V

Ralf P. Richter, Nicolas Maury and Alain R. Brisson

On the effect of the solid support on the inter-leaflet distribution of lipids in supported lipid bilayers.

Accepted in Langmuir

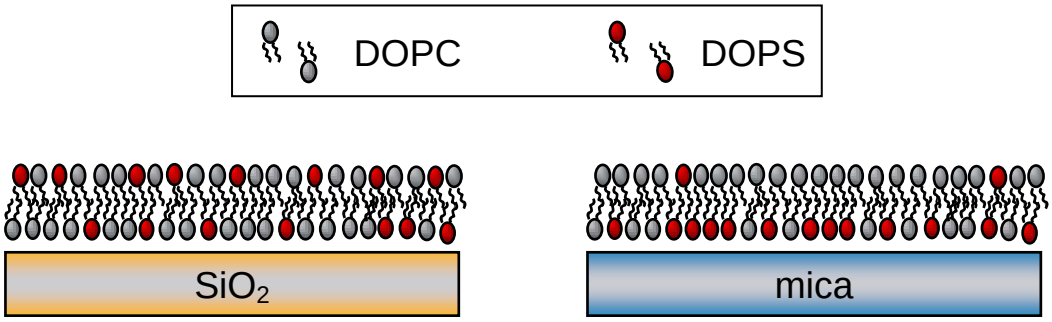

On the effect of the solid support on the inter-leaflet distribution of lipids in supported lipid bilayers

RUNNING TITLE: Lipid redistribution in SLBs

Ralf P. Richter, Nicolas Maury and Alain R. Brisson*

Laboratoire d'Imagerie Moléculaire et Nano-Bio-Technologie, IECB, UMR-CNRS 5471, Université Bordeaux I, 2 Rue Robert Escarpit, 33607 Pessac Cedex, France

*Corresponding author. E-mail: a.brisson@iecb.u-bordeaux.fr

KEYWORDS: mica; silica; quartz crystal microbalance with dissipation monitoring (QCM-D); supported lipid bilayer (SLB); prothrombin; coagulation factor II; dioleoylphospatidylserine (DOPS); dioleoylphosphatidylcholine (DOPC)

ABSTRACT

The adsorption and spreading of lipid vesicles on solid supports has become a popular way to create supported lipid bilayers (SLBs) but little attention has yet been paid to the possible redistribution of lipid material between the two leaflets of an SLB. We use the technique of Quartz Crystal Microbalance with Dissipation Monitoring (QCM-D) to follow the adsorption of prothrombin on SLBs formed from sonicated unilamellar vesicles containing mixtures of dioleoylphosphatidylcholine (DOPC) and dioleoylphospatidylserine (DOPS). The specific interaction of prothrombin with negatively charged lipids is quantified and serves as a reporter of the content of accessible DOPS in SLBs. We compare results obtained on silica and mica and find that the underlying support can induce

substantial redistribution of lipid material between the two leaflets. In particular, SLBs formed on mica showed a substantially depleted amount of accessible DOPS in the presence of calcium. The mechanisms that lead to the lipid redistribution process are discussed.

INTRODUCTION

Supported lipid bilayers (SLBs) have become popular[1,2] as model systems for cell membranes[3,4] and as a building block for biofunctional surfaces[5-7]. The creation of SLBs by adsorption and spreading of vesicles on hydrophilic supports[8] is attractive by its simplicity and important insights into the nature of this self-organization process have been gained during the last years[9-24]. Recent studies by us[21-23] and others[9,12,25,26] provide evidence that the solid support plays a determinant role in the lipid deposition process, giving rise to a multitude of SLB-formation pathways or even preventing SLB-formation.

In addition, the solid support can have pronounced effects on the properties of the SLB, once formed. This may be illustrated by our observation that annexin A5, a protein that adsorbs to DOPS-containing bilayers in a calcium-dependent manner[27], self-assembles into two-dimensional (2D) crystals on SLBs formed on mica[28,29], whereas only a close-packed layer of annexin A5 can be found on silica-SLBs under otherwise identical conditions[30]. While the origin of this effect remains unclear, it prompted us to further investigate the properties of DOPS-containing SLBs on mica and silica.

Little attention has so far been paid to the trans-bilayer distribution of lipids in SLBs that are formed from vesicles containing a mixture of different types of lipids. Commonly, the lipid molecules are assumed to be distributed equally between the two SLB-leaflets, neglecting that the solid support may interact differently with the support-facing (proximal) and the bulk-facing (distal) leaflet.

The objective of this study was to develop an assay that allows measuring the amount of DOPS accessible in the distal leaflet of SLBs formed on silica and on mica. A promising strategy to quantify the amount of accessible lipids is to follow the adsorption of a molecular entity that binds specifically to the lipid in question. An important and - as the example of annexin A5 demonstrates - non-trivial prerequisite for such an assay is that the adsorption and 2D organization of the molecule is not biased by the underlying solid support.

Here we make use of the quartz crystal microbalance with dissipation monitoring (QCM-D) technique to follow the adsorption of prothrombin to DOPS-containing SLBs. As annexin A5,

prothrombin binds to DOPS, in a calcium-dependent manner[31,32]. However, no membrane-induced clustering has been reported to date. The QCM-D technique is by now established as a versatile tool to characterize interfacial processes such as SLB-formation[12,21,26] or protein adsorption[33]. Recently, we have demonstrated that QCM-D measurements can be performed on mica-coated sensors[22], opening up for comparative measurements between silica and mica.

After establishing that prothrombin is indeed a suitable reporter for the DOPS-content in SLBs we demonstrate here that the solid support can indeed have a profound influence on the trans-bilayer distribution of DOPS.

MATERIALS AND METHODS

Materials:

Dioleoylphosphatidylcholine (DOPC) and dioleoylphospatidylserine (DOPS) were purchased from Avanti Polar-Lipids (AL, USA). Lyophilized prothrombin (factor II) from human plasma and other chemicals were purchased from Sigma. Ultrapure water with a resistivity of 18.2 MΩ (Millipore, Molsheim, France) was used.

QCM-D sensor crystals (5 MHz) with a final coating of 50 nm reactively sputter-coated silicon oxide were purchased from Q-SENSE (Gothenburg, Sweden). Muscovite mica disks of 12 mm diameter and low viscosity epoxy glue (EPOTEK 377) for the mica-coating of the QCM-D sensors were purchased from Metafix (Montdidier, France) and Gentec Benelux (Waterloo, Belgium), respectively.

A buffer solution made of 150 mM NaCl, 3 mM NaN_3 and 10 mM HEPES, pH 7.4, was prepared in ultrapure water, and 2 mM $CaCl_2$ or EDTA were added, as indicated in the text. Small unilamellar vesicles (SUVs) of desired lipid mixture were prepared by sonication as described earlier[21]. Lipid concentrations were deduced from the mass of the lipids dissolved and checked by phosphorus content determination[34] of the final lipid suspensions. Errors of less than 10% were obtained. Before use vesicle suspensions were diluted at 0.05 mg/mL, if not otherwise stated.

Lyophilized prothrombin was reconstituted in ultrapure water as described by the manufacturer. Small aliquots were stored at -20°C. Before use the prothrombin solution was thawed at 4°C and used within two days. The protein concentration was determined from optical density measurements at a wavelength of 280 nm using $\varepsilon_{280} = 1.53\ g^{-1}\cdot L\cdot cm^{-1}$.

Substrate preparation:

Silica-coated QCM-D sensors were cleaned by two cycles of exposure to 2% sodium dodecyl sulfate solution for 15 min, rinsing with ultrapure water, blow-drying with nitrogen, and exposure to ultraviolet (UV)/ozone[21] (BHK, Claremont, USA) for 10 min. Cleaned substrates were stored in air and

again exposed to UV/ozone (10 min) prior to use. Mica was glued on QCM-D sensor crystals and verified to operate stably according to a previously described protocol[22].

Quartz Crystal Microbalance with Dissipation Monitoring (QCM-D):

QCM-D measurements were performed with the Q-SENSE D300 system equipped with an Axial Flow Chamber (QAFC 302) (Q-SENSE AB, Gothenburg, Sweden) as described in detail elsewhere[35]. Briefly, upon interaction of (soft) matter with the surface of a sensor crystal, changes in its resonance frequency, Δf, related to attached mass (including coupled water), and in its dissipation, ΔD, related to frictional (viscous) losses in the adlayer are measured with a time resolution of better than 1 s.

The system was operated in slow flow mode. Degassed sample liquid was continuously delivered to the measurement chamber by the aid of a peristaltic pump (ISM832A, Ismatec, Zürich, Switzerland). The T-loop in the measurement chamber was bypassed and flow rates were kept sufficiently low (40 or 80 µL/min, as indicated in the text) to ensure stable operation at a working temperature of 24°C. In order to switch between sample liquids, the flow was interrupted for a few seconds without disturbing the QCM-D signal. A lag time of 2 to 4 minutes remained until the sample reached the QCM-D sensor. With this setup, adsorption and interfacial processes can be followed *in situ* while subsequently exposing different solutions to the surface. The system can be operated at relatively small sample concentrations (1 µg/mL and less) as the flow limits depletion (enrichment) of the bulk upon adsorption (desorption) of sample to (from) the sensor surface or the chamber walls.

Resonance frequency and dissipation were measured at several harmonics (15, 25, 35 MHz), simultaneously. If not stated otherwise, changes in dissipation and normalized frequency ($\Delta f_{norm} = \Delta f_n/n$, with n being the overtone number) of the third overtone ($n = 3$, i.e., 15 MHz) are presented. Adsorbed (wet) masses, Δm, were calculated according to the Sauerbrey equation[36], $\Delta m = -C \cdot \Delta f_{norm}$, with $C = 17.7\ \text{ng}\cdot\text{cm}^{-2}\cdot\text{Hz}^{-1}$. The equation has been demonstrated to be a good approximation for lipid bilayers, adsorbed non-ruptured SUVs or globular proteins on the supports investigated here[12,18,22]. The validity of the equation was further verified by comparison with the

RESULTS

SLB-formation and prothrombin adsorption

In a first step towards using prothrombin as a reporter of the content of accessible DOPS in SLBs, we characterized the adsorption of prothrombin on model SLBs of DOPC/DOPS (molar ratio 4:1) on silica and of DOPC/DOPS (1:1) on mica. Both the formation of the SLB and the adsorption/desorption of prothrombin were followed by QCM-D (figure 1).

The QCM-D response upon exposure of lipid material to the support revealed, as expected, a characteristic two-phase behavior, reflecting the initial adsorption of intact vesicles which is followed by the formation of an SLB[12,22]. The final frequency shift of -25±1 Hz and the low dissipation shift of less than $0.2 \cdot 10^{-6}$ confirm the formation of a lipid bilayer that entirely covered the support with no or only minor defects[18,23].

On a silica-SLB (figure 1A), stepwise addition of prothrombin solution of increasing concentration induced a stepwise decrease of the frequency, indicating adsorption, until equilibration. Rinsing with prothrombin-free buffer caused desorption of more than 80% of the prothrombin over the time scale of one hour. Addition of a buffer containing the calcium chelator EDTA resulted in rapid unbinding of the remaining prothrombin. The results confirm (i) that the adsorption of prothrombin is reversible and (ii) calcium dependent, as previously known[31,32].

Whereas the frequency provides information on the adsorbed amounts, the dissipation can reveal details about the "pathway" of adsorption taken by the prothrombin. It is interesting to note that, after an initial increase with decreasing frequency, the dissipation decreased (figure 1A, asterisk) once the amount of prothrombin adsorbed was higher than an amount corresponding to $\Delta f = -28$ Hz. The decrease in dissipation clearly indicates a rigidification of the adsorbed layer when approaching high protein coverage.

In order to further characterize the state of the prothrombin layer, we make use of the ΔD-Δf-plot (graph A in figure 2). The plot relates the changes in dissipation (i.e., the rigidity of the adlayer) to

changes in frequency (i.e., the adsorbed mass). Consequently, such a graph gives a qualitative fingerprint of how the conformational state (rigid/non-rigid) of the adsorbed layer evolves with coverage[33,38]. As time is not explicit in this plot, it allows for the direct comparison of adsorption and desorption data of several measurements with varying kinetics. Notably, the ΔD-Δf-plots corresponding to both the adsorption phase and the desorption phase superposed exactly. In addition, the ΔD-Δf-plots were identical, both when the bulk prothrombin concentration was increased stepwise (c.f. figure 1A) or when it was maintained at maximum (68 μg/mL) throughout the entire adsorption process (data not shown).

These observations, together with the observed complete reversibility, confirm that the adsorbed amounts of prothrombin are determined entirely by the equilibrium between the prothrombin concentration in the bulk and on the surface and do not dependent on the history of adsorption. This corroborates the validity of our working hypothesis that prothrombin binding can be characterized by the amounts of prothrombin adsorbed at equilibrium for several bulk concentrations.

On SLBs formed on mica (Figure 1B) an adsorption curve for prothrombin similar to that observed on silica-SLBs was obtained. Again the adsorption is almost completely reversible[i] and the ΔD-Δf-plots (graph B in figure 2) for adsorption and desorption follow (i) closely each other as well as (ii) the plots for the silica-SLB (graph A in figure 2). This indicates that the adsorption processes on mica and silica are identical, and thus that the adsorbed amounts on mica and silica can be strictly compared in order to deduce the amount of accessible DOPS.

Dependence of prothrombin adsorption on the DOPS-content

In a second step we measured the adsorption of prothrombin to SLBs over the range of DOPS-contents for which SLBs could be obtained, and systematically investigated the adsorbed amounts at (or close to) equilibrium for various bulk prothrombin concentrations. We employed the ΔD-Δf-plot to

[i] Adsorption was reversible to within less than 10% of the maximum coverage. The remaining frequency shift of -3 Hz may be attributed to minor drifts on the generally less stable mica surfaces.

distinguish between typical and anomalous adsorption behavior. Indeed, most adsorption curves resulted in the typical ΔD-Δf-plots (c.f. graphs A-B in figure 2), with some exceptions (described below in paragraph "Reproducibility", figure 1C and graph C in figure 2) that were discarded. The results for silica and mica are shown in figure 3.

(Almost) no prothrombin adsorbed to pure DOPC, demonstrating the specificity of prothrombin for DOPS. As expected from previous studies[31,32], adsorbed amounts increased with increasing DOPS-content. Importantly the adsorbed amounts vary widely over the entire range of accessible DOPS-concentrations, confirming that prothrombin is a suitable reporter of the DOPS-content. The maximum amounts of bound prothrombin were identical for silica and mica (Δf_{max} = -52±2 Hz), corresponding to a mass of 920±35 ng·cm^{-2}. Comparing the QCM-D mass, that includes coupled water, with reported values of the dry protein mass (~350±60 ng·cm^{-2} [31]), we obtain an effective water content of 55 to 70%, which is in the upper range reported for (sub)monolayers of globular proteins[ii]. The resulting density of ~1.13 g·cm^{-3} (assuming a protein density of 1.35 g·cm^{-3}) gives an effective thickness of the prothrombin layer of around 8 nm, in agreement with available structural data for the prothrombin molecule [42,43].

Intriguingly, the amounts of adsorbed prothrombin for a given nominal DOPS-content (i.e., the content determined by the molar mixing-ratio of DOPC and DOPS) differ markedly between silica-SLBs and mica-SLBs. For example, at a nominal DOPS concentration of 20%, the exposure of prothrombin at a concentration of 8.5 μg/mL led to frequency shifts of -30 Hz with a silica-SLB and -5 Hz with a mica-SLB (figure 3). For a given DOPS-content, the adsorption of prothrombin was systematically higher on silica than on mica, indicating that the amount of accessible DOPS, i.e. the DOPS in the distal lipid leaflet, was higher on silica than on mica. The data demonstrate that the

[ii] For comparison, albumin, ferritin and fibrinogen, both adsorbing at submonolayer coverage on a solid support, showed a solvent content of ~43%[39], ~56%[40] and ~64%[39], respectively. For streptavidin, coupled to a biotinylated-SLB, a solvent content of ~55% was reported[41].

underlying support has a profound influence on the amount of DOPS that is accessible to the protein, and provide indications for an unequal distribution of DOPS molecules between the distal and the proximal leaflet in the SLB on at least one of the solid supports.

In order to investigate which of the solid supports induces an asymmetry in the lipid distribution, we hypothetically assumed a balanced lipid distribution between the two leaflets of the SLB on either silica or mica, taken as a reference, and estimated the amount of accessible DOPS on mica (silica), by comparing the adsorbed amounts of prothrombin with the corresponding "reference" (table 1). The ratio between the nominal and the accessible DOPS-content obtained for silica was smaller than 0.5, for the nominal DOPS-contents of 5, 10 and 20%. A ratio of 0.5 corresponds to the extreme situation, for which the entire DOPS-content in the bilayer is contained in the distal leaflet. Values below 0.5 are thus physically not reasonable. This inconsistency disproves that mica can be a proper reference and, in consequence, indicates that the DOPS-distribution is asymmetric in mica-SLBs.

In contrast, the results obtained for mica with the silica-"reference" remain consistent in the frame of this comparison. Thus, while the presentation in table 1 allowed determining that the distribution of DOPS in mica-SLBs must be asymmetric, it does not enable us to draw any conclusions about the distribution on silica. In principle, the lipid distribution may or may not be asymmetric on silica and independent reference data would be needed to settle this question[iii].

Analysis of the kinetics of adsorption of prothrombin

The full reversibility of prothrombin adsorption implies that one important prerequisite for a simple kinetic model, the Langmuir model, is fulfilled[47]. Plotting the equilibrium adsorbed amounts against the bulk concentration of prothrombin (figure 4), however, reveals sigmoid-shaped (and not Langmuir-

[iii] In recent investigations with annexin A5 [44], we determined the calcium concentration, $[Ca]_{½}$, that is needed to attain half-maximal protein coverage on SLBs formed from DOPC/DOPS (4:1) and found 0.2 mM on silica. This value agrees well with those previously reported on SLBs formed by Langmuir-Blodgett deposition[45] (0.2 mM for DOPC/DOPS (4:1)) and on

isotherm-like) curves, that become particularly apparent for low DOPS-content. In order to compare our data with kinetic constants reported in literature, we have, though, attempted to fit our results to the Langmuir isotherm by neglecting the equilibrium adsorbed amounts at low protein concentration (table 2). The resulting effective dissociation constants, k_D, vary between 0.2 and 0.02 μM over a range of 10 to 50% DOPS. These values are in the range of 0.3 to 0.01 μM reported previously for less than 50% DOPS[31,48-50]. A more rigorous comparison of our results with those reported in literature is obscured by variations in the experimental conditions (such as calcium content and temperature) and the methods used to determine k_D. We therefore did not attempt to employ literature data as an independent reference to evaluate the DOPS-distribution.

Influence of the history of the SLB on the amount of accessible DOPS

In order to investigate the influence of the SLB-formation process on the amount of accessible DOPS in mica-SLBs, we performed the prothrombin test on SLBs that were formed from vesicles (DOPC/DOPS (4:1)) at extreme concentrations of 0.5 mg/mL and 0.015 mg/mL which mark the limits of the experimentally accessible time range for SLB-formation (~30 s to ~20 min). The prothrombin adsorption behavior was identical in both cases (data not shown), indicating that the SLB-formation time does not influence the amount of accessible DOPS.

Also, varying the delay time from SLB-formation to prothrombin exposure over a range of 5 to 60 minutes did not significantly alter the prothrombin adsorption, indicating that slow lipid redistribution between the two leaflets of the mica-SLB is not responsible for the varying amount of accessible DOPS.

Reproducibility

Most of the QCM-D responses obtained for the adsorption and desorption of prothrombin resulted in the typical ΔD-Δf-plot, shown for graphs A and B in figure 2. In some cases, however, significantly

---

vesicles[46] (0.13 mM and 1 mM for DOPC/DOPS (3:1) and (5:1), respectively), suggesting that the inter-leaflet distribution of DOPS in silica-SLBs is indeed symmetrical.

different responses were observed. An example is given in figure 1C, corresponding to a DOPC/DOPS (2:1)-SLB on mica. At a prothrombin concentration of 8.5 μg/mL, the frequency decreased surprisingly (to around -40 Hz of adsorbed prothrombin) whereas the dissipation increased to anomalous levels. A similar phenomenon could be observed at 68 μg/mL and both effects lead to characteristic changes in the slope in the ΔD-Δf-plot (graph C in figure 2). In accordance with these results, the dissipation does not decrease to values close to zero after close-to-complete desorption of prothrombin. Such an anomalous behavior was occasionally observed for SLBs both on silica and on mica and the reason for this behavior is at present not clear. The analysis of freshly prepared prothrombin stock solution by SDS-PAGE analysis revealed some faint bands in addition to the main band, which became more pronounced when the protein was stored at 4°C for a few days (and even faster when kept at room temperature), and thus suggests protein degradation as a possible reason for the observed anomalies. It is notable that the ΔD-Δf-plot allows discriminating between different types of adsorption phenomena and we used this plot as a quality control of our experimental data.

viscoelastic model[37] as implemented in the software QTools 2 (Q-Sense, Gothenburg, Sweden). Deviations of less than 5% were obtained.

Analysis of adsorption kinetics:

Dissociation constants, k_D, and maximum adsorbed amounts, Δf_{max}, were determined by fitting the equilibrium frequency shifts, Δf_e, established at various bulk concentrations, c, of prothrombin to the Langmuir isotherm, $\Delta f_e = \Delta f_{max} \times c / (k_D + c)$.

DISCUSSION

Lipid redistribution induced by the nature of the solid support

The prothrombin assay described here provides evidence for substantial differences in the amount of DOPS present in the distal SLB-leaflet between SLBs formed on mica and on silica, from SUVs with identical DOPS-content. Our results allow attributing these differences to a surface-induced redistribution of DOPS between the two SLB-leaflets.

In particular, the comparison between mica and silica provides indications that the distal leaflet in mica-SLBs is depleted in DOPS. As no indications were found for significant changes in the amount of DOPS in the distal leaflet after completion of SLB-formation, the lipid redistribution must occur during the SLB-formation process. Furthermore, as changes in the SLB-formation kinetics over the experimentally accessible time range (in the order of 10 to 10^3 seconds) did not significantly alter the amount of accessible DOPS, we conclude that the lipid redistribution process takes place on time scales below 10 seconds.

We have previously shown that bilayer patches of sizes ranging from 10^{-4} to 1 μm^2 present an intermediate state in the SLB-formation[15,21,23]. The flip-flop of a lipid molecule across a closed bilayer is commonly considered a slow process (hours and more)[51,52], due to the barrier associated to shuttling the hydrophilic lipid headgroup through the bilayer's hydrophobic interior. On the other hand, a lipid transfer across the edge of the bilayer patches would not be hampered by this barrier and would therefore be much faster. Given that the area covered by a diffusing lipid molecule is in the order of 1 $\mu m^2 \cdot s^{-1}$ [53], we obtain a time of less than 1 s for the lipid transport towards the edge. Assuming that the transfer across the edge occurs at similar time scales or faster[54], this mechanism of lipid redistribution is consistent with the limit experimentally observed for the redistribution time.

Importantly, the proposed mechanism of lipid redistribution implies that the SLB-formation time is sufficient to install an equilibrium state in the lipid distribution with respect to the interaction of the involved lipid species with the underlying support. Consequently, the lipid distribution in the final SLB

would be determined by the properties of the underlying support rather than the genuine lipid distribution in SUVs. In particular, the observed lipid redistribution adds a new aspect to the controversial question of how the lipid leaflets of a rupturing vesicle are oriented on a solid support[3,16,55].

The adsorption behavior of prothrombin – implications for the DOPS-assay

It has already been reported that the adsorption of prothrombin[31,48,56] or prothrombin fragment 1 [32] is not satisfactorily described by the Langmuir model with independent and identical binding sites, even though the adsorption is fully reversible. The sigmoidal shape of the curves shown in figure 4 and the dissociation constants obtained in our study (table 2) are consistent with previously reported results. To avoid interpretational artifacts, we refrained from a more detailed analysis in this study and used the equilibrium frequency shifts in order to quantitatively characterize the adsorption of prothrombin with respect to the DOPS-content in the SLBs. We interpret the similitude in the ΔD-Δf-plots (c.f. figure 2) for most of our measurements over a large range of DOPS-content and for the different supports as a strong indication that the adsorption pathways are identical. Equilibrium adsorbed amounts of prothrombin (c.f. figure 3) can thus serve as a reliable reporter for the accessible DOPS-content.

Comments on the dissipation signal

Phenomenologically, the results shown in figures 1 and 2 demonstrate that the dissipation, in particular the ΔD-Δf-plot, is a sensitive mean to distinguish between different adsorption pathways and/or to identify anomalies in the adsorption behavior[33]. The dissipation signal thus constitutes a relatively simple tool to validate the quality of a measurement and to identify artifacts. Such information is often more difficult to access with other techniques that are commonly used to characterize adsorption phenomena, such as surface sensitive optical techniques (e.g., surface plasmon resonance[57] or ellipsometry) or quartz crystal microbalance without dissipation monitoring[58].

The lateral interaction of neighboring proteins is likely to be at the origin of the coverage-dependent rigidification of the prothrombin layer, evidenced by the response in dissipation (c.f. asterisks in

figure 1A-B). It remains unclear, however, whether the observed decrease in dissipation results from the dense overall packing of prothrombin molecules or from their two-dimensional clustering or ordering. Complementary studies, e.g., by AFM, may answer this question but are outside the scope of this work.

CONCLUSION AND PERSPECTIVES

Our results show that the support has a determining influence on the distribution of lipids between the two leaflets of an SLB that is formed by the spreading of SUVs. In particular, the distal leaflet of mica-SLBs can be the considerably depleted in DOPS. This work thus stresses the importance in understanding the details of the SLB-formation process, in particular the interaction between the solid support and the lipids, in order to be able to predict and control the properties of SLBs, an important step towards designing biofunctional surfaces.

The QCM-D technique was shown to be a reliable tool to characterize the adsorption of prothrombin to SLBs. The dissipation served as an important parameter to distinguish different adsorption pathways and/or to identify anomalies in the adsorption behavior.

ACKNOWLEDGEMENTS

Ralf Richter is the recipient of a Ph.D. fellowship of the Conseil Régional d'Aquitaine, France. This research was supported by the Conseil Régional d'Aquitaine, the Fonds Européen de Développement Régional, and EC grants QLG3-CT2001-00902 and FP6-NMP4-CT2003-505868 Project "Nanocues".

REFERENCES

(1) Sackmann, E. *Science* **1996**, *271*, 43-48.

(2) Boxer, S. G. *Curr. Opin. Chem. Biol.* **2000**, *4*, 704-709.

(3) Salafsky, J.; Groves, J. T.; Boxer, S. G. *Biochemistry* **1996**, *35*, 14773-14781.

(4) Milhiet, P. E.; Giocondi, M.-C.; Baghdadi, O.; Ronzon, F.; Roux, B.; Grimellec, C. le *EMBO reports* **2002**, *3*, 485-490.

(5) Bieri, C.; Ernst, O. P.; Heyse, S.; Hofmann, K. P.; Vogel, H. *Nat. Biotechn.* **1999**, *17*, 1105-8.

(6) Sapuri, A. R.; Baksh, M. M.; Groves, J. T. *Langmuir* **2003**, *19*, 1606-1619.

(7) Kam, L.; Boxer, S. G. *Langmuir* **2003**, *19*, 1624-1631.

(8) Watts, T. H.; Brian, A. A.; Kappler, J. W.; Marrack, P.; McConnell, H. M. *Proc. Natl. Acad. Sci. USA* **1984**, *81*, 7564-7568.

(9) Rädler, J.; Strey, H.; Sackmann, E. *Langmuir* **1995**, *11*, 4539-4548.

(10) Nollert, P.; Kiefer, H.; Jähnig, F. *Biophys. J.* **1995**, *69*, 1447-1455.

(11) Seifert, U. *Adv. Phys.* **1997**, *46*, 13-137.

(12) Keller, C. A.; Kasemo, B. *Biophys. J.* **1998**, *75*, 1397-1402.

(13) Cremer, P. S.; Boxer, S. G. *J. Phys. Chem. B* **1999**, *103*, 2554-2559.

(14) Keller, C. A.; Glasmästar, K.; Zhdanov, V. P.; Kasemo, B. *Phys. Rev. Lett.* **2000**, *84*, 5443-5446.

(15) Reviakine, I.; Brisson, A. *Langmuir* **2000**, *16*, 1806-1815.

(16) Jass, J.; Tjärnhage, T.; Puu, G. *Biophys. J.* **2000**, *79*, 3153-3163.

(17) Zhdanov, V. P.; Kasemo, B. *Langmuir* **2001**, *17*, 3518-3521.

(18) Reimhult, E.; Höök, F.; Kasemo, B. *J. Chem. Phys.* **2002**, *117*, 7401-7404.

(19) Reimhult, E.; Höök, F.; Kasemo, B. *Phys. Rev. E* **2002**, *66*, 051905-1-4.

(20) Johnson, J. M.; Taekijp, H.; Chu, S.; Boxer, S. G. *Biophys. J.* **2002**, *83*, 3371-3379.

(21) Richter, R. P.; Mukhopadhay, A.; Brisson, A. *Biophys. J.* **2003**, *85*, 3035-3047.

(22) Richter, R. P.; Brisson, A. *Langmuir* **2004**, *20*, 4609-4613.

(23) Richter, R. P.; Brisson, A. *Biophys. J.* **submitted**.

(24) Zhdanov, V. P.; Keller, C. A.; Glasmästar, K.; Kasemo, B. *J. Chem. Phys.* **2000**, *112*, 900-909.

(25) Starr, T. E.; Thompson, N. L. *Langmuir* **2000**, *16*, 10301-10308.

(26) Reimhult, E.; Höök, F.; Kasemo, B. *Langmuir* **2003**, *19*, 1681-1691.

(27) Govorukhina, N.; Bergsma-Schutter, A.; Mazères-Dubut, C.; Mazères, S.; Drakopoulou, E.; Bystrykh, L.; Oling, F.; Mukhopadhyay, A.; Reviakine, I.; Lai Kee Him, J.; Brisson, A. In *Annexins: Biological importance and annexin-related pathologies*; Bandorowicz-Pikula, J., Ed.; Landes Bioscience/Eurekah.com: Georgetown, Tex., 200337-55.

(28) Reviakine, I.; Bergsma-Schutter, A.; Morozov, A. N.; Brisson, A. *Langmuir* **2001**, *17*, 1680-1686.

(29) Reviakine, I.; Bergsma-Schutter, W.; Brisson, A. *J. Struct. Biol.* **1998**, *121*, 356-361.

(30) Richter, R. P.; Brisson, A. *Langmuir* **2003**, *19*, 1632-1640.

(31) Kop, J. M. M.; Cuypers, P. A.; Lindhout, T.; Hemker, H. C.; Hermens, W. T. *J. Biol. Chem.* **1984**, *259*, 13993-13998.

(32) Pearce, K. H.; Hiskey, R. G.; Thompson, N. L. *Biochemistry* **1992**, *31*, 5983-5995.

(33) Höök, F.; Larsson, C.; Fant, C. In *Encyclopedia of Surface and Colloid Science*; Marcel Dekker, Inc.: digital publisher, 2002774-791.

(34) Rouser, G.; Fleischer, S.; Yamamoto, A. *Lipids* **1975**, *5*, 494-496.

(35) Rodahl, M.; Höök, F.; Krozer, A.; Brzezinski, P.; Kasemo, B. *Rev. Sci. Instrum.* **1995**, *66*, 3924-3930.

(36) Sauerbrey, G. *Z. Phys.* **1959**, *155*, 206-222.

(37) Voinova, M. V.; Rodahl, M.; Jonson, M.; Kasemo, B. *Phys. Scripta* **1999**, *59*, 391-396.

(38) Höök, F.; Ray, A.; Nordén, B.; Kasemo, B. *Langmuir* **2001**, *17*, 8305-8312.

(39) Höök, F.; Vörös, J.; Rodahl, M.; Kurrat, R.; Böni, P.; Ramsden, J. J.; Textor, M.; Spencer, N. D.; Tengvall, P.; Gold, J.; Kasemo, B. *Colloids Surf. B* **2002**, *24*, 155-170.

(40) Caruso, F.; Furlong, D. N.; Kingshott, P. *J. Colloid Interface Sci.* **1997**, *186*, 129-140.

(41) Larsson, C.; Rodahl, M.; Höök, F. *Anal. Chem.* **2003**, *75*, 5080-5087.

(42) Lim, T. K.; Bloomfield, V. A.; Nelsestuen, G. L. *Biochemistry* **1977**, *16*, 4177-4181.

(43) Tulinsky, A.; Park, C. H.; Skrzypczak-Jankun, E. *J. Mol. Biol.* **1988**, *202*, 885-901.

(44) Richter, R. P.; Lai Kee Him, J.; Brisson, A. *manuscript in preparation*.

(45) Andree, H. A. M.; Reutelingsperger, C. P. M.; Hauptmann, R.; Hemker, H. C.; Hermens, W. T.; Willems, G. M. *J. Biol. Chem.* **1990**, *265*, 4923-4928.

(46) Pigault, C.; Follenius-Wund, A.; Schmutz, M.; Freyssinet, J.-M.; Brisson, A. *J. Mol. Biol.* **1994**, *236*, 199-208.

(47) Norde, W. *Adv. Coll. Int. Sci.* **1986**, *25*, 267-340.

(48) Nelsestuen, G. L.; Broderius, M. *Biochemistry* **1977**, *16*, 4172-4177.

(49) Lecompte, M. F.; Miller, I. R.; Elion, J.; Benarous, R. *Biochemistry* **1980**, *19*, 3434-3439.

(50) Andree, H. A. M.; Hermens, W. T.; Willems, G. M. *Colloids Surf. A* **1993**, *78*, 133-141.

(51) Israelachvili, J. N., *Intermolecular and Surface Forces*. 2 ed. 1992, London: Academic Press Limited.

(52) John, K.; Schreiber, S.; Kubelt, J.; Herrmann, A.; Müller, P. *Biophys. J.* **2002**, *83*, 3315-3323.

(53) Benda, A.; Benes, M.; Marecek, V.; Lhotský, A.; Hermens, W. T.; Hof, M. *Langmuir* **2003**, *19*, 4120-4126.

(54) Kasson, P. M.; Pande, V. S. *Biophys. J.* **2004**, *86*, 3744-3749.

(55) Contino, P. B.; Hasselbacher, C. A.; Ross, J. B.; Nemerson, Y. *Biophys. J.* **1994**, *67*, 1113-1116.

(56) Corsel, J. W.; Willems, G. M.; Kop, J. M. M.; Cuypers, P. A.; Hermens, W. T. *J. Colloid Interface Sci.* **1986**, *111*, 544-554.

(57) Knoll, W. *Ann. Rev. Phys. Chem.* **1998**, *49*, 569-638.

(58) Janshoff, A.; Galla, H.-J.; Steinem, C. *Angew. Chemie Int. Ed.* **2000**, *39*, 4004-4032.

TABLES

TABLE 1

Comparison of the nominal and the accessible DOPS-content for SLBs on mica (A) and on silica (B), as obtained by the prothrombin assay (figure 3), considering as references either silica (A) or mica (B).

	support	hypothetical reference	DOPS-content			
			nominal (%)	accessible[a] (%)	nominal/ accessible	proximal leaflet/ distal leaflet[b]
A	mica	silica	0	0	-	-
			10	3 ± 1	3.3 ± 1.1	5.7 ± 3.4
			20	7 ± 1	2.9 ± 0.5	4.7 ± 1.0
			33	13 ± 2	2.5 ± 0.5	4.1 ± 1.0
			50	20 ± 2	2.5 ± 0.3	4.0 ± 0.6
			67	> 55	< 1.2	< 1.4
			80	> 60	< 1.3	< 1.7
B	silica	mica	0	0	-	-
			5	16 ± 4	0.31 ± 0.11 [c]	- [c]
			10	32 ± 4	0.31 ± 0.05 [c]	- [c]
			20	50 ± 2	0.40 ± 0.02 [c]	- [c]
			33	65 ± 3	0.51 ± 0.03	0.02 ± 0.06
			50	72 ± 3	0.69 ± 0.03	0.39 ± 0.06

[a] The amount of accessible DOPS was determined by fitting the set of equilibrium frequency shifts, Δf_e, obtained on a mica-SLB (A) (a silica-SLB (B)) of given nominal DOPS-content to the set of (hypothetical) reference curves for the silica-SLB (mica-SLB); [b] Distribution of DOPS between the proximal and the distal leaflet of the SLB, given by 2 × nominal DOPS-content / accessible DOPS-content – 1. It is assumed that the nominal DOPS-content corresponds to the overall DOPS-content in the SLB; [c] Values for the ratio between nominal and accessible DOPS-content below 0.5 are physically unreasonable (see text for details) and no meaningful values for the DOPS-distribution between the bilayer leaflets can therefore be obtained.

TABLE 2

Effective kinetic constants obtained for the adsorption of prothrombin on silica-SLBs (data from figure 4A, the regime of low coverage ($|\Delta f| < 20$ Hz) was neglected).

DOPS (%)	k_D (10^{-8} M)	Δf_{max} (-Hz)
10	21.9 ± 6.9	40.5 ± 3
20	5.6 ± 2.3	50 ± 2
33	2.9 ± 1.0	54.5 ± 2
50	1.9 ± 0.8	53.5 ± 2

FIGURE LEGENDS

FIGURE 1

Changes in frequency, Δf (-○-), and dissipation, ΔD (---), for the formation of SLBs and the subsequent adsorption of prothrombin. SLBs were formed from SUVs of a DOPC/DOPS-mixture with molar ratio 4:1 on silica (25 MHz) (A), 1:1 on mica (15 MHz) (B) and 2:1 on mica (15 MHz) (C). Solid arrows indicate the exposure of SUVs and prothrombin; associated numbers denote the prothrombin concentration in μg/mL. Dashed arrows indicate the rinse with buffer containing 2 mM Ca^{2+}, no Ca^{2+} or 2 mM EDTA, as denoted. The decrease in dissipation above around 28 Hz (asterisks in (A) and (B)) indicates a rigidification of the prothrombin layer with increasing coverage. The flow speed was 40 μL/min for the exposure with lipids and prothrombin at a concentration of ≥ 17 μg/mL and 80 μL/min for all other adsorption and desorption steps.

FIGURE 2

Plots of ΔD versus Δf for the adsorption (desorption) of prothrombin on (from) SLBs. Whereas the plots for the adsorption of prothrombin on DOPC/DOPS (4:1) on silica (A) and on DOPC/DOPS (1:1) on mica (B) are almost identical, anomalous responses are observed for a measurement with DOPC/DOPS (2:1) on mica (C). The data corresponds to the measurements shown in figure 1. The time course, starting at $\Delta f = \Delta D = 0$ is implicit in this plot and indicated by solid arrows.

FIGURE 3

Equilibrium frequency shifts, Δf_e, for the adsorption of prothrombin on SLBs of varying nominal DOPS-content on silica (A) and mica (B). Bulk concentrations of prothrombin were 1.7 (○), 4.3 (□), 8.5 (◇), 17 (×), 34 (+) and 68 μg/mL (△), respectively. Lines are included to guide the eye.

FIGURE 4

Equilibrium frequency shifts, Δf_e, as a function of bulk concentrations for the adsorption of prothrombin on SLBs on silica (A) and mica (B). SLBs were formed from SUVs of DOPC (○) and

DOPC/DOPS-mixtures (molar ratio) 19:1 (□), 9:1 (◇), 4:1 (×), 2:1 (+), 1:1 (△) and 1:4 (●). Lines are included to guide the eye.

FIGURE 1

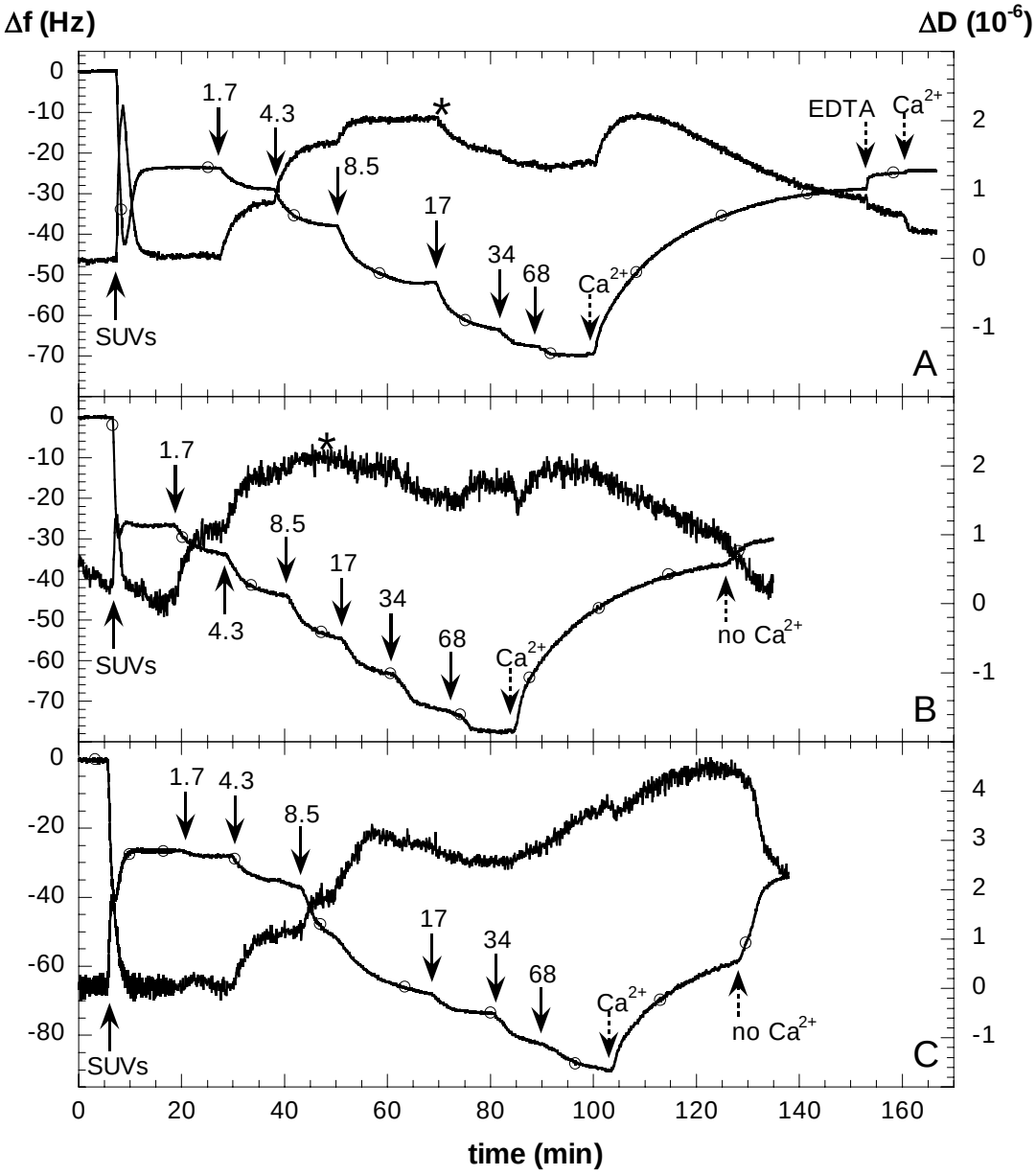

FIGURE 2

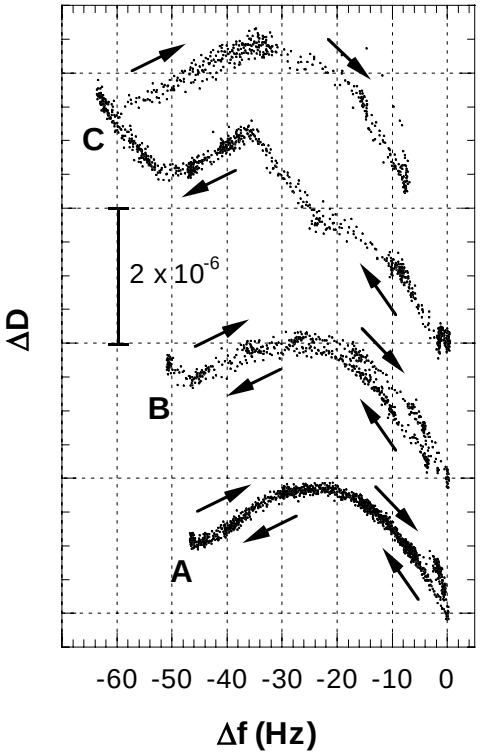

FIGURE 3

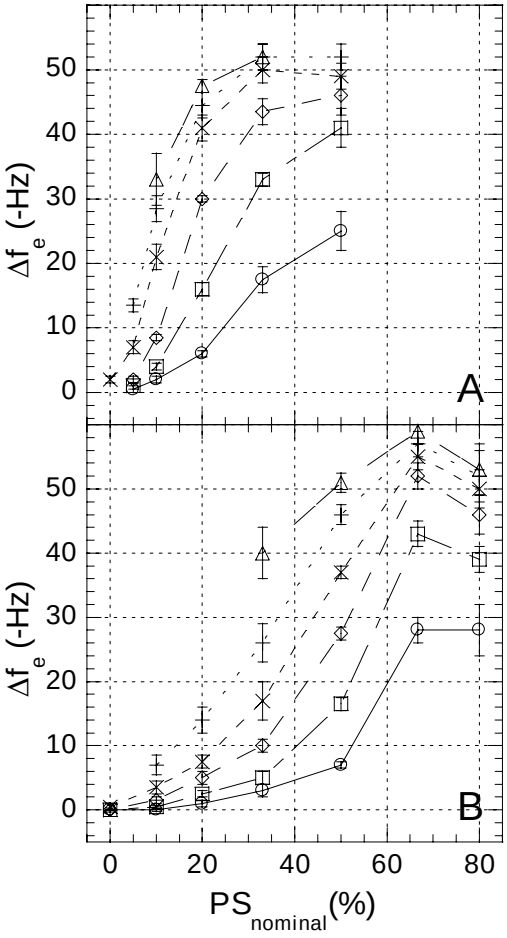

FIGURE 4

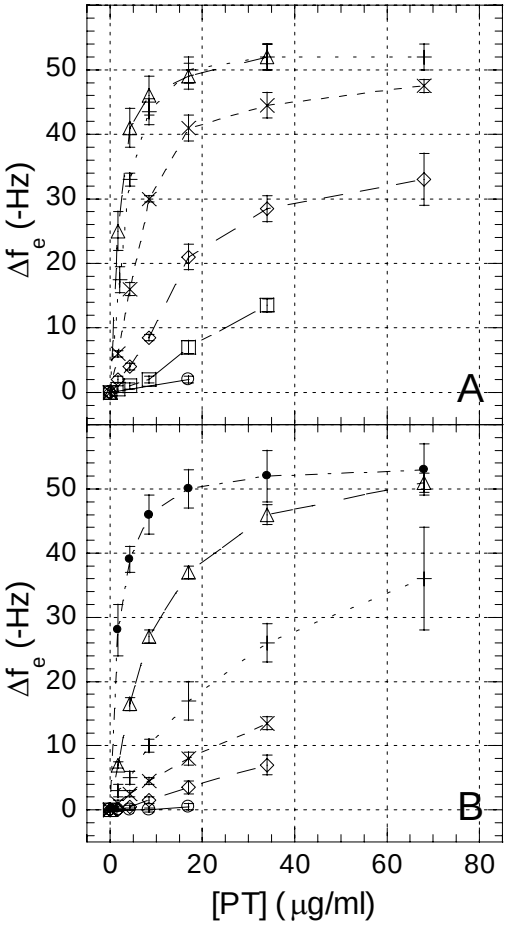

IV. Adsorption and self-assembly of proteins on supported lipid membranes

Historically, the desire to form protein crystals, both in 3D and in 2D, has been largely driven be their usefulness in obtaining information on the protein's molecular structure[330], down to the atomic level, by X-ray crystallography and transmission electron microscopy (TEM). Procedures to obtain crystals have remained largely empirical, though recent years have witnessed a tendency towards rationalization of macromolecular crystallization[331,332]. 2D crystals have been implicated as intermediates in the formation of 3D crystals[333] and 2D nucleation has been identified as one of the mechanisms by which 3D crystals grow[334].

The emergence of nanotechnology and biotechnology has added a new perspective to the applications of macromolecular self-assembly in general and protein 2D crystals in particular. Biochemical methods allow linking other biomolecules, such as nucleic acids[201] or proteins, nanoparticles, or more complex edifices such as membranes[143] to self-assembling proteins, and thus enable their immobilization in two dimensions, in a controlled manner. The variety in phase-transitions that is often exhibited by crystallizing entities[112,335] further enriches the playground for the creation of functionalized surfaces. In this context, annexin A5 is a particularly interesting protein as it unites several interesting properties: (i) it self-assembles in two dimensions, (ii) it adsorbs quasi irreversibly to membranes and (iii) it can be released from membranes in a controlled manner (by the removal of calcium).

While some proteins form 2D crystals in solution[336], we will here focus on the formation of 2D crystals at interfaces, in particular at the solid-liquid interface. 2D crystallization at interfaces is highly complex, involving a multitude of processes, such as the transport of proteins to the interface, their adsorption and diffusion in two dimensions, the nucleation of the crystal and the adsorption/desorption of protein molecules to/from the crystal. Self-assembly in two dimensions thus presents a challenging problem in fundamental science which becomes particularly interesting, as the limitation to two dimensions is expected to induce a distinctly different behavior as compared to 3D systems[337].

In this chapter we will investigate some of the features of 2D crystallization of annexin A5. In the course of this study it turned out that the adsorption of annexin A5 to mica-SLBs exhibits several particularities, as compared to earlier results on

other membrane models. Adsorption and crystallization are intimately related and an important part of the work presented here is thus dedicated to understanding the adsorption of annexin A5. For the matter of comparison, the adsorption and crystallization of another protein, streptavidin, are also investigated briefly.

IV.1. The influence of the solid support

It is commonly believed that the structure and the properties of fluid SLBs are efficient in screening the interface between the membrane and the bulk liquid from the influence of the solid support. In this context, our observations that the solid support can profoundly influence the adsorption of annexin A5 and its 2D self-assembly constitute maybe the most surprising results in this study.

IV.1.1. Adsorption of annexin A5 to SLBs on mica and on silica

In the initial phase of our studies we observed strong differences in the adsorption behavior of annexin A5 on SLBs made on mica and silica, as measured by QCM-D. For a given DOPS-content in the vesicles from which the SLBs were formed, the amounts of adsorbed annexin A5 were systematically lower on mica than on silica (c.f. Paper VI). This prompted us to investigate the inter-leaflet distribution of DOPS in SLBs. The results are presented in Paper V and provide evidence that the solid support can induce a considerable asymmetry in the lipid distribution. In particular, we found that mica can attract DOPS into the support-facing lipid leaflet, thus depleting the bulk-facing leaflet in this lipid species. This depletion effect provided a satisfactory explanation for the support-dependent differences in the adsorption of annexin A5 at short time scales, as discussed in Paper VI.

IV.1.2. 2D crystallization of proteins on SLBs

While annexin A5 readily crystallizes in two dimensions on mica-SLBs, crystalline structures of p6 symmetry have as yet remained elusive on silica-SLBs, as demonstrated and discussed in Papers I and VI.

Recent results illustrate that subtle differences in the support's properties can modify the propensity of annexin A5 to order: when annexin A5 is adsorbed to SLBs made on glass, a surface that is commonly expected to exhibit surface properties very similar to silica, some small ordered domains could be found (figure IV.1)

Remarkably, another protein, streptavidin, can be crystallized on SLBs supported by mica[143] as well as by silica wafers (Paper I) and no influence of the solid support on its adsorption (discussed below) and its self-assembly (paper I) has so far been observed. This raises the question whether the support-dependence in the propensity to crystallization may be specific to annexin A5 or its ligand-lipid DOPS. The exact role of the solid support in the self-assembly process of annexin A5, however, remains obscure (Paper VI).

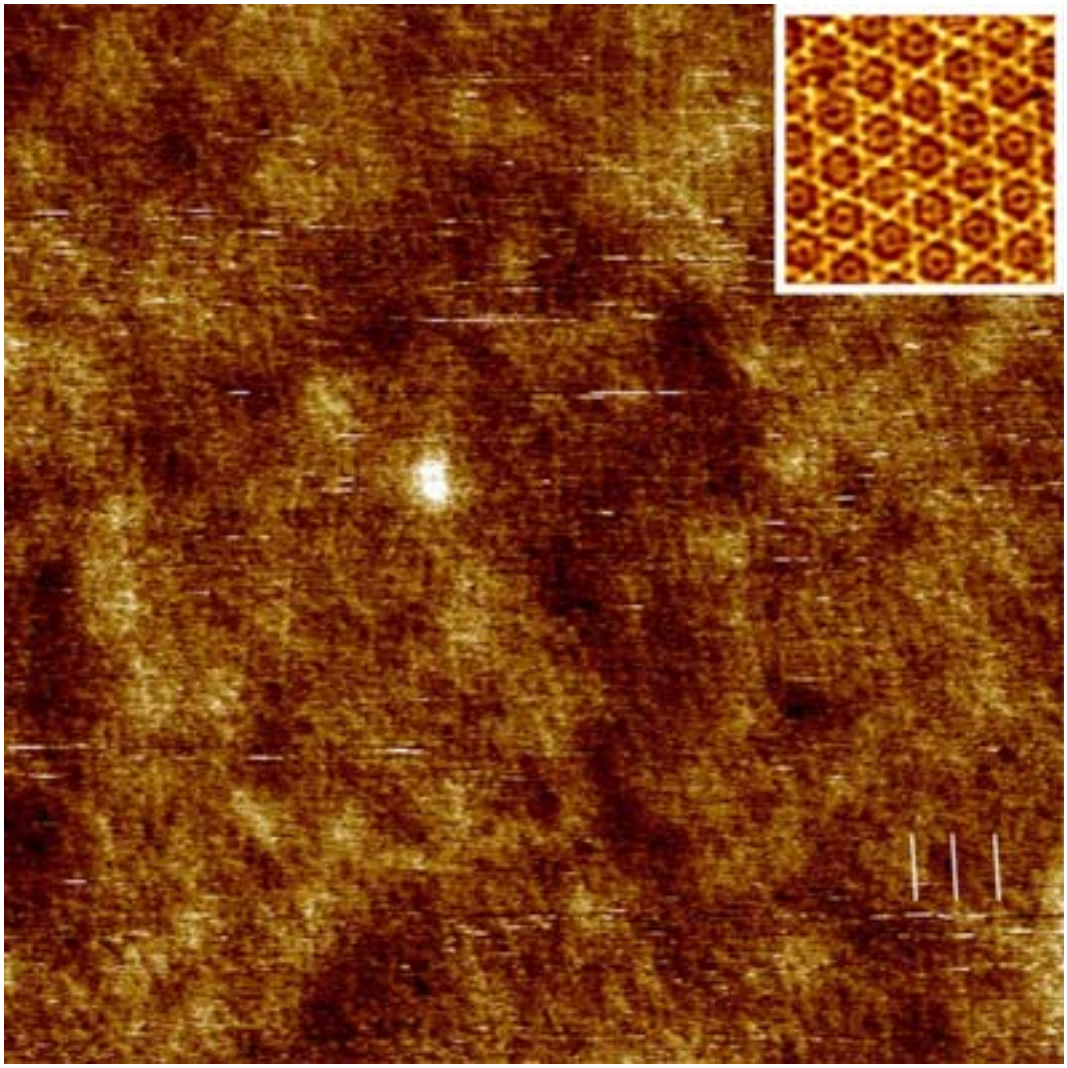

FIGURE IV.1 AFM-image of annexin A5 incubated on glass-SLBs made from SUVs of DOPC/DOPS (4:1). Some lines with a length between 50 and 250 nm and different orientations are observed over the entire image. Some of these lines (continued by *white lines* in the lower right corner) are parallel and exhibit a regular spacing that is close to the characteristic spacing in p6 crystals of annexin A5 (*inset*) which are commonly observed on mica-SLBs. Such lines could be imaged repeatedly and were found to be stable, indicating that the tracked structures are immobile. The stability and the local order of the observed structure may be indicative for the presence of nano-crystallites. This image was obtained in collaboration with Remy Bérat and Pierre Bonnafous in our lab.

IV.2. What can the adsorption kinetics reveal about 2D crystallization?

In many cases, and in particular for annexin A5, the confinement in two dimensions is a precursor to clustering and 2D crystallization of proteins. The adsorption of a protein thus influences the kinetics of its 2D reorganization. On the other hand, the change in the 2D packing, induced by clustering and crystallization, can modify the space that is available for further adsorption and thus influence adsorption. Hence, adsorption and 2D reorganization are intimately linked.

An obvious question that has not been covered explicitly by the included papers was therefore, what a protein's adsorption kinetics can reveal about its clustering or 2D crystallization. From the experimental point of few, this question is relevant as methods that provide information about adsorbed amounts, such as ellipsometry or QCM-D, rarely allow distinguishing between the different self-assembly states (monomers, oligomers, crystals) that are expected to coexist on the surface[i].

Adsorption processes are though notoriously complex[338,339], as they are influenced by many, often interdependent, parameters, such as the transport of the molecules towards the surface (the "mass transport", by convection or diffusion)[254,339,340], the number of available binding sites[339], the affinity and reversibility of binding, lateral mobility or clustering. It is therefore not straightforward to identify the exact influence of a given parameter on the adsorption process and appropriate model systems and experimental setups are needed. The following brief examples on the adsorption of annexin A5 and streptavidin to SLBs may illustrate what information about the 2D reorganization of proteins can (or cannot) be obtained by investigating adsorption kinetics alone.

To measure adsorption kinetics we have chosen an ellipsometry setup (c.f. Paper VI and refs. [84,248]) that provides constant adsorption rates in the case of mass-transport limited adsorption[254]. For the proteins investigated here we will indeed see, that the adsorption at low coverage is generally limited by the transport of the molecules to the surface. The chosen setup thus allows determining, in a simple way, at which state of surface coverage the adsorption becomes limited by other factors, such as surface blocking effects.

IV.2.1. Adsorption of streptavidin to biotinylated SLBs

Streptavidin is popular as a biotechnological tool[88,143,200,341-343] thanks to its unique property of possessing several high-affinity binding sites for biotin. The protein binds to biotinylated SLBs[143,200] and has been shown to form 2D crystals of c222-symmetry on SLBs supported both by mica[143] and by silica wafers (Paper I) under the conditions investigated here.

[i] For QCM-D, the dissipation can though in some cases serve as an excellent tool to distinguish different adsorption phases, such as adsorbed vesicles and bilayers (c.f. Chapter III).

In figure IV.2 the adsorption kinetics for streptavidin on SLBs formed on mica and on silica wafers[ii], respectively, are presented and compared. We note that the binding curves superpose well[iii]. Thus, for streptavidin, both the adsorption kinetics and the final-adsorption state do not depend on the employed solid-support.

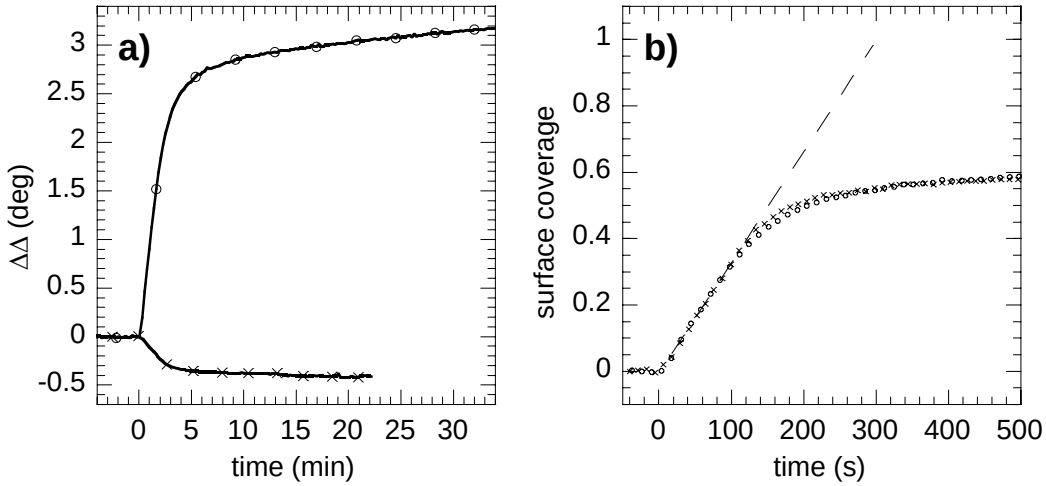

FIGURE IV.2 Comparison of the adsorption behavior of streptavidin on SLBs on silica (-○-) and on mica (-×-). (a) Time-dependent shifts in the ellipsometric angle, Δ. Streptavidin was incubated at 5 μg/mL on SLBs made from SUVs of DOPC/DOPS/DPPE-CAP-B (6:3:1). (b) Time-dependent surface coverage. The final surface coverage was assumed to be ~65%, as calculated from streptavidin's dimensions and 2D crystalline arrangement[111]. The ellipsometric responses in ΔΔ, taken from (a), were scaled accordingly. The regime of mass-transport limited adsorption is indicated with a *dotted line*.

IV.2.2. Adsorption of annexin A5 to DOPS-containing SLBs

As described above, annexin A5 crystallizes readily in two dimensions on mica-SLBs[109,142] while crystallization is not observed on silica-SLBs. The membrane-induced formation of trimers, believed to be a precursor state of crystallization[108,113], however, seems to be present on both types of SLBs (c.f. Papers I and VI). A comparison between the adsorption kinetics of annexin A5 on mica-SLBs and on silica-SLBs, as presented in figure IV.3, thus constitutes a rare occasion to study the effect of 2D crystallization on protein adsorption without the interference of other parameters.

Remarkably, we find that the adsorption behavior is very similar on both supports, indicating that the influence of 2D crystallization on the adsorption kinetics is minor for annexin A5.

[ii] While the presented data has been obtained on silica wafers, it is not yet clear, whether the same result can be obtained on silica-coated QCM-D crystals that exhibit a considerably higher roughness (c.f. Paper I).

[iii] The fact that the curves are identical confirms that the shifts in the ellipsometric angle, Δ, can be used for a reliable comparison between the adsorption kinetics on mica and on silica wafers (c.f. Chapter I).

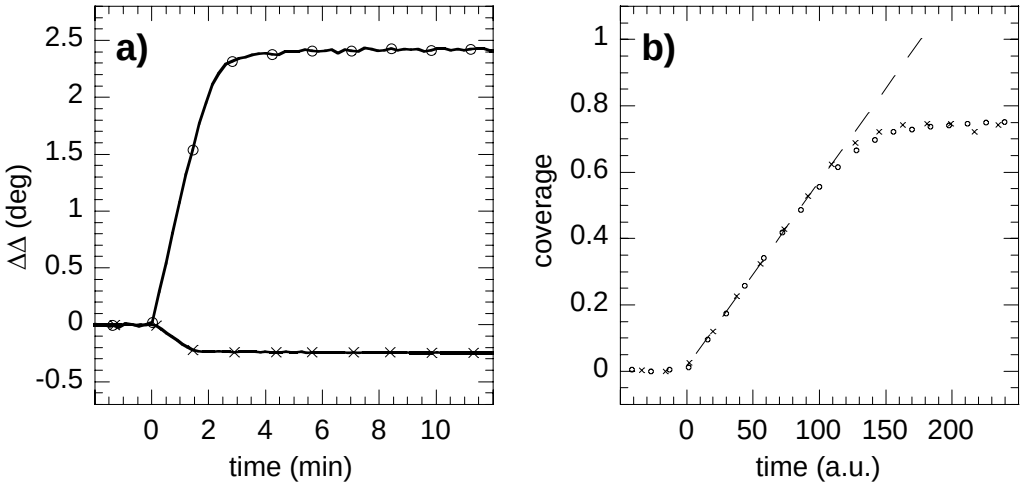

FIGURE IV.3 Comparison of the adsorption behavior of annexin A5 on a silica-SLB (-○-, made from DOPC/DOPS (4:1)-SUVs) and on a mica-SLB (-×-, made from DOPC/DOPS (1:1)-SUVs). (a) Time-dependent shifts in the ellipsometric angle, Δ. Annexin A5 was incubated at 2 μg/mL (5 μg/mL) on the silica-SLB (mica-SLB). (b) Time-dependent surface coverage. The final surface coverage was taken to be ~75% on the mica-SLB, as expected for a crystal of p6-symmetry[111]. The surface coverage on the silica-SLB was assumed to be similar. The ellipsometric responses in ΔΔ, taken from (a), were scaled accordingly. The time was scaled such that the linear adsorption regimes (*dotted line*) superpose.

IV.2.3. Comparing the adsorption kinetics of annexin A5 and streptavidin

In figure IV.4 the adsorption curves for both annexin A5 and streptavidin on mica-SLBs are compared[iv]. Even though both processes involve 2D crystallization, substantial differences are observed. Streptavidin leaves the linear adsorption regime at ~42% surface coverage, much earlier than annexin A5 (~63%)[v]. Furthermore, the extended final regime of slow adsorption of streptavidin contrasts with the quickly-reached plateau for annexin A5.

The fact that the adsorption of annexin A5 is mass-transport limited up to very high levels of surface coverage may be explained by the rapid clustering of the adsorbed molecules: The tighter packing associated with clustering liberates membrane space onto which new annexin A5 molecules can adsorb thus keeping the adsorption rate high. A comparison with the results from figure IV.3b suggests that the formation of trimers (and not the 2D crystallization) would be responsible for this effect. A comparison of our results with the adsorption of annexin A5 mutants that do not form trimers may provide a direct mean to test the hypothesis of clustering-enhanced adsorption.

[iv] Note that in order to keep the adsorption kinetics comparable, the curves are normalized for their expected final surface coverage[339]. This is not a trivial step as this can only be done when the final structure of the protein layer is known (as in our case from AFM-data).

[v] A comparison of the adsorption rates of annexin A5 and streptavidin with those obtained by others[344] with a similar setup confirmed that the linear adsorption regime corresponds to the regime of mass-transport limited adsorption and *not* to kinetically limited adsorption.

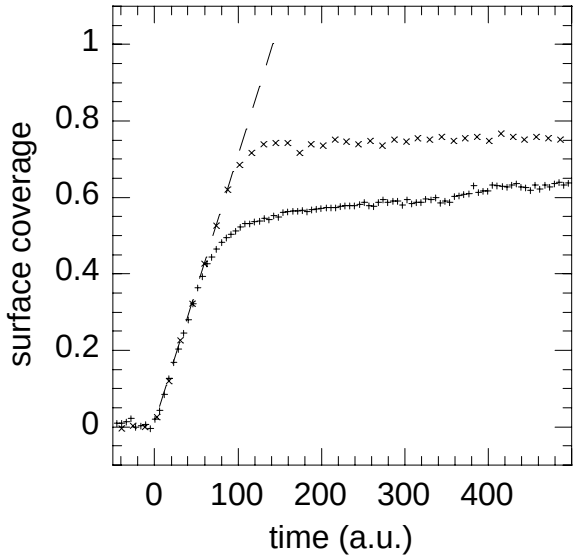

FIGURE IV.4 Comparison of the adsorption behavior of annexin A5 (×) and streptavidin (+) on mica-SLBs. The data were scaled such that the linear adsorption regimes (*dotted line*) superpose. Final surface coverages of 77% and 66% were assumed for annexin A5 (p6 crystal form) and streptavidin (c222 crystal form), respectively. Data as in figures IV.2 and IV.3.

In reverse, the slow final adsorption of streptavidin indicates the presence of obstacles to further binding. Packing constraints, induced by the non-spherical shape of streptavidin may contribute to this phenomenon as reported for other proteins with high aspect ratio[339]. However, if the crystallization of streptavidin was sufficiently quick, such packing constraints would not occur. Hence, it is tempting to attribute the slow adsorption kinetics to a slowly progressing crystallization of this protein. This would point to a marked difference in the kinetics of crystallization between annexin A5 and streptavidin. Another possibility that can not be fully excluded is that the availability of binding sites, i.e. biotynilated lipids, is the limiting factor for further adsorption at high coverage. Additional measurements on SLBs with varying content in DPPE-CAP-Biotin may settle this question.

In summary, we find (i) that the adsorption kinetics of streptavidin is independent of the solid support used, (ii) that the effect of 2D crystallization of annexin A5 on its adsorption kinetics is minor and (iii) that the adsorption kinetics of annexin A5 and streptavidin, albeit both 2D crystallizing proteins, differ markedly. A comparison of the given results with additional experimental and theoretical model systems appears though necessary to confirm the exact influence of the clustering of annexin A5 and the 2D crystallization of streptavidin on the proteins' adsorption kinetics. Multi-technique approaches may provide a mean to determine the potential difference between the crystallization of streptavidin and annexin A5.

IV.3. Persisting questions and perspectives

In this study we have clarified some important aspects of the adsorption of annexin A5 to SLBs and refined the phase diagram of this protein in its membrane-bound state. The results are expected to constitute a valuable base for detailed investigations of the dynamics of 2D crystallization of this protein.

With the advent of the AFM, a unique technique has become available to track the dynamics of protein 2D crystallization down to the level of the crystal's building unit. The image sequence in figure IV.5 illustrates that it is possible to follow the crystallization process of annexin A5 *in situ*. The rather low scanning speed, the influence of the AFM-cantilever on adsorption kinetics as well as difficulties to image proteins in their monomeric state (c.f. Chapter II) currently present some limitations to the use of AFM that have to be taken into account for the experimental design. Multi-technique approaches such as the one described in this study allow, in principle, to quantify both the overall density of surface-bound proteins, the fraction of proteins that has crystallized and the geometry of the growing crystals, and provide thus a more detailed picture than AFM alone. Other techniques, such as fluorescence microscopy[345] or TEM[111], constitute interesting complements.

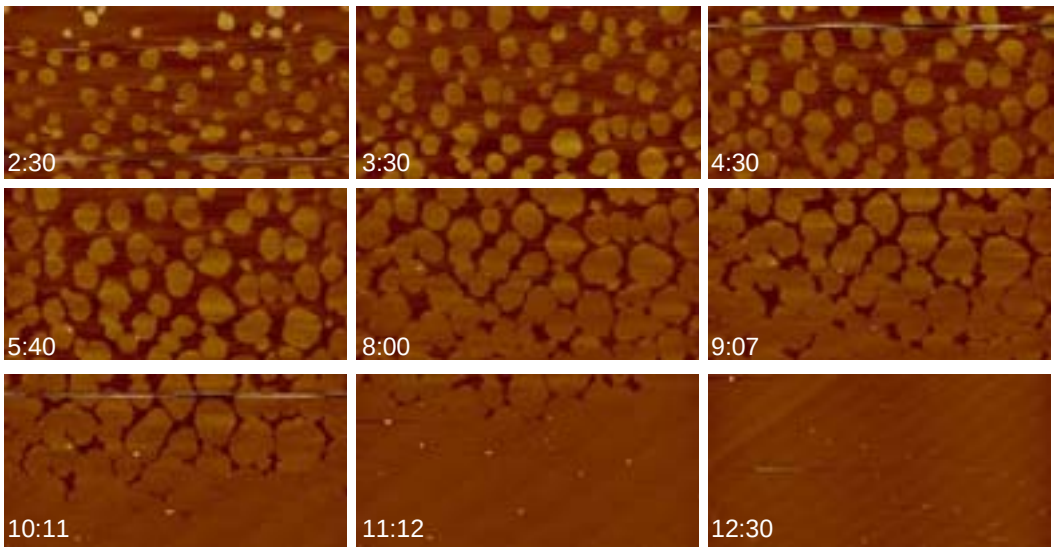

FIGURE IV.5 Growth of a crystalline layer of annexin A5. Annexin A5 was incubated at 20 µg/mL on mica-SLBs of DOPC/DOPS (1:2). All images are acquired with the slow scan direction from top to bottom; the image acquisition time is ~1 min; incubation times at the end of each image are indicated (min:s). Image size (z-limit): 10 µm × 5 µm (10 nm).

It is expected that images such as the ones in figure IV.5 and the outlined technical approaches can provide experimental data that allow verifying theoretical concepts of 2D crystallization[346] and extracting relevant parameters that characterize the dynamics of this process. Interestingly, the 2D self-assembly of some molecules that are simpler than proteins, such as formation of molecular films by molecular beam epitaxy[347] or the formation of self-assembled monolayers (SAMs)[348,349], has already been studied previously and quantitative approaches to describe 2D crystallization phenomena are emerging.

Paper VI

Ralf P. Richter, Josephine Lai Kee Him and Alain R. Brisson

On the kinetics of adsorption and two-dimensional self-assembly of annexin A5 on supported lipid bilayers.

Manuscript in preparation

On the kinetics of adsorption and two-dimensional self-assembly of annexin A5 on supported lipid bilayers

RUNNING TITLE: protein 2D crystallization kinetics

Ralf P. Richter, Josephine Lai Kee Him and Alain R. Brisson*

Laboratoire d'Imagerie Moléculaire et Nano-Bio-Technologie, IECB, UMR-CNRS 5471, Université Bordeaux I, 2 Rue Robert Escarpit, 33607 Pessac Cedex, France

*Corresponding author. E-mail: a.brisson@iecb.u-bordeaux.fr

KEYWORDS: mica; silica; quartz crystal microbalance with dissipation monitoring (QCM-D); atomic force microscopy (AFM); ellipsometry; supported lipid bilayer (SLB); dioleoylphospatidylserine (DOPS); dioleoylphosphatidylcholine (DOPC); annexin A5

ABSTRACT

Annexin A5 is a protein that binds to membranes containing negatively charged phospholipids in a calcium-dependent manner. Here we use atomic force microscopy, ellipsometry and quartz crystal microbalance with dissipation monitoring to correlate the adsorption kinetics of annexin A5 on lipid bilayers (SLBs), supported on silica and mica with its two-dimensional (2D) self-assembly. We find that the adsorption behavior is similar on mica-SLBs and on silica-SLBs, exhibiting a strong dependence on the concentration of DOPS in the SLB and on the calcium content in solution. On the other hand, 2D crystals of annexin A5 form readily on mica-SLBs, while these were not found on silica-SLBs. In addition, we report on long-time effects in the adsorption and 2D crystallization of

annexin A5 on mica-SLBs, which point towards the protein-induced recruitment of DOPS from the SLB's support-facing leaflet.

INTRODUCTION

Historically, the formation of protein crystals, both in three dimensions and in two dimensions, was attractive for structure determination (McPherson, 2003), down to the atomic level, by X-ray crystallography and transmission electron microscopy. Procedures to obtain crystals have remained largely empirical, though recent years have witnessed a tendency towards rationalization of macromolecular crystallization (Doudevski et al., 1998; Giegé and Ducruix, 1999; Reviakine et al., 2001; Chernov, 2003). Two-dimensional (2D) crystals have been implicated as intermediates in the formation of three-dimensional (3D) crystals (Hemming et al., 1995) and 2D nucleation has been identified as one of the mechanisms by which 3D crystals grow (Malkin et al., 1995).

In recent years interest has grown in the use of 2D protein crystals for biotechnological applications. The possibility to link other molecules such as nucleic acids (Larsson et al., 2003) or proteins and more complex objects such as nanoparticles or membranes (Wetzer et al., 1997; Reviakine and Brisson, 2001; Proux-Delrouyre et al., 2002) to self-assembling proteins and the variety in phases inherent in many crystallizing systems (Farah et al., 2001; Reviakine et al., 2001) constitute a rich potential playground for the creation of biofunctionalized surfaces.

2D crystallization at interfaces is highly complex (Doudevski et al., 1998), involving a multitude of processes, such as the transport of proteins to the interface, their adsorption and diffusion in two dimensions and the nucleation and growth of the crystal. 2D self-assembly thus presents a challenging problem in fundamental science which becomes particularly interesting as the limitation to two dimensions is expected to induce a distinctly different behavior as compared to 3D systems (Strandburg, 1988).

The protein annexin A5 binds to negatively charged phospholipids, in particular dioleoylphosphatdylcholine (DOPS), in a calcium-dependent manner (Seaton, 1996). Using ellipsometry (Andree et al., 1990; Andree et al., 1992), quartz crystal microbalance with dissipation monitoring (QCM-D) (Govorukhina et al., 2003) and fluorescence techniques (Meers, 1990; Meers and

Mealy, 1993; Pigault et al., 1994) the adsorption of the protein to various types of lipid membranes has been investigated and the important roles of the calcium concentration in solution and the DOPS-content in the SLB have been characterized.

Annexin A5 is commonly observed to undergo 2D crystallization on lipid monolayers at the air-water interface (Brisson et al., 1999) and on mica-supported lipid bilayers (SLBs) containing DOPS and the protein's self-assembly properties have been suggested to be relevant for its biological function. Using TEM (on lipid monolayers) and atomic force microscopy (AFM) (on SLBs), a trimeric intermediate - the trimer (Brisson et al., 1991) - and two common crystal forms – a low density form with p6 symmetry (Brisson et al., 1991; Reviakine et al., 1998) and a high density form with p3 symmetry (Reviakine et al., 2000) - have been identified and the phase transitions between these states have been investigated (Brisson et al., 1999; Reviakine et al., 2001; Noro et al., 2002), resulting in the self-assembly scheme presented in figure 1 (Govorukhina et al., 2003). In some cases, other structures have also been observed (Oling et al., 2001) or crystallization was found to be inhibited (Richter and Brisson, 2003).

While the intermediates of the self-assembly process and the adsorbed amounts of annexin A5 have been characterized extensively, relatively little is known about the kinetics of adsorption and self-assembly of annexin A5. In particular, a correlation between the membrane-binding behavior and the crystallization behavior is lacking. The kinetics of the self-assembly process is expected to be of importance for a fundamental description of the 2D crystallization process.

We have recently demonstrated the strength of combining AFM and QCM-D (and to some extent ellipsometry) for the characterization of processes that involve the adsorption and 2D self-organization of biomolecules at the solid-liquid interface (Richter et al., 2003; Richter and Brisson, 2004; Richter and Brisson). AFM gives access to spatially resolved structural information on the nanometer scale, while QCM-D and ellipsometry allow following the overall binding dynamics, which renders the techniques highly complementary.

In this study we combine AFM and QCM-D, complemented by ellipsometry, to characterize the binding (adsorption and desorption) and the 2D self-assembly of annexin A5 on lipid bilayers supported by silica and mica. Two parameters of importance for the binding of annexin A5, the calcium concentration in solution and the DOPS-content in the bilayer were systematically varied over a large range. The combined study allows correlating the protein's 2D crystallization with its binding behavior. We provide evidence for the profound influence of the solid support on the self-assembly behavior of annexin A5.

MATERIALS AND METHODS

Materials:

Dioleoylphosphatidylcholine (DOPC), dipalmitoylphosphatidylcholine (DPPC) and dioleoylphosphatidylserine (DOPS) were purchased from Avanti Polar-Lipids (AL, USA). Recombinant rat annexin A5 was overexpressed in *Escherichia coli* (Reviakine et al., 2000). Other chemicals were purchased from Sigma. Ultrapure water with a resistivity of 18.2 MΩ was used (Maxima, USF ELGA, France).

Muscovite mica disks of 12 mm diameter were purchased from Metafix (Montdidier, France). Plates of silicon wafer of (11 × 11) mm^2 (for AFM) were provided by the CEA (Grenoble, France). Slides of (40 × 8) mm^2 (for ellipsometry) were cut from silicon wafers from Wacker Chemitronic (n-type, phosphorus doped), purchased from Aurel GmbH (Landsberg, Germany). QCM-D sensor crystals (5 MHz), reactively sputter-coated with 50 nm silicon oxide, were purchased from Q-SENSE (Gothenburg, Sweden). Low viscosity epoxy glue (EPOTEK 377) for mica-gluing was purchased from Gentec Benelux (Waterloo, Belgium).

A buffer solution made of 150 mM NaCl, 3 mM NaN_3 and 10 mM HEPES, pH 7.4, was prepared in ultrapure water, and EDTA or $CaCl_2$ were added as indicated. Small unilamellar vesicles (SUVs) of desired lipid mixture were prepared by sonication as described earlier (Richter et al., 2003). For SLB-formation, vesicle suspensions were diluted at 0.1 mg/mL in buffer containing 2 mM $CaCl_2$.

Quartz Crystal Microbalance with Dissipation Monitoring (QCM-D):

QCM-D measurements (Rodahl et al., 1995) were performed with the Q-SENSE D300 system equipped with an Axial Flow Chamber (QAFC 302) (Q-SENSE AB, Gothenburg, Sweden). Briefly, upon interaction of (soft) matter with the surface of a sensor crystal, changes in the resonance frequency, f, related to attached mass (including coupled water), and in the dissipation, D, related to frictional (viscous) losses in the adlayer, are measured with a time resolution of better than 1 s.

Silica-coated QCM-D sensors were cleaned by two cycles of exposure to 2% sodium dodecyl sulfate solution for 15 min, rinsing with ultrapure water, blow-drying with nitrogen, and exposure to ultraviolet light (UV)/ozone (Richter et al., 2003) (BHK, Claremont, USA) for 10 min. Cleaned substrates were stored in air and again exposed to UV/ozone (10 min) prior to use. Mica-coated QCM-D sensor crystals were prepared and verified to operate stably according to a previously described protocol (Richter and Brisson, 2004).

Measurements were performed in exchange mode (Richter et al., 2003), if not otherwise stated. This mode allows following processes of adsorption and surface adlayer changes *in situ* while subsequently exposing different solutions to the surfaces. Occasionally, flow mode was employed (Richter et al., in press). The working temperature was 24°C.

Resonance frequency and dissipation were measured at several harmonics (15, 25, 35 MHz) simultaneously. If not stated otherwise, changes in dissipation and/or in normalized frequency ($\Delta f_{norm} = \Delta f_n/n$, with n being the overtone number) of the fifth overtone ($n = 5$, i.e., 25 MHz) are presented. Adsorbed masses (including coupled water), Δm, were calculated according to the Sauerbrey equation (Sauerbrey, 1959), $\Delta m = -C \cdot \Delta f_{norm}$, with $C = 17.7$ ng·cm^{-2}·Hz^{-1}. The changes in the viscosity and density of the buffer upon variation of its content in $CaCl_2$ or EDTA significantly influenced the QCM-D signal. These changes were accounted for by calibration against a clean silica-coated QCM-D sensor.

For the transfer of QCM-D sensors with adsorbed material from the QCM-D chamber to the AFM, sensors were unmounted with the aid of a suction holder (Meni CUP, Menicon Pharma, Illkirch Graffenstaden, France), ensuring that the sample remained permanently covered with liquid.

Ellipsometry:

Ellipsometry is an optical technique based on the measurement of changes in the ellipsometric angles, Δ and Ψ (Cuypers et al., 1983; Tompkins, 1993), of elliptically polarized light upon reflection at a planar surface. These changes are sensitive to the presence of thin deposited films and,

consequently, the method allows monitoring adsorption phenomena *in situ*. The employed null-ellipsometer setup with a time resolution of 10 to 15 s is described in detail elsewhere (Cuypers et al., 1983; Corsel et al., 1986). In the frame of the present study we consider the change in the angle Δ only, which is approximately proportional to the (dry) protein mass adsorbed to mica or silica (Benes et al.).

Prior to first use, silicon-slides were pre-cleaned by exposure to concentrated detergent solution (Sparkleen, Calgon, Pittsburg, PA), rinsing with water, exposure to 30% chromic sulfuric acid (80°C for 20 min) and extensive rinsing in ultrapure water. Further cleaning before each use was performed as described for silica-coated QCM-D sensors. Mica disks were rendered opaque on their back side with emery paper and glued on an aluminum slide over a hole (8 mm diameter) using melted wax (Benes et al., 2002). Uniform mica-surfaces were obtained by cleavage of the front side with adhesive tape and used immediately.

Measurements were performed in an open cuvette system (Corsel et al., 1986), at room temperature. The buffer solution (~3 mL) was stirred with a magnetic stirrer (~1000 rpm). Samples were pipetted at appropriate concentrations into the solution. Such a setup generates constant adsorption rates provided the adsorption is mass-transport limited (Hermens et al., 2004). Rinses were realized by injecting ~30 mL of buffer (injection rate ~1 mL/s) while simultaneously withdrawing excess liquid.

Atomic Force Microscopy (AFM):

AFM measurements were performed in liquid using a Nanoscope IV-Multimode (VEECO, Dourdan, France), equipped with a J-scanner (120 μm). Before use, the contact mode fluid cell was washed in successive baths of ethanol and ultrapure water, followed by extensive rinsing in ethanol and blow-drying in a stream of nitrogen. Tubings and O-ring were sonicated in ethanol and water, rinsed with ethanol and blow-dried in nitrogen. Oxide-sharpened silicon nitride cantilevers with a nominal spring constant of 0.06 N/m (Digital Instruments, CA, USA) were exposed to UV/ozone (BHK, CA, USA) for 10 min prior to use.

Silicon plates were cleaned as described for the silica-coated QCM-D sensors, attached to Teflon-coated (BYTAC, NORTON, OH, USA) metal discs using double-sided tape (TESA, Hamburg, Germany) and immediately covered with buffer solution. Mica disks were glued to Teflon-coated metal discs using the epoxy glue, cleaved with adhesive tape and immediately covered with buffer solution. For AFM-investigations subsequent to QCM-D measurements, mica-coated QCM-D sensors, covered with the sample, were attached to Teflon-coated metal discs using double-sided tape and installed on the AFM scanner.

Contact mode images were acquired at scanning rates of 4-8 Hz while manually adjusting the force to a minimum (< 200 pN). Images were second-order plane-fitted and subsequently zero-order flattened except otherwise stated.

RESULTS

Adsorption of annexin A5 on silica-SLBs

We employed the QCM-D technique to characterize the adsorption of annexin A5 on silica-SLBs. The measurement shown in figure 2, obtained for an SLB formed from SUVs of DOPC/DOPS (molar ratio 9:1), is representative of our experimental approach.

The QCM-D response upon exposure of SUVs to the support (figure 2, at 0 min) reveals, as expected, a characteristic two-phase behavior, reflecting the initial adsorption of intact vesicles that is followed by the formation of an SLB (Keller and Kasemo, 1998; Richter et al., 2003). The final frequency shift of -25±1 Hz and the low dissipation shift of less than $0.2 \cdot 10^{-6}$ confirm the formation of a lipid bilayer that entirely covered the support with no or only minor defects (Reimhult et al., 2002; Richter and Brisson).

Incubation of the SLB with annexin A5 (figure 2, *solid arrows*) leads to adsorption of the protein, witnessed by the decreases in frequency, in a calcium-dependent manner. As expected (Andree et al., 1990; Pigault et al., 1994), increasing calcium concentrations enhanced protein binding: while a negligible amount of annexin A5 bound at 200 μM $CaCl_2$, a coverage of Δf = -18±0.5 Hz was reached for 200 mM. As demonstrated in figure 2 and observed for all measurements, the dissipation remained almost unchanged throughout the entire process of protein adsorption, suggesting that the protein associates tightly with the SLB.

The adsorption of annexin A5 at 20 mM $CaCl_2$ (figure 2, at 54 min) reveals some typical properties of the immobilization of annexin A5 on silica-SLBs. The adsorption of annexin A5 reached equilibrium within a few minutes after exposure for the employed protein concentrations. The final adsorbed amounts changed only little upon increase of the annexin A5 concentration from 20 to 80 μg/mL. Only a part (here corresponding to 3 Hz) of annexin A5 was displaced upon rinsing in a buffer solution that contained the same amount of calcium as used during adsorption. Also additional rinses (figure 2) or continuous flow (in flow mode, data not shown) with such a buffer did not lead to

further release of annexin A5. This provides indications for the presence of two different populations of bound annexin A5: for a given calcium content a small amount of annexin A5 can easily be displaced (reversible binding) while the rest binds irreversibly.

Annexin A5 could, however, be displaced by rinsing with decreasing calcium concentrations or in the presence of the calcium chelator EDTA (figure 2, *dotted arrows*). For DOPC/DOPS (9:1), Δf returned to the value characteristic for a bare SLB at 20 μM $CaCl_2$ (not shown) or in the presence of EDTA. We further tested the reversibility of protein binding at low calcium concentration by performing several cycles of incubation with annexin A5 at 20 mM $CaCl_2$, followed by rinses in EDTA-containing buffer, on the same SLB (not shown). We obtained identical QCM-D responses, which confirms that the silica-SLB can be recovered without significant perturbations and motivates our approach to perform several incubations with annexin A5 on the same bilayer.

We note also that, once adsorbed, the amount of annexin A5 that remains after rinsing in a buffer solution of a given calcium concentration is the same independent of the way the protein was incubated (c.f. figure 2, *dotted lines* for 2 and 20 mM $CaCl_2$[1]). The same phenomenon was observed for *all* measurements conducted on silica-SLBs, indicating that the reversibility of protein binding is independent on the history of annexin A5 deposition over the investigated time-scale. In consequence, our results indicate that the amount of irreversibly bound annexin A5 is entirely determined by the calcium content, [Ca], in solution and the DOPS-content, [DOPS], in the SLB.

Based on these observations, we investigated the equilibrium adsorbed amounts, Δf_e, of annexin A5 on silica-SLBs in a systematic manner as a function of [DOPS], [Ca] and the bulk concentrations of the protein, [A5]. The results are summarized in figure 3 and table 1.

As already reported by others (Andree et al., 1990; Pigault et al., 1994), we found that the adsorption of annexin A5 increases with [Ca] and [DOPS]. The dependence is sigmoidal for both

[1] The response for 200 μM $CaCl_2$ constitutes a notable exception to this observation.

[DOPS] (at a given [Ca], figure 3) and [Ca] (at a given [DOPS], not shown). In particular, the calcium concentrations required to reach the half-maximal frequency shift for 0, 5 and 20% DOPS are close to those reported by Andrée et al. (Andree et al., 1990) on silica-SLBs formed by Langmuir-Blodgett deposition (c.f. table 1 and figure 7). We note that annexin A5 binds also to pure DOPC at high calcium concentrations (≥ 20 mM), as discussed in previous work (Govorukhina et al., 2003).

The maximum adsorbed amount was $\Delta f_{max} = -18 \pm 0.5$ Hz, over the entire range of [DOPS] investigated, suggesting that this value corresponds to the full coverage of the SLB with a monolayer of annexin A5.

Three different regimes can be discerned in terms of reversibility of annexin A5 binding upon rinsing in protein-free solution containing the same amount of [Ca] as used for adsorption (figure 3):

(i) Annexin A5 binding was found to be fully irreversible, once the plateau of full coverage is reached for elevated [DOPS] and [Ca].

(ii) In the range of intermediate binding (i.e. around the inflection point of the sigmoidal curve), most of the protein was irreversibly bound for [Ca] ≤ 2 mM. A small fraction (up to 3 Hz), however, was bound reversibly for the employed annexin A5 concentrations.

(iii) In strong contrast, binding to pure DOPC, which is considerable at 20 mM calcium and more, was completely (for 20 mM) or in part (for 200 mM) reversible. Also for SLBs containing small amounts of DOPS (up to 10%) a part of the adsorption can be reversible at [Ca] ≥ 20 mM.

Adsorption kinetics of annexin A5: The adsorption of annexin A5 at 200 mM $CaCl_2$ and 20 μg/mL protein concentration (c.f. figure 2, 89 min) is representative for the adsorption kinetics that we observed under all employed conditions that led to (close-to-) maximal coverage. We note that it takes less than 5 minutes for the adsorption to reach completion, which is in the time range expected for

mass-transport limited adsorption[2]. To further investigate the adsorption kinetics, we performed measurements by ellipsometry under experimental conditions that provide constant adsorption rates under mass-transport limited conditions (Hermens et al., 2004). As demonstrated in figure 4, the adsorption curve is linear up to more than 65% of the final coverage, confirming that the adsorption is indeed to a large extent mass-transport limited (Andree et al., 1990). Even though some deviations from the mass-transport limited regime occur at higher coverage, the adsorption goes quickly to completion.

2D self-assembly of annexin A5 on silica-SLBs

We have previously reported that 2D crystals of annexin A5 are not present on silica-SLBs formed with DOPC/DOPS (4:1) (Richter and Brisson, 2003); while 2D crystals are commonly observed on mica (Reviakine et al., 2001). Here we have extended our investigations, using AFM, to a larger range of DOPS-concentrations (0, 10 and 20%) under conditions for which substantial protein coverage was expected according to our QCM-D results. Despite numerous trials and the fact that the support was flat enough to resolve 2D protein assemblies down to the molecular level (Richter and Brisson, 2003), we did not find any supramolecular structures exhibiting long range order. Neither did we find the characteristic 2D crystalline patches, that are easily visible on incompletely covered mica-SLBs (Reviakine et al., 1998).

Instead, we observed characteristic jumps on an otherwise fairly smooth surface which occurred as a function of the scanning speed and force and led to images exhibiting two different apparent height levels, separated by ~2 nm (figure 5). These jumps were not observed on SLBs that had not been incubated with annexin A5, confirming that they are due to the presence of the protein. We suggest that the "water-skiing effect", earlier reported by Rädler et. al. (Rädler et al., 1994) on lipid bilayers,

[2] With the employed setup of still liquid, the adsorbed amount is given by $\Gamma = 2c\sqrt{Dt/\pi}$ for mass-transport limited adsorption (Hermens et al., 2004). Assuming a bulk diffusion coefficient, D = 60 μm^2/s, and a concentration, c = 20 μg/mL, of the protein, this corresponds to a time, $t \approx$ 200 s, to reach a coverage of Γ = 250 ng/cm^2.

provides a reasonable explanation for our observation: at low forces and/or high scanning speed the tip slides over the layer of annexin A5 molecules while it jumps down through the layer at slightly increased forces and/or decreased scanning speed. Indeed, the observed jump-height of ~2 nm (figure 5, inset) is only slightly lower than the height (2.6 nm) of 2D crystals of annexin A5, previously observed on mica (Reviakine et al., 1998). The occurrence of such sliding and indentation implies that annexin A5 is laterally mobile. We have reported earlier (Richter and Brisson, 2003) that scratches can be introduced in the annexin A5 layer and that these scratches heal quickly, providing further evidence for the presence and for the lateral mobility of annexin A5 on silica-SLBs.

We note that the silica supports employed for the QCM-D measurements were considerably rougher than the supports used for the AFM-investigations (Richter and Brisson, 2003). As roughness is not expected to improve the propensity to crystallization, we consider it unlikely that annexin A5 does crystallize on any of the silica supports employed in this study.

The presence of annexin A5 trimers: Evidence has accumulated in previous studies, that the surface-induced oligomerization into trimers is a precursor to the 2D crystallization of annexin A5 (Oling et al., 2001; Govorukhina et al., 2003). Provided our observations that 2D crystals do not form on silica-SLBs, an obvious question is whether trimers do actually form on silica-SLBs. The high lateral mobility of the protein renders the imaging of monomers or oligomers of annexin A5 by AFM difficult[3] and we could not find direct evidence for the presence of annexin A5 trimers on SLBs composed of DOPC and DOPS only. It should, however, be noted that AFM-images on mixtures of

[3] The lateral diffusion of SLB-bound annexin A5 can be as high as the diffusion of the lipid molecules to which it is bound, i.e., in the order of 1 μm^2 per second. This is more than the area covered by the AFM-tip (0.1 μm^2 per second) under common high-resolution imaging conditions. The comparison illustrates the difficulties associated to image mobile proteins on SLBs.

DOPC, DOPS and DPPC, showed that trimers of annexin A5 *can* exist on silica-SLBs (Richter and Brisson, 2003)[4].

Adsorption of annexin A5 on mica-SLBs

Having investigated the adsorption and 2D self-assembly of annexin A5 on silica-SLBs we now turn to its deposition on mica-SLBs. Figure 6 gives an overview of the (equilibrium) adsorbed amounts. The data were obtained in a similar manner as described for silica, with some modifications that will be discussed in detail in a later section.

When comparing the adsorption behavior at nominal [DOPS] (figures 6A-D and 3), i.e. the DOPS-content given by the molar mixing ratio of DOPC and DOPS in the SUVs, we observe that the adsorbed amounts on mica are generally lower than on silica for a given [DOPS]. This result is not unexpected. As discussed earlier (Richter et al., in press), the inter-leaflet distribution of DOPS in mica–SLBs is asymmetric, leading to DOPS-concentrations in the bulk-facing leaflet, i.e. accessible [DOPS], that are considerably lower than for silica-SLBs.

We have accounted for the for the difference in accessible [DOPS] between SLBs on silica and on mica, according to earlier quantifications (Richter et al., in press) (figure 6E-H) and find that the adsorption behavior of annexin A5 on both surfaces is, in many aspects, similar. At low [A5], the overall dependence on [Ca] and [DOPS] is the same, within experimental error, as witnessed by identical values for [Ca] and [DOPS] to reach the half-maximum frequency shifts (table 1). As for silica, binding is entirely irreversible at high [DOPS] and [Ca] (c.f. figures 3 and 6). Also, the adsorption of annexin A5 on pure DOPC is very similar on both surfaces, exhibiting a high degree of reversibility. A remarkable difference, however, is that at an intermediate range of [DOPS] and for [Ca] ≤ 2mM, mica-SLBs show slightly higher amounts of reversible binding (e.g., compare the binding

[4] The fact that trimers of annexin A5 could in this case be resolved by AFM may be explained by a decreased lateral diffusion of the lipids due to the introduction of the DPPC lipids.

at $[DOPS]_{accessible}$ = 13% and [Ca] = 0.2 mM ($[DOPS]_{accessible}$ = 7% and [Ca] = 2 mM) on mica (figure 3) with respective conditions on silica (figure 6)).

2D crystallization of annexin A5 on mica-SLBs

In strong contrast to silica-SLBs, annexin A5 2D crystals could be observed on *all* types of mica-SLBs investigated. Figure 7A provides an overview of the self-assembly structures found by AFM, and the adsorbed amounts found by QCM-D, as a function of [DOPS] and [Ca]. Three different regimes can be discerned: (i) no adsorption takes place; crystalline patches with (ii) p6 symmetry and (iii) p3 symmetry are present. In all investigated cases and in agreement with previous studies (Reviakine et al., 2001), exclusively the p6 crystal form could be observed at low coverage of annexin A5 and the p3 crystal form started to appear only after an intermediate of complete surface coverage with the p6 crystal form was surpassed. The combination of QCM-D and AFM on mica allowed to identify frequency shifts of Δf_{p6} = -17.8 ± 1 Hz and Δf_{p3} = -19 ± 1 Hz as representative for the presence of complete crystalline layers of p6 and p3 symmetry, respectively (Richter and Brisson, 2004).

It is remarkable, that complete p6 crystals could also be found on pure DOPC at [Ca] ≥20 mM (figure 7B). In agreement with QCM-D results, the annexin A5 crystal was found to disappear completely upon rinsing in 20 mM $CaCl_2$.

Kinetics of adsorption and 2D self-assembly of annexin A5 on mica-SLBs

With the aim to characterize the relationship between adsorption and 2D self-assembly, we investigated the kinetics of both processes in more detail.

Adsorption kinetics until formation of a complete layer of p6 crystals: Ellipsometric measurements (figure 8) on SLBs made of DOPC/DOPS (1:2) in 0.2 mM $CaCl_2$ showed a linear adsorption regime, indicating mass-transport limited adsorption, until more than 70% of the apparent equilibrium coverage of ΔΔ = -0.24° which was reached quickly (after around 2 min). Based on further ellipsometry data (not shown) and on the observation, by AFM, that the transition towards a p3 crystal is rather slow under the employed conditions, we attribute the shift in Δ of -0.24° to a complete p6 crystalline layer. Both

the persistence of the purely mass-transport limited regime and the overall adsorption kinetics are similar on mica (figure 8) and on silica (figure 4), suggesting a rather limited influence of the crystallization on the adsorption kinetics.

When does trimer-formation and crystallization start? In order to investigate when the crystallization of annexin A5 sets in, we followed the adsorption of annexin A5 on mica-SLBs (DOPC/DOPS (2:1)) by QCM-D and interrupted the adsorption by rinsing after a few Hz of coverage were reached (figure 9, *inset*). Subsequent imaging of the surface by AFM revealed small domains (figure 9) exhibiting the topography of a p6 crystal (not shown). Similar results were obtained on SLBs formed from DOPC/DOPS (1:2). This demonstrates that a small coverage (≤10%) with annexin A5 is sufficient to initiate crystallization. In agreement, previous studies on lipid-monolayers (Govorukhina et al., 2003) had reported the presence of trimers for very low concentrations of surface-bound annexin A5.

Kinetics of p6 crystal growth: We followed the growth of the p6 crystals by AFM *in situ*, after injection of annexin A5 on a preformed SLB (figure 10). Initially, a number of small crystalline patches appeared (figure 10A). The smallest visible patches have a diameter of ~150 nm. Most of the patches then grow (figure 10B-H) until they cover the entire surface (figure 10I). It is notable that no new patches are formed after 2.5 min of incubation. Instead, a few patches (figure 10, *arrowheads*) were found to diminish in size before disappearing completely.

We note that the time to get to complete crystallization (~12 min) is in the same range as the time needed for complete adsorption at similar annexin A5 concentrations (figure 2). A rigorous comparison of the kinetics is though not possible, as the presence of AFM-tip and cantilever is susceptible to modify the mass-transport conditions for the adsorption of the protein. This is witnessed by the slightly heterogeneous crystal growth rates in figure 10 (e.g., compare the lower half of figure 10G with the upper half of figure 10H) and has already been reported elsewhere (Leitner et al., 2000).

Kinetics of the p6 to p3 transition: Relatively small changes in adsorbed mass upon transition from a p6 to a p3 crystal[5] and relatively slow kinetics rendered reliable measurements of the transition kinetics by QCM-D or ellipsometry cumbersome. However, both crystal forms could be clearly distinguished by AFM: at small image sizes, the differences in the crystalline structure were identified directly (figure 11A), while at large image sizes, both crystalline states could be distinguished by small but detectable differences in the crystal height (figure 11B-C). We therefore employed AFM to follow the kinetics of the transition from a p6 to a p3 crystalline state. The observed times for the transition from a crystalline layer of pure p6 symmetry to pure p3 symmetry ranged from 10 min (e.g., for DOPC/DOPS (1:1) and 20 mM $CaCl_2$) to 60 min (e.g., for DOPC/DOPS (1:1) and 2mM $CaCl_2$) at [A5] = 20 μg/mL. These is clearly much longer than what was commonly needed for the formation of a complete p6 crystalline layer[6].

Effects of long time incubation of annexin A5: In the beginning of our investigations on mica-SLBs, we observed a rather irregular behavior in the adsorbed amount, as measured by QCM-D, and in the kinetics of p6 crystal growth, as followed by AFM, of annexin A5 at intermediate DOPS-concentrations, in particular for DOPC/DOPS (4:1) at 2 mM $CaCl_2$. This condition is situated close to the inflection point of the sigmoidal curves that describe the dependence of adsorption on [DOPS] or [Ca] (c.f. figure 6). Some scatter is therefore expected as small changes in [DOPS] or [Ca] lead to rather large changes in the adsorbed amount. However, the observed variations were significantly larger than expected from the experimental error in [DOPS] and [Ca]. This prompted us to investigate the long-term crystallization behavior of annexin A5 under this condition (figure 12).

[5] The difference in protein mass between a complete p6 and a complete p3 crystalline layer is 36 ng/cm^2, or 18% of the mass of a p6 crystalline layer, including its central trimers (Richter and Brisson, 2004).

[6] The slow kinetics implies that the recruitment of additional proteins from the solution is not mass-transport limited. Hence, the influence of AFM-tip and cantilever on the kinetics is expected to be small in this case.

When incubating the protein at 40 µg/mL, p6 crystals were observed. We found that these crystals grew extremely slowly, over the time span of several hours (figure 12A-E). Eventually though, a p6 crystalline layer formed that covered the entire surface (figure 12F). We emphasize that this strongly contrasts with previously presented results on the kinetics of adsorption and crystallization. Subsequent incubation with buffer containing 0.02 mM calcium removed the annexin A5 (and induced a few defects in the membrane) (not shown). Most intriguingly, immediate re-incubation of annexin A5 as before led to complete coverage with a p6 crystalline layer within about an hour (figure 12G-L). While this is still more than what was commonly found for crystallization kinetics, it is significantly less than what was needed for the first incubation, indicating that the propensity of the SLB to bind annexin A5 has changed considerably. It appears that the long-time exposure of annexin A5 changes the membrane's properties. In the light of our results and previous studies (Richter et al., in press), we propose that annexin A5 is able to induce the enrichment of the bulk-facing SLB-leaflet with DOPS in the time range of several hours.

The described experiment is illustrative for the dependence of annexin A5 adsorption and crystallization on the history of a given mica-SLB. Furthermore, the measurement showed that, at least under some conditions, SLBs can be unstable against rinsing in buffer containing low amounts of calcium or EDTA. In case such potential problems applied, the above described QCM-D measurements were performed without repeatedly incubating annexin A5 to a given membrane and with restrictions on the incubation times.

DISCUSSION

We have investigated the adsorption and 2D self-assembly of annexin A5 on silica-SLBs and on mica-SLBs. Figures 3, 6 and 7 provide an overview of the obtained results. Our finding that the amount of adsorbed annexin A5, both on silica-SLBs and on mica-SLBs, is essentially determined by the amount of accessible DOPS and by the concentration of calcium correlates well with previous work (Andree et al., 1990; Andree, 1992; Pigault et al., 1994).

We find that while annexin A5 readily 2D crystallizes on mica-SLBs, it does not do so on silica. This remarkable difference allows us to compare the adsorption of annexin A5 on membranes with and without crystallization and thus to gain insight into the influence of the crystallization on the adsorption and on the stability of adsorbed molecules. The behavior of adsorption and desorption is predominantly very similar on both surfaces indicating that the effects of the crystal are limited. Only in some exceptional cases, i.e., at intermediate [DOPS] and [Ca] ≤ 2 mM, we found slightly increased amounts of reversibly bound annexin A5 on mica-SLBs[7].

The desorption of membrane-bound annexin A5

This study provides evidence that, when rinsing in calcium-containing buffer the adsorption of annexin A5 on pure DOPC can be completely reversible (at 20 mM $CaCl_2$). This strongly contrasts with our observations on DOPS-containing SLBs and thereby suggests that this adsorption behavior reflects the genuine calcium-mediated interaction between annexin A5 and DOPC. An alternative explanation for adsorption of annexin A5 at zero percent nominal DOPS-content would be that DOPC is contaminated with negatively charged lipids. However, the observed differences in the desorption behavior on DOPC-SLBs and DOPS-containing SLBs makes this possibility unlikely. The adsorption of annexin A5 to DOPC has been addressed in several earlier studies, though the conclusions varied widely. While some reports found no binding to DOPC (Pigault et al., 1994), others indicated

[7] Under these particular conditions the incorporation of annexin A5 into a crystal may act as a secondary binding transition which enhances the apparent binding affinity of annexin A5.

substantial binding (Andree et al., 1990; Meers and Mealy, 1993; Govorukhina et al., 2003). In addition to previous investigations (Govorukhina et al., 2003) which suggested that variations in the type of membrane models (vesicles, lipid monolayers, SLBs) may influence the binding and self-assembly of annexin A5, we propose that the differences in the bulk concentration of annexin A5 may be at the origin of the observed variations.

In SLBs containing mixtures of DOPC and DOPS, the adsorption to both types of lipids may coexist. The interaction with DOPS is much stronger than with DOPC and the former will thus dominate at high DOPS-concentrations, as observed. Substantial amounts of reversibly bound annexin A5 for [DOPS] ≤ 10% and [Ca] ≥ 20 mM (c.f. figures 3 and 6) are though likely to present the reminiscence of this coexistence.

An interesting finding is that, in terms of reversibility, a minor population of reversibly bound proteins can coexist with another population of irreversibly bound annexin A5 under conditions of incomplete coverage at [Ca] ≤ 2 mM (c.f. figures 2, 3 and 6). As this response is observed both on silica and on mica, we consider it unlikely that this effect is induced by crystallization (that would only occur on mica) or by roughness effects (that would only occur on silica). The coexistence of a (more stable) trimeric state and a (less stable) monomeric state could provide an explanation for the observed distinct populations as the surface-induced trimerization of annexin A5 is likely to occur on both types of SLBs. Indeed, the rate of monomer exchange in a trimer has been reported to be slow (Langen et al., 1998) and the trimeric state is therefore expected to be stable, both as an oligomer and in its binding to the membrane. It remains, however, unclear why a distinct population of non-trimerizing monomers should persist on the surface. Yet another possibility that may be envisaged is the existence of different populations of trimers. Trimers may, for example, be distinguished by the number of DOPS molecules with which they interact.

While the differences in the propensity of annexin A5 to crystallize on silica-SLBs and on mica-SLBs revealed fortuitous for our study, the origin of these variations remains unclear. The support's

roughness may be invoked as a potential reason for the non crystallization on silica-SLBs (Richter and Brisson, 2003). However, the silica supports employed for AFM exhibit a roughness of only a few Angstroms (Richter and Brisson, 2003), which is little as compared to the thickness of the SLB (~4 nm) together with the water-layer (~1 nm) (Bayerl and Bloom, 1990; Johnson et al., 1991) that is expected to space the SLB from the solid support. It is thus doubtful whether roughness alone can explain the observed effects. Further studies on other similar surfaces such as crystalline silica or glass may reveal more insight, but are outside the scope of this study.

Kinetics of annexin A5 2D crystallization

Different phases in the 2D self-assembly of annexin A5 on mica-SLBs as well as the principle phase transitions involved have been described in previous studies (Reviakine et al., 2001; Govorukhina et al., 2003). In comparison to these reports we have extended the range of employed DOPS-concentrations (including pure DOPC) and calcium concentrations (0 to 200 mM). We find that the previously outlined phases and phase transitions apply over the entire range of investigated concentrations of DOPS and calcium: At low protein coverage the p6 crystalline form can be observed exclusively, while p3 crystals occur only once the state of complete coverage with a p6 crystal has been surpassed. Figure 7 demonstrates that the propensity to form p6 and p3 crystals is generally determined by the concentration of [DOPS] and [Ca]. For a given [Ca], a critical concentration of [DOPS] exists above which the transition to the p3 crystal form can occur.

The fact that stable 2D crystals of annexin A5 were found at a protein coverage that corresponds only to a small fraction of the maximum coverage (c.f. figure 9) provides evidence that a low 2D protein density is sufficient to initiate the crystal's nucleation and growth.

The growth of p6 crystals: Under the experimental conditions employed, the time window for crystal nucleation is small (c.f. figure 10). No new crystalline domains appear shortly after the formation of the first domains. This suggests that the growth of existing crystals keeps the density of adsorbed non-crystalline proteins sufficiently low to prevent further nucleation. Some crystallites

actually diminish in size and disappear (c.f. figure 10), which may be indicative of Ostwald-ripening. Thus, the protein adsorption is expected to limit crystal growth which is consistent with our findings that (i) adsorption is mass-transport limited up to high coverage and reaches equilibrium quickly as well as that (ii) crystallization rates and adsorption rates are similar.

Our observation that the crystallization starts at low protein coverage (≤10%) (c.f. figure 9) and with high rates (c.f. figure 10) confirms that the formation of trimers, the precursor of crystallization, is fast and occurs at very low density of membrane-bound proteins, as previously reported on vesicles (for annexin A12, another member of the annexin family which exhibits strong similarities to annexin A5 in its membrane binding properties) (Langen et al., 1998) and on lipid monolayers (Govorukhina et al., 2003).

In comparison to most other 2D crystals, the p6 crystal form of annexin A5 exhibits a particularity: the open structure of this crystal form leaves space for the adsorption of additional trimers, that do *not* participate in the crystalline lattice. These "central trimers", once filled, make up one third of the mass of the p6 crystalline layer, and thus contribute considerably to the adsorbed mass. As the binding state of central trimers and crystallized trimers is not identical one may expect distinct differences in their stability. However, as discussed previously, the 2D crystalline state of annexin A5 does not have a pronounced effect on the stability of surface-bound proteins. Consequently, crystalline trimers and central trimers should not differ much in their desorption behavior. We found indeed no indications for different populations of desorbing annexin A5 on mica-SLBs.

The transition from p6 to p3: The solid-solid phase transition from the p6 to the denser p3 crystal form is of first order (Reviakine et al., 2001). p3 nuclei that form at the grain boundaries or in defects of the p6 crystallites will be stabilized and grow by the adsorption of additional annexin A5 molecules into liberated surface areas. The membrane surface available for binding is thus determined by the local fluctuations in the crystalline state and generally expected to be small. Consequently, the adsorption in this regime is strongly limited by surface-blocking effects, consistent with our finding that the growth

of p3 crystals is generally slower than the growth of p6 crystals. In addition to these surface blocking effects, the density of available binding sites, as determined by [DOPS] and [Ca], is expected to restrict the rates of adsorption and p3 crystal growth. This rationalizes our observation that the p3 crystallization rate increases with increasing [DOPS] and [Ca].

The memory-effect of annexin A5 on SLBs

Figure 12 demonstrates that the long-time incubation of annexin A5 can substantially affect the membrane's affinity for this protein. With respect to the previously outlined principal binding properties of annexin A5 to SLBs, we interpret this as a strong indication that the amount of accessible DOPS has changed. The memory-effect is established on the time scale of hours. This is in the lower range of what is generally considered the time for the flip-flop of lipid molecules across the membrane (Wimley and Thompson, 1990; John et al., 2002; Kol et al., 2003), although little is known about the effect that the confinement of the membrane to a solid support may have on its flip-flop rate. We have previously shown that mica can induce the enrichment of the support-facing lipid leaflet in DOPS and found indications that the asymmetric inter-leaflet distribution of DOPS corresponds to an equilibrium state (Richter et al., in press). We propose that annexin A5, mediated by the association of its oligomers with several DOPS molecules, can fix DOPS-molecules to the bulk-facing leaflet and thus shift the SLB's equilibrium DOPS-distribution. Such a scenario involves only the interaction of annexin A5 with the lipid headgroups which is consistent with the general picture of the membrane-binding mechanism of annexin A5 (Oling et al., 2000). We note that the redistribution of negatively charged lipids induced by membrane-binding molecules has been reported earlier (Yaroslavov et al., 1994; Yaroslavov et al., 1998), suggesting that such effects may be more frequent than commonly appreciated.

The combination of AFM, QCM-D and ellipsometry

We emphasize that the combination of a technique with lateral resolution down to the molecular level, such as AFM, and techniques that measure the total adsorbed amount at high time resolution,

such as QCM-D or ellipsometry, was an essential prerequisite for this study. The employed techniques proved highly complementary. AFM provided detailed information on the structure and growth of self-assembly structures, although its capability to trace adsorbed but laterally mobile molecules is limited (Richter and Brisson, 2003) and the AFM-cantilever is susceptible to affect adsorption kinetics (Leitner et al., 2000). QCM-D or ellipsometry, on the other hand, give access to time-resolved information about the overall adsorbed amount, while being limited in tracing the 2D self-assembly of the protein. The unexpected observation that the 2D self-assembly of annexin A5 depends distinctly on the solid support, illustrates the importance of employing identical (in the case of mica) or similar (in the case of silica) surfaces for all techniques in order to obtain reliable results.

CONCLUSION AND PERSPECTIVES

We have provided a detailed characterization of the adsorption and 2D self-assembly of annexin A5 on SLBs for a large range of calcium concentrations and DOPS-contents, including pure DOPC. In particular, the combination of AFM, QCM-D and ellipsometry allowed correlating the kinetics of adsorption and 2D crystallization.

We found distinctive differences in the self-assembly behavior of annexin A5 on SLBs formed on silica and mica, respectively. While the origin of these differences remains unclear, our results stress that the solid support can have a pronounced influence on the properties of SLBs.

While we have predominantly treated the 2D crystallization kinetics in a qualitative manner, the outlined experimental approaches are expected to be a useful for the quantitative characterization of the 2D self-assembly process (Doudevski et al., 1998).

ACKNOWLEDGEMENTS

We thank Wim Hermens (University of Maastricht, The Netherlands) for providing access to the ellipsometre as well as Aleš Benda and Martin Beneš (Heyrovský Institute, Prague, Czech Republic) for help with its setup. Furthermore, we thank Patrice Caillat and Claude Vauchier (CEA-LETI, Grenoble, France) for the gift of silicon wafers. Discussions with Ilya Reviakine (University of Clausthal, Clausthal-Zellerfeld, Germany) are acknowledged. Ralf Richter was partly supported by the CNRS, the Ministère délégué à la Recherche (France), the Conseil Régional d'Aquitaine (France) and by EC grant FP6-NMP4-CT2003-505868 "Nanocues". This research was supported by the Conseil Régional d'Aquitaine, the Fonds Européen de Développement Régional, and EC grant FP6-NMP4-CT2003-505868 "Nanocues".

REFERENCES

Andree, H.A.M. 1992. Phospholipid Binding and Anticoagulant Action of Annexin V [PhD]. Maastricht: University of Maastricht.

Andree, H.A.M., C.P.M. Reutelingsperger, R. Hauptmann, H.C. Hemker, W.T. Hermens, and G.M. Willems. 1990. Binding of Vascular Anticoagulant α (VACα) to Planar Phospholipid Bilayers. *J. Biol. Chem.* 265:4923-4928.

Andree, H.A.M., M.C.A. Stuart, W.T. Hermens, C.P.M. Reutelingsperger, H.C. Hemker, P.M. Frederik, and G.M. Willems. 1992. Clustering of Lipid-bound Annexin V May Explain Its Anticoagulant Effect. *J. Biol. Chem.* 267:17907-17912.

Bayerl, T.M., and M. Bloom. 1990. Physical properties of single phospholipid bilayers adsorbed to micro glass beads. A new vesicular model system studied by ^{2}H-nuclear magnetic resonance. *Biophys. J.* 58:357-362.

Benes, M., D. Billy, A. Benda, H. Speijer, M. Hof, and W.T. Hermens. Surface-dependent transitions during self-assembly of phospholipid membranes on mica, silica and glass. *Langmuir, accepted*.

Benes, M., D. Billy, W.T. Hermens, and M. Hof. 2002. Muscovite (mica) allows the characterization of supported bilayers by ellipsometry and confocal fluorescence correlation spectroscopy. *Biol. Chem.* 383:337-341.

Brisson, A., A. Bergsma-Schutter, F. Oling, O. Lambert, and I. Reviakine. 1999. Two-dimensional crystallization of proteins on lipid monolayers at the air-water interface and transfer to an electron microscopy grid. *J. Cryst. Growth* 196:456-470.

Brisson, A., G. Mosser, and R. Huber. 1991. Structure of Soluble and Membrane-bound Human Annexin V. *J. Mol. Biol.* 220:199-203.

Chernov, A.A. 2003. Protein crystals and their growth. *J. Struct. Biol.* 142:3-21.

Corsel, J.W., G.M. Willems, J.M.M. Kop, P.A. Cuypers, and W.T. Hermens. 1986. The Role of Intrinsic Binding Rate and Transport Rate in the Asorption of Prothrombin, Albumin and Fibrinogen to Phospholipid Bilayers. *J. Colloid Interface Sci.* 111:544-554.

Cuypers, P.A., J.W. Corsel, M.P. Janssen, J.M.M. Kop, W.T. Hermens, and H.C. Hemker. 1983. The Adsorption of Prothrombin to Phosphatidylserine Multilayers Quantitated by Ellipsometry. *J. Biol. Chem.* 258:2426-2430.

Doudevski, I., W.A. Hayes, and D.K. Schwartz. 1998. Submonolayer Island Nucleation and Growth Kinetics during Self-Assembled Monolayer Formation. *Phys. Rev. Lett.* 81:4927-4930.

Farah, S.J., S.-W. Wang, W.-H. Chang, C.R. Robertson, and A.P. Gast. 2001. Point Mutagenesis and Cocrystallization of Wild-Type and Mutant Proteins: A Study of Solid-Phase Coexistence in Two-Dimensional Protein Arrays. *Langmuir* 17:5731-5735.

Giegé, R., and A. Ducruix. 1999. Crystallization of Nucleic Acids and Proteins: A Practical Approach. Ducruix A, Giegé R, editors. Oxford University Press, Oxford. 1 p.

Govorukhina, N., A. Bergsma-Schutter, C. Mazères-Dubut, S. Mazères, E. Drakopoulou, L. Bystrykh, F. Oling, A. Mukhopadhyay, I. Reviakine, J. Lai Kee Him, and A. Brisson. 2003. Self-Assembly of Annexin A5 on Lipid Membranes. *In* Annexins: Biological importance and annexin-related pathologies. Bandorowicz-Pikula J, editor. Landes Bioscience/Eurekah.com, Georgetown, Tex. 37-55.

Hemming, S.A., A. Bochkarev, S.A. Darst, R.D. Kornberg, P. Ala, D.S.C. Yang, and A.M. Edwards. 1995. The Mechanism of Protein Crystal Growth from Lipid Layers. *J. Mol. Biol.* 246:308.

Hermens, W.T., M. Benes, R.P. Richter, and H. Speijer. 2004. Effects of flow on solute exchange between fluids and supported biosurfaces. An overview. *Biotechn. Appl. Biochem.* 39:277-284.

John, K., S. Schreiber, J. Kubelt, A. Herrmann, and P. Müller. 2002. Transbilayer Movement of Phopholipids at the Main Phase Transition of Lipid Membranes: Implications for Rapid Flip-FLop in Biological Membranes. *Biophys. J.* 83:3315-3323.

Johnson, S.J., T.M. Bayerl, D.C. McDermott, W.A. Adam, A.R. Rennie, R.K. Thomas, and E. Sackmann. 1991. Structure of an adsorbed dimyristoylphosphatidylcholine bilayer measured with specular reflection of neutrons. *Biophys. J.* 59:289-294.

Keller, C.A., and B. Kasemo. 1998. Surface Specific Kinetics of Lipid Vesicle Adsorption Measured with a Quartz Crystal Microbalance. *Biophys. J.* 75:1397-1402.

Kol, M.A., A.N.C.van Laak, D.T.S. Rijkers, J.A. Killian, A.I.P.M. de Kroon, and B. de Kruijff. 2003. Phospholipid Flop Induced by Transmembrane Peptides in Model Membranes Is Modulated by Lipid Composition. *Biochemistry* 42:231-237.

Langen, R., J.M. Isas, H. Luecke, H.T. Haigler, and W.L. Hubbell. 1998. Membrane-mediated assembly of annexins studied by site-directed spin labeling. *J. Biol. Chem.* 273:22453-22457.

Larsson, C., M. Rodahl, and F. Höök. 2003. Characterization of DNA Immobilization and Subsequent Hybridization on a 2D Arrangement of Streptavidin on a Biotin-Modified Lipid Bilayer Supported on SiO_2. *Anal. Chem.* 75:5080-5087.

Leitner, T., G. Friedbacher, T. Vallant, H. Brunner, U. Mayer, and H. Hoffmann. 2000. Investigations of the Growth of Self-Assembled Octadecylsiloxane Monolayers with Atomic Force Microscopy. *Mikrochimica Acta* 133:331-336.

Malkin, A.J., Y.G. Kuznetsov, T.A. Land, J.J. DeYoreo, and A. McPherson. 1995. Mechanisms of growth for protein and virus crystals. *Nat. Struct. Biol.* 2:956.

McPherson, A. 2003. Macromolecular crystallization in the structural genomics area. *J. Struct. Biol.* 142:1-2.

Meers, P. 1990. Location of tryptophans in membrane-bound annexins. *Biochemistry* 29:3325-3330.

Meers, P., and T. Mealy. 1993. Relationship between Annexin V Tryptophan Exposure, Calcium, and Phopholipid Binding. *Biochemistry* 32:5411-5418.

Noro, M.G., M.A. Bates, A. Brisson, and D. Frenkel. 2002. Modeling the Phase Behavior of the Membrane Binding Protein Annexin V. *Langmuir* 18:2988-2992.

Oling, F., W. Bergsma-Schutter, and A. Brisson. 2001. Trimers, Dimers of Trimers, and Trimers of Trimers Are Common Building Blocks of Annexin A5 Two-Dimensional Crystals. *J. Struct. Biol.* 133:55-63.

Oling, F., J. Sopkova-de Oliveira Santos, N. Govorukhina, C. Mazères-Dubut, W. Bergsma-Schutter, G. Oostergetel, W. Keegstra, O. Lambert, A. Lewit-Bentley, and A. Brisson. 2000. Structure of membrane-bound annexin A5 trimers: a hybrid Cryo-EM - X-ray crystallography study. *J. Mol. Biol.* 304:561-573.

Pigault, C., A. Follenius-Wund, M. Schmutz, J.-M. Freyssinet, and A. Brisson. 1994. Formation of Two-dimensional Arrays of Annexin V on Phosphatidylserine-containing Liposomes. *J. Mol. Biol.* 236:199-208.

Proux-Delrouyre, V., C. Elie, J.-M. Laval, J. Moiroux, and C. Bourdillon. 2002. Formation of Tethered and Streptavidin-Supported Lipid Bilayers on a Microporous Electrode for the Reconstitution of Membranes of Large Surface Area. *Langmuir* 18:3263-3272.

Reimhult, E., F. Höök, and B. Kasemo. 2002. Vesicle adsorption on SiO_2 and TiO_2: Dependence on vesicle size. *J. Chem. Phys.* 117:7401-7404.

Reviakine, I., A. Bergsma-Schutter, A.N. Morozov, and A. Brisson. 2001. Two-Dimensional Crystallization of Annexin A5 on Phospholipid Bilayers and Monolayers: A Solid-Solid Phase Transition Between Crystal Forms. *Langmuir* 17:1680-1686.

Reviakine, I., W. Bergsma-Schutter, and A. Brisson. 1998. Growth of Protein 2-D Crystals on Supported Planar Lipid Bilayers Imaged in Situ by AFM. *J. Struct. Biol.* 121:356-361.

Reviakine, I., W. Bergsma-Schutter, C. Mazères-Dubut, N. Govorukhina, and A. Brisson. 2000. Surface Topography of the p3 and p6 Annexin V Crystal Forms Determined by Atomic Force Microscopy. *J. Struct. Biol.* 131:234-239.

Reviakine, I., and A. Brisson. 2001. Streptavidin 2D crystals on Supported Phospholipid Bilayers: Towards Constructing Anchored Phospholipid Bilayers. *Langmuir* 17:8293-8299.

Richter, R.P., and A. Brisson. 2003. Characterization of lipid bilayers and protein assemblies supported on rough surfaces by atomic force microscopy. *Langmuir* 19:1632-1640.

Richter, R.P., and A. Brisson. 2004. QCM-D on mica for parallel QCM-D - AFM studies. *Langmuir* 20:4609-4613.

Richter, R.P., and A. Brisson. submitted. Following the formation of supported lipid bilayers on mica - a study combining AFM, QCM-D and ellipsometry. *Biophys. J.*

Richter, R.P., N. Maury, and A. Brisson. in press. On the effect of the solid support on the inter-leaflet distribution of lipids in supported lipid bilayers. *Langmuir*.

Richter, R.P., A. Mukhopadhay, and A. Brisson. 2003. Pathways of lipid vesicle deposition on solid surfaces: a combined QCM-D and AFM study. *Biophys. J.* 85:3035-3047.

Rodahl, M., F. Höök, A. Krozer, P. Brzezinski, and B. Kasemo. 1995. Quartz crystal microbalance setup for frequency and Q-factor measurements in gaseous and liquid environments. *Rev. Sci. Instrum.* 66:3924-3930.

Rädler, J., M. Radmacher, and H.E. Gaub. 1994. Velocity-Dependent Forces in Atomic Force Microscopy Imaging of Lipid Films. *Langmuir* 10:3111-3115.

Sauerbrey, G. 1959. Verwendung von Schwingquartzen zur Wägung dünner Schichten und zur Mikrowägung. *Z. Phys.* 155:206-222.

Seaton, B.A., editor. 1996. Annexins: Molecular Structure to Cellular Function: R.G. Landes Company.

Strandburg, K.J. 1988. Two-dimensional melting. *Rev. Mod. Phys.* 60:161-207.

Tompkins, H.G. 1993. A User's Guide to Ellipsometry. Academic Press, Inc., London. 260 p.

Wetzer, B., D. Pum, and U.B. Sleytr. 1997. S-Layer Stabilized Solid Supported Lipid Bilayers. *J. Struct. Biol.* 119:123-128.

Wimley, W.C., and T.E. Thompson. 1990. Exchange and Flip-Flop of Dimyristoylphophatidylcholine in Liquid-Crystalline, Gel, and Two-Component, Two-Phase Large Unilamellar Vesicles. *Biochemistry* 29:1296-1303.

Yaroslavov, A.A., E.A. Kiseliova, O.Y. Udalykh, and V.A. Kabanov. 1998. Integrity of Mixed Liposomes Contacting a Polycation Depends on the Negatively Charged Lipid Content. *Langmuir* 14:5160-5163.

Yaroslavov, A.A., V.E. Kul'kov, A.S. Polinsky, B.A. Baibakov, and V.A. Kabanov. 1994. A polycation causes migration of negatively charged phopholipids from the inner to outer leaflet of the liposomal membrane. *FEBS Lett.* 340:121-123.

TABLES

TABLE 1

Conditions of [DOPS] and [Ca] required for half-maximal binding of annexin A5

	[Ca] (mM)	[DOPS] (%)
figure 3 [a)]	0.2	19 ± 1
	2	9.5 ± 0.5
	20	5.0 ± 0.5
	20..200	0
figure 6 [b)]	0.2	17 ± 2
	2	10 ± 1
	20	6 ± 1
	20..200	0
Andrée et al. [c)]	0.036 ± 0.013	100
	0.22 ± 0.06	20
	1.5 ± 0.5	5
	8.6 ± 2.5	1
	>30	0
Pigault et al. [d)]	0.057	50
	0.13	25
	1	17
	3	9.1
	7	3.8
	12	2
	68	1
Govorukhina et al. [e)]	50	0

[a)] Experimental results obtained by QCM-D on silica-SLBs for the amount of irreversibly bound annexin A5; [b)] Experimental results obtained by QCM-D on mica-SLBs for the amount of irreversibly bound annexin A5; the accessible DOPS-content is stated as determined in ref. (Richter et al., in press) (see figure 6 for details); [c)] From ref. (Andree et al., 1990), obtained with SLBs formed by Langmuir-Blodgett deposition; [d)] From ref. (Pigault et al., 1994), obtained with large unilamellar vesicles; [e)] From ref. (Govorukhina et al., 2003), obtained by QCM-D on silica-SLBs at [A5] = 10 μg/mL.

FIGURE LEGENDS

FIGURE 1

Schematic description of the 2D self-assembly of annexin A5 on a negatively charged phospholipid membrane according to (Govorukhina et al., 2003). Monomeric annexin A5 binds to the membrane in a calcium-dependent manner where it forms trimers. The trimers crystallize in two dimensions. The holes in the honey-comb-like lattice of p6 symmetry can be filled by additional non-crystalline trimers (*marked in red*), also called "central trimers". At high protein coverage, a phase transition of first order into a more densely packed crystal form with p3 symmetry can occur.

FIGURE 2

QCM-D response (frequency, Δf (-○-), and dissipation, ΔD (---), at 35 MHz) for a typical measurement to investigate the adsorption of annexin A5 to SLBs. The SLB was formed by incubation of SUVs of DOPC/DOPS (molar ratio 9:1) on silica (0 min). The adsorption of annexin A5 at various concentrations (injections indicated by *solid arrows*, at concentrations given in μg/mL) was followed in the presence of 0.2, 2, 20 and 200 mM $CaCl_2$ (as indicated). *Dotted arrows* indicate rinses accompanied with changes in the calcium concentration (in mM or EDTA, as indicated). The *dotted lines* indicate the levels of bound annexin A5 after rinses in 20 mM (lower line) and 2 mM (upper line) $CaCl_2$, which are independent on the incubation history. Rinses in EDTA lead to complete unbinding of annexin A5.

FIGURE 3

Equilibrium adsorbed amounts, given by the shifts, Δf_e, in QCM-D frequency, of annexin A5 on silica-SLBs, as a function of the SLB's DOPS-content, [DOPS], and the concentration of annexin A5 for 0.2 (A), 2 (B), 20 (C) and 200 mM (D) $CaCl_2$. Bulk concentrations of annexin A5 were 20 (×) and 80 μg/mL (◇), respectively. The amounts of annexin A5 remaining after rinsing in buffer are also indicated (□) and connected by lines to guide the eye.

FIGURE 4

Adsorption of 2 μg/mL annexin A5 on a silica-SLB made of DOPC/DOPS (4:1) as measured by ellipsometry in stirred buffer at 2 mM $CaCl_2$. The adsorption rate is constant (*dotted line*), indicating mass-transport limited adsorption, until more than 65% of the final coverage.

FIGURE 5

Tracking the presence of annexin A5 on silica-SLBs by AFM. While imaging from top to bottom, the applied force increased, due to thermal drift, from ~50 pN to ~200 pN. These slight variations led to jumps of 2 nm in the height (*cross-section in inset*). This effect is attributed to the "water-ski" effect: at lowest forces (top) the tip is sliding over the disordered layer of laterally mobile annexin A5 while it penetrates to the underlying SLB at slightly higher forces (bottom). *Dotted lines* (*inset*) mark the two height levels that correspond to the top of the annexin A5 (*upper dotted line*) layer and the top of the SLB (*lower dotted line*), respectively. Annexin A5 was incubated on SLBs of DOPC/DOPS (9:1) in 2 mM $CaCl_2$. Image size (z-limit): 2.5 μm (10 nm).

FIGURE 6

Adsorbed amounts, given in QCM-D frequency shifts, Δf_e, of annexin A5 on mica-SLBs, as a function of the SLB's DOPS-content, and the concentration of annexin A5 for 0.2 (A, E), 2 (B, F), 20 (C, G) and 200 mM (D, H) $CaCl_2$. Annexin A5 was incubated at 20 (×) and 80 μg/mL (◇), respectively. The amounts of annexin A5, remaining after rinsing in buffer are also indicated (□) and connected by lines to guide the eye. The abscissa shows the nominal DOPS-content (A-D), given by the molar mixing ratio of DOPC and DOPS, and the accessible DOPS-content (E-H), i.e. the DOPS-content in the bulk facing leaflet of the SLB. The accessible DOPS-contents were determined elsewhere (Richter et al., in press), taking silica-SLBs as reference, to be 3±1%, 7±1%, 13±2%, 20±2%, >55% and >60% for nominal DOPS-contents of 10%, 20%, 33%, 50%, 67% and 80%, respectively.

FIGURE 7

(A) Diagram of the adsorption state of annexin A5 on mica-SLBs as a function of apparent DOPS-content and calcium concentration. A pair of conditions of ([DOPS],[Ca]) is counted as belonging to the zones p6 and p3, if at least partial coverage with respective crystalline lattice has been observed under these conditions. Conditions where approximately half-maximal binding was reached, according to figure 3 (○), figure 6 (□), Andree et al. (◇), Pigault et al. (Δ) and Govorukhina et al. (◆), are indicated. The range of conditions in which minor amounts of annexin A5 adsorb without inducing crystallization is considered very narrow and is omitted in the figure. (B) Annexin A5 crystallizes even on pure DOPC. The p6 crystal was obtained by AFM after incubation of 20 μg/mL annexin A5 (~20 min) at 200 mM $CaCl_2$, and observed to cover the entire surface. Image size (z-limit): 1 μm (5 nm).

FIGURE 8

Adsorption of 5 μg/mL annexin A5 on a mica-SLB made of DOPC/DOPS (1:2) as measured by ellipsometry in stirred buffer at 0.2 mM $CaCl_2$. The adsorption rate is constant (*dotted line*), indicating mass-transport limited adsorption, until more than 70% of the final coverage.

FIGURE 9

AFM-images after an interrupted adsorption of annexin A5 on mica-SLBs of DOPC/DOPS (2:1). 2 μg/mL annexin A5 were incubated at 2 mM $CaCl_2$, until a coverage corresponding to a frequency shift of -2.5 Hz by QCM-D (flow mode) was reached (*inset*). The sample was rinsed in buffer containing 2 mM $CaCl_2$ (*inset*, at 4 min) before transfer to the AFM. Domains of 300 nm to 1.5 μm diameter are visible which did not change in position or size but slightly fluctuated in shape during subsequent scans (not shown) and were identified as p6 crystalline domains. The apparent coverage with crystalline domains was ~3%. Image size (z-limit): 20 μm (10 nm).

FIGURE 10

Growth of a p6 crystalline layer of annexin A5, followed *in situ* by AFM. Annexin A5 was injected at 20 μg/mL on mica-SLBs of DOPC/DOPS (1:2). While most crystalline domains grow with time, a few domains (*arrowheads*) diminish in size and disappear. All images are acquired with the slow scan direction from top to bottom; the image acquisition time is ~1 min; incubation times at the end of each image are indicated (min:s). Drifts are due to instabilities in the AFM-setup. Image size (z-limit): 10 μm × 5 μm (10 nm).

FIGURE 11

AFM-images of coexisting p6- and p3-crystalline domains of annexin A5. (A) The molecular organization of the p3 crystal (*white lines* follow the lattice lines) is predominant. A very small p6 domain (*red arrowhead*) as well as disordered boundaries (*white arrowhead*) can be discerned. 80 μg/mL annexin A5 were incubated in 0.2 mM $CaCl_2$ on DOPC/DOPS (1:4)-SLBs before image acquisition. Image size (z-limit): 300 nm (3 nm). (B-C) Regions of p3-symmetry can be distinguished from regions of p6-symmetry due to slight differences in their height, even at image sizes that prohibit molecular resolution. The images show the advancement of the p3-crystal (lighter area) after 34 (B) and 54 min (C) of incubation of 20 μg/mL annexin A5 in 2 mM $CaCl_2$ on DOPC/DOPS (1:2)-SLBs. In (C) only a few small p6 crystalline areas remain (*asterisks*). Image size (z-limit): 5 μm (1 nm).

FIGURE 12

Series of AFM-images demonstrating the memory-effect of annexin A5 on mica-SLBs. Annexin A5 crystals grew (A-F) after incubation of 40 μg/mL annexin A5 on a mica-SLB that was freshly prepared from SUVs of DOPC/DOPS (4:1) at 2 mM $CaCl_2$. The process of crystal growth is slow (A-E, incubation times denoted in minutes) and more than 4 hours are needed to reach complete coverage (F). A rinse in buffer containing 0.02 mM $CaCl_2$ displaces all annexin A5 (not shown). Upon re-incubation with 40 μg/mL annexin A5 in 2 mM $CaCl_2$ crystal growth proceeds faster than during the first run (G-K) and a complete crystalline layer is formed within only 70 min (L). A few defects are visible

(*arrowhead* in I) that were introduced upon removal of annexin A5 in buffer containing 0.02 mM $CaCl_2$. The crystalline domains were identified as p6 crystals by the pronounced and irregular holes in the lattice, reflecting the absence of some central trimers (*inset* in J, image size: 250 nm). Image size (z-limit): 40 μm (10 nm).

FIGURE 1

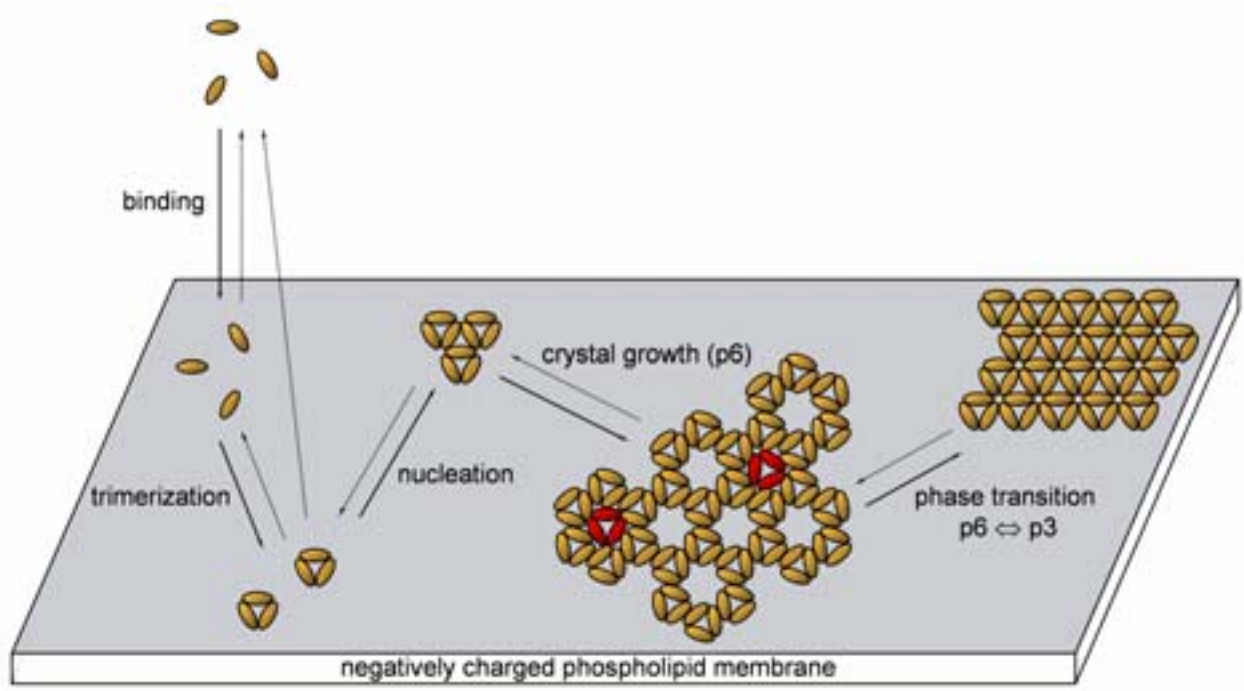
binding
crystal growth (p6)
nucleation
trimerization
phase transition
p6 ⇔ p3
negatively charged phospholipid membrane

FIGURE 2

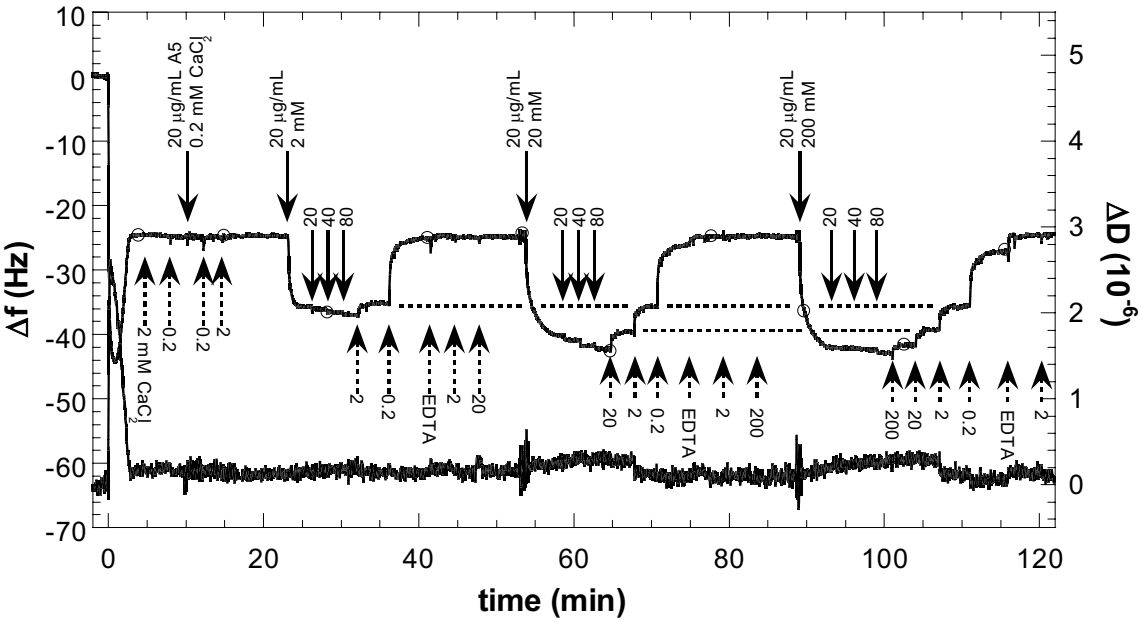
Δf (Hz)
ΔD (10⁻⁶)
time (min)
20 µg/mL A5
0.2 mM CaCl2
20 µg/mL
2 mM
20 µg/mL
20 mM
20 µg/mL
200 mM
2 mM CaCl2
0.2
2
20
40
80
EDTA
200

FIGURE 3

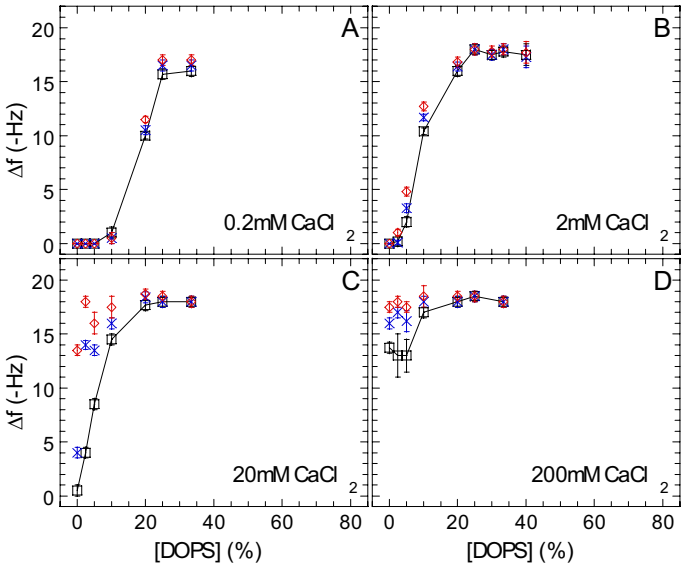
A
B
C
D
0.2mM CaCl2
2mM CaCl2
20mM CaCl2
200mM CaCl2
Δf (-Hz)
[DOPS] (%)
0
5
10
15
20
0
20
40
60
80

FIGURE 4

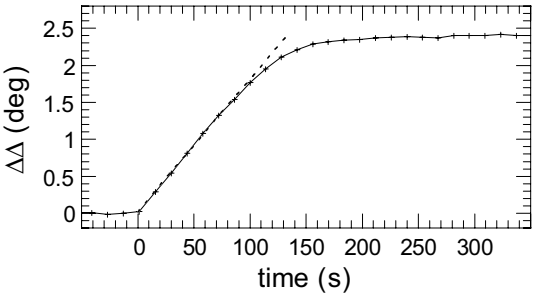

FIGURE 5

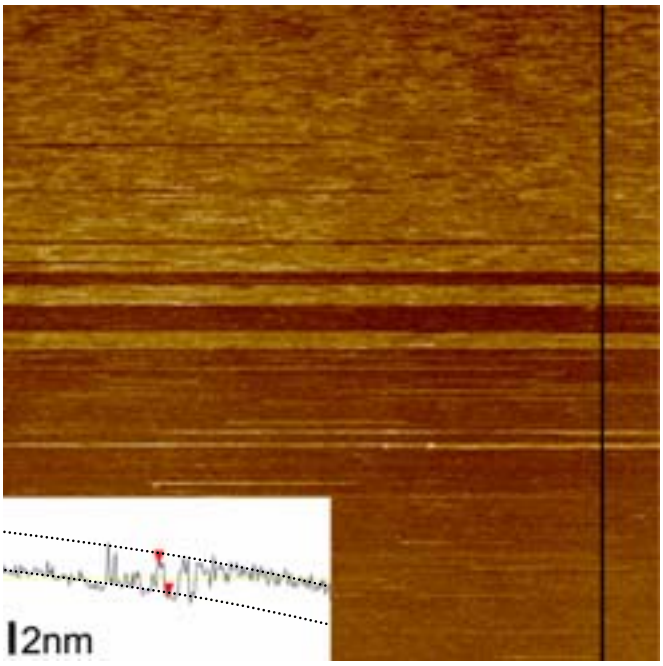

FIGURE 6

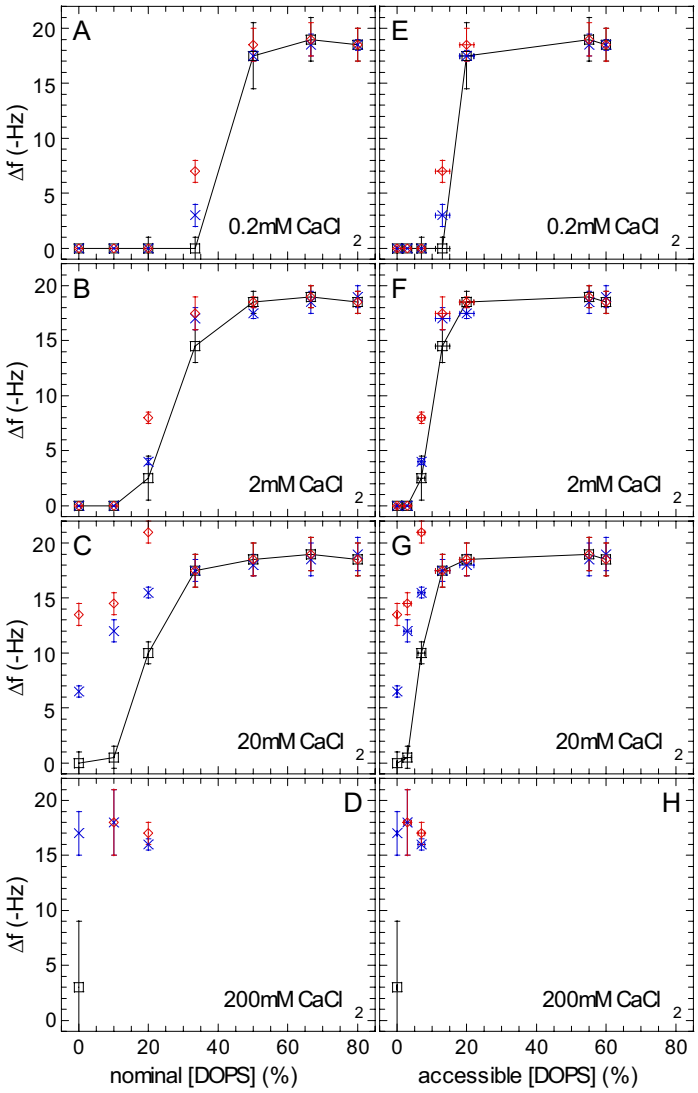
A
E
B
F
C
G
D
H
Δf (-Hz)
0.2mM CaCl2
2mM CaCl2
20mM CaCl2
200mM CaCl2
nominal [DOPS] (%)
accessible [DOPS] (%)

FIGURE 7

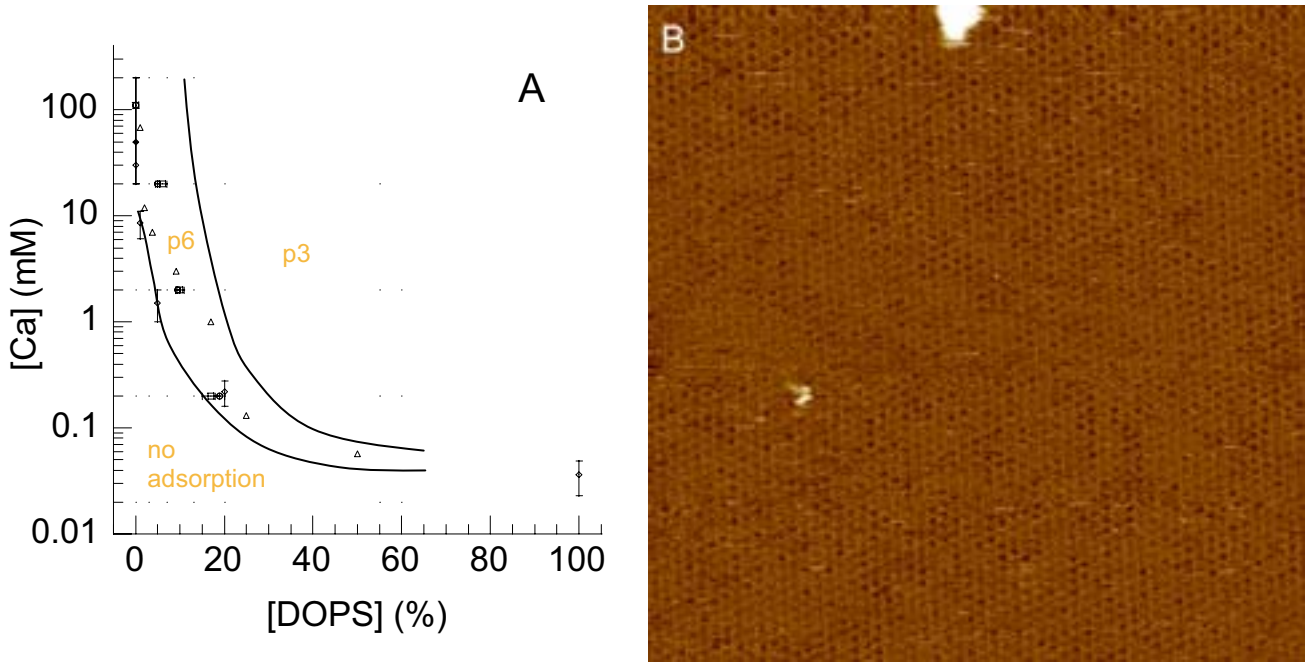

FIGURE 8

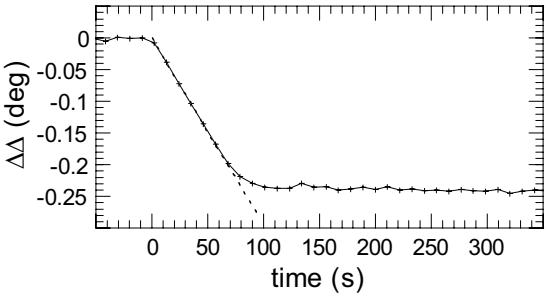

FIGURE 9

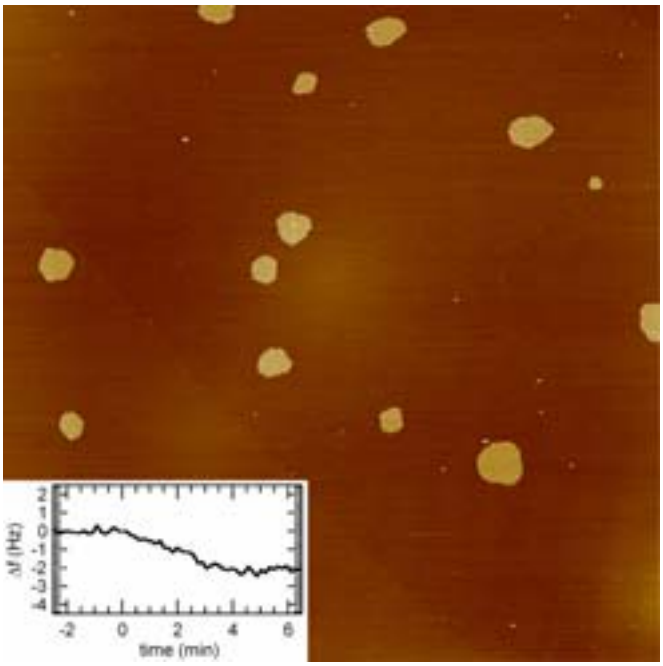

FIGURE 10

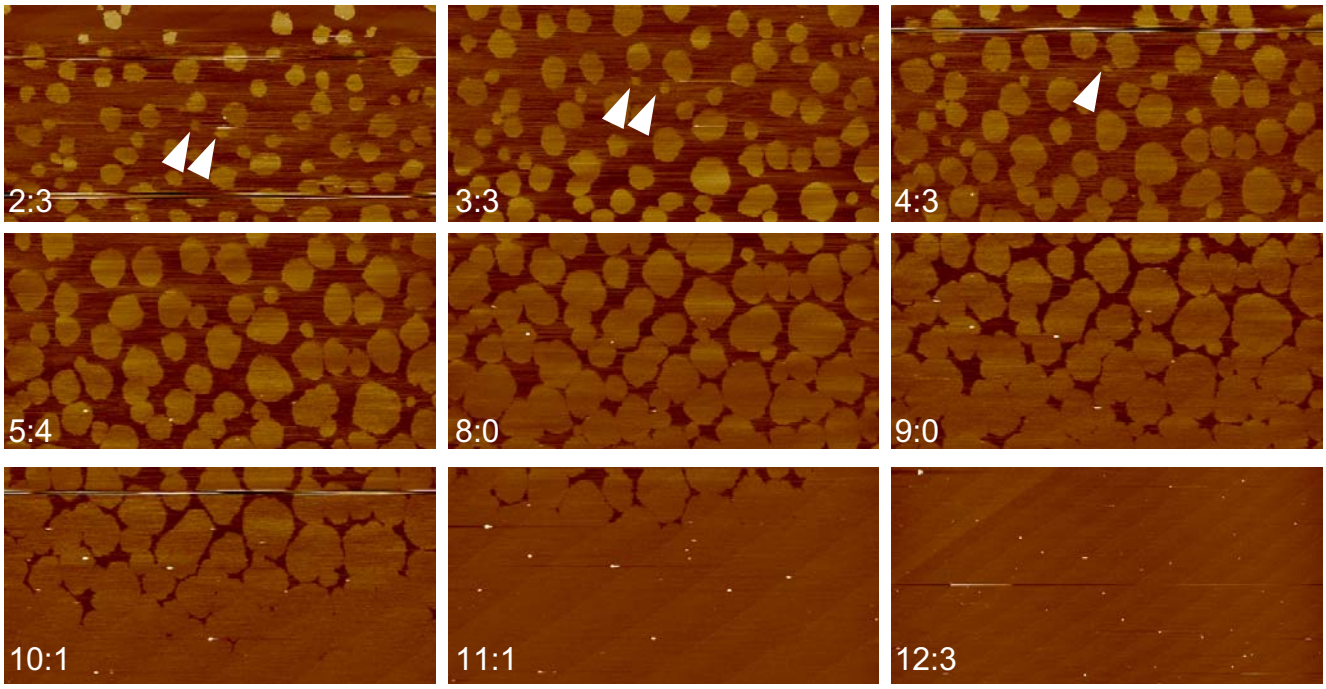

FIGURE 11

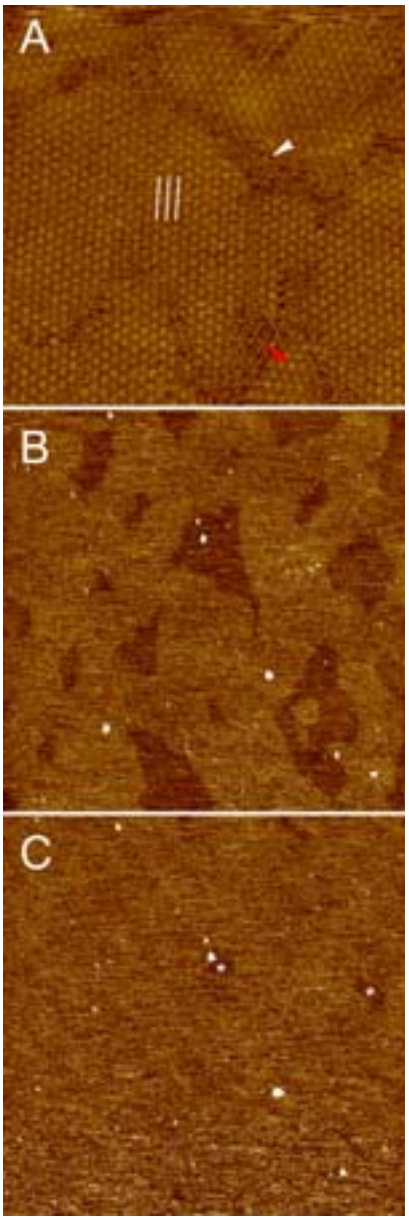

FIGURE 12

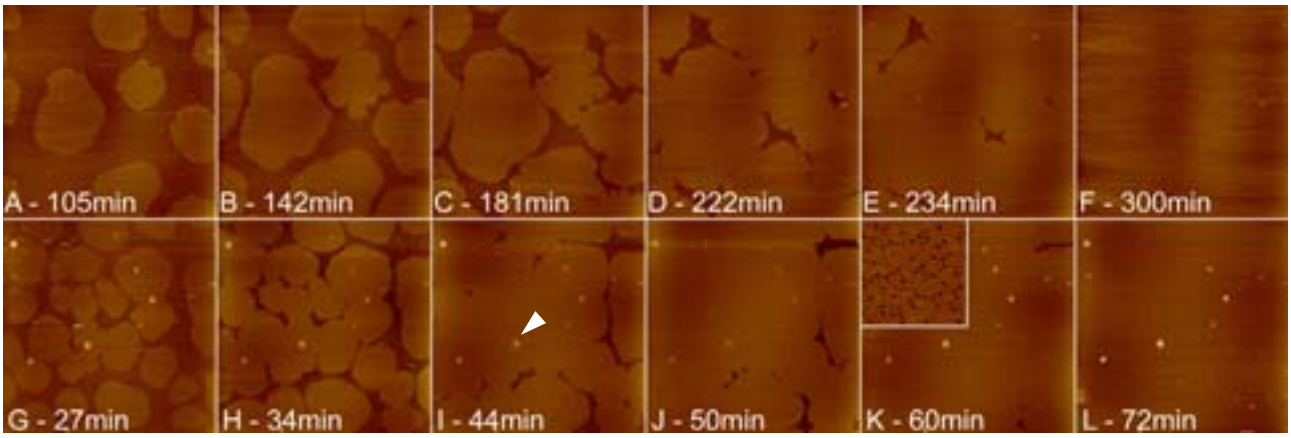
A - 105min
B - 142min
C - 181min
D - 222min
E - 234min
F - 300min
G - 27min
H - 34min
I - 44min
J - 50min
K - 60min
L - 72min

V. Conclusions and Perspectives

The focus of this PhD thesis was to characterize the deposition of lipid vesicles and the formation of supported lipid bilayers on solid supports, and the 2D assembly of the protein annexin A5. The main results, listed below, contribute to our basic understanding of both processes.

Two main methods, AFM and QCM-D, were used extensively, to provide local topographic information and quantitative physico-chemical characterization of the interfacial layers, respectively. We have developed a method to combine AFM and QCM-D on mica and demonstrated the complementarity of both techniques and the value of their combination for the characterization of 2D self-organization processes, such as the formation of SLBs and the 2D crystallization of proteins.

We have provided evidence that a multitude of lipid deposition pathways can be generated on mica and silica and characterized these pathways in detail. Which pathway will be taken is determined by parameters such as the lipid charge and the calcium-EDTA balance. Other parameters such as the solution's pH and ionic strength are expected to play a similar role. The paramount importance of the solid support in the SLB-formation process is outlined and essential differences in the lipid deposition on silica and on mica have been identified. The exact role of the solid support remains, however, poorly understood. Questions remain, such as concerning the mechanisms by which the support influences the lateral mobility of lipid assemblies as well as the properties of the final SLB (e.g., the inter-leaflet lipid distribution or the propensity of membrane-bound annexin A5 to crystallize).

The characterization methods developed here are expected to be applicable for various surface-confined lipid assemblies. In particular, they can easily be extended to more complex systems, such as the formation of SLBs from protein-containing liposomes as well as polymer-cushioned, tethered or pore-spanning SLBs. The development of PEG-modified AFM-tips constituted an important prerequisite for the controlled imaging of lipid assemblies. It brings more quantitative investigations into reach, and thereby opens up for the further evaluation of models of SLB-formation.

We have clarified essential aspects of the adsorption of annexin A5 to SLBs and refined he phase diagram of this protein in its membrane bound state. The results are expected to constitute a valuable base for a detailed investigation of the self-assembly dynamics of this protein. The outlined experimental approach, in correlation with theory, opens the door to the quantitative assessment of parameters involved in the 2D crystallization of proteins and other macromolecules.

In a more general perspective, the techniques used in this work and the illustrated complementary aspects make their combined use attractive for the development and validation of bio-mimetic and bio-functionalized surfaces.

V. Conclusions et Perspectives (version française)

Les principaux objectifs de ce travail de thèse ont été la caractérisation de la formation de bicouches lipidiques supportées par déposition de vésicules lipidiques sur support solide, ainsi que l'étude de l'assemblage 2D de la protéine annexine A5. Les résultats majeurs, détaillés ci-dessous, apportent une contribution notable à notre compréhension générale de ces deux processus.

Deux méthodes principales de caractérisation, l'AFM et le QCM-D, ont été employées de manière extensive, fournissant respectivement une information sur la topographie locale et une caractérisation quantitative des propriétés physico-chimiques des couches interfaciales. Nous avons mis au point une méthode permettant de combiner l' AFM et le QCM-D sur support de mica. Nous avons pu démontrer la complémentarité de ces deux techniques ainsi que la valeur de leur combinaison pour la caractérisation des processus d'auto-organisation 2D, tels que la formation de SLBs et la cristallisation 2D de protéines.

Nous avons montré que le dépôt des vésicules lipidiques et la formation des SLBs peuvent procéder via une multitude de parcours et nous avons caractérisé en détail les mécanismes associés et les paramètres influençant ces processus. La manière dont un SLB se forme est déterminée par la charge des lipides et la balance calcium-EDTA. Il est très probable que d'autres paramètres, comme le pH de la solution ou la force ionique, jouent également un rôle important. L'importance première de la nature du support solide a été mise en évidence et des différences essentielles entre les supports de mica et de silice ont été identifiées en ce qui concerne la formation des SLBs. Le rôle exact du support solide reste cependant peu compris. En particulier, les mécanismes par lesquels le support influence la mobilité latérale des assemblages lipidiques et quelques propriétés de SLBs, telles que la distribution de lipides de nature différentes entre les deux feuillets de la bicouche et leur influence sur la capacité de l'annexine A5 à cristalliser en deux dimensions, restent à clarifier.

Les méthodes développées dans le cadre de ce travail peuvent être appliquées à la caractérisation d'autres types d'assemblages lipidiques. En particulier, elles peuvent être étendues à des systèmes plus complexe, tels que la formation des SLBs à partir de liposomes contenant des protéines ou à la formation de membranes ancrées (« tethered »), espacées (« cushioned ») ou suspendues (« pore-spanning »). Le développement de pointes modifiées par des groupements de type PEG a apporté une amélioration considérable à l'imagerie contrôlée d'assemblages lipidiques. Une caractérisation quantitative de la géométrie des

assemblages lipidiques a ainsi été rendu possible, permettant une évaluation plus rigoureuse des modèles théoriques de la formation de SLBs.

Nous avons clarifié certains aspects essentiels de l'adsorption de l'annexine A5 sur des SLBs et affiné le diagramme de phase de cette protéine liée à des membranes. L'ensemble des résultats constitue une base originale pour une caractérisation détaillée de la dynamique de l'auto-assemblage de l'annexine A5. L'approche expérimentale que nous avons décrite, va permettre une évaluation quantitative, et corrélable aux modèles théoriques existants, des paramètres impliqués dans la cristallisation 2D des protéines et d'autres macromolécules.

Dans une perspective plus générale, les aspects complémentaires des techniques utilisées rendent leur utilisation combinée attractive pour le développement et pour la validation des surfaces bio-mimétiques et bio-fonctionnalisées.

References

(1) Rouser, G.; Fleischer, S.; Yamamoto, A. 1975. Two dimensional thin layer chromatographic separation of polar lipids and determination of phospholipids by phosphorus analysis of spots. *Lipids* 5:494-496.

(2) Mou, J.; Czajkowsky, D. M.; Zhang, Y.; Shao, Z. 1995. High resolution atomic force microscopy of DNA: the pitch of the double helix. *FEBS Lett.* 371:279-282.

(3) Maier, B.; Rädler, J. O. 1999. Conformation and Self-Diffusion of Single DNA Molecules Confined to Two Dimensions. *Phys. Rev. Lett.* 82:1911-1914.

(4) Israelachvili, J.; Wennerström, H. 1996. Role of hydration and water structures in biological and colloidal interactions. *Nature* 379:219-225.

(5) Ball, P. 2003. How to keep dry in water. *Nature* 423:25-26.

(6) Yeagle, P. 1987. The Membranes of Cells. Academic Press, Inc., Orlando.

(7) Israelachvili, J. N. 1992. Intermolecular and Surface Forces. Academic Press Limited, London.

(8) Olbrich, K.; Rawicz, W.; Needham, D.; Evans, E. 2000. Water Permeability and Mechanical Strength of Polyunsaturated Lipid Bilayers. *Biophys. J.* 79:321-327.

(9) Hauser, H.; Oldani, D.; Philips, M. C. 1973. Mechanism of Ion Escape from Phosphatidylcholine and Phophatidylserine Single Bilayer Vesicles. *Biochemistry* 12:4507-4517.

(10) Gennis, R. B. 1989. Biomembranes: molecular structure and function. Cantor, C. R., editor. Springer Verlag, New York.

(11) Wimley, W. C.; Thompson, T. E. 1990. Exchange and Flip-Flop of Dimyristoylphophatidylcholine in Liquid-Crystalline, Gel, and Two-Component, Two-Phase Large Unilamellar Vesicles. *Biochemistry* 29:1296-1303.

(12) John, K.; Schreiber, S.; Kubelt, J.; Herrmann, A.; Müller, P. 2002. Transbilayer Movement of Phopholipids at the Main Phase Transition of Lipid Membranes: Implications for Rapid Flip-FLop in Biological Membranes. *Biophys. J.* 83:3315-3323.

(13) Kol, M. A.; Laak, A. N. C. v.; Rijkers, D. T. S.; Killian, J. A.; Kroon, A. I. P. M. d.; Kruijff, B. d. 2003. Phospholipid Flop Induced by Transmembrane Peptides in Model Membranes Is Modulated by Lipid Composition. *Biochemistry* 42:231-237.

(14) Homan, R.; Pownall, H. J. 1988. Transbilayer diffusion of phopholipids: dependence on headgroup structure and acyl chain length. *Biochim. Biophys. Acta* 938:155-166.

(15) Avanti Polar Lipids - Products Catalog.

(16) Mattai, J.; Hauser, H.; Demel, R. A.; Shipley, G. G. 1989. Interactions of Metal Ions with Phophatidylserine Bilayer Membranes: Effect of Hydrocarbon Chain Unsaturation. *Biochemistry* 28:2322-2330.

(17) Edidin, M. 2003. Lipids on the frontier: a century of cell-membrane bilayers. *Nat. Rev. Mol. Cell Biol.* 4:414-418.

(18) Langmuir, I. 1917. The constitution and fundamental properties of solids and liquids. II. Liquids. *J. Am. Chem. Soc.* 39:1848-1906.

(19) Gorter, E.; Grendl, F. 1925. On bimolecular layers of lipids on the chromocytes of the blood. *J. Exp. Med.* 41:439-443.

(20) Robertson, J. D. 1959. The ultrastructure of cell membranes and their derivatives. *Biochem. Soc. Symposium* 16:3-43.

(21) Frye, L. D.; Edidin, M. 1970. The rapid intermixing of cell surface antigens after formation of mouse-human heterokaryons. *J. Cell Sci.* 7:319-335.

(22) Chapman, D. 1975. Phase trasitions and fluidity characteristics of lipids and cell membranes. *Quart. Rev. Biophys.* 8:185-235.

(23) Singer, S. J.; Nicolson, G. L. 1972. The fluid mosaic model of cell membranes. *Science* 175:720-731.

(24) Tocanne, J.-F.; Cézanne, L.; Lopez, A.; Piknova, B.; Schram, V.; Tournier, J.-F.; Welby, M. 1994. Lipid domains in lipid/protein interactions in biological membranes. *Chem. Phys. Lipids* 73:139-158.

(25) Simons, K.; Ikonnen, E. 1997. Functional rafts in cell membranes. *Nature* 389:569-572.

(26) Edidin, M. 2001. Shrinking patches and slippery rafts: scales of domains in the plasma membrane. *Trends Cell Biol.* 11:492-496.

(27) Edidin, M. 2003. The state of lipid rafts: from model membranes to cells. *Annu. Rev. Biophys. Biomol. Struct.* 32:257-283.

(28) Simons, K.; Vaz, W. L. C. 2004. Model Systems, Lipid Rafts and Cell Membranes. *Annu. Rev. Biophys. Biomolec. Struct.* 33:269-295.

(29) Meer, G. v.; Simons, K. 1986. The function of tight junctions in maintaining differences in lipid composition between the apical and the basolateral cell surface domains of MDCK cells. *EMBO J.* 5:1455-1464.

(30) Devaux, P. F. 1991. Static and Dynamic Lipid Asymmetry in Cell Membranes. *Biochemistry* 30:1163-1173.

(31) Steinmann, R. M.; Mellmann, I. S.; Muller, W. A.; Cohn, Z. A. 1983. Endocytosis and the recycling of plasma membrane. *J. Cell Biol.* 96:1-27.

(32) Gregoriadis, G. 1993. Liposome Technology. CRC Press, Boca Raton. 632 p.

(33) Rigaud, J. L.; Pitard, B.; Levy, D. 1995. Reconstitution of membrane proteins into liposomes: application to energy-transducing membrane proteins. *Biochim. Biophys. Acta* 1231:223-246.

(34) Szoka, F.; Papahadjopoulos, D. 1980. Comparative Properties and Methods of Preparation of Lipid Vesicles (Liposomes). *Ann. Rev. Biophys. Bioeng.* 9:467-508.

(35) Hope, M. J.; Nayar, R.; Mayer, L. D.; Cullis, P. R. 1993. Reduction of liposome size and preparation of unilamellar vesicles by extrusion techniques. *In* Liposome Technology. Gregoriadis, G., editor. CRC Press, Boca Raton. 632.

(36) Szoka, F.; Papahadjopoulos, D. 1978. Procedure for the preparation of liposomes with large internal aqueous space and high capture by reverse-phase evaporation. *Proc. Natl. Acad. Sci. USA* 75:4194-4198.

(37) Batzri, S.; Korn, E. D. 1973. Single bilayer liposomes prepared without sonication. *Biochim. Biophys. Acta* 298:1015-1019.

(38) Deamer, D.; Bangham, A. D. 1976. Large volume liposomes by an ether vaporization method. *Biochim. Biophys. Acta* 443:629-634.

(39) Angelova, M. I. 2000. Liposome electroformation. *In* Giant Vesicles. Luisi, P. L.,Walde, P., editors. John Wiley, Chichester, England. 27-36.

(40) Egelhaaf, S. U.; Wehrli, E.; Müller, M.; Adrian, M.; Schurtenberger, P. 1996. Determination of the size distribution of lecitin liposomes: a comparative study using freeze fracture, cryoelectron microscopy and dynamic light scattering. *J. Microscopy* 184:214-228.

(41) Coldren, B.; Zanten, R. v.; Mackel, M. J.; Zasadzinski, J. A.; Jung, H.-T. 2003. From Vesicle Size Distributions to Bilayer Elasticity via Cryo-Transmission and Freeze-Fracture Electron Microscopy. *Langmuir* 19:5632-5639.

(42) Niggemann, G.; Kummrow, M.; Helfrich, W. 1995. The Bending Rigidity of Phophatidylcholine Bilayers: Dependences on Experimental Method, Sample Cell Sealing and Temperature. *J. Phys. II France* 5:413-425.

(43) Evans, E. 1995. Physical Actions in Biological Adhesion. *In* Structure and Dynamics of Membranes - Generic and Specific Interactions. Lipowsky, R.,Sackmann, E., editors. Elsevier, Amsterdam.

(44) Seifert, U. 1997. Configuration of fluid membranes and vesicles. *Adv. Phys.* 46:13-137.

(45) Baumgart, T.; Hess, S. T.; Webb, W. W. 2003. Imaging coexisting fluid domains in biomembrane models coupling curvature and line tension. *Nature* 425:821-824.

(46) Pécréaux, J.; Döbereiner, H.-G.; Prost, J.; Joanny, J.-F.; Bassereau, P. 2004. Refined contour analysis of giant unilamellar vesicles. *Eur. Phys. J. E* 13:277-290.

(47) Lipowsky, R.; Seifert, U. 1991. Adhesion of Vesicles and Membranes. *Mol. Crys. Liq. Cryst.* 202:17-25.

(48) Karatekin, E.; Sandre, O.; Guitouni, H.; Borghi, N.; Puech, P.-H.; Brochard-Wyart, F. 2003. Cascades of Transient Pores in Giant Vesicles: Line Tension and Transport. *Biophys. J.* 84:1734-1749.

(49) Richter, R. P.; Mukhopadhay, A.; Brisson, A. 2003. Pathways of lipid vesicle deposition on solid surfaces: a combined QCM-D and AFM study. *Biophys. J.* 85:3035-3047.

(50) Kumar, A.; Gupta, C. M. 1984. Transbilayer Distributions of Red Cell Membrane Phospholipids in Unilamellar Vesicles. *Biochim. Biophys. Acta* 769:419-428.

(51) Brian, A. A.; McConnell, H. M. 1984. Allogenic stimulation of cytotoxic T cells by supported planar membranes. *Proc. Natl. Acad. Sci. USA* 81:6195-6163.

(52) Sackmann, E. 1996. Supported Membranes: Scientific and Practical Applications. *Science* 271:43-48.

(53) Boxer, S. G. 2000. Molecular transport and organization in supported lipid membranes. *Curr. Opin. Chem. Biol.* 4:704-709.

(54) Bieri, C.; Ernst, O. P.; Heyse, S.; Hofmann, K. P.; Vogel, H. 1999. Micropatterned immobilization of a G protein-coupled receptor and direct detection of G protein activation. *Nat. Biotechn.* 17:1105-8.

(55) Kung, L. A.; Kam, L.; Hovis, J. S.; Boxer, S. G. 2000. Patterning Hybrid Surfaces of Proteins and Supported Lipid Bilayers. *Langmuir* 16:6773-6776.

(56) Sapuri, A. R.; Baksh, M. M.; Groves, J. T. 2003. Electrostatically Targeted Intermembrane Lipid Exchange with Micropatterned Supported Membranes. *Langmuir* 19:1606-1619.

(57) Srinivasan, M. P.; Ratto, T. V.; Stroeve, P.; Longo, M. L. 2001. Patterned Supported Bilayers on Self-Assembled Monolayers: Confinement of Adjacent Mobile Bilayers. *Langmuir* 17:7951-7954.

(58) Michel, R.; Reviakine, I.; Sutherland, D.; Fokas, C.; Csucs, G.; Danuser, G.; Spencer, N. D.; Textor, M. 2002. A novel Approach to Produce Biologically Relevant Chemical Patterns at the Nanometer Scale: Selective Molecular Assembly Patterning Combined with Colloidal Lithography. *Langmuir* 18:8580-8586.

(59) Svedhem, S.; Pfeiffer, I.; Larsson, C.; Wingren, C.; Borrebaeck, C.; Höök, F. 2003. Patterns of DNA-Labeled and scFv-Antibody-Carrying Lipid Vesicles Directed by Material-Specific Immobilization of DNA and Supported Lipid Bilayer Formation on an Au/SiO_2 Template. *ChemBioChem* 4:339-343.

(60) Morigaki, K.; Kiyosue, K.; Taguchi, T. 2004. Micropatterned Composite Membranes of Polymerized Fluid Lipid Bilayers. *Langmuir* 20:7729-7735.

(61) Kam, L.; Boxer, S. G. 2003. Spatially Selective Manipulation of Supported Lipid Bilayers by Laminar Flow: Steps Toward Biomembrane Microfluidics. *Langmuir* 19:1624-1631.

(62) Swart, R. M. 1990. Monolayers and Multilayers of Biomolecules. *In* Langmuir-Blodgett Films. Roberts, G., editor. Plenum Press, New York. 273-316.

(63) Grandbois, M.; Clausen-Schaumann, H.; Gaub, H. E. 1998. Atomic Force Microscopy Imaging of Phospholipid Degradation by Phospholipase A_2. *Biophys. J.* 74:2398-2404.

(64) Wong, J. Y.; Majewski, J.; Seitz, M.; Park, C. K.; Israelachvili, J.; Smith, G. S. 1999. Polymer-Cushioned Bilayers. I. A Structural Study of Various Preparation Methods Using Neutron Reflectometry. *Biophys. J.* 77:1445-1457.

(65) Ross, M.; Steinem, C.; Galla, H.-J.; Janshoff, A. 2001. Visualization of Chemical and Physical Properties of Calcium-Induced Domains in DPPC/DPPS Langmuir-Blodgett Layers. *Langmuir* 17:2437-2445.

(66) Heyse, S.; Ernst, O. P.; Dienes, Z.; Hofmann, K. P.; Vogel, H. 1998. Incorporation of rhodopsin in laterally structured supported membranes: observation of transducin activation with spatially and time-resolved surface plasmon resonance. *Biochemistry* 37:507-522.

(67) Grant, L. M.; Tiberg, F. 2002. Normal and Lateral Forces between Lipid Covered Solids in Solution: Correlation with Layer Packing and Structure. *Biophys. J.* 82:1373-1385.

(68) Steinem, C.; Janshoff, A.; Ulrich, W.-P.; Sieber, M.; Galla, H.-J. 1996. Impedance analysis of supported lipid bilayer membranes: a scrutiny of different preparation techniques. *Biochim. Biophys. Acta* 1279:169-180.

(69) Keller, C. A.; Kasemo, B. 1998. Surface Specific Kinetics of Lipid Vesicle Adsorption Measured with a Quartz Crystal Microbalance. *Biophys. J.* 75:1397-1402.

(70) Starr, T. E.; Thompson, N. L. 2000. Formation and Characterization of Planar Phospholipid Bilayers Supported on TiO_2 and $SrTiO_3$ Single Crystals. *Langmuir* 16:10301-10308.

(71) Zhao, J.; Tamm, L. K. 2003. FTIR and Fluorescence Studies of Interactions of Synaptic Fusion Proteins in Polymer-Supported Bilayers. *Langmuir* 19:1838-1846.

(72) Baumgart, T.; Offenhäusser, A. 2003. Polysaccharide-Supported Planar Bilayer Lipid Model Membranes. *Langmuir* 19:1730-1737.

(73) Mou, J.; Yang, J.; Shao, Z. 1995. Atomic Force Microscopy of Cholera Toxin B-oligomers Bound to Bilayers of Biologically Relevant Lipids. *J. Mol. Biol.* 248:507-512.

(74) Reviakine, I.; Simon, A.; Brisson, A. 2000. Effect of Ca^{2+} on the Morphology of Mixed DPPC-DOPS Supported Phospholipid Bilayers. *Langmuir* 16:1473-1477.

(75) Schneider, J.; Dufrêne, Y. F.; Barger Jr., W. R.; Lee, G. U. 2000. Atomic Force Microscope Image Contrast Mechanisms on Supported Lipid Bilayers. *Biophys. J.* 79:1107-1118.

(76) Rinia, H. A.; Kruijff, B. d. 2001. Imaging domains in model membranes with atomic force microscopy. *FEBS Lett.* 504:194-199.

(77) Yip, C. M.; Darabie, A. A.; McLaurin, J. 2002. Aβ42-Peptide Assembly on Lipid Bilayers. *J. Mol. Biol.* 318:97-107.

(78) Lawrence, J. C.; Saslowsky, D. E.; Edwardson, J. M.; Henderson, R. M. 2003. Real-Time Analysis of the Effects of Cholesterol on Lipid Raft Behavior Using Atomic Force Microscopy. *Biophys. J.* 84:1827-1832.

(79) Tokumasu, F.; Jin, A. J.; Feigenson, G. W.; Dvorak, J. A. 2003. Nanoscopic Lipid Domain Dynamics Revealed by Atomic Force Microscopy. *Biophys. J.* 84:2609-2618.

(80) Giocondi, M.-C.; Milhiet, P. E.; Dosset, P.; Grimellec, C. l. 2004. Use of Cyclodextrin for AFM Monitoring of Model Raft Formation. *Biophys. J.* 86:861-869.

(81) Janshoff, A.; Bong, D. T.; Steinem, C.; Johnson, J. E.; Ghadiri, M. R. 1999. An Animal Virus-Derived Peptide Switches Membrane Morphology: Possible Relevance to Nodaviral Transfection Processes. *Biochemistry* 38:5328-5336.

(82) Kaizuka, Y.; Groves, J. T. 2004. Structure and Dynamics of Supported Intermembrane Junctions. *Biophys. J.* 86:905-912.

(83) Parthasarathy, R.; Groves, J. T. 2004. Protein Patterns at lipid bilayer junctions. *Proc. Natl. Acad. Sci. USA* 101:12798-12803.

(84) Corsel, J. W.; Willems, G. M.; Kop, J. M. M.; Cuypers, P. A.; Hermens, W. T. 1986. The Role of Intrinsic Binding Rate and Transport Rate in the Asorption of Prothrombin, Albumin and Fibrinogen to Phospholipid Bilayers. *J. Colloid Interface Sci.* 111:544-554.

(85) Andree, H. A. M.; Stuart, M. C. A.; Hermens, W. T.; Reutelingsperger, C. P. M.; Hemker, H. C.; Frederik, P. M.; Willems, G. M. 1992. Clustering of Lipid-bound Annexin V May Explain Its Anticoagulant Effect. *J. Biol. Chem.* 267:17907-17912.

(86) Czaikowsky, D. M.; Shao, Z. 1998. Submolecular resolution of single macromolecules with atomic force microscopy. *FEBS Lett.* 430:51-54.

(87) Milhiet, P. E.; Giocondi, M.-C.; Baghdadi, O.; Ronzon, F.; Roux, B.; Grimellec, C. l. 2002. Spontaneous insertion and partitioning of alkaline phosphatase into model lipid rafts. *EMBO reports* 3:485-490.

(88) Proux-Delrouyre, V.; Elie, C.; Laval, J.-M.; Moiroux, J.; Bourdillon, C. 2002. Formation of Tethered and Streptavidin-Supported Lipid Bilayers on a Microporous Electrode for the Reconstitution of Membranes of Large Surface Area. *Langmuir* 18:3263-3272.

(89) Berquand, A.; Mazeran, P.-E.; Pantigny, J.; Proux-Delrouyre, V.; Laval, J.-M.; Bourdillon, C. 2003. Two-Step Formation of Streptavidin-Supported Lipid Bilayers by PEG-Triggered Vesicle Fusion. Fluorescence and Atomic Force Microscopy Characterization. *Langmuir* 19:1700-1707.

(90) Sackmann, E.; Tanaka, M. 2000. Supported membranes on soft polymer cushions: fabrication, characterization and applications. *Trends Biotechn.* 18:58-64.

(91) Hennesthal, C.; Steinem, C. 2000. Pore-Spanning Lipid Bilayers Visualized by Scanning Force Microscopy. *J. Am. Chem. Soc.* 122:8085-8086.

(92) Römer, W.; Steinem, C. 2004. Impedance Analysis and Singel-Channel Recordings on Nano-Black Lipid Membranes Based on Porous Alumina. *Biophys. J.* 86:955-965.

(93) Seaton, B. A., editor. 1996. Annexins: Molecular Structure to Cellular Function: R.G. Landes Company.

(94) Bandorowicz-Pikula, J., editor. 2003. Annexins: Biological importance and annexin-related pathologies. Georgetown, Tex.: Landes Bioscience/Eurekah.com. 37-55 p.

(95) Funakoshi, T.; Heimark, R. L.; Henrickson, L. E.; McMullen, B. A.; Fujikawa, K. 1987. Human Placental Anticoagulant Protein: Isolation and Characterization. *Biochemistry* 26:5572.

(96) Gerke, V.; Moss, S. E. 1997. Annexins and membrane dynamics. *Biochim. Biophys. Acta* 1357:129-154.

(97) Rand, J. H.; Wu, X. X. 1999. Antibody-mediated disruption of the annexin-V antithrombotic shield: a new mechanism for thrombosis in the antiphospholipid syndrome. *Thromb. Haemost.* 82:649-655.

(98) Lieby, P.; Poindron, V.; Roussi, S.; Klein, C.; Knapp, A.-M.; Cerutti, T.; Martin, T.; Pasquali, J.-L. 2004. Pathogenic antiphospholipid antibody: an antigen-selected needle in a haystack. *Blood* 104:1711-1715.

(99) Brisson, A.; Lewit-Bentley, A. 1996. A Common Trimer of Annexin V as a Basic Unit in 2D and 3D Crystal Forms. *In* Annexins: Molecular Structure to Cellular Function. Seaton, B., editor. R.G. Landes Company. 43-52.

(100) Huber, R.; Schneider, M.; Mayr, I.; Römisch, J. M.; Paques, E. P. 1990. The calcium binding sites in human annexin V by crystal structure analysis at 2.0 A resolution. Implications for membrane binding and calcium channel activity. *FEBS Lett.* 275:15-21.

(101) Oling, F.; Sopkova-de Oliveira Santos, J.; Govorukhina, N.; Mazères-Dubut, C.; Bergsma-Schutter, W.; Oostergetel, G.; Keegstra, W.; Lambert, O.; Lewit-Bentley, A.; Brisson, A. 2000. Structure of membrane-bound annexin A5 trimers: a hybrid Cryo-EM - X-ray crystallography study. *J. Mol. Biol.* 304:561-573.

(102) Voges, D.; Berendes, R.; Burger, A.; Demange, P.; Baumeister, W.; Huber, R. 1994. Three-dimensional structure of membrane-bound annexin V - a correlative electron microscopy-X-ray crystallography study. *J. Mol. Biol.* 238:199-213.

(103) Meers, P. 1990. Location of tryptophans in membrane-bound annexins. *Biochemistry* 29:3325-3330.

(104) Meers, P.; Mealy, T. 1993. Relationship between Annexin V Tryptophan Exposure, Calcium, and Phopholipid Binding. *Biochemistry* 32:5411-5418.

(105) Huber, R.; Römisch, J. M.; Paques, E. P. 1990. The crystal and molecular structure of human annexin V, an anticoagulant protein that binds to calcium and membranes. *EMBO J.* 9:3867-3874.

(106) Sopkova, J.; Renouard, M.; Lewit-Bentley, A. 1993. The Crystal Structure of a New High-calcium Form of Annexin V. *J. Mol. Biol.* 234:816-825.

(107) Concha, N. O.; Head, J. F.; Kaetzel, M. A.; Dedman, J. R.; Seaton, B. A. 1993. Rat annexin V crystal structure: Ca^{2+}-induced conformational changes. *Science* 261:1321-1324.

(108) Govorukhina, N.; Bergsma-Schutter, A.; Mazères-Dubut, C.; Mazères, S.; Drakopoulou, E.; Bystrykh, L.; Oling, F.; Mukhopadhyay, A.; Reviakine, I.; Lai Kee Him, J.; Brisson, A. 2003. Self-Assembly of Annexin A5 on Lipid Membranes. *In* Annexins: Biological importance and annexin-related pathologies. Bandorowicz-Pikula, J., editor. Landes Bioscience/Eurekah.com, Georgetown, Tex. 37-55.

(109) Reviakine, I.; Bergsma-Schutter, W.; Mazères-Dubut, C.; Govorukhina, N.; Brisson, A. 2000. Surface Topography of the p3 and p6 Annexin V Crystal Forms Determined by Atomic Force Microscopy. *J. Struct. Biol.* 131:234-239.

(110) Brisson, A.; Olofsson, A.; Ringler, P.; Schmutz, M.; Stoylova, S. 1994. Two-dimensional crystallization of proteins on planar lipid films and structure determination by electron crystallography. *Biol. Cell* 80:221-228.

(111) Brisson, A.; Bergsma-Schutter, A.; Oling, F.; Lambert, O.; Reviakine, I. 1999. Two-dimensional crystallization of proteins on lipid monolayers at the air-water interface and transfer to an electron microscopy grid. *J. Cryst. Growth* 196:456-470.

(112) Reviakine, I.; Bergsma-Schutter, A.; Morozov, A. N.; Brisson, A. 2001. Two-Dimensional Crystallization of Annexin A5 on Phospholipid Bilayers and Monolayers: A Solid-Solid Phase Transition Between Crystal Forms. *Langmuir* 17:1680-1686.

(113) Oling, F.; Bergsma-Schutter, W.; Brisson, A. 2001. Trimers, Dimers of Trimers, and Trimers of Trimers Are Common Building Blocks of Annexin A5 Two-Dimensional Crystals. *J. Struct. Biol.* 133:55-63.

(114) Noro, M. G.; Bates, M. A.; Brisson, A.; Frenkel, D. 2002. Modeling the Phase Behavior of the Membrane Binding Protein Annexin V. *Langmuir* 18:2988-2992.

(115) Knoll, W. 1998. Interfaces and thin films as seen by bound electromagnetic waves. *Ann. Rev. Phys. Chem.* 49:569-638.

(116) Tompkins, H. G. 1993. A user's guide to ellipsometry. Academic Press, New York.

(117) Shen, Y. R. 1989. Surface properties probed by second-harmonic and sum-frequency generation. *Nature* 337:519-525.

(118) Lambacher, A.; Fromherz, P. 1996. Fluorescence Interference-contrast microscopy on oxidized silicon using a monomolecular dye layer. *Appl. Phys. A* 63:207-216.

(119) Kiessling, V.; Tamm, L. K. 2003. Measuring Distances in Supported Bilayers by Fluorescence Interference-Contrast Microscopy: Polymer Supports and SNARE Proteins. *Biophys. J.* 84:408-418.

(120) Rädler, J.; Sackmann, E. 1993. Imaging optical thicknesses and separation distances of phopholipid vesicles at solid surfaces. *J. Phys. II France* 3:727-748.

(121) Born, M.; Wolf, E. 1999. Total reflection. *In* Principles of Optics. 7 ed. Cambridge University Press, Cambridge, United Kingdom. 49-53.

(122) Clark, S. C.; Walz, J. Y.; Ducker, W. A. 2004. Atomic Force Microscopy Colloid-Probe Measurements with Explicit Measurement of Particle-Solid Separation. *Langmuir* 20:7616-622.

(123) Liebermann, T.; Knoll, W. 2000. Surface-plasmon field-enhance fluorescence spectroscopy. *Colloids Surf. A* 171:115-130.

(124) Binnig, G.; Rohrer, H. 1982. Scanning tunneling microscopy - from birth to adolescence. *Rev. Mod. Phys.* 59:615-625.

(125) Binnig, G.; Quate, C. F.; Gerber, C. 1986. Atomic Force Microscope. *Phys. Rev. Lett.* 56:930-933.

(126) Binnig, G. 1992. Force Microscopy. *Ultramicroscopy* 42-44:7-15.

(127) Shao, Z.; Mou, J.; Czajkowsky, D. M.; Yang, J.; Yuan, J.-Y. 1996. Biological atomic force microscopy: what is achieved and what is needed. *Adv. Phys.* 45:1-86.

(128) Möller, C.; Allen, M.; Elings, V.; Engel, A.; Müller, D. J. 1999. Tapping-Mode Atomic Force Microscopy Produces Faithful High-Resolution Images of Protein Surfaces. *Biophys. J.* 77:1150-1158.

(129) Engel, A.; Müller, D. J. 2000. Observing single biomolecules at work with the atomic force microscope. *Nat. Struct. Biol.* 7:715-718.

(130) Müller, D. J.; Janovjak, H.; Lehto, T.; Kuerschner, L.; Anderson, K. 2002. Observing structure, function and assembly of single proteins by AFM. *Prog. Biophys. Mol. Biol.* 79:1-43.

(131) Müller, D. J.; Anderson, K. 2002. Biomolecular imaging using atomic force microscopy. *Trends Biotechn.* 20:S45-S49.

(132) Weisenhorn, A. L.; Egger, M.; Ohnesorge, F.; Gould, S. A. C.; Heyn, S.-P.; Hansma, H. G.; Sinsheimer, R. L.; Gaub, H. E.; Hansma, P. K. 1991. Molecular-Resolution Images of Langmuir-Blodgett Films and DNA by Atomic Force Microscopy. *Langmuir* 7:8-12.

(133) Butt, H.-J.; Prater, C. B.; Hansma, P. K. 1991. Imaging purple membranes dry and in water with the atomic force microscope. *J. Vac. Sci. Technol. B* 9:1193-1196.

(134) Hofmann, U. G.; Rotsch, C.; Parak, W. J.; Radmacher, M. 1997. Investigating the Cytosceleton of Chicken Cardiocytes with the Atomic Force Microscope. *J. Struct. Biol.* 119:84-91.

(135) Gebeshuber, I. C.; Kindt, J. H.; Thompson, J. B.; Amo, Y. D.; Stachelberger, H.; Brzezinski, M. A.; Stucky, G. D.; Morse, D. E.; Hansma, P. K. 2003. Atomic force microscopy study of living diatoms in ambient conditions. *J. Microscopy* 212:292-299.

(136) Kaasgaard, T.; Leidy, C.; Crowe, J. H.; Mouritsen, O. G.; Jorgensen, K. 2003. Temperature-Controlled Structure and Kinetics of Ripple Phases on One- and Two-Component Supported Lipid Bilayers. *Biophys. J.* 85:350-360.

(137) Tokumasu, F.; Jin, A. J.; Feigenson, G. W.; Dvorak, J. A. 2003. Atomic force microscopy of nanometric liposome adsorption and nanoscopic membrane domain formation. *Ultramicroscopy* 97:217-227.

(138) Enders, O.; Ngezahayo, A.; Wiechmann, M.; Leisten, F.; Kolb, H.-A. 2004. Structural Calorimetry of Main Transition of Supported DMPC Bilayers by Temperature-Controlled AFM. *Biophys. J.* 87:2522-2531.

(139) Mou, J.; Yang, J.; Shao, Z. 1994. Tris(hydroxymethyl)aminomethane ($C_4H_{11}NO_3$) Induced a Ripple Phase in Supported Unilamellar Phospholipid Bilayers. *Biochemistry* 33:4439-4443.

(140) Rinia, H. A.; Snel, M. M. E.; van der Erden, J. P. J. M.; de Kruijff, B. 2001. Visualizing detergent resistent domains in model membranes with Atomic Force Microscopy. *FEBS Lett.* 501:92-96.

(141) Milhiet, P. E.; Domec, C.; Giocondi, M.-C.; Mau, N. v.; Heitz, F.; Grimellec, C. l. 2001. Domain Formation in Models of the Renal Brush Border Membrane Outer Leaflet. *Biophys. J.* 81:547-555.

(142) Reviakine, I.; Bergsma-Schutter, W.; Brisson, A. 1998. Growth of Protein 2-D Crystals on Supported Planar Lipid Bilayers Imaged in Situ by AFM. *J. Struct. Biol.* 121:356-361.

(143) Reviakine, I.; Brisson, A. 2001. Streptavidin 2D crystals on Supported Phospholipid Bilayers: Towards Constructing Anchored Phospholipid Bilayers. *Langmuir* 17:8293-8299.

(144) Rinia, H. A.; Kik, R. A.; Demel, R. A.; Snel, M. M. E.; Killian, J. A.; van der Erden, J. P. J. M.; de Kruijff, B. 2000. Visualization of highly ordered striated domains induced by transmembrane peptides in supported phosphatidylcholine bilayer. *Biochemistry* 39:5852-5858.

(145) Rädler, J.; Radmacher, M.; Gaub, H. E. 1994. Velocity-Dependent Forces in Atomic Force Microscopy Imaging of Lipid Films. *Langmuir* 10:3111-3115.

(146) Rotsch, C.; Radmacher, M. 1997. Mapping Local Electrostatic Forces with the Atomic Force Microscope. *Langmuir* 13:2325-2832.

(147) Muresan, A. S.; Lee, K. Y. C. 2001. Shape Evolution of Lipid Bilayer Patches Adsorbed on Mica: an Atomic Force Microscopy Study. *J. Phys. Chem. B* 105:852-855.

(148) Loi, S.; Sun, G.; Franz, V.; Butt, H.-J. 2002. Rupture of molecular thin films observed in atomic force microscopy. II. Experiment. *Phys. Rev. E* 66:031602-1-7.

(149) Egawa, H.; Furusawa, K. 1999. Liposome Adhesion on Mica Surface Studied by Atomic Force Microscopy. *Langmuir* 15:1660-1666.

(150) Pignataro, B.; Steinem, C.; Galla, H.-J.; Fuchs, H.; Janshoff, A. 2000. Specific Adhesion of Vesicles Monitored by Scanning Force Microscopy and Quartz Crystal Microbalance. *Biophys. J.* 78:487-498.

(151) Liang, X.; Mao, G.; Ng, K. Y. S. 2004. Probing small unilamellar EggPC vesicles on mica surface by atomic force microscopy. *Colloids Surf. B* 34:41-51.

(152) Reviakine, I.; Brisson, A. 2000. Formation of Supported Phospholipid Bilayers from Unilamellar Vesicles Investigated by Atomic Force Microscopy. *Langmuir* 16:1806-1815.

(153) Jass, J.; Tjärnhage, T.; Puu, G. 2000. From liposomes to supported, planar bilayer structures on hydrophilic and hydrophobic surfaces: an atomic force microscopy study. *Biophys. J.* 79:3153-3163.

(154) Leonenko, Z. V.; Carnini, A.; Cramb, D. T. 2000. Supported planar bilayer formation by vesicle fusion: the interaction of phopholipid vesicles with surfaces and the effect of gramicidin on bilayer properties using atomic force microscopy. *Biochim. Biophys. Acta* 1509:131-147.

(155) Karrasch, S.; Hegerl, R.; Hoh, J. H.; Baumeister, W.; Engel, A. 1994. Atomic force microscopy produces faithful high-resolution images of protein surfaces in an aqueous environment. *Proc. Natl. Acad. Sci. USA* 91:836-838.

(156) Müller, D. J.; Dencher, N. A.; Meier, T.; Dimroth, P.; Suda, K.; Stahlberg, H.; Engel, A.; Seelert, H.; Matthey, U. 2001. ATP synthase: constrained stoichiometry of the transmembrane rotor. *FEBS Lett.* 504:219-222.

(157) Müller, D. J.; Engel, A.; Carrascosa, J.; Veléz, M. 1997. The bacteriophage ϕ29 head-tail connector imaged at high resolution with atomic force microscopy in buffer solution. *EMBO J.* 16:2547-2553.

(158) Scheuring, S.; Seguin, J.; Marco, S.; Levy, D.; Breyton, C.; Robert, B.; Rigaud, J. L. 2003. AFM characterization of tilt and intrinsic flexibility of Rhodobacter sphaeroides light harvesting complex 2 (LH2). *J. Mol. Biol.* 325:569-80.

(159) Müller, D. J.; Schoenenberger, C.-A.; Schabert, F.; Engel, A. 1997. Structural Changes in Native Membrane Proteins Monitored at Subnanometer Resolution with the Atomic Force Microscope: A Review. *J. Struct. Biol.* 119:149-157.

(160) Müller, D. J.; Fotiadis, D.; Engel, A. 1998. Mapping flexible protein domains at subnanometer resolution with the atomic force microscope. *FEBS Lett.* 430:105-111.

(161) Fotiadis, D.; Liang, Y.; Filipek, S.; Saperstein, D. A.; Engel, A.; Palczewski, K. 2003. Atomic-force microscopy: Rhodopsin dimers in native disc membranes. *Nature* 421:127-128.

(162) Scheuring, S.; Seguin, J.; Marco, S.; Levy, D.; Robert, B.; Rigaud, J. L. 2003. Nanodissection and high-resolution imaging of the Rhodopseudomonas viridis photosynthetic core complex in native membranes by AFM. *Proc. Natl. Acad. Sci. USA* 100:1690-1693.

(163) Bahatyrova, S.; Frese, R. N.; Siebert, C. A.; Olsen, J. D.; Werf, K. O. v. d.; Grondelle, R. v.; Niederman, R. A.; Bullough, P. A.; Otto, C.; Hunter, C. N. 2004. The native architecture of a photosynthetic membrane. *Nature* 430:1058-1062.

(164) Kowalewski, T.; Holtzman, D. M. 1999. *In situ* atomic force microscopy study of Alzheimer's β-amyloid peptide on different substrates: New insights into mechanism of β-sheet formation. *Proc. Natl. Acad. Sci. USA* 96:3688-3693.

(165) Goldsbury, C.; Kistler, J.; Aebi, U.; Arvinte, T.; Cooper, G. J. S. 1999. Watching Amyloid Fibrils Grow by Time-lapse Atomic Force Microscopy. *J. Mol. Biol.* 285:33-39.

(166) Thomson, N. H.; Kasas, S.; Smith, B.; Hansma, H. G.; Hansma, P. K. 1996. Reversible Binding of DNA to Mica for AFM Imaging. *Langmuir* 12:5905-5908.

(167) Kasas, S.; Thomson, N. H.; Smith, B. L.; Hansma, H. G.; Zhu, X.; Guthold, M.; Bustamante, C.; Kool, E. T.; Kashlev, M.; Hansma, P. K. 1997. E. coli RNA polymerase activity observed using atomic force microscopy. *Biochemistry* 36:461-468.

(168) Zuccheri, G.; Dame, R. T.; Aquila, M.; Muzzalupo, I.; Samori, B. 1998. Conformational fluctuations of supercoiled DNA molecules observed in real time with a scanning force microscope. *Appl. Phys. A* 66:S585-S589.

(169) Nagami, F.; Zuccheri, G.; Samori, B.; Kuroda, R. 2002. Time-Lapse Imaging of Conformational Changes in Supercoiled DNA by Scanning Force Microscopy. *Anal. Biochem.* 300:170-176.

(170) Engel, A.; Schoenenberger, C.-A.; Müller, D. J. 1997. High resolution imaging of native biological sample surfaces using scanning probe microscopy. *Curr. Opin. Struct. Biol.* 7:279-284.

(171) Rief, M.; Grubmüller, H. 2002. Force Spectroscopy of Single Biomolecules. *ChemPhysChem* 3:255-261.

(172) Rief, M.; Gautel, M.; Oesterhelt, F.; Fernandez, J. M.; Gaub, H. E. 1997. Reversible Unfolding of Individual Titin Immunoglobulin Domains by AFM. *Science* 276:1109-1112.

(173) Williams, P. M.; Fowler, S. B.; Best, R. B.; Luis Toca-Herrera, J.; Scott, K. A.; Steward, A.; Clarke, J. 2003. Hidden complexity in the mechanical properties of titin. *Nature* 422:446-9.

(174) Schwaiger, I.; Kardinal, A.; Schleicher, M.; Noegel, A. A.; Rief, M. 2004. A mechanical unfolding intermediate in an actin-crosslinking protein. *Nat. Struct. Mol. Biol.* 11:81-85.

(175) Rief, M.; Clausen-Schaumann, H.; Gaub, H. E. 1999. Sequence-dependent mechanics of single DNA molecules. *Nat. Struct. Biol.* 6:346-349.

(176) Scheuring, S.; Stahlberg, H.; Chami, M.; Houssin, C.; Rigaud, J.-L.; Engel, A. 2002. Charting and unzipping the surface layer of Corynebacterium glutamicum with the atomic force microscope. *Mol. Microbiol.* 44:675-684.

(177) Hansma, H. G.; Laney, D. E. 1996. DNA binding to mica correlates with cationic radius: assay by atomic force microscopy. *Biophys. J.* 70:1933-1939.

(178) Butt, H.-J.-. 1991. Electrostatic interaction in atomic force microscopy. *Biophys. J.* 60:777-785.

(179) Müller, D. J.; Amrein, M.; Engel, A. 1997. Adsorption of Biological Molecules to a Solid Support for Scanning Probe Microscopy. *J. Struct. Biol.* 119:172-188.

(180) Müller, D. J.; Engel, A. 1997. The Height of Biomolecules Measured with the Atomic Force Microscope Depends on Electrostatic Interactions. *Biophys. J.* 73:1633-1644.

(181) Müller, D. J.; Fotiadis, D.; Scheuring, S.; Müller, S. A.; Engel, A. 1999. Electrostatically Balanced Subnanometer Imaging of Biological Specimen by Atomic Force Microscope. *Biophys. J.* 76:1101-1111.

(182) Rossell, J. P.; Allen, S.; Davies, M. C.; Roberts, C. J.; Tendler, S. J. B.; Williams, P. M. 2003. Electrostatic interactions observed when imaging proteins with the atomic force microscope. *Ultramicroscopy* 96:37-46.

(183) Beckmann, M.; Nollert, P.; Kolb, H.-A. 1998. Manipulation and Molecular Resolution of a Phophatidylcholine-Supported Planar Bilayer by Atomic Force Microscopy. *J. Membrane Biol.* 161:227-233.

(184) Butt, H.-J. 1992. Measuring local surface charge densities in electrolyte solutions with a scanning force microscope. *Biophys. J.* 63:578-582.

(185) Czajkowsky, D. M.; Allen, M. J.; Elings, V.; Shao, Z. 1998. Direct visualization of surface charge in aqueous solution. *Ultramicroscopy* 74:1-5.

(186) Johnson, A. S.; Nehl, C. L.; Mason, M. G.; Hafner, J. H. 2003. Fluid Electric Force Microscope for Charge Density Mapping in Biological Systems. *Langmuir* 19:10007-10010.

(187) Philippsen, A.; Im, W.; Engel, A.; Schwirmer, T.; Roux, B.; Müller, D. J. 2002. Imaging the Electrostatic Potential of Transmembrane Channels: Atomic Probe Microscopy of OmpF Porin. *Biophys. J.* 82:1667-1676.

(188) Richter, R. P.; Brisson, A. 2003. Characterization of lipid bilayers and protein assemblies supported on rough surfaces by atomic force microscopy. *Langmuir* 19:1632-1640.

(189) Lyubchenko, Y. L.; Shlyakhenko, L. S. 1997. Visualization of supercoiled DNA with atomic force microscopy in situ. *Proc. Natl. Acad. Sci. USA* 94:496-501.

(190) Viani, M. B.; Schäffer, T. E.; Chand, A.; Rief, M.; Gaub, H. E.; Hansma, P. K. 1999. Small cantilevers for force spectroscopy of single molecules. *J. Appl. Phys.* 86:2258-2262.

(191) Ando, T.; Kodera, N.; Takai, E.; Maruyama, D.; Saito, K.; Toda, A. 2001. A High-speed Atomic Force Microscope for Studying Biological Macromolecules. *Proc. Natl. Acad. Sci. USA* 98:12468-12472.

(192) Kindt, J. H.; Fantner, G. E.; Cutroni, J. A.; Hansma, P. K. 2004. Rigid design of fast scanning probe microscopes using finite element analysis. *Ultramicroscopy* 100:259-265.

(193) Schitter, G.; Stark, R. W.; Stemmer, A. 2004. Fast contact-mode atomic force microscopy on biological specimen by model-based control. *Ultramicroscopy* 100:253-257.

(194) Rodahl, M.; Höök, F.; Krozer, A.; Brzezinski, P.; Kasemo, B. 1995. Quartz crystal microbalance setup for frequency and Q-factor measurements in gaseous and liquid environments. *Rev. Sci. Instrum.* 66:3924-3930.

(195) Muratsugu, M.; Ohta, F.; Miya, Y.; Hosokawa, T.; Kurosawa, S.; Kamo, N.; Ikeda, H. 1993. Quartz Crystal Microbalance for the Detection of Microgram Quantities of Human Serum Albumin: Relationship between the Frequency Change and the Mass of Protein Adsorbed. *Anal. Chem.* 65:2933-2937.

(196) Caruso, F.; Furlong, D. N.; Kingshott, P. 1997. Characterization of Ferritin Adsorption onto Gold. *J. Colloid Interface Sci.* 186:129-140.

(197) Höök, F.; Rodahl, M.; Brzezinski, P.; Kasemo, B. 1998. Energy dissipation kinetics for protein and antibody-antigen adsorption under shear oscillation on a quartz crystal microbalance. *Langmuir* 14:729.

(198) Höök, F.; Vörös, J.; Rodahl, M.; Kurrat, R.; Böni, P.; Ramsden, J. J.; Textor, M.; Spencer, N. D.; Tengvall, P.; Gold, J.; Kasemo, B. 2002. A comparative study of protein adsorption on titanium oxide surfaces using in situ ellipsometry, optical waveguide lightmode spectroscopy and quartz crystal microbalance/dissipation. *Colloids Surf. B* 24:155-170.

(199) Nishino, H.; Nihira, T.; Mori, T.; Okahata, Y. 2004. Direct Monitoring of Enzymatic Glucan Hydrolysis on a 27-MHz Quartz-Crystal Microbalance. *J. Am. Chem. Soc.* 126:2264-2265.

(200) Höök, F.; Ray, A.; Nordén, B.; Kasemo, B. 2001. Characterization of PNA and DNA Immobilization and Subsequent Hybridization with DNA Using Acoustic-Shear-Wave Attenuation Measurements. *Langmuir* 17:8305-8312.

(201) Larsson, C.; Rodahl, M.; Höök, F. 2003. Characterization of DNA Immobilization and Subsequent Hybridization on a 2D Arrangement of Streptavidin on a Biotin-Modified Lipid Bilayer Supported on SiO_2. *Anal. Chem.* 75:5080-5087.

(202) Glasmästar, K.; Höök, F.; Kasemo, B. 2002. Protein Resistance and Controlled Protein Adsorption on Supported Phospholipid Bilayers. *J. Colloid Interface Sci.* 246:40-47.

(203) Kastl, K.; Ross, M.; Gerke, V.; Steinem, C. 2002. Kinetics and Thermodynamics of Annexin A1 Binding to Solid-Supported Membranes. *Biochemistry* 41:10087-10094.

(204) Granéli, A.; Rydström, J.; Kasemo, B.; Höök, F. 2003. Formation of Supported Lipid Bilayer Membranes on SiO2 from Proteoliposomes Containing Transmembrane Proteins. *Langmuir* 2003:3.

(205) Ross, M.; Gerke, V.; Steinem, C. 2003. Membrane Composition Affects the Reversibility of Annexin A2t Binding to Solid Supported Membranes: A QCM Study. *Biochemistry* 42:3131-3141.

(206) Richter, R. P.; Lai Kee Him, J.; Brisson, A. 2003. Supported Lipid Membranes. *Materials Today* 6:32-37.

(207) Pope, L. H.; Allen, S.; Davies, M. C.; Roberts, C. J.; Tendler, S. J.; Williams, P. M. 2001. Probing DNA Duplex Formation and DNA-Drug Interactions by the Quartz Crystal Microbalance Technique. *Langmuir* 17:8300-8304.

(208) Fant, C.; Elwing, H.; Höök, F. 2002. The Influence of Cross-Linking on Protein-Protein Interactions in a Marine Adhesive: The Case of two Byssus Plaque Proteins from the Blue Mussel. *Biomacromolecules* 3:732-741.

(209) Höök, F.; Kasemo, B.; Nylander, T.; Fant, C.; Scott, K.; Elwing, H. 2001. Variations in Coupled Water, Viscoelastic Properties, and Film Thickness of a Mefp-1 Protein Film during Adsorption and Cross-Linking: A Quartz Crystal Microbalance with Dissipation Monitoring, Ellipsometry, and Surface Plasmon Resonance Study. *Anal. Chem.* 73:5796-5804.

(210) Fredriksson, C.; Kihlman, S.; Rodahl, M.; Kasemo, B. 1998. The piezoelectric quartz crystal mass and dissipation sensor: a means of studying cell adhesion. *Langmuir* 14:248-251.

(211) Reiss, B.; Janshoff, A.; Steinem, C.; Seebach, J.; Wegener, J. 2003. Adhesion Kinetics of Functionalized Vesicles and Mammalian Cells: A Comparative Study. *Langmuir* 19:1816-1823.

(212) Höök, F.; Larsson, C.; Fant, C. 2002. Biofunctional Surfaces Studied by Quartz Crystal Microbalance with Dissipation Monitoring. *In* Encyclopedia of Surface and Colloid Science. Marcel Dekker, Inc., digital publisher. 774-791.

(213) Svedhem, S.; Dahlberg, D.; Ekeroth, J.; Kelly, J.; Höök, F.; Gold, J. 2003. In Situ Peptide-Modified Supported Lipid Bilayers for Controlled Cell Attachment. *Langmuir* 19:6730-6736.

(214) Janshoff, A.; Galla, H.-J.; Steinem, C. 2000. Piezoelectric Mass-Sensing Devices as Biosensors - An Alternative to Optical Biosensors? *Angew. Chemie Int. Ed.* 39:4004-4032.

(215) Keller, C. A.; Glasmästar, K.; Zhdanov, V. P.; Kasemo, B. 2000. Formation of supported membranes from vesicles. *Phys. Rev. Lett.* 84:5443-5446.

(216) Reimhult, E.; Höök, F.; Kasemo, B. 2002. Vesicle adsorption on SiO_2 and TiO_2: Dependence on vesicle size. *J. Chem. Phys.* 117:7401-7404.

(217) Reimhult, E.; Höök, F.; Kasemo, B. 2002. Temperature dependence of formation of a supported phospholipid bilayer from vesicles on SiO_2. *Phys. Rev. E* 66:051905-1-4.

(218) Reimhult, E.; Höök, F.; Kasemo, B. 2003. Intact vesicle adsorption and supported biomembrane formation from vesicles in solution: influence of surface chemistry, vesicle size, temperature and osmotic pressure. *Langmuir* 19:1681-1691.

(219) Richter, R. P.; Brisson, A. 2004. QCM-D on mica for parallel QCM-D - AFM studies. *Langmuir* 20:4609-4613.

(220) Seantier, B.; Breffa, C.; Félix, O.; Decher, G. 2004. In Situ Investigations of the Formation of Mixed Supported Lipid Bilayers Close to the Phase Transition Temperature. *Nano Letters* 4:5-10.

(221) Picart, C.; Lavalle, P.; Hubert, P.; Cuisinier, F. J. G.; Decher, G.; Schaaf, P.; Voegel, J.-P. 2001. Buildup Mechanism for Poly(L-lysine)/Hyaluronic Acid Films onto a Solid Surface. *Langmuir* 17:7414-7424.

(222) Plunkett, M. A.; Claesson, P. M.; Ernstsson, M.; Rutland, M. W. 2003. Comparison of the Adsorption of Different Charge Density Polyelectrolytes: A Quartz Crystal Microbalance and X-ray Photoelectron Spectroscopy Study. *Langmuir* 19:4673-4681.

(223) Halthur, T. J.; Elofsson, U. M. 2004. Multilayers of Charged Polypeptides As Studied by in Situ Ellipsometry and Quartz Crystal Microbalance with Dissipation. *Langmuir* 20:1739-1745.

(224) Hübsch, E.; Ball, V.; Senger, B.; Decher, G.; Voegel, J.-C.; Schaaf, P. 2004. Controlling the Growth Regime of Polyelectrolyte Multilayer Films: Changing from Exponential to Linear Growth by Adjusting the Composition of Polyelectrolyte Mixtures. *Langmuir* 20:1980-1985.

(225) Munro, J. C.; Frank, C. W. 2004. Adsorption of Lipid-Functionalized Poly(ethylene glycol) to Gold Surfaces as a Cushion for Polymer-Supported Lipid Bilayers. *Langmuir* 20:3339-3349.

(226) Andersson, J.; Larsson, R.; Richter, R. P.; Ekdahl, K. N.; Nilsson, B. 2001. Binding of a model regulator of complement activation (RCA) to a biomaterial surface: surface-bound factor H inhibits complement activation. *Biomaterials* 22:2435-2443.

(227) Andersson, J. 2003. Complement Activation Triggered by Biomaterial Surfaces. Mechanisms and Regulation [PhD]. Uppsala, Sweden: Uppsala University.

(228) Andersson, J.; Sanchez, J.; Ekdahl, K. N.; Elgue, G.; Nilsson, B.; Larsson, R. 2003. Optimal heparin surface concentration and antithrombin binding capacity as evaluated with human non-anticoagulated blood *in vitro*. *Journal of Biomedical Materials Reseach* 67A:458-466.

(229) Sauerbrey, G. 1959. Verwendung von Schwingquartzen zur Wägung dünner Schichten und zur Mikrowägung. *Z. Phys.* 155:206-222.

(230) Voinova, M. V.; Rodahl, M.; Jonson, M.; Kasemo, B. 1999. Viscoelastic Accoustic Response of Layered Polymer Films at Fluid-Solid Interfaces: Continuum Mechanics Approach. *Phys. Scripta* 59:391-396.

(231) Stockbridge, C. D. 1966. Effects of gas pressure on quartz-crystal microbalances. *In* Vacuum Microbalance Techniques. Plenum Press, New York. 147.

(232) Kanazawa, K. K.; Gordon III, J. G. 1985. Frequency of a quartz microbalance in contact with liquid. *Anal. Chem.* 57:1770-1771.

(233) Rodahl, M.; Kasemo, B. 1996. On the measurement of thin liquid overlayers with the quartz-crystal microbalance. *Sens. Actuators A* 54:448-456.

(234) Geelhood, S. J.; Frank, C. W.; Kanazawa, K. 2002. Transient Quartz Crystal Microbalance Behaviors Compared. *J. Electrochem. Soc.* 149:H33-H38.

(235) Vörös, J. 2004. The Density and Refractive Index of Adsorbing Protein Layers. *Biophys. J.* 87:553-561.

(236) Reimhult, E. 2004. On the Formation of Supported Phospholipid Bilayers [PhD]. Göteborg, Sweden: Chalmers University of Technology and Göteborg University.

(237) Martin, S. J.; Frye, G. C.; Ricco, A. J. 1993. Effect of Surface Roughness on the Response of Thickness-Shear Mode Resonators in Liquids. *Anal. Chem.* 65:2910-2922.

(238) Martin, S. J.; Frye, G. C.; Wessendorf, K. O. 1994. Sensing liquid properties with thickness-shear mode resonators. *Sens. Actuators A* 44:209-218.

(239) Spikes, H.; Granick, S. 2003. Equation for Slip of Simple Liquids at Smooth Solid Surfaces. *Langmuir* 19:5065-5071.

(240) Borovsky, B.; Mason, B. L.; Krim, J. 2000. Scanning tunneling microscope measurements of the amplitude of vibration of a quartz crystal oscillator. *J. Appl. Phys.* 88:4017-4021.

(241) Wang, A. W.; Kiwan, R.; White, R. M.; Ceriani, R. L. 1998. A silicon-based ultrasonic immunoassay for detection of breast cancer antigens. *Sens. Actuators B* 49:13-21.

(242) Cooper, M. A.; Dultsev, F. N.; Minson, T.; Ostanin, V. P.; Abell, C.; Klenerman, D. 2001. Direct and sensitive detection of a human virus by rupture event scanning. *Nat. Biotechn.* 19:833-837.

(243) Höök, F. personal communication.

(244) Bucur, R. V.; Carlsson, J.-O.; Mecea, V. M. 1996. Quartz-crystal mass sensors with glued foil electrodes. *Sens. Actuators B* 37:91-95.

(245) Drude, P. 1889. *Ann. Phys.* 272:532.

(246) Winterbottom, A. B. 1955. Optical Studies of Metal Surfaces. *In* The Royal Norwegian Scientific Society Report No. 1. Bruns, F., editor, Trondheim, Norway.

(247) McCrackin, F. L.; Passaglia, E.; Stromberg, R. R.; Steinberg, H. L. 1963. Measurement of the Thickness and Refractive Index of Very Thin Films and the Optical Properties of Surfaces by Ellipsometry. *J. Res. Nat. Bur. Standards* 67A:363-377.

(248) Cuypers, P. A.; Corsel, J. W.; Janssen, M. P.; Kop, J. M. M.; Hermens, W. T.; Hemker, H. C. 1983. The Adsorption of Prothrombin to Phosphatidylserine Multilayers Quantitated by Ellipsometry. *J. Biol. Chem.* 258:2426-2430.

(249) Andree, H. A. M.; Hermens, W. T.; Willems, G. M. 1993. Testing protein adsorption models by off-null ellipsometry: Determination of binding constants from a single adsorption curve. *Colloids Surf. A* 78:133-141.

(250) Benes, M.; Billy, D.; Hermens, W. T.; Hof, M. 2002. Muscovite (mica) allows the characterization of supported bilayers by ellipsometry and confocal fluorescence correlation spectroscopy. *Biol. Chem.* 383:337-341.

(251) Lenne, P. F.; Berge, B.; Renault, A.; Zakri, C.; Vénien-Bryan, C.; Courty, S.; Balavoine, F.; Bergsma-Schutter, W.; Brisson, A.; Grubel, G.; Boudet, N.; Konovalov, O.; Legrand, J. F. 2000. Synchrotron radiation diffraction from two-dimensional protein crystals at the air/water interface. *Biophys. J.* 79:496-500.

(252) Benes, M.; Billy, D.; Benda, A.; Speijer, H.; Hof, M.; Hermens, W. T. 2004. Surface-dependent transitions during self-assembly of phospholipid membranes on mica, silica, and glass. *Langmuir* 20:10129-10137.

(253) Kop, J. M. M.; Cuypers, P. A.; Lindhout, T.; Hemker, H. C.; Hermens, W. T. 1984. The Adsorption of Prothrombin to Phospholipid Monolayers Quantitated by Ellipsometry. *J. Biol. Chem.* 259:13993-13998.

(254) Hermens, W. T.; Benes, M.; Richter, R. P.; Speijer, H. 2004. Effects of flow on solute exchange between fluids and supported biosurfaces. An overview. *Biotechn. Appl. Biochem.* 39:277-284.

(255) Bayerl, T. M.; Bloom, M. 1990. Physical properties of single phospholipid bilayers adsorbed to micro glass beads. A new vesicular model system studied by ^{2}H-nuclear magnetic resonance. *Biophys. J.* 58:357-362.

(256) Johnson, S. J.; Bayerl, T. M.; McDermott, D. C.; Adam, W. A.; Rennie, A. R.; Thomas, R. K.; Sackmann, E. 1991. Structure of an adsorbed dimyristoylphosphatidylcholine bilayer measured with specular reflection of neutrons. *Biophys. J.* 59:289-294.

(257) Kim, J.; Kim, G.; Cremer, P. S. 2001. Investigations of Water Structure at the Solid/Liquid Interface in the Presence of Supported Lipid Bilayers by Vibrational Sum Frequency Spectroscopy. *Langmuir* 17:7255-7260.

(258) Berg, S.; Ruths, M.; Johannsmann, D. 2003. Quartz crystal resonators with atomically smooth surfaces for use in contact mechanics. *Rev. Sci. Instrum.* 74:3845-3852.

(259) Israelachvili, J. N. 1973. Thin Film Studies Using Multiple-Beam Interferometry. *J. Colloid Interface Sci.* 44:259-272.

(260) Bailey, S. W. 1984. Micas. Ribbe, P. R., editor. BookCrafters, Inc., Chelsea, Michigan, USA.

(261) Gaines, G. L.; Tabor, D. 1956. Surface Adhesion and Elastic Properties of Mica. *Nature* 178:1304-1305.

(262) Pashley, R. M. 1981. DLVO and Hydration Forces between Mica Surfaces in Li^+, Na^+, K^+ and Cs^+ Electrolyte Solutions: A Correlation of Double-Layer and Hydration Forces with Surface Cation Exchange Properties. *J. Colloid Interface Sci.* 83:531-546.

(263) Pashley, R. M.; Israelachvili, J. 1984. DLVO and Hydration Forces between Mica Surfaces in Mg^{2+}, Ca^{2+}, Sr^{2+} and Ba^{2+} Chloride Solutions. *J. Colloid Interface Sci.* 97:446-455.

(264) Michel, R.; Lussi, J. W.; Csucs, G.; Reviakine, I.; Danuser, G.; Ketterer, B.; Hubbell, J. A.; Textor, M.; Spencer, N. D. 2002. Selective Molecular Assembly Patterning: A New Approach to Micro- and Nanochemical Patterning of Surfaces for Biological Applications. *Langmuir* 18:3281-3287.

(265) Spatz, J. P. 2002. Nano- and Micropatterning by Organic-Inorganic Templating of Hierarchical Self-Assembled Structures. *Angew. Chemie Int. Ed.* 41:3359-3362.

(266) Spatz, J. P. 2004. Cell-Nanostructure Interactions. *In* Nanobiotechnology. Niemeyer, C.,Mirkin, C., editors. Wiley-VCH Verlag GmbH & Co. KgaA, Weinheim, Germany. 53-65.

(267) Fromherz, P.; Kiessling, V.; Kottig, K.; Zeck, G. 1999. Membrane transistor with giant lipid vesicle touching a silicon chip. *Appl. Phys. A* 69:571-576.

(268) Loidl-Stahlhofen, A.; Kaufmann, S.; Braunschweig, T.; Bayerl, T. M. 1996. The thermodynamic control of protein binding to lipid bilayers for protein chromatography. *Nat. Biotechn.* 14:999-1002.

(269) Iler, R. K. 1979. The Chemistry of Silica. Solubility, Polymerization, Colloid and Surface Properties, and Biochemistry. Wiley-Interscience, New York.

(270) Sneh, O.; George, S. M. 1995. Thermal Stability of Hydroxyl Groups on a Well-Defined Silica Surface. *J. Phys. Chem.* 99:4639-4647.

(271) Penfold, J.; Staples, E.; Tucker, I. 2002. On the Consequences of Surface Treatment on the Adsorption of Nonionic Surfactants at the Hydrophilic Silica-Solution Interface. *Langmuir* 18:2967-2970.

(272) Bolt, G. H. 1957. Determination of the Charge Density of Silica Sols. *J. Phys. Chem.* 61:1166-1169.

(273) Ducker, W. A.; Senden, T. J.; Pashley, R. M. 1992. Measurement of forces in Liquids Using a Force Microscope. *Langmuir* 8:1831-1836.

(274) Chapel, J.-P. 1994. Electrolyte Species Dependent Hydration Forces between Silica Surfaces. *Langmuir* 10:4237-4243.

(275) Considine, R. F.; Drummond, C. J. 2001. Surface Roughness and Surface Force Measurement: A Comparison of Electrostatic Potentials Derived from Atomic Force Microscopy and Electrophoretic Mobility Measurements. *Langmuir* 17:7777-7783.

(276) Rubio, J.; Kitchener, J. A. 1976. The mechanism of adsorption of poly(ethylene oxide) flocculant on silica. *J. Colloid Interface Sci.* 57:132-142.

(277) Atkin, R.; Craig, V. S. J.; Biggs, S. 2002. Adsorption Kinetics and Structural Arrangements of Cationic Surfactants on Silica Surfaces. *Langmuir* 16:9374-9380.

(278) Morigaki, K.; Baumgart, T.; Jonas, U.; Offenhäuser, A.; Knoll, W. 2002. Photopolymerization of Diacetylene Lipid Bilayers and its Application to the Construction of Micropatterned Biomimetic Membranes. *Langmuir* 18:4082-4089.

(279) Brunette, D.; Tengvall, P.; Textor, M.; Thomsen, P., editors. 2001. Titanium in Medicine: Material Science, Surface Science, Engineering, Biological Responses and Medical Applications. Heidelberg and Berlin: Springer Verlag.

(280) Ducheyne, P.; Qiu, Q. 1999. Bioreactive ceramics: the effect of surface reactivity on bone formation and bone cell function. *Biomaterials* 20:2287-2303.

(281) Castner, D. G.; Ratner, B. D. 2002. Biomedical surface science: Foudations to frontiers. *Surf. Sci.* 500:28-60.

(282) Bearinger, J. P.; Vörös, J.; Hubbell, J. A.; Textor, M. 2003. Electrochemical Optical Waveguide Lightmode Spectroscopy (EC-OWLS): A Pilot Study Using Evanescent-Field Optical Sensing Under Voltage Control to Monitor Polycationic Polymer Adsorption onto Indium Tin Oxide (ITO) Coated Waveguide Chips. *Biotechnol. Bioeng.* 82:465-473.

(283) Zhang, Z.; Menges, B.; Timmons, R. B.; Knoll, W.; Förch, R. 2003. Surface Plasmon Resonance Studies of Protein Binding on Plasma Polymerized Di(ethylene glycol) Monovinyl Ether Films. *Langmuir* 19:4765-4770.

(284) Manso, M.; Rossini, P.; Malerba, I.; Valsesia, A.; Gribaldo, L.; Ceccone, G.; Rossi, F. 2004. Combination of ion beam stabilization, plasma etching and plasma deposition for the development of tissue engineering micropatterned supports. *J. Biomater. Sci. Polym. Ed.* 15:161-172.

(285) Arafat, A.; Schroën, K.; Smet, L. C. P. M. d.; Sudhölter, E. J. R.; Zuilhof, H. 2004. Tailor-Made Functionalization of Silicon Nitride Surfaces. *J. Am. Chem. Soc.* 126:8600-8601.

(286) Leckband, D.; Israelachvili, J. 2001. Intermolecular forces in biology. *Quart. Rev. Biophys.* 34:105-267.

(287) Wong, J. Y.; Park, C. K.; Seitz, M.; Israelachvili, J. 1999. Polymer-Cushioned Bilayers. II. An Investigation of Interaction Forces and Fusion Using the Surface Force Apparatus. *Biophys. J.* 77:1458-1468.

(288) Maeda, N.; Senden, T. J.; Meglio, J.-M. d. 2002. Micromanipulation of phospholipid bilayers by atomic force microscopy. *Biochim. Biophys. Acta* 1564:165-172.

(289) Karlsson, A.; Karlsson, R.; Karlsson, M.; Cans, A.-S.; Strömberg, A.; Ryttsén, F.; Orwar, O. 2001. Networks of nanotubes and containers. *Nature* 409:150-152.

(290) Karlsson, M.; Sott, K.; Cans, A.-S.; Karlsson, A.; Karlsson, R.; Orwar, O. 2001. Micropipet-Assisted Formation of Microscopic Networks of Unilamellar Lipid Bilayer Nanotubes and Containers. *Langmuir* 17:6754-6758.

(291) Roux, A.; Capello, G.; Cartaud, J.; Prost, J.; Goud, B.; Bassereau, P. 2002. A minimal system allowing tubulation using molecular motors pulling on giant liposomes. *Proc. Natl. Acad. Sci. USA* 99:5394-5399.

(292) Huang, N.-P.; Vörös, J.; De Paul, S. M.; Textor, M.; Spencer, N. D. 2002. Biotin-Derivatized Poly(L-lysine)-*g*-poly(ethylene glycol): A Novel Polymeric Interface for Bioaffinity Sensing. *Langmuir* 18:220-230.

(293) Yam, C.-M.; Xiao, Z.; Gu, J.; Boutet, S.; Cai, C. 2003. Modification of Silicon AFM Cantilever Tips with an Oligo(ethylene glycol) Derivative for Resisting Proteins and Maintaining a Small Tip Size for High Resolution Imaging. *J. Am. Chem. Soc.* 125:7498-7499.

(294) Wagner, P.; Hegner, M.; Güntherrodt, H.-J.; Semenza, G. 1995. Formation and *in Situ* Modification of Monolayers Chemisorbd on Ultraflat Template-Stripped Gold Surfaces. *Langmuir* 11:3867-3875.

(295) Stamou, D.; Gourdon, D.; Liley, M.; Burnham, N. A.; Kulik, A.; Vogel, H.; Duschl, C. 1997. Uniformly Flat Gold Surfaces: Imaging the Domain Structure of Organic Monolayers Using Scanning Force Microscopy. *Langmuir* 13:2425-2428.

(296) Priest, C. I.; Jacobs, K.; Ralston, J. 2002. Novel Approach to the Formation of Smooth Gold Surfaces. *Langmuir* 18:2438-2440.

(297) Rossetti, F. F.; Reviakine, I.; Textor, M. 2003. Characterization of Titanium Oxide Films Prepared by the Template-Stripping Method. *Langmuir* 19:10116-10123.

(298) Denis, F. A.; Hanarp, P.; Sutherland, D.; Gold, J.; Mustin, C.; Rouxhet, P. G.; Dufrêne, Y. F. 2002. Protein Adsorption on Model Surfaces with Controlled Nanotopography and Chemistry. *Langmuir* 18:819-828.

(299) Wetzer, B.; Pum, D.; Sleytr, U. B. 1997. S-Layer Stabilized Solid Supported Lipid Bilayers. *J. Struct. Biol.* 119:123-128.

(300) Ehahoun, H.; Gabrielli, C.; Keddam, M.; Perrot, H.; Cetre, Y.; Diguet, L. 2001. Corrosion, Passivation, and Anodic Films - Electrochemical Quartz Crystal Microbalance Corrosion Sensor for Solid Metals and Metal Alloys - Application to the Dissolution of 304 Stainless Steel. *J. Electrochem. Soc.* 148:B333-B336.

(301) Leitner, T.; Friedbacher, G.; Vallant, T.; Brunner, H.; Mayer, U.; Hoffmann, H. 2000. Investigations of the Growth of Self-Assembled Octadecylsiloxane Monolayers with Atomic Force Microscopy. *Mikrochimica Acta* 133:331-336.

(302) Berg, S.; Johannsmann, D. 2003. High Speed Microtribology with Quartz Crystal Resonators. *Phys. Rev. Lett.* 91:145505-1-4.

(303) Seifert, U.; Lipowsky, R. 1990. Adhesion of vesicles. *Phys. Rev. A* 42:4768-4771.

(304) Seifert, U.; Lipowsky, R. 1995. Morphology of Vesicles. *In* Structure and Dynamics of Membranes. From Cells to Vesicles. Lipowsky, R.,Sackmann, E., editors. Elsevier, Amsterdam. 403-464.

(305) Bernard, A.-L.; Guedeau-Boudeville, M.-A.; Jullien, L.; Meglio, J.-M. d. 2000. Strong Adhesion of Giant Vesicles on Surfaces: Dynamics and Permeability. *Langmuir* 16:6809-6820.

(306) Zhdanov, V. P.; Kasemo, B. 2001. Comments on Rupture of Adsorbed Vesicles. *Langmuir* 17:3518-3521.

(307) Zhdanov, V. P.; Keller, C. A.; Glasmästar, K.; Kasemo, B. 2000. Simulation of adsorption kinetics of lipid vesicles. *J. Chem. Phys.* 112:900-909.

(308) Kasson, P. M.; Pande, V. S. 2004. Molecular Dynamics Simulation of Lipid Reorientation at Bilayer Edges. *Biophys. J.* 86:3744-3749.

(309) Jiang, F. Y.; Bouret, Y.; Kindt, J. H. 2004. Molecular Dynamics Simulations of the Lipid Bilayer Edge. *Biophys. J.* 87:182-192.

(310) Rädler, J.; Strey, H.; Sackmann, E. 1995. Phenomenology and Kinetics of Lipid Bilayer Spreading on Hydrophilic Surfaces. *Langmuir* 11:4539-4548.

(311) Nissen, J.; Gritsch, S.; Wiegand, G.; Rädler, J. O. 1999. Wetting of phospholipid membranes on hydrophilic surfaces - Concepts towards self-healing membranes. *Eur. Phys. J. B* 10:335-344.

(312) Zhdanov, V. P.; Kasemo, B. 2000. Simulation of Diffusion of Vesicles at a Solid-Liquid Interface. *Langmuir* 16:4416-4419.

(313) Cremer, P. S.; Boxer, S. G. 1999. Formation and Spreading of Lipid Bilayers on Planar Glass Supports. *J. Phys. Chem. B* 103:2554-2559.

(314) Cremer, P. S.; Groves, J. T.; Kung, L. A.; Boxer, S. G. 1999. Writing and Erasing Barriers to Lateral Mobility into Fluid Phospholipid Bilayers. *Langmuir* 15:3893-3896.

(315) Nollert, P.; Kiefer, H.; Jähnig, F. 1995. Lipid Vesicle Adsorption versus Formation of Planar Bilayers on Solid Surfaces. *Biophys. J.* 69:1447-1455.

(316) Weng, K. C.; Stålgren, J. J. R.; Duval, D. J.; Risbud, S. H.; Frank, C. W. 2004. Fluid Biomembranes Supported on Nanoporous Aerogel/Xerogel Substrates. *Langmuir* 20:7232-7239.

(317) Johnson, J. M.; Taekijp, H.; Chu, S.; Boxer, S. G. 2002. Early Steps of Supported Bilayer Formation Probed by Single Vesicle Fluorescence Assays. *Biophys. J.* 83:3371-3379.

(318) Toikka, G.; Hayes, R. A. 1997. Direct Measurement of Colloidal Forces between Mica and Silica in Aqueous Electrolyte. *J. Colloid Interface Sci.* 191:102-109.

(319) Pashley, R. M. 1981. Hydration forces between mica surfaces in aqueous electrolyte solutions. *J. Colloid Interface Sci.* 80:153-162.

(320) Peschel, G.; Belouschek, P.; Müller, M. M.; Müller, M. R.; König, R. 1982. The interaction of solid surfaces in aqueous systems. *Colloid Polymer Sci.* 260:444-451.

(321) Colic, M.; Fisher, M. L.; Franks, G. V. 1998. Influence of Ion Size on Short-Range Repulsive Forces between Silica Surfaces. *Langmuir* 14:6107-6112.

(322) Vigil, G.; Xu, Z.; Steinberg, S.; Israelachvili, J. 1994. Interaction of Silica Surfaces. *J. Colloid Interface Sci.* 165:367-385.

(323) Nishimura, S.; Biggs, S.; Scales, P. J.; Healy, T. W.; Tsunematsu, K.; Tateyama, T. 1994. Molecular-Scale Structure of the Cation Modified Muscovite Mica Basal Plane. *Langmuir* 10:4554-4559.

(324) Xu, L.; Salmeron, M. 1998. An XPS and Scanning Polarization Force Microscopy Study of the Exchange and Mobility of Surface Ions on Mica. *Langmuir* 14:5841-5844.

(325) Du, Q.; Freysz, E.; Shen, Y. R. 1994. Vibrational Spectra of Water Molecules at Quartz/Water Interfaces. *Phys. Rev. Lett.* 72:238-241.

(326) Wilschut, J.; Hoekstra, D. 1984. Membrane fusion: from liposomes to biological membranes. *Trends Biochem. Sci.*:479-483.

(327) Ekeroth, J.; Konradsson, P.; Höök, F. 2002. Bivalent-Ion-Mediated Vesicle Adsorption and Controlled Supported Phospholipid Bilayer Formation on Molecular Phosphate and Sulfate Layers on Gold. *Langmuir* 18:7923-7929.

(328) Salafsky, J.; Groves, J. T.; Boxer, S. G. 1996. Architecture and Function of Membrane Proteins in Planar Supported Bilayers: A Study with Photosynthetic Reaction Centers. *Biochemistry* 35:14773-14781.

(329) Contino, P. B.; Hasselbacher, C. A.; Ross, J. B.; Nemerson, Y. 1994. Use of an oriented transmembrane protein to probe the assembly of a supported phospholipid monolayer. *Biophys. J.* 67:1113-1116.

(330) McPherson, A. 2003. Macromolecular crystallization in the structural genomics area. *J. Struct. Biol.* 142:1-2.

(331) Giegé, R.; Ducruix, A. 1999. Crystallization of Nucleic Acids and Proteins: A Practical Approach. Ducruix, A.,Giegé, R., editors. Oxford University Press, Oxford. 1 p.

(332) Chernov, A. A. 2003. Protein crystals and their growth. *J. Struct. Biol.* 142:3-21.

(333) Hemming, S. A.; Bochkarev, A.; Darst, S. A.; Kornberg, R. D.; Ala, P.; Yang, D. S. C.; Edwards, A. M. 1995. The Mechanism of Protein Crystal Growth from Lipid Layers. *J. Mol. Biol.* 246:308.

(334) Malkin, A. J.; Kuznetsov, Y. G.; Land, T. A.; DeYoreo, J. J.; McPherson, A. 1995. Mechanisms of growth for protein and virus crystals. *Nat. Struct. Biol.* 2:956.

(335) Farah, S. J.; Wang, S.-W.; Chang, W.-H.; Robertson, C. R.; Gast, A. P. 2001. Point Mutagenesis and Cocrystallization of Wild-Type and Mutant Proteins: A Study of Solid-Phase Coexistence in Two-Dimensional Protein Arrays. *Langmuir* 17:5731-5735.

(336) Nettles, J. H.; Li, H.; Cornett, B.; Krahn, J. M.; Snyder, J. P.; Downing, K. H. 2004. The binding mode of epothilone A on alpha,beta-tubulin by electron crystallography. *Science* 305:866-869.

(337) Strandburg, K. J. 1998. *Rev. Mod. Phys.* 60:161.

(338) Norde, W. 1986. Adsorption of Proteins from Solution at the Solid-Liquid Interface. *Adv. Coll. Int. Sci.* 25:267-340.

(339) Adamczyk, Z.; Siwek, B.; Zembala, M.; Belouschek, P. 1994. Kinetics of localized adsorption of colloid particles. *Adv. Coll. Int. Sci.* 48:151-280.

(340) Crank, J. 1975. The Mathematics of Diffusion. Clarendon Press, Oxford.

(341) Bayer, E. A.; Ben-Hur, H.; Wilchek, M. 1990. Isolation and Properties of Streptavidin. *Methods Enzymol.* 184:80-89.

(342) Ringler, P.; Müller, W.; Ringsdorf, H.; Brisson, A. 1997. Functionalized Lipid Tubules as Tools for Helical Crystallization of Proteins. *Chem. Eur. J.* 3:620-625.

(343) Holden, M. A.; Jung, S.-Y.; Yang, T.; Castellana, E. T.; Cremer, P. S. 2004. Creating Fluid and Air-Stable Solid Supported Lipid Bilayers. *J. Am. Chem. Soc.* 126:6512-6513.

(344) Giesen, P. L. A. 1992. Production of Thrombin at Macroscopic Surfaces [PhD]. Maastricht: Rijksuniversiteit Limburg te Maastricht. 127 p.

(345) Yatcilla, M. T.; Robertson, C. R.; Gast, A. P. 1998. Influence of pH on Two-Dimensional Streptavidin Crystals. *Langmuir* 14:497-503.

(346) Zhdanov, V. P.; Höök, F.; Kasemo, B. 2001. Simulation of Two-Dimensional Streptavidin Crystallization. *Proteins* 43:489-498.

(347) Amar, J. G.; Family, F. 1996. Kinetics of submonolayer and multilayer epitaxial growth. *Thin Solid Films* 272:208-222.

(348) Doudevski, I.; Hayes, W. A.; Schwartz, D. K. 1998. Submonolayer Island Nucleation and Growth Kinetics during Self-Assembled Monolayer Formation. *Phys. Rev. Lett.* 81:4927-4930.

(349) Doudevski, I.; Schwartz, D. K. 2001. Self-assembled monolayers in the context of epitaxial film growth. *Appl. Surf. Sci.* 175-176:17-26.

(350) Horn, R. G.; Smith, D. T.; Haller, W. 1989. Surface Forces and Viscosity of Water Measured between Silica Surfaces. *Chem. Phys. Lett.* 162:404-408.

(351) Hillier, A. C.; Kim, S.; Bard, A. J. 1996. Measurement of Double-Layer Forces at the Electrode/Electrolyte Interface Using the Atomic Force Microscope: Potential and Anion Dependent Interactions. *J. Phys. Chem.* 100:18808-18817.

(352) Moura, S. P.; Carmona-Ribeiro, A. M. 2003. Cationic Bilayer Fragments on Silica at Low Ionic Strength: Competitive Adsorption and Colloidal Stability. *Langmuir* 19:6664-6667.

(353) Raviv, U.; Laurat, P.; Klein, J. 2002. Time dependence of forces between mica surfaces in water and its relation to the release of surface ions. *J. Chem. Phys.* 116:5167-5172.

Appendix

List of publications

Richter, R. P.; Lai Kee Him, J.; Brisson, A. On the kinetics of adsorption and two-dimensional self-assembly of annexin A5 on supported lipid bilayers. *manuscript in preparation*.

Richter, R. P.; Brisson, A. Following the formation of supported lipid bilayers on mica - a study combining AFM, QCM-D and ellipsometry. *Biophys. J. submitted*.

Richter, R. P.; Maury, N.; Brisson, A. On the effect of the solid support on the inter-leaflet distribution of lipids in supported lipid bilayers. *Langmuir, in press*.

Hermens, W. T.; Benes, M.; Richter, R. P.; Speijer, H. 2004. Effects of flow on solute exchange between fluids and supported biosurfaces. An overview. *Biotechn. Appl. Biochem.* 39:277-284.

Richter, R. P.; Brisson, A. 2004. QCM-D on mica for parallel QCM-D - AFM studies. *Langmuir* 20:4609-4613.

Richter, R. P.; Brisson, A. 2003. Characterization of lipid bilayers and protein assemblies supported on rough surfaces by atomic force microscopy. *Langmuir* 19:1632-1640.

Richter, R. P.; Lai Kee Him, J.; Brisson, A. 2003. Supported Lipid Membranes. *Materials Today* 6:32-37.

Richter, R.; Mukhopadhay, A.; Brisson, A. 2003. Pathways of lipid vesicle deposition on solid surfaces: a combined QCM-D and AFM study. *Biophys. J.* 85:3035-3047.

Andersson, J.; Larsson, R.; Richter, R. P.; Ekdahl, K. N.; Nilsson, B. 2001. Binding of a model regulator of complement activation (RCA) to a biomaterial surface: surface-bound factor H inhibits complement activation. *Biomaterials* 22:2435-2443.

Surface potential and surface charge of silica

TABLE A.1 Surface potential and surface charge of silica as a function of pH and electrolyte as determined by various methods. ψ_0 and ψ_ζ are the surface potential and the ζ-potential, respectively. Corresponding charges, σ_0 and σ_ζ, are determined using the Grahame equation (page 234 in ref. [7]).

solution			potential		surface charge		reference (remarks)
pH	salt	mM	ψ_0 (mV)	ψ_ζ (mV)	σ_0 (nm^{-2})	σ_ζ (nm^{-2})	
4	KNO_3	0.1	-60±18	-58±2	-0.015	-0.014	275 a), d), f)
4		1	-39±15	-45±2	-0.020	-0.024	
4		10	-45±12	-50±2	-0.073	-0.083	
4		100	-20±4	-20±3	-0.092	-0.092	
6		0.1	-102±22	-85±2	-0.026	-0.019	
6.2		1	-82±16	-77±4	-0.055	-0.049	
6.2		10	-48±14 g)	-70±2	-0.079 g)	-0.13	
6		100	-25±6 g)	-36±6	-0.12 g)	-0.18	
7		100	-30±6	-44±6	-0.14	-0.22	
8.2		0.1	-105±20	-93±2	-0.028	-0.022	
8		1	-82±10	-81±3	-0.055	-0.054	
8		10	-45±12 g)	-78±2	-0.073 g)	-0.16	
8		100	-26±6 g)	-50±6	-0.12 g)	-0.26	
5.8	NaCl	0.13	-90		-0.023		274 b), f)
5.7		1.5	-83		-0.068		(pyrogenic silica)
5.3		8	-63		-0.1		
5.6		100	-45		-0.23		
5.4	KCl	0.19	-71		-0.019		
5.5		1.6	-69		-0.052		
5.1		14	-52		-0.1		
5.2		140	-32		-0.18		
6.1	LiCl	0.11	-119		-0.039		
5.8		1.1	-104		-0.090		
5.5		11	-96		-0.24		
6.0		100	-86		-0.59		
5.4	CsCl	0.11	-70		-0.014		
5.3		1.1	-53		-0.03		
5.5		11	-65		-0.13		
5.7		100	-54		-0.29		
	NaCl	0.11	-40 b		-0.007		350 b), f)
		1.1	-32		-0.016		(pyrogenic silica,
		11	-28		-0.044		pH not determined)
		110	-23		-0.11		
2	NaCl	1	-13		-0.019		273 c)
2.6		1	-35		-0.028		(cantilever not calibrated)
3		1	-35		-0.027		
4		1	-48		-0.029		
5.7		0.11	-61		-0.018		
5.7		1	-53		-0.028		
5.7		10	-34 g)		-0.048 g)		
5.7		100	-21 g)		-0.083 g)		
7		1	-60		-0.038		
10		1	-67		-0.037		

solution			potential		surface charge		reference (remarks)
pH	salt	mM	ψ_0 (mV)	ψ_ζ (mV)	σ_0 (nm^{-2})	σ_ζ (nm^{-2})	
5	NaCl	1			-<0.013		[272] e)
5		10			-0.019		
5		100			-0.038		
5		1000			-0.075		
6		1			-0.031		
6		10			-0.056		
6		100			-0.094		
6		1000			-0.14		
7		1			-0.063		
7		10			-0.11		
7		100			-0.2		
7		1000			-0.31		
8		1			-0.14		
8		10			-0.24		
8		100			-0.39		
8		1000			-0.61		
3	NaCl	0.2	-35	-15	-0.019	-0.008	[318] a), d), f)
4		0.2	-55	-30	-0.016	-0.008	(observed variations for
5.8		0.2	-91	-42	-0.030	-0.01	different types of silica)
5.8		2	-54		-0.041		
6		0.2	-85	-52	-0.026	-0.012	
7		0.2	-82	-62	-0.024	-0.016	
8		0.2	-78	-70	-0.022	-0.019	
9		0.2	-82	-70	-0.024	-0.019	
10		0.2	-82	-82	-0.024	-0.024	
5.5	KCl	0.1	-65		-0.012		[351] c), f)
5.5		1	-41		-0.020		(glass cover slips)
5.5		10	-19 g)		-0.029 g)		
5.5		100	-5.5 g)		-0.046 g)		
6.5	KCl	1		-45		-0.023	[352] d), f)

a) ψ_0 determined with a colloidal probe AFM, configuration of two μm-sized spheres.
b) ψ_0 determined with the surface force apparatus.
c) ψ_0 determined with a colloidal probe AFM, configuration of a μm-sized sphere and a planar support.
d) ψ_ζ determined by electrophoretic mobility measurements of a solution of colloidal silica.
e) σ_0 calculated from the number of protonated SiOH groups as determined from the free ion concentration in a solution of colloidal silica.
f) σ_0 or σ_ζ are not given in the references but were determined using the Grahame equation, taking into account the concentration of H^+ [262].
g) Values are likely underestimated due to roughness effects [275].

Surface potential and surface charge of mica

TABLE A.2 Surface potential and surface charge of mica as a function of pH and electrolyte as determined by various methods. ψ_0 and ψ_ζ are the surface potential and the ζ-potential, respectively. Corresponding charges, σ_0 and σ_ζ, are determined using the Grahame equation (page 234 in ref. [7]).

solution			potential		surface charge		reference (remarks)
pH	salt	mM	ψ_0 (mV)	ψ_ζ (mV)	σ_0 (nm^{-2})	σ_ζ (nm^{-2})	
5.7	NaCl	0.04	-123		-0.026		262 b), d)
5.7		0.1	-112		-0.032		
5.7		1.4	-143		-0.22		
5.7		10	-72		-0.14		
5.7	KCl	0.04	-90		-0.013		
5.7		0.3	-100		-0.044		
5.7		1	-90		-0.065		
5.7		10	-55		-0.094		
5.4	LiCl	0.1	-90		-0.021		
5.4		1	-95		-0.072		
5.4		10	-114		-0.33		
5.4		60	-95		-0.55		
5.8	CsCl	0.04	-110		-0.020		
5.8		0.1	-92		-0.021		
5.8		1	-80		-0.052		
5.8	H_2O [f]	0.005	-150		-0.009		263 b), e)
5.8	$CaCl_2$ [g]	0.03	-90		-0.066		
5.8		0.5	-50		-0.056		
5.8		1	-35		-0.041		
2.9	H_2O [f]	0.007	-130		-0.11		319 b)
4.9	H_2O [f]	0.007	-100		-0.019		
5.1	H_2O [f]	0.007	-165		-0.023		
6.2	KBr	0.5	-100		-0.055		
6.3	NaCl	5	-100		-0.2		
6.5	H_2O [f]	0.007	-150		-0.015		
8.9	NaCl	0.5	-93		-0.049		
11.1	KCl	1.2	-67		-0.056		
5.8	NaCl	0.2	-73		-0.02		318 a), d)
5.8		0.2	-21 [h]		-0.004 [h]		
5.8		2	-5 [h]		-0.003 [h]		
6.1	H_2O [f]	0.006	-110		-0.012		353 b) (observed memory effect)
5.5	KCl	1		-110		-0.097	323 c), d)

pH	solution salt	mM	potential ψ_0 (mV)	potential ψ_ζ (mV)	surface charge σ_0 (nm^{-2})	surface charge σ_ζ (nm^{-2})	reference (remarks)
	NaCl	0.02		-112		-0.015	149 c), d)
		0.2		-80		-0.024	(ph not determined though
		2		-65		-0.053	likely to be between 5 and 6)
		20		-60		-0.15	
	$CaCl_2$	0.02		-80		-0.037	
		0.2		-55		-0.043	
		2		-25		-0.036	
		20		-12		-0.046	
	$LaCl_3$	0.02		8			
		0.2		25			
		2		45			
		20		54			

[a] ψ_0 determined with a colloidal probe AFM, configuration of a μm-sized sphere and a planar support.
[b] ψ_0 determined with the surface force apparatus.
[c] ψ_ζ determined by the plane interface technique. The configuration involves the measurement of a flow profile in a rectangular cell with one mica-wall and one silica wall.
[d]) σ_0 or σ_ζ are not given in the references but were determined using the Grahame equation, taking into account the concentration of H^+ [262].
[e]) σ_0 are not given in the reference but were determined using the Grahame equation, taking into account the concentration of H^+ [263].
[f]) Measurements performed in ultrapure water.
[g]) Other divalent cations gave similar results[263].
[h]) Values obtained upon exposure to air between cleavage and wetting[318].

Sommaire (version française)

Les membranes lipidiques déposées sur support solide sont couramment utilisées comme modèle de membranes cellulaires et présentent des applications potentielles dans le domaine des biotechnologies. Ce travail de thèse a permis de caractériser, en détail, les processus de dépôt de liposomes et la formation des bicouches lipidiques supportées (SLBs) sur support de mica et de silice. L'influence de la charge des lipides et le rôle des ions Ca^{2+} dans la formation des SLBs ont été caractérisés. De plus nous avons réalisé une étude de la liaison spécifique et de l'autoassemblage de la protéine annexine A5 sur les SLBs.

Les deux principales techniques de caractérisation utilisées pour cette étude sont la microscopie à force atomique (AFM) et la microbalance à cristal de quartz avec mesure de dissipation (QCM-D). Les obstacles techniques majeurs associés à l'imagerie par AFM des assemblages lipidiques ont été résolus. L'utilisation en parallèle des techniques QCM-D et AFM sur support de mica a été mise au point. La complémentarité de ces deux techniques a permis de caractériser la cinétique et de visualiser les structures intermédiaires formées lors des processus d'auto-organisation bidimensionnelle des lipides et des protéines.

Mots clés : microscopie à force atomique (AFM) ; microbalance à cristal de quartz avec mesure de dissipation (QCM-D) ; bicouche lipidique déposée sur support solide (SLB) ; vésicule unilamellaire préparée par sonication (SUV) ; assemblage bidimensionnel ; dioleoylphosphatidylcholine (DOPC) ; dioleoylphosphatidylsérine (DOPS) ; dioleoyltrimethylammoniumpropane (DOTAP) ; annexine A5 ; mica ; silice ; calcium

Abstract (English version)

Supported lipid membranes (SLBs) are popular models of cell membranes with potential biotechnological applications. In this work we characterize the process of vesicle deposition and SLB-formation on solid supports in detail. In particular, the role of the support (mica and silica), the lipid charge and the presence of calcium as determinants of the lipid deposition pathway are highlighted.

We exploit the SLBs as a biomimetic surface, in order to investigate the adsorption and two-dimensional self-assembly of annexin A5, a membrane-binding protein.

The main characterization techniques are the Quartz Crystal Microbalance with Dissipation Monitoring (QCM-D) and Atomic Force Microscopy (AFM). These methods are demonstrated to be highly complementary, providing global kinetic information and local structural information on the self-organization processes simultaneously. In order to fully exploit the methods' complementarities, some technical obstacles had to be overcome. We identify and remedy artifacts associated with AFM-imaging of surface-confined lipid assemblies and combine QCM-D and AFM on identical supports, including mica.

Keywords: atomic force microscopy (AFM); quartz crystal microbalance with dissipation monitoring (QCM-D); supported lipid bilayer (SLB); small unilamellar vesicle (SUV); two-dimensional self-assembly; dioleoylphosphatidylcholine (DOPC); dioleoylphosphatidylserine (DOPS); dioleoyltrimethylammoniumpropane (DOTAP); annexin A5; mica; silica; calcium

Laboratoire d'Imagerie Moléculaire et Nano-Bio-Technologie
IECB, UMR-CNRS 5471, UNIVERSITE BORDEAUX I
2 rue Robert Escarpit
33607 Pessac, France